CRANFIELD UNIVERSITY

GRANT MCLELLAND

Aerodynamics of vortex ingestion for aero-engines

School of Engineering
Full-time Ph.D.

Submitted for the degree of Ph.D.
Academic Year: 2013 - 2014

Supervisor: Dr. David MacManus
December 2013

CRANFIELD UNIVERSITY

School of Engineering
Full-time Ph.D.

Submitted for the degree of Ph.D.

Academic Year 2013 - 2014

GRANT MCLELLAND

Aerodynamics of vortex ingestion for aero-engines

Supervisor: Dr. David MacManus
December 2013

This thesis is submitted in partial fulfilment of the requirements for the degree of Ph.D.

Executive Summary

The potential impact of inlet flow distortion on the stability and performance of aircraft engines remains a key concern for engine-airframe integration. Current and future configurations, such as Unmanned Combat Air Vehicles (UCAVs), and possible civil aircraft with large rear-mounted engines, feature closely-coupled intake and airframe aerodynamics. Such configurations are susceptible to the ingestion of streamwise vorticity generated upstream on the aircraft. There is a dearth of understanding of this ingestion process which, crucially, determines the nature of the flow distortion presented to the turbomachinery. To assess the risk of engine stability and performance deterioration, it is therefore necessary to understand and model the vortex ingestion process.

This research provides a novel application of Stereoscopic Particle Image Velocimetry (Stereo PIV) to obtain quantitative measurements of a streamwise vortex inside a contracting intake capture streamtube. The experiments were conducted in the $8' \times 6'$ low-speed wind tunnel using a $1/30^{th}$ scale intake model. Vortex generators were employed to create a streamwise vortex in the flow upstream of the intake. The streamtube contraction levels, vortex generator type, and vortex generator configuration were varied to establish fundamental understanding on the flow physics of vortex ingestion.

The vortex experiences notable levels of intensification as it passes through the contracting streamtube. The evolution of the vortex is strongly dependent on the streamtube contraction levels, the initial characteristics of the vortex prior to ingestion, and the trajectory that the vortex follows inside the capture streamtube.

In addition, detailed studies have been performed using Computational Fluid Dynamics (CFD) to establish an approach to simulate vortex ingestion flows. A number of guidelines have been developed using experimental measurements to ensure that the flow physics of vortex ingestion are captured. This approach permits vortex ingestion simulations to be performed to evaluate the inlet flow distortion characteristics in full-scale intake flows.

Acknowledgements

Firstly, I would like to acknowledge my supervisor, Dr. David MacManus. I am extremely grateful for his endless guidance, support and suggestions which have been crucial to the success of this research. I would also like to thank Rolls-Royce for their financial and technical support. In particular, I would like to acknowledge Chris Sheaf of Installations, and all of those from Rolls-Royce who attended the many technical presentations and meetings throughout the duration of my research. I also greatly appreciate the support and assistance of the technicians at the wind tunnel facility and in the test area at Cranfield University.

Special thanks to all of my friends and colleagues with whom I have shared great memories (and many coffee breaks) during my time at Cranfield.

Finally, I wish to express my gratitude to my parents, my sister Natalie, and my partner Marina. They have inspired me and supported me throughout the highs and lows of the PhD. I could not have done this without them.

Contents

List of Tables

Nomenclature

Roman Symbols

(d_x, d_y, d_z) Flow direction components

(I_{max}, J_{max}) Circular zone resolution in (r, θ) direction for VDM analysis

(x_v, y_v) Vortex centre location in Cartesian coordinates (m)

$\dot{m}_i$ Intake mass flow (kgs^{-1})

$\dot{m_\infty}$ Intake mass flow (kgs^{-1})

$\overline{P_{60}}$ Mean total pressure in 60^o sector with greatest total pressure loss

$\vec{V}$ Velocity vector (ms^{-1})

A Vatistas vortex model constant, streamwise momentum parameter (m^2s^{-1})

a_1 Empirical constant for Squire vortex model

A_i Intake inner (throat) area (m^2)

A_∞ Capture streamtube area far upstream of intake (m^2)

AR Wing planform aspect ratio

C_p Static pressure coefficient

C_μ Constant in turbulent dissipation rate equation

C_{P_0} Total pressure coefficient

D Intake outer diameter (m)

D_i Intake inner diameter at throat (m)

D_L Intake highlight plane diameter (m)

$DC60$ DC60 total pressure distortion descriptor (%)

k Turbulent kinetic energy ($m^2 s^{-2}$)

k_{max} Peak turbulent kinetic energy ($m^2 s^{-2}$)

l Turbulence length scale (m)

L_i Intake sideline length (m)

M Mach number

M_i Intake flow Mach number

N_{sl} Number of vortex swirl loops

p Static pressure (Pa)

P_0 Total pressure (Pa)

P_f Fan-face area-weighted average total pressure

q_f Fan-face area-weighted average dynamic pressure (Pa)

q_∞ Freestream dynamic pressure (Pa)

r, θ, z Polar coordinates ($m, ^o, m$)

r_c Vortex core radius (m)

r_f Vortex filament radius (m)

r_i Intake inner radius (m)

r_∞ Capture streamtube radius far upstream of intake (m)

r_{max} Circular zone radius for VDM analysis (m)

Re_c Chord Reynolds number

Re_v Vortex Reynolds number $= \left(\frac{\Gamma}{\nu}\right)$

S_{xy} In-plane mean strain rate (s^{-1})

$SC60$ SC60 total pressure distortion descriptor (%)

SI Swirl intensity distortion descriptor (^{o})

SI_{av} Average Swirl Intensity (^{o})

t Time (s)

t_{sl} Time for one vortex swirl loop (s)

TI Turbulence Intensity $= \left(\sqrt{\frac{1}{3}(u'^2 + v'^2 + w'^2)}\right)$ (ms^{-1})

$u', v', w')$ Mean Cartesian velocity turbulent fluctuations (ms^{-1})

VR Intake velocity ratio $\left(= \frac{W_i}{W_\infty}\right)$

w_c Streamwise velocity at vortex centre (ms^{-1})

W_i Intake flow average velocity (ms^{-1})

W_∞ Freestream velocity (ms^{-1})

x, y, z Cartesian coordinates (m)

x_{sl}, z_{sl} Streamwise distance corresponding to one vortex swirl loop (m)

(u, v, w) Velocity components in Cartesian coordinate system (ms^{-1})

(V_r, V_θ, V_z) Velocity components in polar coordinate system (ms^{-1})

$(V_{\theta,max})$ Peak tangential velocity (ms^{-1})

b Wing span (m)

c Wing chord (m)

VG Vortex generator

Abbreviations

BWB Blended Wing-Body

CFD Computational Fluid Dynamics

CL Centreline

DEHS Di-ethyl-hexyl-sebacate

FWHM Full-Width at Half-Maximum

LPS Linear Pressure Strain

MUSCL Monotone Upstream-Centred Schemes for Conservation Laws

OA Off-axis

PIV Particle Image Velocimetry

RANS Reynolds-Averaged Navier-Stokes

RSM Reynolds Stress Model

SA Spalart-Allmaras

SST Shear Stress Transport

UCAV Unmanned Combat Air Vehicle

VDM Vorticity Disk Method

VF Vortex Filament model

Greek Symbols

α Flow angle $\left(= tan^{-1}\frac{V_\theta}{V_z}\right)$

α^* Change in peak flow angle $= \left(\frac{tan\alpha_{max}}{tan\alpha_{max,0}}\right)$

α_{lo} Lamb-Oseen vortex model constant = 1.25643

α_{max} Peak flow angle (^{o})

α_{sw} Swirl angle $\left(= tan^{-1}\frac{V_{\theta,max}}{w_c}\right)$ (^{o})

α_{vg} Vortex generator angle of attack (^{o})

δ Apparent diffusion coefficient

δ_i Apparent diffusion coefficient for vortex intensification

ϵ Turbulent dissipation rate (m^2s^{-3})

Γ Circulation (m^2s^{-1})

Γ_0 Vortex total circulation (m^2s^{-1})

Γ_c Vortex core circulation (m^2s^{-1})

ν Kinematic viscosity ($m^2 s^{-1}$)

ν_t Turbulent viscosity ($m^2 s^{-1}$)

Ω Angular velocity $\left(= \frac{\omega_{z,av}}{2}\right)$

ω Specific dissipation rate (s^{-1})

ω_z Streamwise vorticity (s^{-1})

$\omega_{z,av}$ Average core vorticity (s^{-1})

ρ_i Intake flow density (kgm^{-3})

ρ_∞ Freestream density (kgm^{-3})

Subscripts

0 Initial value/value in unperturbed flow

max Peak value

RMS Root-mean square value

Chapter 1

Introduction

1.1 Overview

The potential impact of inlet flow distortion on the stability and performance of aircraft engines remains a key concern for engine-airframe integration. Inlet flow distortion has been the subject of continued study over the past 60 years, due to the associated risk of intake and engine performance degradation. The severity of the inlet flow distortion, and the subsequent response of the engine, depends on a number of factors, such as the aircraft operating condition, features of the intake design, and the tolerance of the engine to distortion [2]. One possible scenario which results in inlet flow distortion is the case where an externally-generated distortion is ingested by the intake. This has become increasingly likely in recent years since airframe manufacturers continue to explore highly unconventional engine airframe configurations for both civil and military aircraft.

Many proposed civil aircraft architectures feature rear-mounted ultra-high bypass ratio turbofan engines or open rotor engines, such as those depicted in Figure 1.1(a). Depending on the airframe arrangement and flight condition, these new engine installation arrangements may feature an increased risk of the ingestion of streamwise vortices generated on the upstream airframe. Examples of such vortices include those generated at the wing-tip of a canard, wing-junction vortices, and body or fuselage vortices. Furthermore, Blended Wing-Body (BWB) platforms (Figure 1.1(b)) which feature podded or embedded powerplants at the rear of the fuselage may also be at risk of streamwise vorticity ingestion. Recent experiments conducted by Gatlin et al [5] on a sub-scale BWB configuration highlighted that an intense streamwise vortex is generated at the leading edge

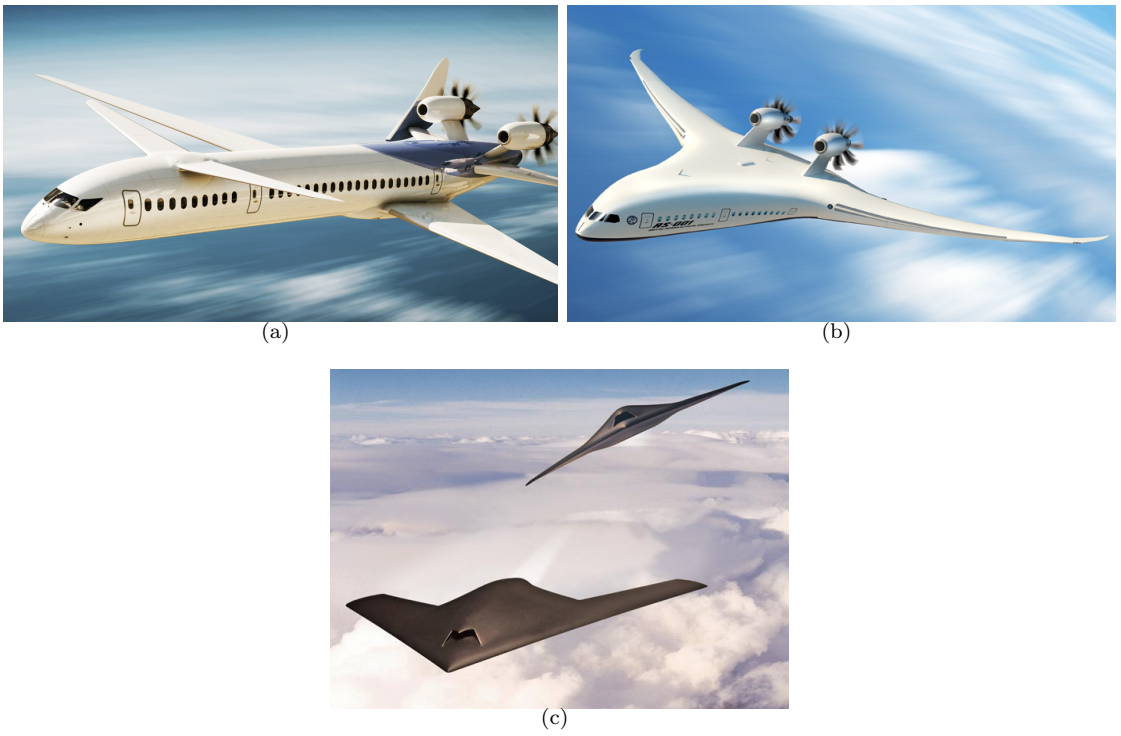

(a) (b)

(c)

FIGURE 1.1: Possible future civil aircraft engine airframe configurations, (a): Rear-mounted open rotor engines [3], (b): Blended Wing Body (BWB) airframe configuration with rear-mounted open rotor engines [3], (c): Example of an Unmanned Combat Air Vehicle (UCAV) [4]

of the wing at high angles of attack. The trajectory of the vortex, indicated from surface flow visualisation, suggests that the vortex will likely be ingested by a rear-mounted powerplant.

Vortical inlet flow distortion is also a possibility on Unmanned Combat Air Vehicles (UCAVs) (Figure 1.1(c)), which feature deeply embedded engines and complex intake designs. Such configurations feature a strong aerodynamic coupling between the intake and the airframe. Therefore, there is potential for vortical flow to be ingested by the intake at key points in the flight envelope. In addition, it has been found that the streamwise vortex generated by leading edge extensions on conventional combat aircraft can be ingested during dynamic manoeuvres with large changes in angle of attack and can result in an increase in the total pressure distortion levels within the intake [6].

The inlet flow distortion which results from the ingestion of a vortex is known to induce a loss in compressor surge margin and efficiency, and may cause the compressor to surge [7, 8, 9]. The distorted intake flow can also induce fan blade vibration and high-cycle fatigue

[10]. The detrimental effects on the engine performance and operability are therefore of ongoing concern. It has been recognised that the behaviour of the aircraft engine which is subject to swirl distortion is not consistent with the results from conventional methods which are used to predict the response of an engine to inlet flow distortion [8]. To address this shortcoming, the S-16 Turbine Engine Inlet Flow Distortion Committee [11] established inlet flow descriptor methods to permit the correlation of surge margin loss for a range of inlet swirl distortions. However, work is currently underway to establish the large datasets required to allow correlations to be developed. Furthermore, an emphasis has recently been placed on the need to correctly simulate such vortical inlet flow distortion using CFD [12]. It is clear, however, that there remains a lack of understanding of the impact of vortical distortion on turbomachinery performance and operability.

1.2 Project rationale

This research is concerned with the possible scenario where a streamwise vortex which has been generated on the airframe upstream of the aircraft engine location is subsequently ingested into the intake. This scenario is distinguished from the case of ground vortex ingestion, which results from an aerodynamic coupling between the intake aerodynamics and nearby boundary layer vorticity. This may occur due to the close proximity of the atmospheric boundary layer [7, 13] or on other surfaces such as the fuselage [14]. A schematic a possible vortex ingestion scenario which is of interest in this research is shown in Figure 1.2. In general, the scenario can be considered to be composed of three distinct vortex flow phases, namely, vortex generation, vortex convection, and vortex ingestion. The vortex generation process is concerned with the initial creation of the vortical flow, and the subsequent formation of a discrete vortex whose axis is approximately parallel to the streamwise direction. In the vortex convection phase, the vortex moves and evolves with the surrounding flow. If the vortex is contained within the capture streamtube of an engine intake, then the vortex will undergo an ingestion process. Importantly, the vortex generation and vortex convection processes have received considerable attention in the literature. However, there have been no prior studies on the behaviour of a streamwise vortex as it passes through the intake capture streamtube. As a consequence, there is a dearth of understanding on the likely characteristics of the vortex once it is inside the intake. This lack of understanding has direct implications for engine integration studies. Firstly, there is currently little information to allow an assessment of the possible inlet flow distortion levels which result from the ingestion of a vortex. Thus, it is not possible to

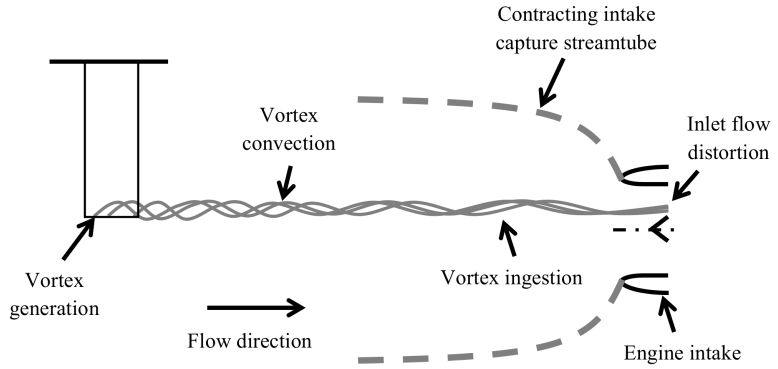

FIGURE 1.2: Schematic of streamwise vortex ingestion by an aircraft intake, illustrating the key flow phases experienced by an externally-generated streamwise vortex during ingestion

evaluate the likely impact that the vortex may have on the engine performance. Furthermore, there are no details to elucidate the influence that a change in vortex characteristics or intake conditions have on the details of the vortex ingestion process.

In summary, there are new challenges from the engine-airframe integration perspective which must be addressed to ensure compatibility between the engine and the airframe across the entire flight envelope. There is surprisingly little knowledge or understanding of the evolution of a streamwise vortex inside an intake capture streamtube, and no prior measurements. Without understanding of the fundamental fluid dynamics of vortex ingestion, or without the capability provided by an engineering model, the risk of engine performance degradation on novel engine airframe configurations cannot be assessed.

1.3 Aims and objectives

The purpose of this research is to establish fundamental understanding of the behaviour of a streamwise vortex inside the contracting capture streamtube of an aircraft intake. A wide range of vortex ingestion configurations, comprising different intake flow conditions and vortex characteristics, are investigated. The research has the following objectives:

- Establish Stereoscopic Particle Image Velocimetry as a measurement method for vortex ingestion experiments.

- Obtain quantitative measurements of streamwise vortex ingestion on a sub-scale intake model.

- Identify the fundamental flow physics which govern the behaviour of a streamwise vortex inside an intake capture streamtube.

- Assess the influence of the streamtube contraction levels, intake operating condition, initial vortex characteristics, and ingestion trajectory, on the vortex ingestion process.

- Develop a model of vortex ingestion which can be used to aid preliminary design calculations for engine-airframe integration studies.

- Establish and validate CFD methods and procedures to successfully perform simulations of vortex ingestion.

Chapter 2

Literature review

The purpose of this chapter is to provide a review of the most pertinent prior research on streamwise vortices, their behaviour when subjected to a streamwise contraction, and their effect on turbomachinery performance. It is first necessary to elucidate the most fundamental aspects of aircraft engine intake aerodynamics, which will establish the most important characteristics of the intake flow to which the ingested vortex will be subjected. In addition, the characteristics and the perturbation field attributed to vortices which are likely to be ingested are identified. Such characteristics play a central role in the definition of vortical distortions, along with the analysis of their behaviour during ingestion. The review then focusses on the current understanding of the behaviour of streamwise vortices in contracting flows, and the impact of streamwise vortices on inlet flow distortion characteristics and aircraft engine performance. The final section of the review highlights the challenges associated with the simulation of vortices using Computational Fluid Dynamics (CFD). This chapter is concluded with a summary of the current state-of-the-art, and identifies the deficiencies in knowledge which are addressed in this research.

2.1 Intake aerodynamics

The qualitative nature of the intake capture streamtube flow associated with a typical aircraft intake is illustrated in Figure 2.1. The extent of the intake capture streamtube is defined by the streamline which lies on the boundary between the flow which enters the intake and that which remains external to the intake. The mass flow through the capture streamtube is constant, and is equal to the mass flow requirement of the engine,

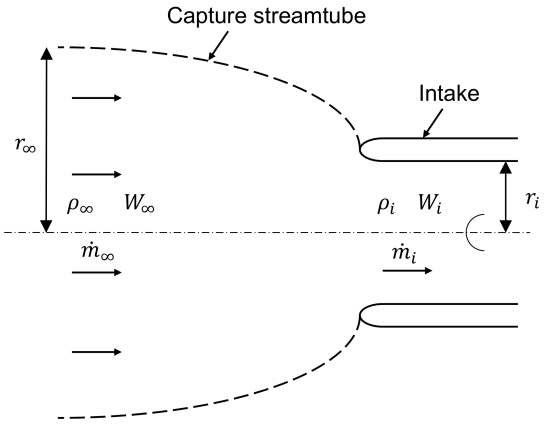

FIGURE 2.1: Schematic of a typical aircraft intake with key geometric parameters and flow properties

$\dot{m}_i$. Therefore, the characteristics of the flow inside the capture streamtube can be estimated with use of the continuity equation, Eq. 2.1, where ρ is the density, W is the average streamwise velocity and A is the capture streamtube cross-sectional area. Note that subscript ∞ refers to the conditions far upstream of the intake where the intake perturbation field is negligible, and subscript i refers to the conditions inside the intake.

$$\rho_\infty W_\infty A_\infty = \rho_i W_i A_i \tag{2.1}$$

In this research, it is assumed that the there are no surfaces, such as the aircraft fuselage or the wing, in close proximity to the aircraft intake. It is thus appropriate to assume that the capture streamtube is axisymmetric, such that Eq. 2.1 can be expressed in terms of the radius of the capture streamtube in the freestream (r_∞) and the intake inner radius, r_i, Eq. 2.2.

$$\left(\frac{r_\infty}{r_i}\right)^2 = \frac{\rho_i}{\rho_\infty}\frac{W_i}{W_\infty} \tag{2.2}$$

Under the assumption of incompressible flow, the dimensions of the capture streamtube are related directly to the intake velocity ratio $VR = W_i/W_\infty$, Eq. 2.3.

$$\left(\frac{r_\infty}{r_i}\right)^2 = \frac{W_i}{W_\infty} = VR \tag{2.3}$$

TABLE 2.1: Typical high bypass ratio civil aircraft engine dimensions and operating conditions at take-off

M_i	0.44
D_i (m)	2.61
$\dot{m}_i$ (kgs^{-1})	870
W_i (ms^{-1})	145

When the intake velocity ratio is greater than 1.0, the capture streamtube is larger than the intake inner diameter ($D_i = 2r_i$), and the flow inside the capture streamtube experiences a streamwise contraction. Similarly, when the intake velocity ratio is less than 1.0, the flow experiences a streamwise diffusion. It is of interest to ascertain the nature of the intake velocity ratio VR at key points in the aircraft flight envelope. For example, consider a large civil airliner equipped with modern high bypass ratio engines. Representative values of the engine dimensions and operating conditions at take-off are provided in Table 2.1. As the aircraft accelerates from stationary, there is an increase in the freestream velocity, W_∞. During the take-off phase, the intake flow velocity W_i remains approximately constant, so there is a corresponding reduction in the intake velocity ratio (Figure 2.2(a)). In addition, the intake capture streamtube radius reduces, Figure 2.2(b).

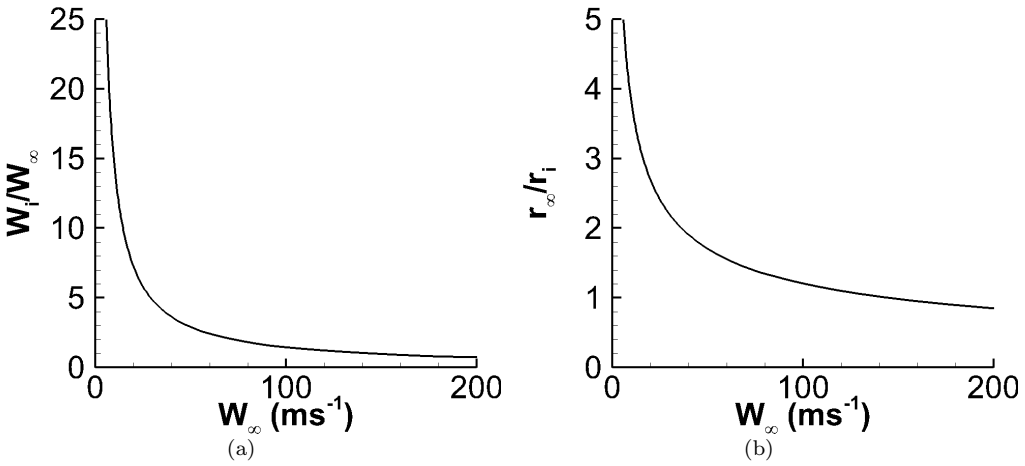

FIGURE 2.2: Evolution of intake capture streamtube characteristics for a typical civil airliner (Table 2.1) assuming incompressible flow, (a) Intake velocity ratio as a function of flight speed, (b), Intake capture streamtube radius as a function of freestream velocity

A typical twin-engined civil airliner will rotate and lift off the runway at approximately $80ms^{-1}$. At this freestream velocity, the intake velocity ratio (VR) and intake capture

streamtube radius (r_∞/r_i) will be 1.8 and 1.3, respectively. Therefore, during the take-off and initial climb-out phases of flight, the intake capture streamtube is larger than the intake diameter, and the flow inside the streamtube characterised by a streamwise contraction. As the aircraft continues on to the climb and cruise flight phases, the flight speed increases, and the engine mass flow will decrease. Therefore, there is a further reduction in the intake velocity ratio and capture streamtube diameter, such that the intake velocity ratio is close to, or less than, a value of 1.0. During approach and landing, the aircraft velocity will be similar to that during the initial climb-out flight phase. It is therefore possible that the capture streamtube will be greater than 1.0. For example, if the aircraft must perform a go-around manoeuvre, the engine mass flow will increase, which will cause a corresponding rise in the intake velocity ratio.

Based on the preceding discussion, it is possible to make some qualitative observations about the likeliness of vortex ingestion at different phases of a typical flight envelope. A diffusing capture streamtube will typically occur during the high speed and low engine mass flow conditions experienced during climb, cruise and descent. Streamwise vortex ingestion is unlikely during these conditions for a number of reasons. Firstly, since the intake capture streamtube has a diameter close to that of the engine, it is unlikely that a source of streamwise vorticity will be located inside the intake capture streamtube. Secondly, during the climb, cruise and descent phases of flight, the aircraft airframe angles of attack are small. Therefore, it is unlikely that vortices will be generated on the airframe. However, during the take-off and climb-out phases of flight, the intake capture streamtube is likely to be contracting, since the flight speeds are low and the engine mass flow is large. The risk of vortex ingestion is high because the capture streamtube size in the upstream region is larger than the intake diameter, and thus there is a greater possibility that a streamwise vortex will be contained in the intake capture streamtube. Furthermore, during off-design and low-speed flight, the aerodynamic angle of attack on various components on the aircraft is increased, the lift coefficients are usually higher and there is a greater possibility that vortices will be generated.

To summarise, the likeliness of vortex ingestion is greatest during conditions which correspond to a contracting intake capture streamtube. As a result, there is a need to develop understanding of the behaviour of streamwise vortices in a streamwise contraction.

2.2 An overview of vortex characteristics

Before considering the behaviour of vortical flow during ingestion, it is first necessary to establish the characteristics of the streamwise vortices which are likely to occur upstream of the intake. Fortunately, the characteristics of such vortices are generally well understood. In general, it is possible to classify the vortical flow which is generated by an aircraft in terms of four separate phases [15], Figure 2.3.

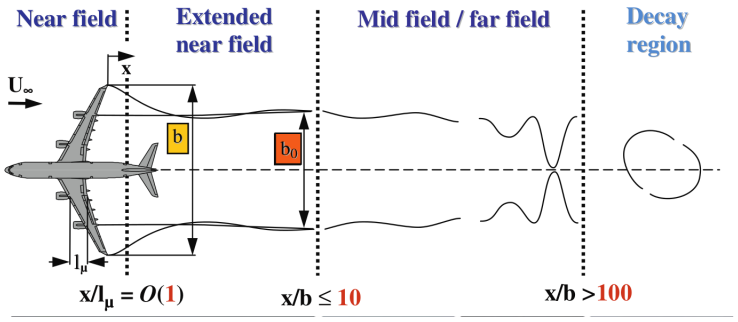

FIGURE 2.3: Definition of vortex wake regions downstream of a typical civil airliner [15], where U_∞ is the freestream velocity, b is the wing span, x is the distance downstream of the wing-tip trailing edge, and l_μ is the mean aerodynamic chord

The first phase is termed the near field, which extends from the vortex generation point to a distance which typically corresponds to half a wing span. In this region, the flow in the near field downstream of a civil airliner normally contains a number of discrete vortices from the wing-tip, the flap edges, and the junction between the wing and the fuselage, Figure 2.4.

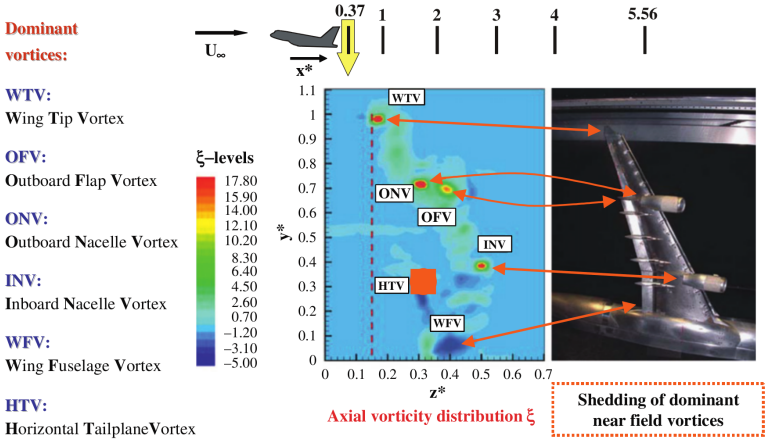

FIGURE 2.4: Contours of streamwise vorticity in the near field downstream of a sub-scale civil airliner model [15]

The second phase, termed the extended near field, is defined as the region extending from the near field to approximately 10 wing span lengths downstream of the aircraft. In this phase, the wake generated by the wing and the fuselage rolls up into the discrete vortices, and the flow gradually evolves to form two counter-rotating vortices. In the latter phases, termed the mid-field, far-field and dispersion region, there is an interaction between the two counter-rotating vortices which gradually leads to their destruction. Based on the preceding classification, the vorticity which may be ingested by an engine located at the rear of the fuselage is likely to be in the near field or the extended near field.

2.2.1 Velocity and pressure field

To characterise the perturbation field associated with typical vortices as observed in the flowfield of an aircraft, it is constructive to consider wing-tip vortices, for which there is a large amount of measurements and simulations in the literature. Wing-tip vortices are relevant for this research since it is possible that such vortices may be generated by wing surfaces, such as canards, placed upstream of an engine intake. A streamwise vortex is typically formed at the wing-tip of a lifting wing as a result of the differing pressure levels on the upper and lower levels of the wing [16]. More than one vortex may initially be formed, depending on the details of the wing geometry. For example, Lee and Pereira [17] obtained three-component (3C) velocity measurements along the wing-tip of a NACA 0012 rectangular semi-span wing. The wing was mounted inside a low-speed wind tunnel at an angle of attack of 10^o and at conditions which correspond to a Reynolds number based on the wing chord, ($Re_c = W_\infty c/\nu$), of 3.1×10^5. The measurements were acquired using a 7-hole pressure probe on planes which are perpendicular to the freestream flow at streamwise locations between $x/c = -0.5$ and $x/c = 4$, where x is the streamwise distance from the wing-tip trailing edge, and c is the wing chord. The streamwise vorticity contours which have been obtained from the in-plane velocity measurements at $x/c = -0.5$, Figure 2.5(a), indicate the presence of two vortices, denoted as the "main vortex" (MV) and a "secondary vortex" (SV). The peak streamwise vorticity levels are notably larger for the main vortex. These vortices quickly merge to form a single vortex at the wing trailing edge, Figure 2.5(b), and the vortex approaches an axisymmetric shape after a few chord lengths downstream of the trailing edge of the wing 2.5(d).

The streamwise vorticity profile exhibits a dominant peak at the vortex centre, and most of the vorticity is contained inside the vortex core (Figure 2.6(a)). An important characteristic which defines a streamwise vortex is the circulation Γ. This is defined as the

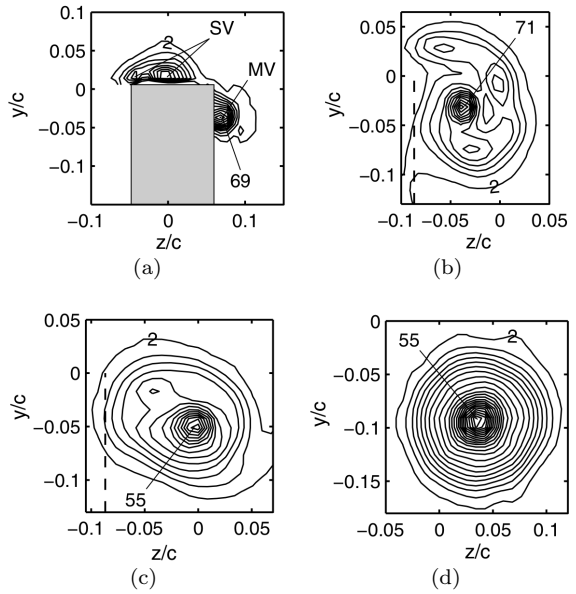

FIGURE 2.5: Measurements of streamwise vorticity on planes perpendicular to the freestream direction downstream of a sub-scale semispan wing [17] (a): $x/c = -0.5$, (b): $x/c = 0.05$, (c): $x/c = 0.5$, (d): $x/c = -4$, where x is the distance downstream of the wing trailing edge, and c is the wing chord

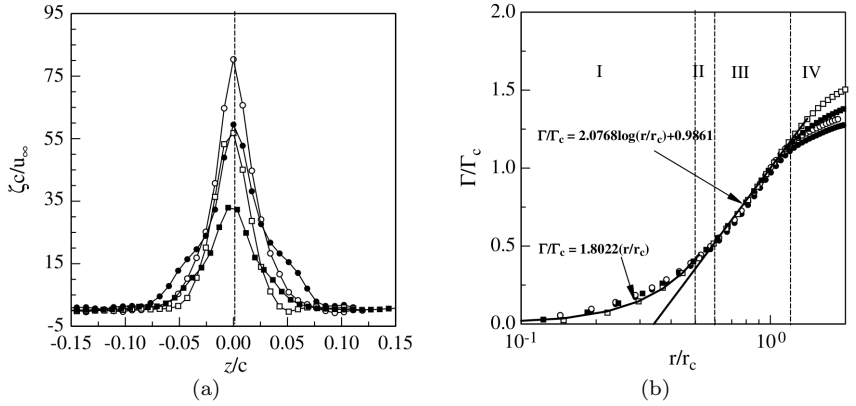

FIGURE 2.6: Wing-tip vortex measurements at a distance of $x/c = 4$ downstream of the wing trailing edge, [17], (a): Profile of normalised streamwise vorticity (denoted as ζ in the figure) through the vortex centre, (b): Typical circulation distribution as a function of distance from the vortex centre

area integral of the streamwise vorticity ω_z or, through Stokes Theorem [18], as the line integral of the velocity field around a contour in which the vortex is contained.

$$\Gamma = \int\int_S \omega_z dS = -\oint_C \vec{V} \cdot d\vec{s} \tag{2.4}$$

The circulation can be calculated using the measured vortex velocity field as a function of distance from the vortex centre, Figure 2.6(b). The vortex circulation increases from zero at the vortex centre, and approaches a constant value known as the total circulation Γ_0 at a large distance from the vortex centre. It is possible to characterise the strength of the vortex using the vortex Reynolds number, Eq. 2.5, where ν is the kinematic viscosity. Note that it is also possible to define the vortex Reynolds number in terms of the circulation measured at the vortex core radius (Γ_c). Note that an increase in the vortex Reynolds number also signifies a rise in the vortex size and the vortex tangential velocities, since $\Gamma_c = 2\pi r_c V_\theta$ for approximately axisymmetric vortices such as the ones of interest in this research. Therefore, when the vortex Reynolds number increases, so does the importance of the inertial terms relative to the viscous terms. As detailed in section 2.3, the vortex Reynolds number has an important influence on the evolution of the vortex.

$$Re_v = \frac{\Gamma_0}{\nu} \tag{2.5}$$

The total circulation of the vortex is closely related to the wing characteristics and operating conditions. From lifting line theory, the wing-tip vortex total strength is equal to the maximum wing circulation. Thus, from the Kutta-Joukowski theorem [18], the vortex total strength (Γ_0) can be determined from the total lift of the wing, Eq. 2.6, where S_p is the wing planform area, and C_L is the wing lift coefficient.

$$\rho W_\infty \Gamma_0 b = \frac{1}{2}\rho W_\infty^2 S_p C_L \tag{2.6}$$

As a result of Eq. 2.6, the vortex total circulation increases in proportion to the freestream velocity, wing chord length, and the wing lift coefficient, Eq. 2.7.

$$\Gamma_0 = \frac{1}{2} W_\infty c C_L \tag{2.7}$$

An important feature of the circulation distribution in Figure 2.6(b) is that the circulation continues to rise, in an asymptotic manner, beyond the core radius of the vortex. This

behaviour is a result of the presence of additional vorticity in the flow which surrounds the vortex core. Based on fundamental lifting line theory and Helmholtz vortex theory, it can be demonstrated that a sheet of streamwise vorticity is produced along the entire trailing edge of the wing, in which the vorticity is concentrated at the wing-tip in the form of the wing-tip vortex [16]. As the wing-tip vortex and the sheet of vorticity move downstream, the vortex sheet rolls up into a spiral and is gradually entrained into the wing-tip vortex. This behaviour can have a notable influence on the wing-tip vortex circulation measurements. Measurements from a number of wing-tip vortex measurements from a variety of wing planforms, cross-sectional geometries and wing-tip shapes have demonstrated that this roll-up process is typically complete after two or three chord lengths downstream of the wing trailing edge [16]. However, if a notable portion of the vortex sheet remains outside of the vortex core, then the circulation profile will continue to increase slowly with distance from the vortex centre, as observed in Figure 2.6(b). Similar trends have been reported throughout the literature. For example, Devenport et al. [1] used a miniature four sensor hot wire to obtain three-component velocity measurements of the wing-tip vortex flow which was generated by a NACA 0012 rectangular semi-span wing. The wing had a chord of 0.20m and a semispan of 0.88m, and was mounted in a low-speed tunnel at an angle of attack of 5^o for a chord Reynolds number of 5.3×10^5. It was found that the streamwise vorticity and turbulent kinetic energy measurements showed the presence of the vorticity sheet as a spiral surrounding the vortex core after 29 chord lengths downstream of the wing trailing edge. The circulation inside the vortex core corresponded to between 25% and 29% of the total circulation as expected from lifting line theory. The circulation profile continued to increase steadily beyond the vortex core radius, and a maximum of 70% of the theoretical value of Γ_0 was measured at the edge of the measurement region which corresponded to approximately $15r_c$ from the vortex centre. Consequently, the degree to which the vortex roll-up process is complete is of interest for wing-tip vortex measurements. Spreiter and Sacks [19] performed a theoretical analysis on the motion of the vortex sheet in two dimensional, unsteady and incompressible flow. Under the assumption of an elliptic lift distribution, it was demonstrated that the streamwise distance from the trailing edge of the wing to the point where the vortex is considered fully rolled up (e/c) is proportional to the aspect ratio of the wing, and is inversely proportional to the lift coefficient of the wing. In particular, it is noted that the rate of the vortex roll-up process is closely linked to the lift distribution along the wing span. Consequently, for a given wing chord, the distance required for the wing-tip vortex to roll up will increase for wings is governed by the wing span and, as the wing span is increased, the roll-up process will be complete at a greater distance downstream of the wing.

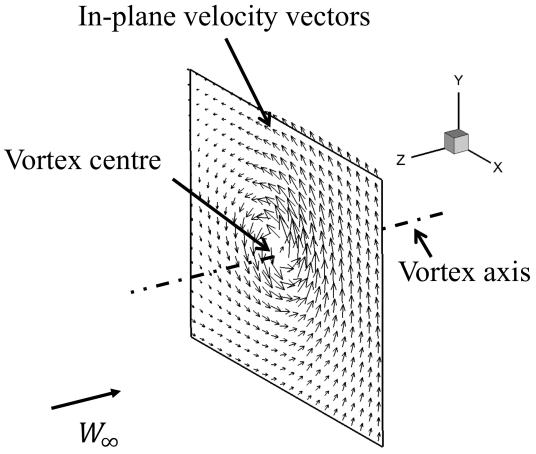

FIGURE 2.7: Illustration of typical vortex flow in-plane velocity vectors on a plane perpendicular to the vortex axis

Consider a streamwise vortex which is superimposed on a uniform freestream flow with a velocity of W_∞, Figure 2.7. The in-plane velocity vectors on a plane which is perpendicular to the vortex axis will typically indicate a flow which is rotating around the centre of the vortex. This flow is considered to consist of a central vortical region which is dominated by the effects of diffusion, surrounded by a flow which behaves almost as a potential flow [20].

The perturbation field with respect to the flow in which the vortex is contained can be considered to consist of tangential, axial and radial velocities, defined in a polar coordinate system located at the vortex centre, $\mathbf{V}=(V_r, V_\theta, V_z)$. Measurements of the typical velocity field which is associated with a wing-tip vortex were obtained Dosanjh et al. [21]. A 5-hole pressure probe was employed to measure the three-component velocity field downstream of a NACA 0009 semispan wing with a chord of 0.28m and a semispan of 0.51m. The wing was mounted in a low-speed wind tunnel at an angle of attack of 8^o and at freestream conditions which correspond to a chord Reynolds number of 1×10^4. The tangential velocity (Figure 2.8(a)) reaches a maximum value at a certain distance from the vortex centre, known as the core radius, r_c. The velocity distribution in the core region is proportional to r in a manner which is similar to that of a solid body rotation. Beyond the vortex core, the tangential velocity distribution decreases as a function of the inverse of the radius. The peak tangential velocity and vortex core radius are a function of a number of factors, including the wing angle of attack α_{vg}, the wing-tip shape, and the distance downstream of the wing trailing edge [16]. For example, Lee and Pereira [17] measured a peak tangential velocity and core radius of approximately $0.70W_\infty$ and

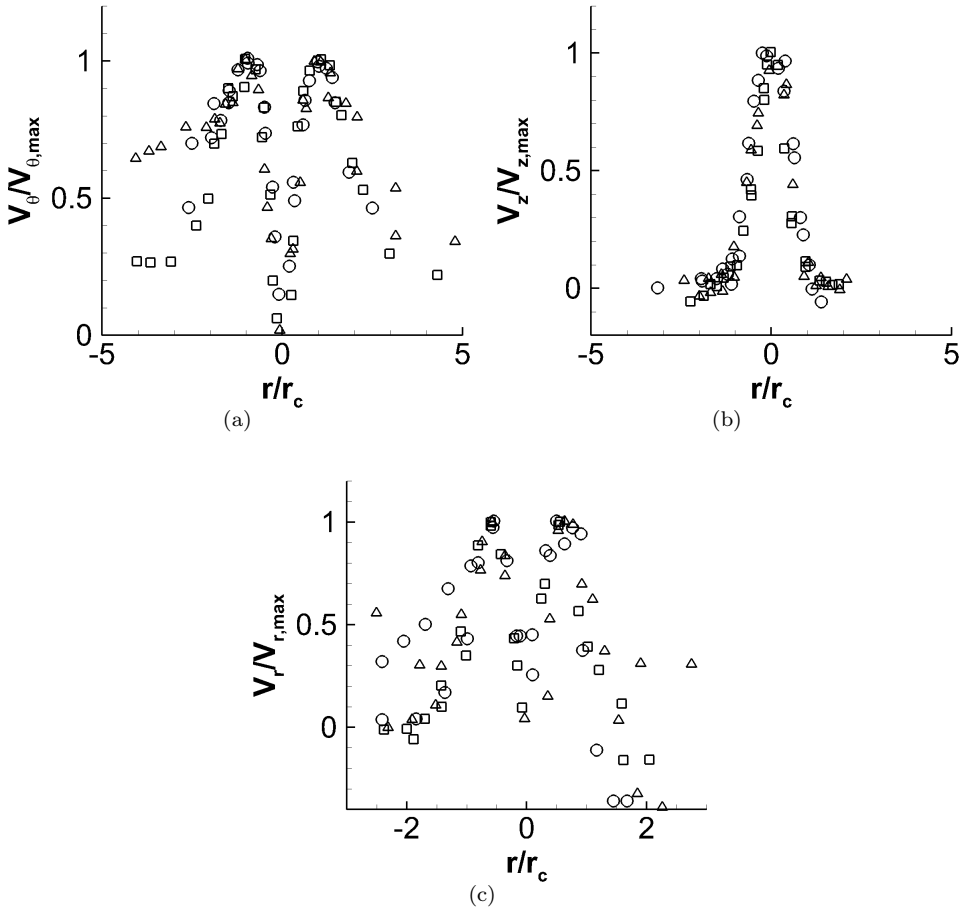

FIGURE 2.8: Normalised wing-tip vortex velocity profiles at measurement planes between $z/c = 1$ and $z/c = 6$ downstream of a sub-scale wing, data extracted from Dosanjh et al. [21], (a): Tangential velocity ($V_\theta/V_{\theta,max}$), (b): Streamwise velocity ($V_z/V_{z,max}$), (c): Radial velocity ($V_r/V_{r,max}$)

$0.06c$ respectively at a measurement plane 5 chord lengths downstream of a NACA 0012 unswept semispan wing at the maximum lift coefficient. A streamwise velocity perturbation relative to the freestream flow (Figure 2.8(b)) is often measured inside the core of wing-tip vortices. The streamwise velocity perturbation is defined as the difference between the streamwise velocity at the vortex centre and that in the freestream, that is, $(V_z - W_\infty)$. Experimental measurements have demonstrated that the streamwise velocity perturbation can be positive or negative, referred to as a streamwise velocity excess or deficit, respectively. For example, Chow et al. [22] and [23] employed a 7-hole pressure probe to measure the velocity field close to the wing-tip of a NACA 0012 semispan wing which featured a semispan of 0.91m and a chord of 1.22m. The measurements were acquired for an angle of attack of 12^o and a Reynolds number based on the wing chord of

4.6×10^6. measured a streamwise velocity excess corresponding to $0.77W_\infty$. In contrast, in the measurements of Devenport et al. [1], a streamwise velocity deficit of $0.15W_\infty$ was measured at a distance of 4c downstream of the NACA 0012 semispan wing.

To explain the behaviour of the streamwise velocity inside a wing-tip vortex, it is instructive to consider the nature of the static pressure field inside the vortex. As an illustrative example, consider a vortex with a tangential velocity distribution which corresponds to the Rankine vortex model inside the vortex core, which consists of a solid body rotation velocity profile, Eq. 2.8, where Ω is the angular velocity.

$$V_\theta = \frac{\Gamma r}{2\pi r_c^2} \tag{2.8}$$

It can be shown [16] that the static pressure field in the core of a Rankine vortex is a function of the vortex size and strength, Eq. 2.9, where p_c is the static pressure at the vortex centre.

$$p - p(r) = \frac{\rho\Gamma^2}{4\pi^2 r_c^2}\left(1 - \frac{r^2}{2r_c^2}\right) \tag{2.9}$$

Thus, as a result of the tangential velocity, the static pressure inside the vortex core is lower than that surrounding the vortex. Insight into the importance of the static pressure field was provided by the theoretical analysis of Batchelor [24] for steady, axisymmetric, incompressible, inviscid flow. Furthermore, gradients of velocity in the streamwise direction, and the radial velocity components, are assumed to be small in comparison to the streamwise and tangential velocity components. It was subsequently shown that the radial momentum equation reduces to Eq. 2.10, where p_∞ is the freestream static pressure, at a location far from the vortex, p is the static pressure, ρ is the density, and r is the distance from the vortex centre.

$$\frac{p_\infty - p}{\rho} = \int_r^\infty \frac{V_\theta^2}{r} dr \tag{2.10}$$

It is assumed that the streamlines in the flow originate from a steady, uniform freestream flow with a streamwise velocity of W_∞. The Bernoulli function, Eq. 2.11, can then be employed for any streamline in the flow. To account for the possibility that some of the streamlines may have passed through the wing boundary layer, or inside a region of the

flow where dissipation takes place, a loss in total head (ΔH) has been incorporated into Eq. 2.11.

$$\frac{p}{\rho} + \frac{1}{2}\left(V_z^2 + V_r^2 + V_\theta^2\right) = \frac{p_\infty}{\rho} + \frac{1}{2}W_\infty^2 - \Delta H \tag{2.11}$$

It is then possible to substitute Eq. 2.10 into the Bernoulli function (Eq. 2.11). Through the use of $C = rV_\theta$, which represents $(1/2\pi)$ times the circulation evaluated at a radius of r from the centre of the vortex, and assuming that V_r is small, the streamwise velocity along a streamline in the flow is given by Eq. 2.12.

$$V_z^2 = W_\infty^2 + \int_r^\infty \frac{1}{r^2}\frac{\partial C^2}{\partial r}dr - 2\Delta H \tag{2.12}$$

The second term on the right hand side of Eq. 2.12 represents the contribution to the streamwise velocity perturbation from the static pressure field which is generated by the rotational motion of the flow inside the vortex. In wing-tip vortex measurements, such as that demonstrated in Figure 2.6(b), the circulation distribution typically increases monotonically with distance from the vortex centre. Therefore, the second term in Eq. 2.12 will result in a positive contribution to the streamwise velocity relative to the freestream velocity. The value of the streamwise velocity, however, depends on the magnitude of the dissipation effects relative to the contribution from the circulation distribution. This behaviour has been demonstrated in the measurements of Chow et al. [23]. The static pressure at the vortex centre was found to be lower than the surrounding flow, Figure 2.9(a), and reduced during the vortex roll-up process to approximately three times the dynamic pressure of the freestream flow.

As a consequence, a favourable streamwise pressure gradient was generated inside the vortex core, and the vortex core flow accelerated to a maximum streamwise velocity of approximately 77% of the freestream velocity (Figure 2.9(b)). The total pressure coefficient reduced progressively during the vortex roll-up process, and reached a minimum value of -0.76, which corresponds to approximately 1.2% of the freestream total pressure. This is an important result, since it indicates that a wing-tip vortex consists of relatively low levels of total pressure loss.

Importantly, Eq. 2.12 and demonstrates that if the effects of dissipation remain constant, then the streamwise velocity at the vortex centre will increase with the strength of the vortex. This was investigated experimentally by Anderson and Lawton [25] using a NACA

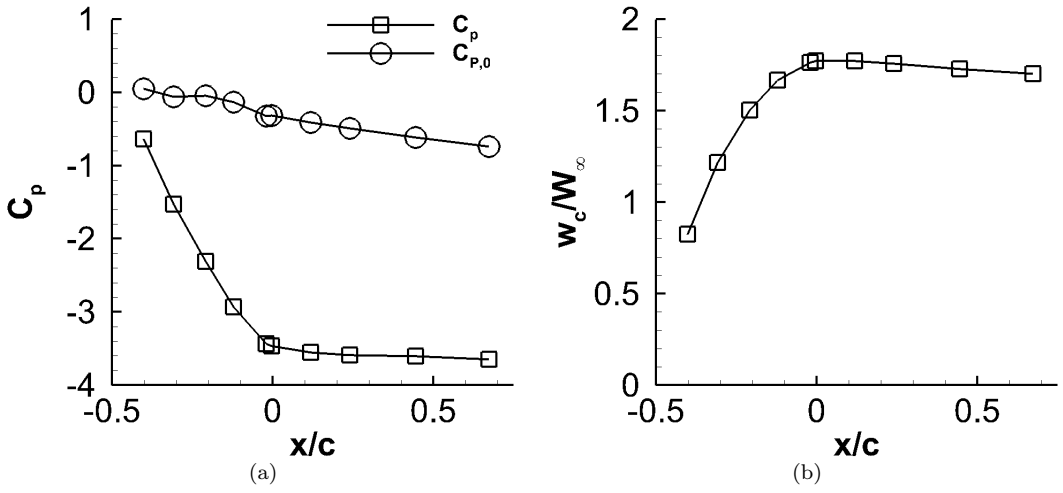

FIGURE 2.9: Measurements at the centre of a wing-tip vortex (data extracted from Chow et al. [23], and is corresponding to that reported in Chow et al. [22]), (a): Static and total pressure coefficients at vortex centre ($C_p = (p - p_\infty)/q_\infty$) and $C_{P,0} = (P_0 - P_{0,\infty})/q_\infty$) respectively), (b): Streamwise velocity at vortex centre normalised by freestream velocity (w_c/W_∞),

0015 semispan wing which featured an unswept, rectangular planform, with a chord and semispan of 0.76m and 0.61m respectively. Chord Reynolds numbers of between 7.5×10^5 and 1.25×10^6 were investigated using a low-speed wind tunnel for angles of attack ranging from $4 - 10^o$. The three-component velocity field was measured at a distance of 1c and 2c downstream of the wing trailing edge using a triple-wire hot wire probe. At the lowest angle of attack investigated, the vortex consisted of a streamwise velocity deficit at the vortex centre. As the angle of attack was increased, there was a rise in the vortex strength and the streamwise velocity at the vortex centre. The streamwise velocity perturbation transitioned from a deficit into an excess at approximately $\alpha = 8^o$. Lee and Pereira [17] demonstrated that this transition occurs at the angle of attack which corresponds to the maximum lift to drag ratio of the wing. It has also been found that the nature of the streamwise velocity perturbation is dependent on the details of the wing-tip geometry, and the distance downstream of the wing [16].

Finally, a radial velocity is often measured close to the vortex, Figure 2.8(c). The radial velocity perturbation is small in comparison to the tangential and streamwise velocities [21] and is often neglected [16]. The sign of the radial velocity is linked to the streamwise velocity perturbation. In the case of a streamwise velocity deficit, the radial velocity is negative [21], which denotes flow inward towards the vortex centre. Conversely, a positive radial velocity will exist in the case of a streamwise velocity excess. In general, it has been

found that the vortex velocity profiles are self-similar with distance downstream of the wing when normalised by the peak tangential velocity and the core radius. This is evident in Figures 2.8(a) to 2.8(c), which consists of measurements at different planes between 1 and 6 chord lengths downstream of the trailing edge of a wing.

In summary, a streamwise vortex consists of notable deviations in velocity and pressure from the uniform freestream flow. After the generation and roll-up phases, the profiles of the tangential, radial and streamwise velocities generally become self-similar when normalised by the vortex core radius, along with the maximum values of each respective velocity component. However, the vortex characteristics show a strong dependence on the freestream conditions, the angle of attack, and the details of the geometry which created the vortex.

2.2.2 Vortex wandering

It is often acknowledged that the measurement of intense vortices such as wing-tip vortices is challenging [16]. A notable source of measurement uncertainty arises due to a characteristic known as meandering or wandering, whereby the vortex core position fluctuates randomly in time. It is believed that vortex wandering is a result of turbulent flow in the vortex, which results in an intermittent transfer of fluid from the vortex core to the surrounding flow [26, 16] and a subsequent displacement of the vortex position. This presents a significant problem for point-based measurement methods where the time-averaged vortex velocity, vorticity and core radius measurements erroneously indicate a larger and weaker vortex than that which truly arises. For example, Devenport et al. [1] used a statistical-based approach to correct hot-wire measurements of a wing-tip vortex. The results suggested that the core radius was over-estimated by 12%, and that the peak tangential velocity and streamwise velocity perturbation were under-predicted by 15% and 11%, respectively.

Zhou et al. [27] employed Particle Image Velocimetry (PIV) to measure the wing-tip vortex which was generated by an unswept, rectangular, NACA 0012 semispan wing at angles of attack of 8^o and 16^o and chord Reynolds numbers of between 3.4×10^4 and 2.7×10^5. The in-plane velocity measurements at $x/c = 3$ showed that the peak streamwise vorticity, without correction for wandering, was 33% lower than the corrected measurement. In addition, due to the large velocity gradients close to the vortex centre, the change in instantaneous vortex position produces an apparent velocity fluctuation, which introduces a large uncertainty in unsteadiness measurements [1]. Wandering is typically small

within 1 chord length of the trailing edge [16] and at low angles of attack, and increases as a function of downstream distance [1]. The effects of wandering must be mitigated or corrected to ensure that the vortex characteristics can be correctly measured. A number of conditional-sampling approaches have been employed for fixed probe measurements [28, 29, 30]. In addition, some statistical-based techniques have also been shown to be helpful [31, 1, 32]. To conclude, it is apparent that vortex wandering has the potential to introduce large measurement uncertainties in streamwise vortex measurements. Global measurement methods, such as PIV, offer distinct advantages since it is possible to track the position of the vortex on each instantaneous measurement. Therefore, the detrimental effects of wandering on vortex measurements can be avoided.

2.2.3 Vortex turbulence

Existing literature suggests that sub-scale wing-tip vortices contain turbulent flow. For example, the wing-tip vortex measurements of Chow et al. [22] demonstrated in-plane and streamwise RMS velocity fluctuations of more than 20% of the freestream velocity inside the vortex core during the vortex generation process, and fluctuations close to 10% at $0.7c$ following generation.

Tung et al. [28] employed a single hot wire probe to measure the in-plane velocity field of the wing-tip vortex generated by a two-bladed helicopter rotor at a chord Reynolds number of approximately 6.9×10^5. The rotor blades were of a rectangular, untapered planform, with a radius and a chord of $0.105m$ and chord of $0.076m$, respectively. The measured circulation profile inside the vortex was employed to demonstrate that the wing-tip vortex consisted of four distinct regions:

- A viscous core, where viscous diffusion is dominant and the velocity distribution is akin to a solid-body rotation.
- A turbulent mixing region, which contains the peak tangential velocity, and where turbulent diffusion is large.
- A transition region, where the flow transitions from the turbulent region to the outer potential flow. There are discontinuous jumps in the circulation distribution due to the remaining spirals of the vorticity sheet which are yet to be rolled up into the vortex core.
- An irrotational region, where circulation is constant with radius.

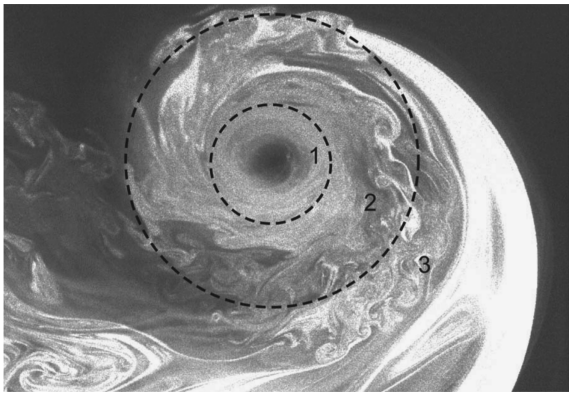

FIGURE 2.10: Visualisation of flow inside a wing-tip vortex showing vortex structure [30]

Such a transitional structure is in agreement with the flow visualisations performed by Martin et al. [33] and Ramasamy and Leishman [34] on a single-blade helicopter rotor in hover. The rotor blade was of an untwisted, rectangular planform with a NACA 2415 section, a chord of $0.043m$ and a radius of $0.406m$. The chord Reynolds number corresponded to 2.5×10^5. Three regions were identified by Ramasamy and Leishman [34] (Figure 2.10) which correspond to the first three identified by Tung et al. [28]. In the first region, interactions between layers of fluid in the vortex core at different radii are small, and the flow appears to be laminar. In the second region, the flow contains turbulent structures with a range of sizes, which marks a form of transition from the stratified flow at the centre of the vortex to the final turbulent region surrounding the vortex.

It is unsurprising that laminar-like flow has been observed in the vortex core, since turbulent flows may undergo relaminarisation where the rotation rate is high. An example of this is given by Narasimha [35], who report that turbulent flow contained in a pipe was found to undergo relaminarisation when the angular velocity of the flow was increased. Such relaminarisation effects have also been observed in wing-tip vortex flows. Bandyopadhyay [26] employed a 7-hole pressure probe, single wire hot wire, and flow visualisation, to investigate the turbulence characteristics of the wing-tip vortex which is generated at the junction between two oppositely-loaded NACA 0012 rectangular wings. The measurements were acquired for a chord Reynolds number of 1×10^5 and for an angle of attack of 8^o. It was found that there was an intermittent transfer of fluid between the vortex core and the surrounding flow, and that turbulent portions of fluid which entered the vortex core were relaminarised by the large rotational velocities. The possibility of relaminarisation in a vortex can be indicated by the Richardson number, Eq. 2.13, as given by Holzapfel et al. [36].

$$Ri = \left[\frac{2V_\theta}{r^2}\frac{\partial\left(V_\theta r\right)}{\partial r}\right] / \left[r\frac{\partial\left(V_\theta/r\right)}{\partial r}\right]^2 \tag{2.13}$$

Note that Eq. 2.13 has been modified from the original formulation introduced by Bradshaw [37] to capture the impact of streamline curvature or flow rotation on turbulent flow. Holzapfel [36] reported that the original formulation is incorrectly expressed in a combination of inertial and fixed reference frames and thus, in Eq. 2.13, the numerator and denominator are both expressed in the same inertial frame. The Richardson number corresponds to the ratio of the potential to kinetic energy in the flow [38]. Therefore, for a known tangential velocity distribution, it is possible to determine the value of Ri as a function of radius from the vortex centre. Cotel and Breidenthal [38] and Cotel [39] showed that, for a typical vortex tangential velocity profile, the Richardson number increases exponentially as the distance from the vortex centre is reduced. Therefore, it was concluded that turbulence could not penetrate to smaller radii when the Richardson number rises above $Re_v^{0.25}$ and, under such conditions, turbulence could not be sustained.

Ramasamy and Leishman [40] analysed the rotor wing-tip vortex results reported in [34] and found that the Richardson number exceeded the maximum threshold for sustaining turbulence at approximately $r/r_c = 0.5$ (Figure 2.11). It was argued that the variation in turbulence characteristics from the vortex centre to the flow surrounding the vortex has an influence on the vortex velocity distribution. A model for the tangential velocity and circulation profiles which accounts for the stratification effects was then developed and compared with the experimental measurements, Figures 2.12(a) and 2.12(b). In addition, the model results were compared profiles given by the Lamb-Oseen [41] and Iversen [42] vortex models, which assume fully laminar and fully turbulent flow, respectively. It was

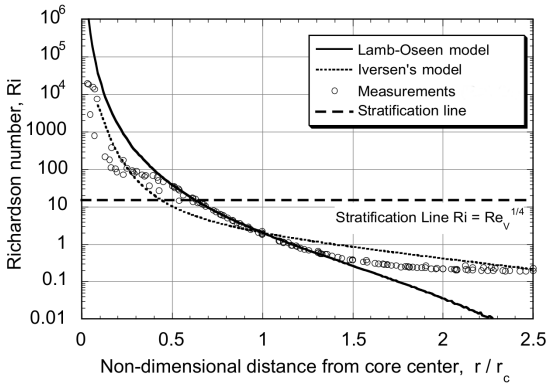

FIGURE 2.11: Variation of Richardson number through a wing-tip vortex [40]

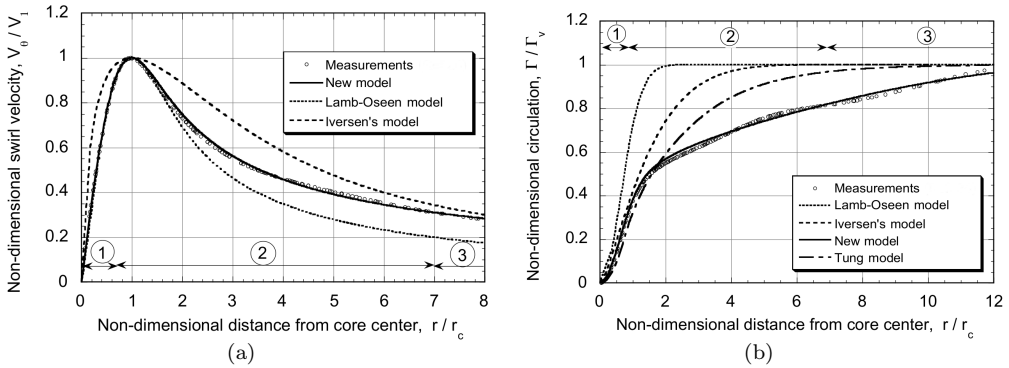

FIGURE 2.12: A comparison of wing-tip vortex measurements with the laminar Lamb-Oseen vortex model, the turbulent Iversen model, and the transitional R-L vortex model [40], (a): Tangential velocity profile, (b): Circulation distribution

found that the profile was in very good agreement with the experimental measurements, although it should be noted that empirical factors contained in the model had to be determined using existing measurements. It is also of importance to note in Figure 2.12(a) the differences between the experimental measurements and the Lamb-Oseen and Iversen vortex models. In the vortex core, the experimental measurements are in close agreement with the laminar Lamb-Oseen model, which validates somewhat the observations of laminar flow in the flow visualisation (Figure 2.10). This is also in agreement with the findings of Devenport et al. [1], who provided evidence which supported the assertion of laminar flow in the vortex core. The turbulent Iversen vortex model over-predicts the slope of the tangential velocity distribution inside the vortex core, which suggests that turbulent core flow experiences greater levels of strain between fluid elements in the vortex core. However, beyond the vortex core, the experimental measurements deviate from the laminar model and approach the profile given by the turbulent vortex model. It should be noted that the circulation distribution in Figure 2.12(b) continues to increase beyond the vortex core radius, and slowly approaches Γ/Γ_0 of 1.0. This demonstrates that a notable amount of streamwise vorticity remains in the flow surrounding the vortex core. It was emphasised in section 2.2.1 that such behaviour indicates that the vortex roll-up process is not complete for the measurements shown in Figure 2.12(b). As a consequence, the circulation profile continues to rise at radii beyond the vortex core radius due to the streamwise vorticity which is contained in the vortex sheet of the wing.

However, a considerable number of measurements suggest the presence of turbulent flow throughout the vortex. For example, Han et al. [43] obtained three-component velocity

and turbulent stress measurements in the wing-tip vortex of a helicopter rotor in hover using Laser Doppler Velocimetry. The rotor consisted of a single, rectangular and untwisted blade, with a chord and radius of 0.0445m and 0.406m, respectively. The measurements were acquired from 2.8c to 17c downstream of the rotor trailing edge for a chord Reynolds number of 2.5×10^5. It was found that there were notable turbulence levels at the vortex centre, with a peak close to the edge of the vortex core. Further downstream, the peak values reduced, and the peak moved inwards to the vortex centre. Chow et al. [22] found that, during the roll-up process, the peak turbulence levels were located close to the core radius. After less than one chord downstream, the turbulence peak was located at the vortex centre. This rapid change of characteristics was attributed to the turbulence damping associated with the large rotational velocities. Similar trends were also reported by Singh and Uberoi [44], who employed a four wire hot wire to measure the flowfield associated with the wing-tip vortex which was generated using a NACA $64_3 - 618$ semispan wing with a chord of 0.127m and a semispan of 0.458m. The wing angle of attack was 13^o, and the measurements were acquired at positions between 0.8c and 80c downstream of the wing trailing edge.

The measurements of Chow et al. [23] also identified some important characteristics of the normal stresses in the wing-tip vortex flow. The streamwise velocity fluctuations (Figure 2.13(a)) where smaller than the corresponding in-plane fluctuations (Figures 2.13(b) and 2.13(c)). Interestingly, the in-plane turbulence contours, when observed in a Cartesian reference frame, were elliptic in shape. This result indicates that the radial fluctuations are larger than those in the circumferential direction [23], which has also been observed in the sub-scale rotor measurements of Han et al. [43] and Ramasamy et al. [30].

In addition to the strong turbulence damping effects, some mechanisms exist which can lead to turbulence production in the vortex. Han et al. [43] demonstrated that the in-plane turbulence production could be expressed in polar coordinates as Eq. 2.14.

$$P_k = -\left[\bar{V_\theta'V_r'}\frac{\partial V_\theta}{\partial r} + \bar{V_\theta'V_r'}\frac{V_\theta}{r} - 2\bar{V_r'^2}\frac{V_\theta}{r} + \bar{V_\theta'V_z'}\frac{\partial V_z}{\partial r}\right] \tag{2.14}$$

The first three terms of Eq. 2.14 are related to the tangential velocity profile, and were found to be dominant in the near field. The latter term was found to be an order of magnitude smaller than in the near field. Importantly, Figure 2.14 indicates that the greatest levels of turbulence production occur inside the vortex core radius, which is a result of the large in-plane Reynolds stresses and the tangential velocity profile gradient. In addition, the last term of Eq. 2.14 suggests that a gradient in the streamwise velocity profile,

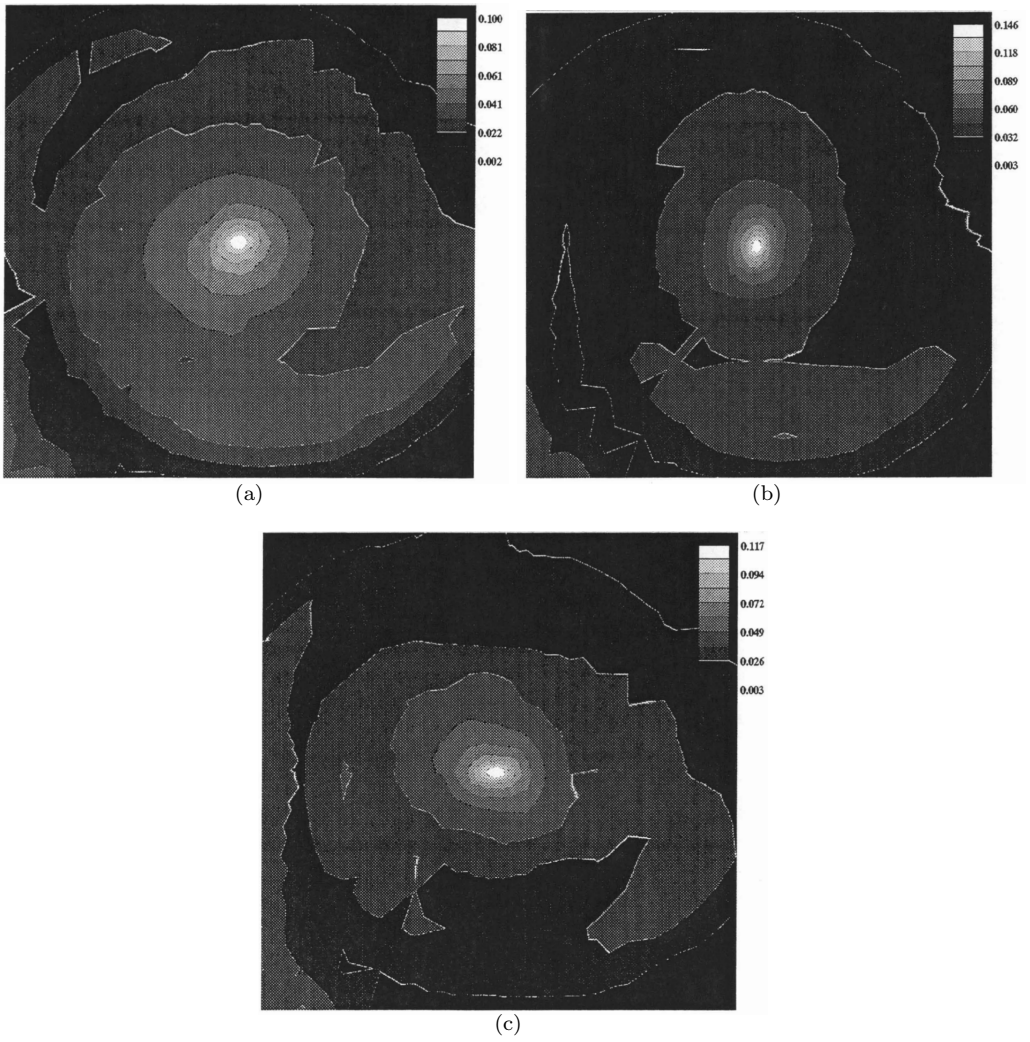

FIGURE 2.13: Wing-tip vortex turbulence measurements in the near field [23], (a): Streamwise RMS velocity, (b): Vertical RMS velocity, (c): Lateral RMS velocity

which will exist in the presence of a streamwise velocity perturbation, can also contribute to turbulence production. Phillips and Graham [45] used a two wire hot wire to obtain measurements of the three-component velocity and turbulent stress fields associated with the wing-tip vortex which was created by two oppositely-loaded wings. A nacelle was located between the two wing-tips with the purpose of modifying the streamwise velocity inside the vortex core. The measurements were acquired in a low-speed wind tunnel, at a chord Reynolds number of 7.4×10^4 and a wing angle of attack of 9^o. It was found that, in the presence of a large streamwise velocity perturbation, high levels of turbulence were sustained for considerable distances downstream of the wing. Furthermore, Chow et al. [22] suggested that the streamwise velocity perturbation was the primary source

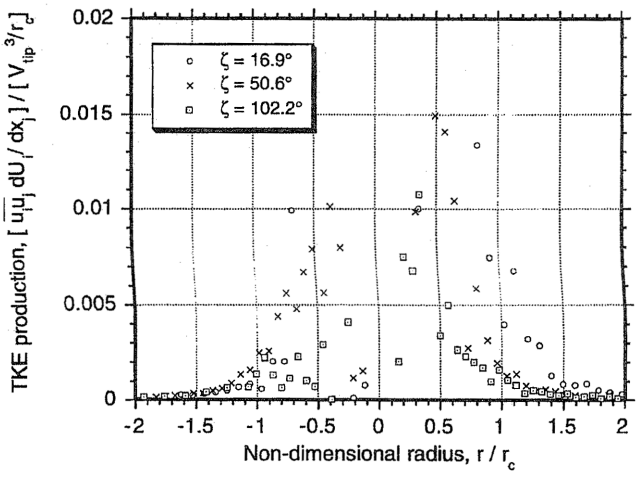

FIGURE 2.14: Turbulent kinetic energy production levels inside a wing-tip vortex in the near field, evaluated using Eq. 2.14 [43]

of turbulence production inside the vortex core. Bandyopadhyay et al. [26] employed the Rossby number, Eq. 2.15, to characterise the relative magnitudes of the streamwise velocity perturbation and the peak tangential velocity. It was found that the turbulence levels inside the vortex strongly correlated with the Rossby number, Eq. 2.15, rather than the vortex Reynolds number. In addition, it was suggested that a lower value of Rossby number, corresponding to a smaller streamwise velocity perturbation, will promote relaminarisation. Ragab and Sreedhar [46] performed LES simulations of an isolated streamwise vortex in a uniform flow which corresponded to a Mach number of 0.2. The vortex was prescribed at the inlet boundary using the tangential and streamwise velocity profiles which were generated using the q-vortex model (see [47] for details). It was found that a large streamwise velocity perturbation forces the generation of turbulence in the vortex core. This turbulent fluid causes a redistribution of momentum, which reduces the size of the streamwise velocity perturbation. After this transient process, the core flow returns to a laminar state as a result of relaminarisation.

$$Ro = \frac{W_\infty - w_c}{V_{\theta,max}} \tag{2.15}$$

To summarise, wing-tip vortices may contain notable velocity fluctuations as a result of turbulence, although the details of the turbulence characteristics are dependent on a number of factors, including the location of the measurement point relative to the wing-tip trailing edge. The literature suggests that the turbulence inside the vortex core

can influence the characteristics of the mean velocity field. There is a balance between turbulence production, as a result of the in-plane and out-of-plane mean velocity field, and turbulence damping due to the large tangential velocities. Therefore, the turbulent structure inside the vortex is likely to depend on the precise details of the vortex generation process and the mean velocity field.

2.3 Streamwise vortex evolution in a uniform flow

Following creation, the vortex will convect with the surrounding flow and may persist for a notable period of time. The manner in which the vortex evolves during convection is of considerable interest for vortex ingestion flows. Firstly, the vortex may be generated some distance upstream of the intake, and so the vortex characteristics at the beginning of the streamtube contraction may be notably different from those observed at a position close to the vortex generation position. Secondly, the way in which the vortex evolves over time may help to elucidate some of the important flow physics which could influence the vortex ingestion process.

For a purely laminar flow, a streamwise vortex will experience vorticity diffusion as a result of molecular viscosity. This effect can be demonstrated by the Lamb-Oseen vortex model [41], which is an exact solution of the axisymmetric Navier-Stokes Equations for two-dimensional flow. The model is time dependent, such that the flow at $t = 0$ consists of vorticity concentrated on an infinitesimal line surrounded by irrotational flow. The streamwise vorticity and tangential velocity distributions are given by Eq. 2.16 and 2.17. The evolution of the streamwise vorticity and tangential velocity are shown in Figure 2.15(a) and 2.15(b) respectively.

$$\omega_z(r,t) = \frac{\Gamma_0}{4\pi\nu t} exp\left(-\frac{r^2}{4\nu t}\right) \tag{2.16}$$

$$V_\theta(r,t) = \frac{\Gamma_0}{2\pi r}\left(1 - exp\left(-\frac{r^2}{4\nu t}\right)\right) \tag{2.17}$$

For $t > 0$, peak vorticity is dramatically reduced, and there is a radial diffusion of vorticity to the flow surrounding the vortex axis. (Figure 2.16(c)) The tangential velocity distribution (Figure 2.16(b)) quickly develops into the characteristic tangential velocity distribution which is typically observed in wing-tip vortices (Figure 2.8(a)), and the radial location of the peak gradually moves outward from the vortex centre. This evolution of

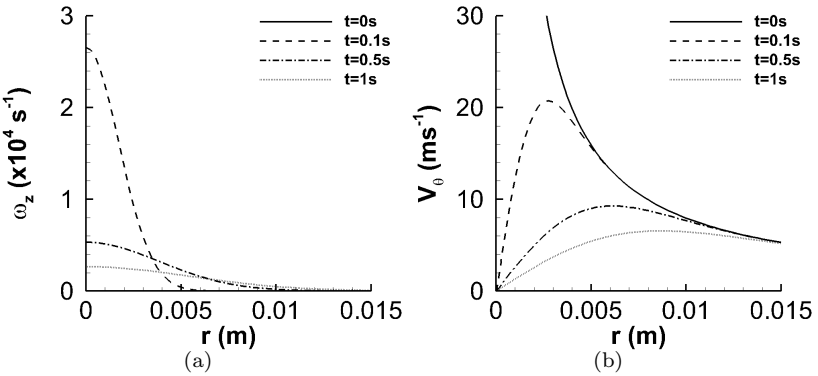

FIGURE 2.15: Lamb-Oseen vortex model profiles as a function of distance from the vortex centre (r) for a vortex total circulation of $\Gamma_0 = 0.5m^2s^{-1}$, (a): Streamwise vorticity (ω_z), (b): Tangential velocity (V_θ)

the tangential velocity profile illustrates that the effect of viscous diffusion is to drive the core flow towards a solid body rotation. From the tangential velocity distribution, Eq. 2.17, it is possible to determine an expression for the vortex core radius as a function of time, Eq. 2.18, where α_{lo} is equal to 1.25643.

$$r_c = \sqrt{4\alpha_{lo}\nu t} \tag{2.18}$$

$$V_{\theta,max} = \frac{\Gamma_0}{2\pi r_c}\left(1 - exp\left(-\alpha_{lo}\right)\right) \tag{2.19}$$

$$\omega_{z,max} = \frac{\Gamma_0}{4\pi\nu t} \tag{2.20}$$

The evolution of the core radius, peak tangential velocity and peak streamwise vorticity as a function of time and vortex total strength (Γ_0) are shown in Figure 2.16(a), Figure 2.16(b) and Figure 2.16(c). The vortex diffusion process results in an increasing core radius with a corresponding reduction in peak tangential velocity and peak streamwise vorticity. This behaviour is consistent with wing-tip vortex measurements following the roll-up process (for example, [21, 31, 27]). The core radius growth is independent of the vortex strength, which appears to be valid when the vortex Reynolds number is less than 10^5 [48, 39]. However, the reduction in peak tangential velocity and peak streamwise vorticity as a function of time are greater when the vortex strength is increased. This demonstrates that the effects of diffusion become more pronounced as the velocity gradients inside the

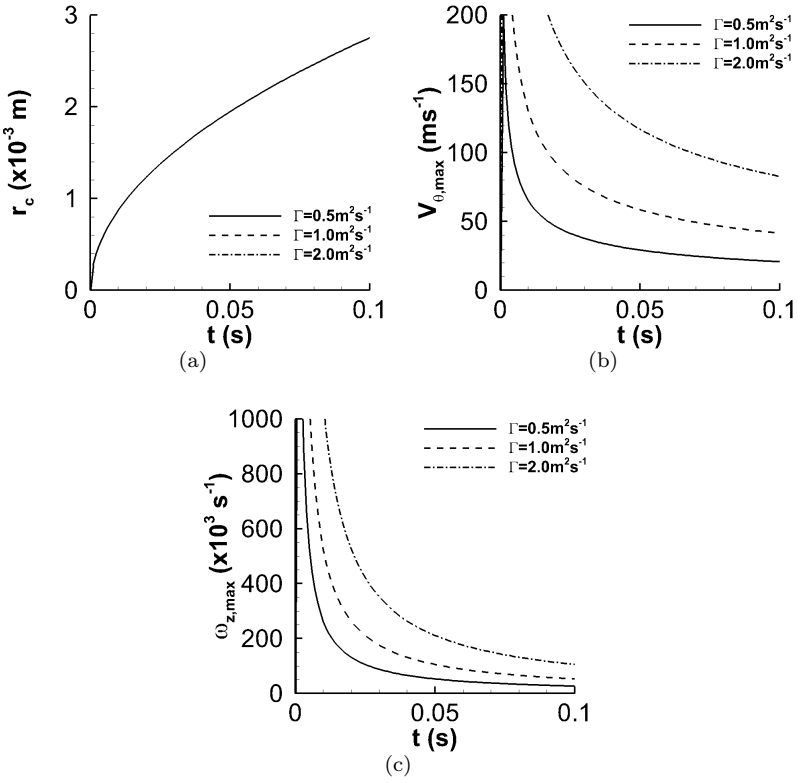

FIGURE 2.16: Temporal evolution of vortex characteristics defined by Lamb-Oseen vortex model as a function of vortex total circulation, (a): Vortex core radius (r_c), Eq. 2.18, (b): Peak tangential velocity ($V_{\theta,max}$), Eq. 2.19, (c): Peak streamwise vorticity ($\omega_{z,max}$), Eq. 2.20

core are increased. Alternatively, it can be stated that as the core vorticity levels increase, so does the rate at which viscosity diffuses the vorticity.

It has been found that experimentally-measured vortex growth rates in the near field are often larger than those given by the Lamb-Oseen vortex model, Eqs. 2.18 to 2.20. Squire [49] hypothesised that this is a result of accelerated vorticity diffusion due to turbulence in the vortex flow, which could be modelled using an apparent eddy viscosity $\nu_t = \delta\nu$, where δ is the apparent viscosity coefficient. It was hypothesised that the apparent eddy viscosity is proportional to the vortex strength, such that the apparent viscosity coefficient can be defined as a function of the vortex Reynolds number, Eq. 2.21, [50], where $a_1 = 6.5 \times 10^{-5}$ is an empirically-derived constant [51].

$$\delta = 1 + a_1 \left(\frac{\Gamma_0}{\nu} \right) \tag{2.21}$$

In addition, Squire [49] proposed an effective off-set such that a finite core radius $r_{c,0}$ could be defined at the wing trailing edge. Therefore, Eq. 2.18 can be rewritten, Eq. 2.22.

$$r_c = \sqrt{r_{c,0}^2 + 4\alpha_{lo}\delta\nu t} \tag{2.22}$$

Bhagwat and Leishman [50] calculated the value of δ for a wide range of experimental measurements which consisted of vortex Reynolds numbers of between 10^3 and 10^7, Figure 2.17. The results suggest that for vortex Reynolds numbers of greater than 10^4, the vortex growth rate rises with the vortex Reynolds number in a manner consistent with the Squire model (Eq. 2.21). This provides strong evidence that the effects of turbulent diffusion increase in proportion to the vortex strength. Similar results were obtained by Iversen [42], who calculated δ using the peak tangential velocity measurements from a range of wing-tip vortex measurements for vortex Reynolds numbers between 10^4 and 10^7. There is some scatter in the data presented in Figure 2.17, which can be attributed to a number of factors. Firstly, it is possible that some of the data has been affected somewhat by vortex wandering [50], which would tend to indicate larger growth rates than that which truly exists and would therefore produce an over-estimate of the apparent viscosity. In addition, it is apparent that turbulent diffusion may influence only a portion of the vortex downstream evolution. It was emphasised in section 2.2.3 that the details of the vortex turbulence structure are strongly dependent on the vortex generation process, and the vortex core may indeed contain turbulent flow which may be relaminarised further downstream. Therefore, it is possible that the evolution of the vortex may be characterised by a combination of large growth rates close to the generation point, followed by reduced growth rates some distance downstream. This may provide at least a partial explanation as to why the growth rates measured by Devenport et al [1] were close to laminar ($\delta = 1$), whereas Bhagwat and Leishman [50] at similar vortex Reynolds numbers reported growth rates consistent with $\delta = 10$. Laminar-like vortex growth rates were also observed in the measurements of Jacob et al. [52], who employed PIV to measure the in-plane velocity of a wing-tip vortex which was generated using a rectangular, unswept, semispan NACA 0012 wing. The measurements were acquired in a low-speed towing tank at a chord Reynolds number between 2 and 6×10^4 and a vortex Reynolds number of between 0.42 to 3.74×10^4. These conditions are similar to those investigated by Devenport et al. [1] and Bhagwat and Leishman [50]. Nevertheless, the results obtained in Figure 2.17 strongly suggest that turbulent diffusion plays a role in the vortex evolution at Reynolds numbers of interest at both sub-scale and full-scale conditions. Furthermore, the results suggest that turbulence

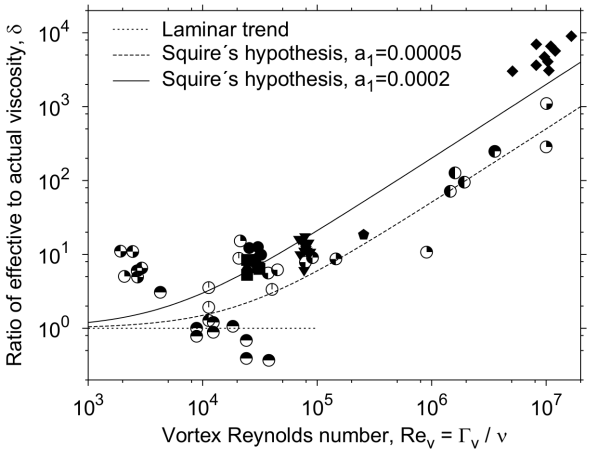

FIGURE 2.17: Apparent viscosity coefficient (δ) calculated for a wide range of wing-tip vortex measurements as a function of vortex Reynolds number (Re_v) [50]

diffusion increases with the vortex Reynolds number. It is clear that both laminar and turbulent diffusion may influence the characteristics of a vortex as it passes through the intake capture streamtube and, therefore, may have a notable impact on the nature of the distortion which results inside the intake.

2.4 Vortex intensification

An important feature of vortical flow is the link between the flow velocity and vorticity, as demonstrated by the unsteady vorticity equation, Eq. 2.23, assuming incompressible flow and conservative body forces [53].

$$\frac{D\vec{\omega}}{Dt} = (\vec{\omega} \cdot \nabla)\,\vec{V} + \nu\nabla^2\vec{\omega} \tag{2.23}$$

The first term on the right hand side of Eq. 2.23 represents the rate of change of vorticity as a result the stretching and tilting of the vortex lines. Thus, an increase in velocity which is aligned with the local vorticity vector will produce an increase in vorticity, and conversely for a reduction in velocity. The second term refers to the diffusion of vorticity under the action of laminar viscosity. Streamwise vortices feature a similar sensitivity to changes in the surrounding flow [54], and can experience a change in vorticity in the presence of velocity gradients [55]. Therefore, it is anticipated that the evolution of a vortex undergoing ingestion will be dependent on the details of the capture streamtube flow.

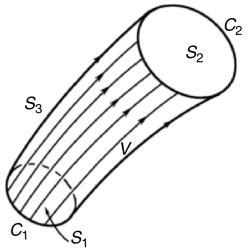

FIGURE 2.18: Illustration of a vortex line and vortex tube [55], where C refers to a closed curve around the vortex tube, S refers to the bounding surfaces of the vortex tube, and V refers to the volume of fluid contained inside the vortex tube

This section will focus first on the fundamental and theoretical lessons which establish the laws of vortex motion. Thereafter, the findings of a range of experimental measurements will be provided.

2.4.1 Theoretical models

To better understand vortex intensification, it is first necessary to consider the fundamental laws which govern the motion of vortical flow. Such flows can be considered to be composed of vortex lines, which are defined as lines parallel to the local vorticity vector $\vec{\omega}$, and represent the local axis of rotation of the fluid particles at that location [56]. The definition of a vortex line is analogous to that of a streamline, which is parallel to the local velocity vector. A collection of vortex lines passing through a surface in space is termed a vortex tube, as illustrated in Figure 2.18, which features bounding surfaces S_1, S_2 and S_3. By definition, the vorticity normal to a vortex tube is zero.

The first Helmholtz law of vortex motion states that, for a fixed time, the integrated vorticity flux through the vortex tube is constant, Eq. 2.24 [55]. Equivalently, this states that the circulation of a vortex tube is constant, Eq. 2.25.

$$\iint_{S_1} \boldsymbol{\omega_1} \cdot \boldsymbol{n_1} dS = \iint_{S_2} \boldsymbol{\omega_2} \cdot \boldsymbol{n_2} dS \tag{2.24}$$

$$\oint_{C1} \vec{V} \cdot d\vec{s} = \oint_{C,2} \vec{V} \cdot d\vec{s} \tag{2.25}$$

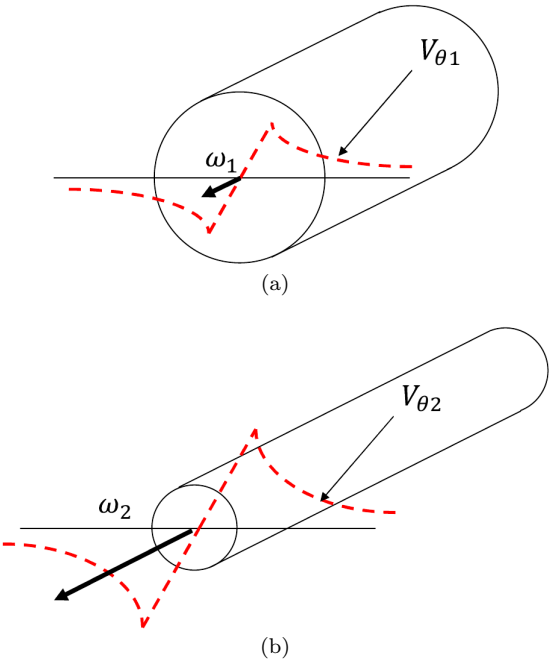

FIGURE 2.19: The qualitative behaviour of a vortex filament, (a): Prior to vortex intensification, (b): After vortex intensification

Further important laws are derived based on the temporal evolution of vortical flow. If it is assumed that the flow is barotropic and inviscid, and that body forces are conservative, then the circulation along any material loop is constant and the flow is circulation-preserving. This is Kelvin's circulation theorem. The second and third Helmholtz laws state that a material vortex tube moves with the fluid, and that the strength of a vortex tube is constant in time [55]. The Helmholtz vortex laws provide an explanation for the existence of the vortex intensification term in the vorticity equation (Eq. 2.23). Consider a streamwise vortex tube contained in an incompressible circulation-preserving flow. If the vortex tube experiences a flow contraction which is aligned with the tube axis, then continuity dictates that the tube will experience a reduction in cross-sectional area which is proportional to the increase in velocity. Since the strength of the vortex tube remains constant, the tube vorticity will increase in proportion to the reduction in the tube cross-sectional area. This is easily appreciated from Eq. 2.24, and is illustrated qualitatively in Figure 2.19(a) and Figure 2.19(b). Physically, vortex intensification causes a reduction in the moment of inertia of the fluid elements, and so their angular velocity increases to satisfy conservation of angular momentum [53]. In a similar manner, a vortex will experience a reduction in vorticity when a streamwise diffusion takes place.

The behaviour of vortical flow inside a flow contraction can be elucidated using the concept

of a vortex filament, which is defined as a vortex tube of infinitesimal size surrounded by irrotational fluid [57]. As a result of the Helmholtz vortex laws, a vortex filament will experience vorticity intensification when it passes through a streamwise contraction. This concept was employed by Prandtl [58] in the study of the evolution of freestream turbulence in a wind tunnel contraction, and has subsequently formed the basis of a range of studies of contracted freestream turbulence [59, 60, 61]. It was assumed that the turbulent eddies contained in the freestream flow consisted of discrete vortex filaments, such that in-plane velocity fluctuations are attributed to vortex filaments whose axes were oriented parallel to that of the wind tunnel. Similarly, the out-of-plane velocity fluctuations were assumed to be a result of vortex filaments oriented perpendicular to the tunnel axis. Consider a position inside a streamwise contraction which is characterised by a velocity ratio of w/W_∞, where w is the average local streamwise velocity, and W_∞ is the average streamwise velocity prior to entering the contraction. The cross-sectional area of the vortex filament is inversely proportional to the velocity ratio, and so the radius of the vortex filament, r_f, is inversely proportional to the square root of the velocity ratio, Eq. 2.26, where $r_{f,0}$ refers to the filament radius in the unperturbed flow.

$$\frac{r_f}{r_{f,0}} = \sqrt{\frac{W_\infty}{w}} \tag{2.26}$$

The streamwise-oriented vortex filament will then experience an increase in average streamwise vorticity which is equal to w/W_∞, Eq.2.27, where $\omega_{z,av,0}$ is the average streamwise vorticity prior to the flow contraction.

$$\frac{\omega_{z,av}}{\omega_{z,av,0}} = \frac{w}{W_\infty} \tag{2.27}$$

It was then assumed that the tangential velocity associated with the vortex filament could be considered as equal to the product of the average vorticity and the vortex filament radius ($V_\theta = \omega_{z,av} r_f$). Therefore, the tangential velocity increased in proportion to the square root of the velocity ratio, Eq. 2.28.

$$\frac{V_\theta}{V_{\theta,0}} = \sqrt{\frac{w}{W_\infty}} \tag{2.28}$$

The preceding vortex filament theory assumes incompressible, inviscid flow where circulation is preserved. Furthermore, it is assumed that the vortex filament is of an infinitesimal size, and that the streamwise velocity w inside the vortex filament is precisely equal to that

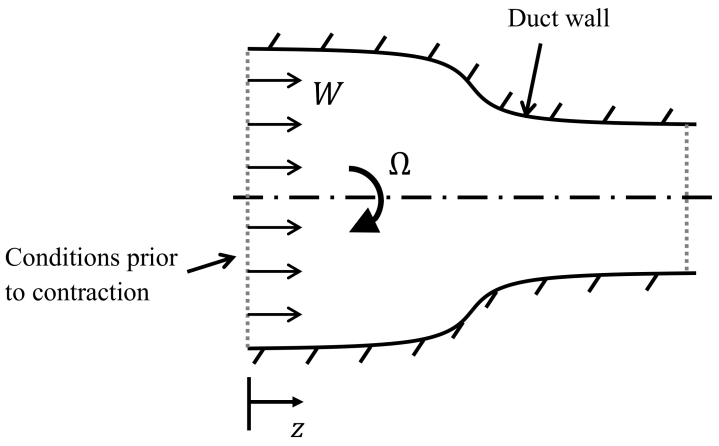

FIGURE 2.20: Schematic of the Batchelor model [62] for a confined flow inside an axisymmetric contraction

associated with the mean flow. However, Batchelor [62] demonstrated that for vortices with a finite cross-section, there is a coupling between the in-plane and out-of-plane velocity distributions which can have a notable impact on the vortex intensification process. Consider a steady, inviscid, incompressible, axisymmetric flow inside a duct, consisting of a uniform streamwise velocity W with a solid body rotation ($V_\theta = \Omega r$) around the streamwise axis, Figure 2.20, where Ω is the average vorticity of the vortex. Note that this model is for a bounded flow only, and that the boundary layers on the duct walls are neglected. Under such conditions, the governing equation of motion can be expressed as Eq. 2.29, ψ is the stream function, Eq. 2.30.

$$\frac{\partial^2\psi}{\partial z^2} + \frac{\partial^2\psi}{\partial r^2} - \frac{1}{r}\frac{\partial\psi}{\partial r} = \frac{2\Omega^2}{W}r^2 - \frac{4\Omega^2}{W^2}\psi \tag{2.29}$$

$$V_z = \frac{1}{r}\frac{\partial\psi}{\partial r}, V_r = -\frac{1}{r}\frac{\partial\psi}{\partial z} \tag{2.30}$$

It is possible to obtain analytical solutions [62] of the governing equation (Eq. 2.29) by defining a stream function in terms of the change in flow conditions from the initial state prior to intensification, Eq. 2.31. Note that F is the departure of the stream function from the initial condition prior to the flow contraction [62].

$$\psi(z,r) = \frac{1}{2}Wr^2 + rF(z,r) \tag{2.31}$$

As a result, it is possible to re-write the governing equation as Eq. 2.32, where $k = 2\Omega/W$.

$$\frac{d^2F}{dz^2} + \frac{d^2F}{dr^2} + \frac{1}{r}\frac{dF}{dr} + \left(k^2 - \frac{1}{r^2}\right)F = 0 \tag{2.32}$$

It is then supposed that the flow experiences an axisymmetric transition in the streamwise direction, such that the diameter of the duct changes. For example, the flow may experience a contraction, such that the diameter of the duct is reduced. If we consider only the conditions far downstream of the transition, then the streamwise gradients are negligible, and the governing equation reduces to Eq. 2.33.

$$\frac{d^2F}{dz^2} + \frac{d^2F}{dr^2} + \frac{1}{r}\frac{dF}{dr} + \left(k^2 - \frac{1}{r^2}\right)F = 0 \tag{2.33}$$

The general solution of Eq. 2.33 is given as a function of Bessel functions, Eq. 2.34, where J_1 and Y_1 are Bessel functions of the first and second kind. The constants A and B can be determined based on the boundary conditions of the flow under consideration, along with the initial and final radii of the duct [62].

$$F = AJ_1(kr) + BY_1(kr) \tag{2.34}$$

The model given in Eq. 2.33 has been solved for a range of swirling flows inside a confined contraction or a diffusion [63, 64, 65, 66]. However, the results from the confined swirling flow studies are of limited applicability to the flow contraction experienced in an unconfined intake capture streamtube. Leclaire et al. [65] employed a cross-wire hot wire to measure the effect of a contraction on the three-component velocity and turbulence characteristics of a rotating flow inside a duct. A rotating honeycomb arrangement was employed to impart a solid body rotation to an initially uniform low-speed flow in a duct. The flow subsequently entered a confined contraction with contraction ratios $(R_1/R_0)^2$ of 4 and 9, where R is the duct radius and the subscripts "0" and "1" refer to the conditions prior to, and downstream of, the contraction. The measurements demonstrated that flow separation occurred in the duct boundary layers just upstream of the contraction, and can thus have an influence on the swirling flow characteristics. In addition Rusak and Meder [64] and Rusak et al. [66] performed numerical studies on the effect of flow contraction on a swirling flow inside a duct. Asymptotic solutions were obtained for inviscid, incompressible, axisymmetric flow inside a pipe, where the initial flow condition comprised a uniform streamwise flow in conjunction with a q-vortex tangential velocity profile. Similarly to

the experimental measurements of Leclaire et al. [65], flow separation was observed on the walls of the duct inside the contraction. Of course, such a flow features will not occur inside an intake capture streamtube. In fact, very little attention has been given to the case of an unbounded swirling flow, and only Batchelor [62] has provided a theoretical analysis based on Eq. 2.33. It was assumed that an isolated vortex tube of initial radius $r_{c,1}$ is contained in an irrotational flow with a uniform streamwise velocity W_1. The tangential velocity profile consisted of a solid body rotation inside the vortex tube, and a potential vortex velocity distribution in the surrounding irrotational region, Eq. 2.35.

$$V_\theta(r) = \begin{cases} \Omega r & \text{if } r \leq r_{c,1} \\ \frac{\Omega r_{c,1}^2}{r} & \text{if } r \geq r_{c,1} \end{cases} \tag{2.35}$$

It was then assumed that the flow just outside the vortex undergoes a transition in streamwise velocity from W_1 to W_2, and that the radius of the vortex tube experiences a change from $r_{c,1}$ to $r_{c,2}$. After the transition, it was assumed that the conditions given in Eq. 2.36 prevail.

$$\begin{gathered} V_z = W_2 \text{ at } r = r_{c,2} \\ \psi = \tfrac{1}{2} W_1 r_{c,1}^2 \end{gathered} \tag{2.36}$$

The radius of the vortex tube, $r_{c,2}$, can be calculated using Eq. 2.37, where $k = 2\Omega/W_1$. Note that J_0 and J_1 are the Bessel functions of the first kind, of orders 0 and 1, respectively, Eqs. 2.38 and 2.39 [67].

$$\frac{W_2}{W_1} = 1 + \left(\frac{r_{c,1}^2}{r_{c,2}^2} - 1 \right) \frac{\frac{1}{2} k r_{c,2} J_0(k r_{c,2})}{J_1(k r_{c,2})} \tag{2.37}$$

$$J_0(k r_{c,2}) = \sum_{m=0}^{\infty} \frac{(-1)^m (k r_{c,2})^{2m}}{2^{2m} (m!)^2} \tag{2.38}$$

$$J_1(k r_{c,2}) = \sum_{m=0}^{\infty} \frac{(-1)^m (k r_{c,2})^{2m+1}}{2^{2m+1} m! (m+1)!} \tag{2.39}$$

It is assumed that the streamwise velocity is equal to W_2 at the edge of the vortex tube. Following calculation of the radius of the vortex tube, it is then possible to calculate the

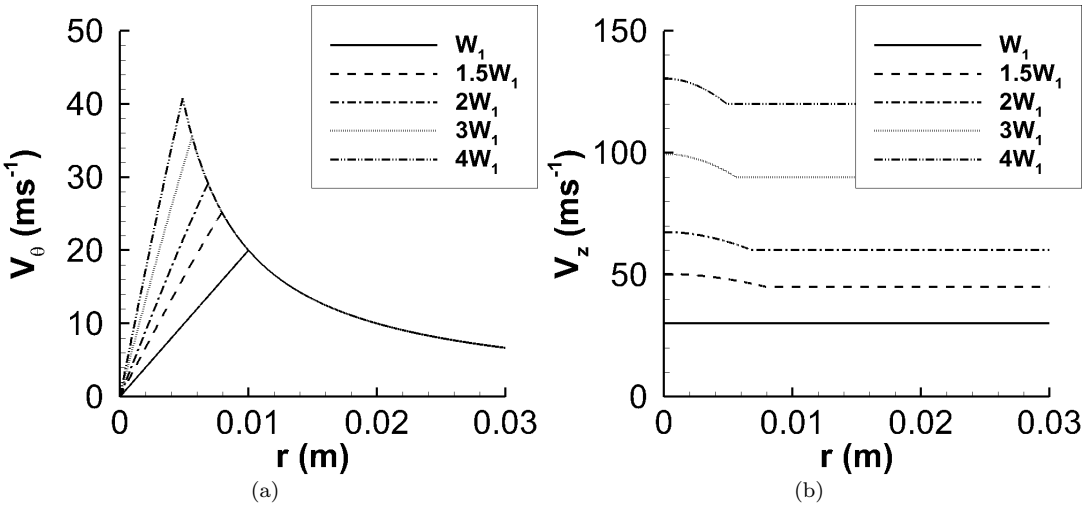

(a) (b)

FIGURE 2.21: Sample data generated using Batchelor model for $\Omega = 2000s^{-1}$, $r_{c,1} = 0.01m$ and $W_1 = 30ms^{-1}$ (a) Tangential velocity profile as a function of r (Eq. 2.41), (b) Streamwise velocity profile as a function of r (Eq. 2.40)

streamwise and tangential velocity profiles, Eq. 2.40 and Eq. 2.41, respectively, which have been derived from the solution of Eq. 2.33, [62].

$$\frac{V_z}{W_2} = 1 + \left(\frac{r_{c,1}^2}{r_{c,2}^2} - 1\right) \frac{\frac{1}{2} k r_{c,2} J_o(kr)}{J_1(k r_{c,2})} \tag{2.40}$$

$$\frac{V_\theta}{\Omega r} = 1 + \left(\frac{r_{c,1}^2}{r_{c,2}^2} - 1\right) \frac{r_{c,2} J_1(kr)}{J_1(k r_{c,2})} \tag{2.41}$$

Sample tangential and streamwise velocity distributions (Figure 2.21(a) and 2.21(b)) have been generated for a range of final streamwise velocities W_2, given a vortex of initial core radius $r_{c,1}$ equal to $0.01m$, an angular velocity Ω of $2000s^{-1}$ and an initial streamwise velocity W_1 of $30ms^{-1}$.

The model suggests that a streamwise velocity excess is generated inside the vortex core during the intensification process. This excess reaches a value of approximately 10% for the example provided in Figure 2.21(b) when the final streamwise velocity is four times that of the initial streamwise velocity. This effect can be attributed to the change in the vortex static pressure field when the vortex is intensified [62], and is similar to that which occurs during the vortex generation process (section 2.2.1). Prior to intensification, the pressure at the vortex centre is lower than that in the surrounding flow. When the vortex

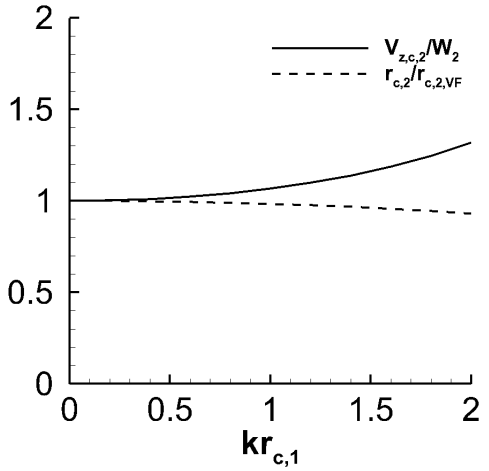

FIGURE 2.22: Influence of the initial vortex characteristics ($kr_{c,1}$) on the evolution of the vortex in a streamwise contraction corresponding to $W_2/W_1 = 2.0$, [62], where ($V_{z,c,2}/W_2$) is the ratio of the vortex centreline streamwise velocity to the surrounding freestream velocity, and ($r_{c,2}/r_{c,2,VF}$) is the ratio of the Batchelor model vortex core radius to the vortex core radius as given by vortex filament theory

undergoes intensification, the vortex peak tangential velocity increases, and the core static pressure is reduced as a result of radial equilibrium. This reduction in static pressure is even greater than the static pressure drop experienced in the flow surrounding the vortex due to the flow contraction. Therefore, the favourable streamwise static pressure gradient inside the vortex during intensification is greater than the static pressure gradient associated with the flow contraction, and a streamwise velocity excess is produced as a result.

This coupling between the tangential and streamwise velocities is dependent on the initial characteristics of the vortex, as well as the intensity of the streamwise contraction. For a given streamwise contraction, the size of the streamwise velocity excess, expressed as the ratio of the vortex centreline streamwise velocity and the streamwise velocity beyond the vortex core ($V_{z,c,2}/W_2$), increases as a function of $kr_{c,1}$, Figure 2.22. Therefore, the size of the streamwise velocity excess increases with the initial vortex strength and core radius. Note that wing-tip vortices may be characterised by values of $kr_{c,1}$ close to 1 [62]. An additional effect of the vortex intensification process is also highlighted in Figure 2.22. When the vortex features an infinitesimal initial core radius, that is, $r_{c,1} \to 0$, then the change in core radius ($r_{c,2}/r_{c,1}$) approaches the value given by vortex filament theory (Eq. 2.26) [62]. The vortex core radius becomes smaller than that given by the vortex filament model ($r_{c,2,VF}$) when the value of $kr_{c,1}$ is increased (Figure 2.22). This is due to

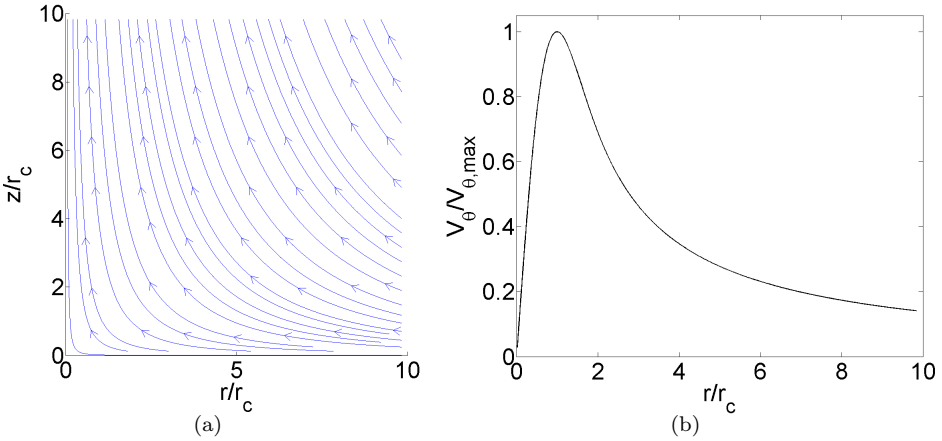

(a) (b)

FIGURE 2.23: Illustration of the flowfield associated with the steady Rott vortex model [68] for an inflow gradient of $a = 1s^{-1}$, (a) Streamlines in the $r - z$ plane, (b) Tangential velocity profile as a function of distance from the vortex centre (r/r_c)

the additional intensification which is brought about by the generation of a streamwise velocity excess.

An important question which arises from the preceding theory is to what extent viscous and turbulent diffusion affect the intensification process. The inviscid model developed by Batchelor features a discontinuity in the tangential and streamwise velocity profiles, which is not consistent with experimental measurements of wing-tip vortices (section 2.2.1). An exact solution of the Navier-Stokes equations for axisymmetric, incompressible, laminar viscous flow was investigated by Rott [68]. The model assumes that the flow experiences an increasing uniform streamwise velocity, Eq. 2.42, in addition to a negative radial velocity profile, Eq. 2.43, where $a = -\partial V_r/\partial r$. The streamlines which correspond to this flow are shown in Figure 2.23(a).

$$V_z = 2az \tag{2.42}$$

$$V_r = -ar \tag{2.43}$$

Under such conditions, the flow can be expressed as a linear second-order differential equation, Eq. 2.44, where σ is a transformed variable. If it is assumed that the inflow gradient a is constant in time, then it is then possible to obtain a solution for the tangential velocity profile, Eq. 2.45.

$$\frac{\partial \Gamma}{\partial t} - ar\frac{\partial \Gamma}{\partial r} = \nu\left[\frac{\partial^2 \Gamma}{\partial r^2} - \frac{1}{r}\frac{\partial \Gamma}{\partial r}\right] \tag{2.44}$$

$$V_\theta = \frac{\Gamma_0}{2\pi r}\left[1 - exp\left(\frac{-ar^2}{2\nu}\right)\right] \tag{2.45}$$

The solution given in Eq. 2.45, Figure 2.23(b) represents the tangential velocity distribution for t$\rightarrow \infty$, and is equivalent to the Burger's vortex [55]. The vortex flow is steady, such that the flux of vorticity convected from the surrounding flow by the negative radial velocity is balanced by the viscous diffusion [55]. An exact solution for the unsteady case with a constant inflow gradient can also be obtained. The governing equation is re-written in terms of a transformed variable σ, such that $\Gamma = \Gamma(\sigma)$, Eq. 2.46, where $\sigma = rF(t)$. Rott demonstrated that Eq. 2.46 can be solved analytically for $F(t)$ when the governing equation is expressed as Eq. 2.47. As a result, the tangential velocity distribution for a constant inflow gradient is given by Eq. 2.48, where β is an integration constant [68]

$$\left(\frac{\partial F}{\partial t} - aF\right)\sigma\frac{d\Gamma}{dt} = \nu F^3\left[\frac{d^2\Gamma}{d\sigma^2} - \frac{1}{\sigma}\frac{d\Gamma}{d\sigma}\right] \tag{2.46}$$

$$F' - aF = -cF^3 \tag{2.47}$$

$$V_\theta = \frac{\Gamma_0}{2\pi r}\left[1 - exp\left(-\frac{ar^2}{2\nu}\frac{1}{1+\beta exp(-2at)}\right)\right] \tag{2.48}$$

It is also possible to obtain solutions for the case where the inflow gradient is a function of time ($a(t)$). However, an exact analytical solution is not possible and, instead, numerical solutions to Eq. 2.47 must be obtained. The tangential velocity distribution is representative of a typical wing-tip vortex flow. However, the radial velocity is of the same order of magnitude as the tangential and radial velocities, and increases linearly as a function of distance from the vortex centre. This behaviour is not representative of wing-tip vortex flows, in which the radial velocity is typically an order of magnitude smaller than the streamwise and tangential velocities (section 2.2.1). Furthermore, wing-tip vortex flows feature a radial velocity perturbation close to the vortex only. Consequently, this model

is not suitable for capturing the flow physics of a wing-tip vortex inside a streamtube contraction.

The review of vortex intensification theory has demonstrated that, for an inviscid, incompressible flow, a vortex will experience a reduction in core radius, coupled with an increase in tangential velocity and vorticity, in response to an increase in velocity in the direction of the vortex axis. The change in streamwise velocity is a principal parameter in the definition of the vortex characteristics. A streamwise velocity excess relative to the surrounding flow may be generated during the intensification process as a result of the static pressure gradient generated by the change in tangential velocity. The magnitude of this excess, however, is dependent on the magnitudes of the streamwise contraction, the vortex strength and the vortex size. The Rott vortex model [68] accounts for viscosity during the vortex intensification process. However, the velocity field assumed by the model is not representative of wing-tip vortex flows. Furthermore, it has been demonstrated that the presence of turbulence has a notable effect on the evolution of a vortex in a uniform flow (section 2.3). It is currently not known to what extent turbulent diffusion affects the vortex intensification process.

2.4.2 Experimental measurements

A small number of experimental measurements have been focussed on streamwise vortex intensification for the vortex Reynolds numbers of interest for vortex ingestion.

Ananthan and Leishman [69] and Ramasamy and Leishman [34] studied the evolution of a wing-tip vortex produced by a hovering sub-scale helicopter rotor located close to a ground surface. The wing-tip vortex was generated by a single bladed rotor with a rectangular planform and a NACA 2415 section. The vortex Reynolds number and chord Reynolds number were approximately 4×10^4 and 2.72×10^5. Three component velocity measurements were acquired using Laser Doppler Velocimetry. It was found that the core radius of the vortex increased downstream of the rotor in a manner consistent with vortex growth (Figure 2.24(a)). However, after a certain time following generation, the core radius ceased to grow and subsequently reduced. This was attributed to an interaction between the rotor flowfield and the ground surface, such that the wing-tip vortex was stretched along its axis (Figure 2.24(b)). The effects of the strain were incorporated into the Squire vortex model for application in a free-vortex model. It was assumed that the wing-tip vortex could be considered as a vortex filament, for which the Helmholtz vortex theorems apply (section 2.4.1). Consider a section of the vortex filament, of initial length

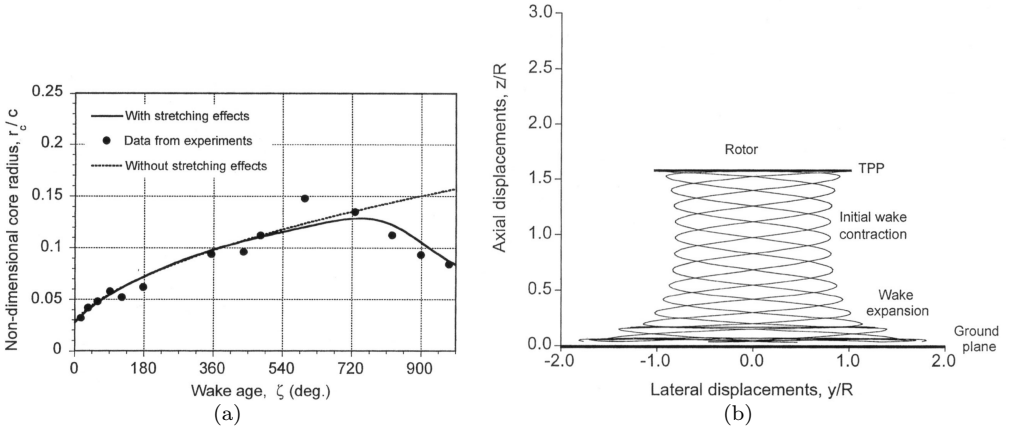

FIGURE 2.24: Rotor wing-tip vortex filament stretching [69], (a) Measurements of vortex core radius evolution as a function of wake age, with Squire vortex model (Eq. 2.22) and combined growth and strain model (Eq. 2.50), (b) Wake expansion as a result of interaction with the ground surface

l. When the filament is subjected to a strain along its axis, the length of the vortex filament will increase to $l + \Delta l$. It is thus possible to define the strain on the filament as $\epsilon = \Delta l/l$. It can thus be shown, under the assumption of conservation of mass, that the change in the vortex core radius can be determined with Eq. 2.49, [69, 34].

$$\Delta r_c = r_c \left[1 - \frac{1}{\sqrt{1+\epsilon}} \right] \tag{2.49}$$

This was implemented into the Squire vortex model as given in Eq. 2.50. It was found that the vortex model results were in good agreement with the growth model for a constant turbulent viscosity coefficient (δ), (Figure 2.24(a)).

$$r_c = \sqrt{r_{c,0}^2 + \frac{4\alpha_{lo}\delta\nu}{\Omega} \int_{\zeta 0}^{\zeta} (1+\epsilon)^{-1} d\zeta} \tag{2.50}$$

Garbeff et al. [70] conducted measurements of a wing-tip vortex with a vortex Reynolds number of approximately 2×10^4 in a mild wind tunnel contraction. A sub-scale NACA 0015 semi-span wing with a rectangular planform was mounted upstream of a mild contraction which featured a velocity ratio of approximately 1.4. Measurements of the three component velocity field were acquired using a hot wire probe. It was found that the peak tangential velocity increased in a manner consistent with vortex intensification (section 2.4.1), but the vortex core radius remained approximately constant. Results obtained

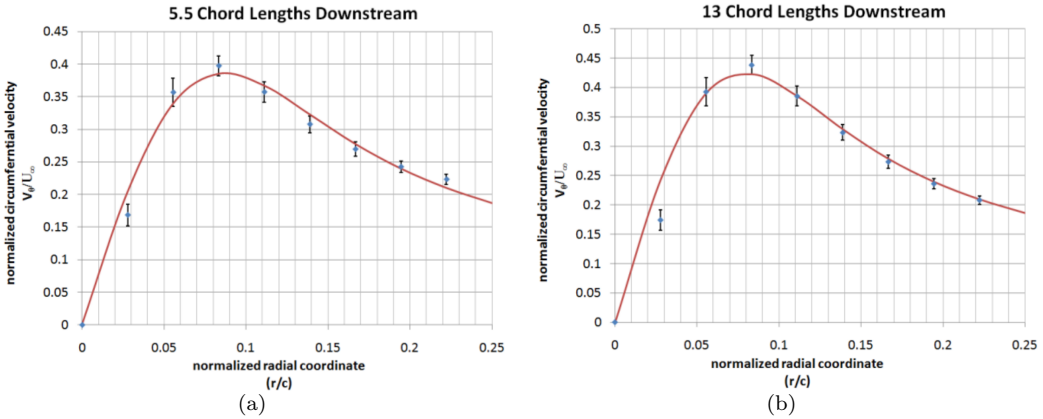

(a) (b)

FIGURE 2.25: Measurements of a wing-tip vortex in a wind tunnel contraction, tangential velocity compared with Rott vortex model profile [70], (a) Upstream of the wind tunnel contraction, (b) Downstream of the wind tunnel contraction

from the Rott vortex model for an unsteady inflow gradient (section 2.4.1) were compared with the measurements using a curve fit of the tangential velocity profile just upstream of the contraction as an initial condition for the vortex model, Figure 2.25(a). It was found that the increase in tangential velocity given by the vortex model was in good agreement with the measurements. However, the model results indicated a decrease in core radius which was not observed in the measurements. It was concluded that vortex wandering may have contaminated the measurements and resulted in an artificially large core radius.

A limited number of measurements of vortex intensification have been conducted at vortex Reynolds numbers of interest for sub-scale vortex ingestion studies. The experimental measurements suggest that a streamwise vortex will experience a reduction in vortex core radius and an increase in peak tangential velocity, in a manner consistent with vortex theory (section 2.4.1). However, the existing measurements provide only limited information on the details of the fundamental behaviour of a vortex during intensification. Based on the existing knowledge from experimental measurements of vortex intensification and wing-tip vortex flows, it is possible to identify a number of important aspects which guide the selection of an appropriate approach in this research to measure vortex intensification.

The first aspect concerns the choice of measurement method. The flowfield associated with a general vortex ingestion scenario is likely to feature notable perturbations in the in-plane and streamwise velocity components due to the vortex (section 2.2.1), in conjunction with the streamwise velocity which is attributed to the capture streamtube flow. Thus, it is necessary to employ a measurement method which can capture the three-component (3C) velocity field inside the capture streamtube. In addition, it was emphasised in section 2.2.2

that wing-tip vortices such as those of interest in this research can demonstrate random fluctuations of the in-plane location of the vortex centre. This presents a notable difficulty for fixed-position measurement methods, such as pressure probes or hot wire probes, since it is not possible to determine the true location of the vortex core. Consequently, a measurement method which captures an instantaneous measurement of the entire 3C flowfield is advantageous, since it is possible to identify the true location of the vortex centre, and thus mitigate the effects of wandering on the measurements. A final consideration for the measurement method is that wing-tip vortices may be sensitive to the presence of measurement probes in the flow (section 2.2.2). Therefore, a non-intrusive measurement method, which avoids the placement of probes in the flow, is desirable. Based on the preceding requirements, Stereoscopic Particle Image Velocimetry (Stereo PIV) has been selected for use in this research.

The second aspect concerns the influence of the vortex characteristics on the vortex intensification process. Experimental and theoretical studies of streamwise vortices in a uniform streamwise flow have demonstrated that the influence of vorticity diffusion, and so the evolution of the vortex, is closely related to the vortex Reynolds number (section 2.3). There is currently no knowledge of the role the vortex Reynolds number during vortex intensification. As highlighted in section 2.2.1, the strength of a wing-tip vortex is proportional to the lift coefficient of the generating wing and the freestream velocity. Consequently, these parameters have been selected in this research to vary the vortex Reynolds number of the wing-tip vortex prior to intensification.

Finally, existing measurements in the literature have been acquired for fixed flow contraction levels. The characteristics of an intake capture streamtube can be defined by the intake velocity ratio ($VR = W_i/W_\infty$), given by relative magnitudes of the freestream flow and the flow inside the intake (section 2.1). As highlighted in the preceding paragraph, the freestream velocity can be employed to control the vortex Reynolds number of the wing-tip vortex which is produced by a vortex generator at a fixed lift coefficient. Consequently, a requirement for the present research is to perform controlled parametric studies for a range of intake and freestream velocities, and for a range of subsequent streamtube contraction levels.

2.5 Impact of vortex ingestion on aircraft engines

Although there has been no detailed survey to date of streamwise vortex ingestion, there have been a small number of experimental and CFD studies which are focussed on the

impact of a streamwise vortex on the intake flow quality and the turbomachinery response. This section provides a summary of the most important conclusions and consequences.

2.5.1 Intake flow characteristics

The purpose of the intake is to deliver an undistorted, uniform airflow to the engine throughout the operating range of both the engine and the airframe. However, it is possible that the inlet flow may be adversely affected once an engine is installed on an airframe. There have been a number of instances where engine-airframe compatibility has been found to be poor under certain flight conditions, and the engine performance and operability have been significantly reduced [2]. In general, inlet flow distortion may be characterised by nonuniformities of pressure, temperature, and any deviation in flow direction from that parallel to the intake axis [2]. As outlined in section 2.2.1, a streamwise vortex generally consists of perturbations of static and total pressure, in-plane velocity and out-of-plane velocity, relative to the freestream flow. Therefore, when ingested by an intake, a vortex is anticipated to produce a distortion inside the intake flow. The purpose of this section is to review the current understanding of the impact of an ingested streamwise vortex on the quality of the intake flow.

The total pressure distortion which results from the ingestion of vortical flow was investigated experimentally by Talwar [71] using a $1/30^{th}$ scale civil aircraft intake model at intake velocity ratios of 1.2 and 4.0. Streamwise vorticity was generated upstream of the intake and close to the intake centreline using a semi-span delta wing. At an intake velocity ratio of 1.2, the total pressure measurements inside the intake revealed extensive total pressure distortion across the entire intake flow, Figure 2.26(a). The intake flow consisted of three distinct peaks of total pressure loss. The first two peaks, located at circumferential positions of 30^o and 120^o, corresponded to the two streamwise vortices which were generated by the semi-span wing. The third peak at 240^o resulted from the support bar which was used to mount the delta wing in the tunnel. Despite the presence of the vortex, there were no separations on the inlet boundary layers. Although the extent of the total pressure distortion was large, the total pressure loss values attributed to the distortion were low. The maximum total pressure loss attributed to the delta wing vortices was no more than 0.01% of the freestream total pressure. By comparison, the total pressure loss associated with ground vortices can reach as much as 30% of the freestream total pressure [72].

The total pressure distortion can be characterised by the DC60 distortion descriptor, Eq. 2.51, where $\overline{P_f}$ is the fan face area-weighted average total pressure, $\overline{P_{60}}$ is the mean total

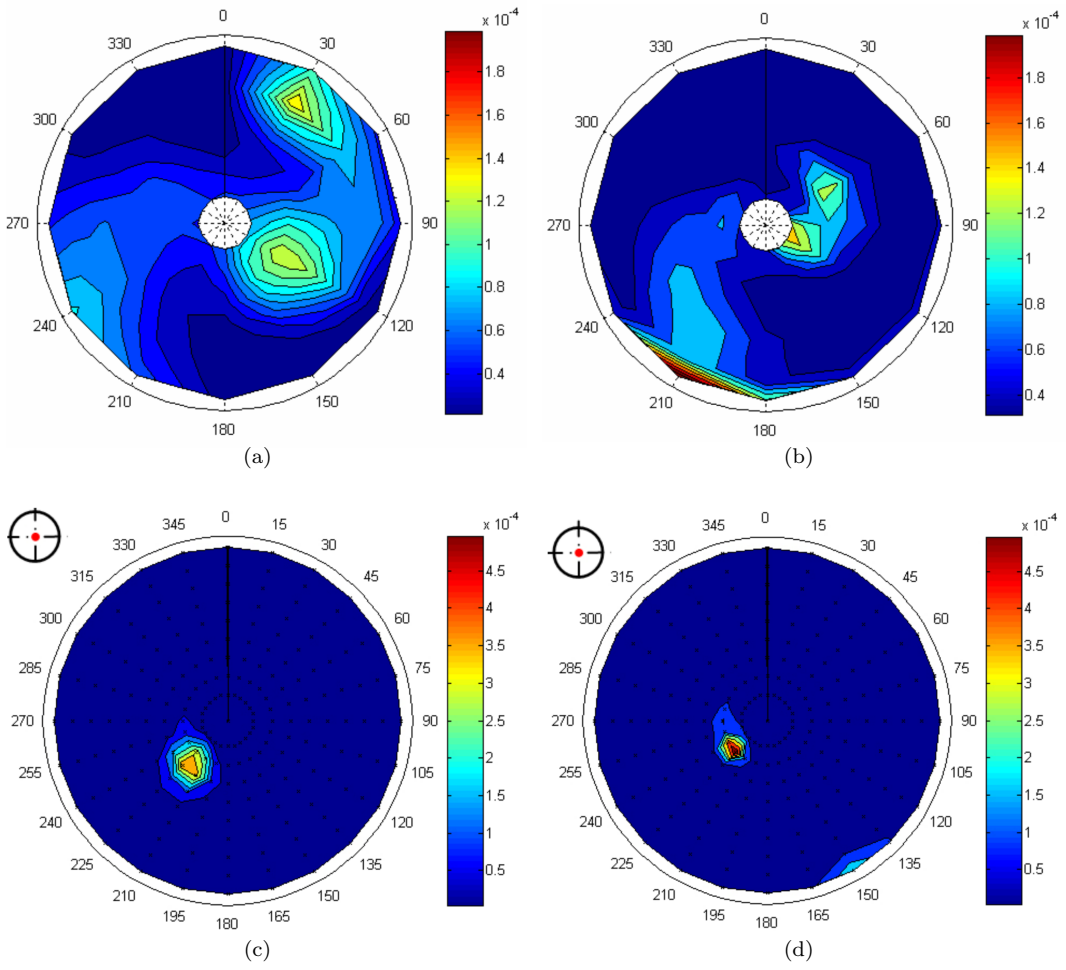

FIGURE 2.26: Sub-scale measurements of total pressure coefficient inside intake ($(P_{0,\infty} - P_0)/P_{0,\infty}$) following ingestion of a streamwise vortex close to the intake centreline, (a): Delta wing vortex, VR=1.2[71], (b): Delta wing vortex, VR=4.0[71], (c): Rectangular wing, VR=1.2[73], (d): Rectangular wing, VR=3.8[73]

pressure in the 60^o sector where the mean total pressure is lowest, and q_f is the mean dynamic pressure at the fan face.

$$DC60 = \frac{\overline{P_f} - \overline{P_{60}}}{q_f} \tag{2.51}$$

The DC60 value for centreline ingestion was found to be 0.035, which indicates low levels of total pressure distortion. For example, DC60 values of between 0.05 and 0.10 are often considered as being an appropriate limit to ensure compatibility between the intake and the engine [74, 75], and values of the order 0.4-0.6 may induce engine surge [76]. The

DC60 parameter increased in response to the change vortex ingestion position, Figure 2.27. This was attributed to an interaction between the vortex and the intake inner surface boundary layer fluid. However, the interactions did not produce a notable increase in the total pressure distortion levels. The distortion levels were found to decrease by an order of magnitude when the intake velocity ratio was increased from 1.2 to 4.0. This is a result of two effects indicated by a comparison between Figures 2.26(a) and 2.26(b). Firstly, when the intake velocity ratio is increased, the distortion associated with the vortex is distributed over a smaller area of the intake flow. This is consistent with the vortex filament theory outlined in section 2.4.1, which suggests that streamwise vortices will experience a reduction in core area which is inversely proportional to the streamtube contraction levels. Therefore, the total pressure loss contained inside the vortex cores will be distributed over a reduced area of the intake flow when the intake velocity ratio is increased. Secondly, the total pressure loss inside the vortex was found to be approximately constant for a change in intake velocity ratio. As a result, the denominator in Eq. 2.51 increases in proportion to the square of the intake velocity, and the DC60 value is reduced. The intensity of the total pressure distortion observed close to 240^o increased when the intake velocity ratio was increased. It was suggested that a boundary layer separation may have been induced by the interaction between the vortex and the low-momentum boundary layer fluid on the intake inner lip surface. The intensity of the boundary layer separation was, however, small, and the total pressure distortion levels remained low.

Similar distortion levels were measured by Hodjatzadeh [73], who measured the intake flow distortion which results from the ingestion of a wing-tip vortex generated by an unswept, high aspect ratio wing. For an intake velocity ratio of 1.2, the peak value of total pressure loss was approximately 3 times greater than that associated with the delta wing, 2.26(c). However the rectangular wing distortion is distributed across a far smaller region of the intake flow. This was attributed to the fact that, unlike the delta wing, the distortion field produced by the rectangular wing consisted of only one discrete wing-tip vortex. As a result, the DC60 values measured by Hodjatzadeh were close to those measured by Talwar (Figure 2.27). Similar conclusions could be drawn from the distortion measurements at an intake velocity ratio of 3.8, Figure 2.26(d).

Measurements of flow angularity were also acquired by Hodjatzadeh [73]. The intake flow consisted of large flow angles, Figure 2.28(a), which ranged between $+22^\circ$ and -19° in the region close to the vortex centre. These notable levels of flow angularity are a result of the vortex tangential velocity field superimposed on the intake flow. The maximum swirl angles were reduced to between $+9^\circ$ and -6° when the intake velocity ratio was increased

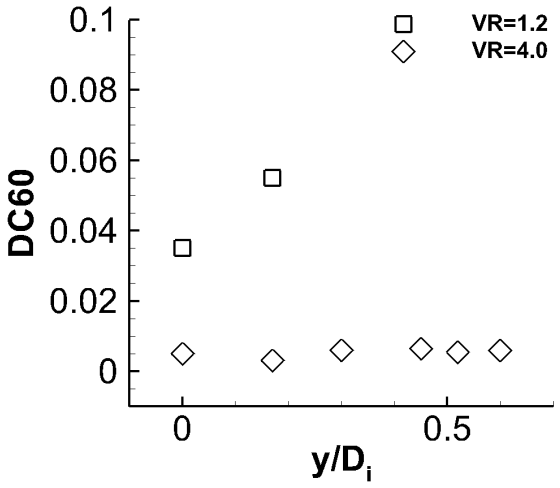

FIGURE 2.27: DC60 values calculated from total pressure distortion of intake flow as a function of distance from the intake centreline (y/D_i) (data extracted from [71])

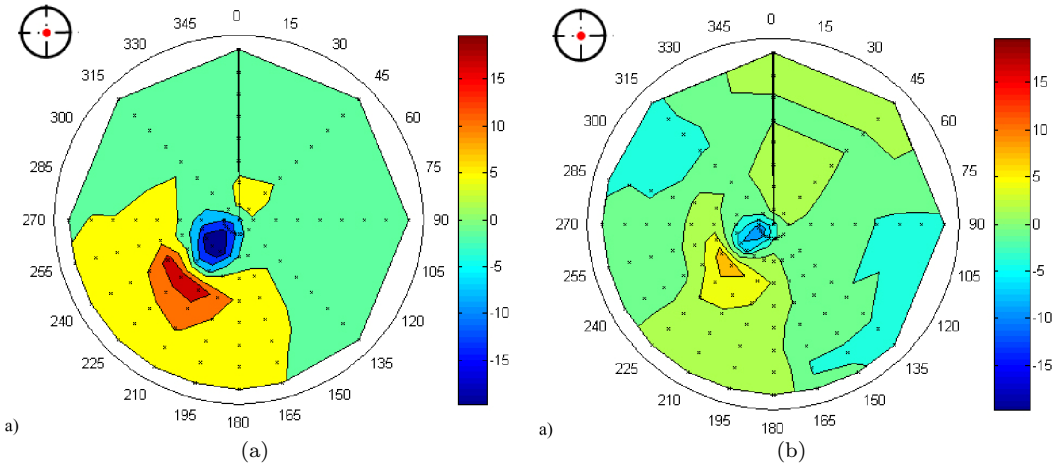

FIGURE 2.28: Sub-scale measurements of intake flow swirl angle following ingestion of a wing-tip vortex close to the intake centreline [73], (a): Intake velocity ratio = 1.2, (b): Intake velocity ratio = 3.8

from 1.2 to 3.8, Figure 2.28(b). This can be explained with reference to the vortex filament theory outlined in section 2.4.1. For an inviscid flow, the vortex filament radius will reach a value which is proportional to the square root of the increase in intake velocity ratio. As a result of conservation of angular momentum, the filament tangential velocity will increase in proportion to the square root of the intake velocity ratio. Therefore, inside the intake, the ratio of the peak tangential velocity to the streamwise velocity will reduce when the intake velocity ratio increases, which will produce a corresponding reduction in the peak flow angularity. This result demonstrates a link between the peak flow angularity and the intake velocity ratio for a given freestream condition, and suggests that vortex ingestion during low intake velocity ratio conditions will produce the greatest levels of swirl distortion. However, the vortex characteristics upstream of the intake were not obtained, so it was not possible to assess the change in peak flow angularity as a result of the ingestion process.

The preceding results have indicated the impact of a vortex on the flow distortion inside a conventional aircraft intake. However, as outlined in the introduction, vortex ingestion may also be a scenario where complex s-shaped intake designs have been employed, such as those installed on military aircraft. Even in the absence of an ingested vortex, such flows are typically characterised by notable levels of total pressure and swirl distortion which are induced as a result of the change of direction experienced by the flow inside the intake. An important aspect which must be addressed is whether an ingested vortex will have an influence on the distortion characteristics. Anderson [77] conducted simulations of the behaviour of a streamwise vortex inside a military aircraft s-duct geometry. The intake geometry featured flow control vortex generators on the intake surface to mitigate flow separation on part of the intake surface. The ingested vortex imparted notable levels of swirl to the intake flow. When a counter-clockwise rotating vortex was ingested, the flow control vortex generators were rendered ineffective. This result suggests that the ingestion of a streamwise vortex has the potential to cause a deterioration of the flow quality inside the intake. For example, if flow control vortex generators are employed to reduce the intensity of the distortion inside the intake, an ingested vortex may remove the effect of the vortex generators, and the flow distortion intensity may increase. Interestingly, this effect was not observed for a clockwise rotating vortex, which suggests that the effect of the vortex on the flow close to the vortex generators is important. It has also been found that the ingested vortex may interact with the flow distortion inside the s-duct. This was investigated experimentally by Wendt and Reichert [78]. Flow control vortex generators were used upstream of the s-duct to alleviate the flow distortion levels. The intake flow without the presence of the ingested vortex consisted of notable levels of swirl

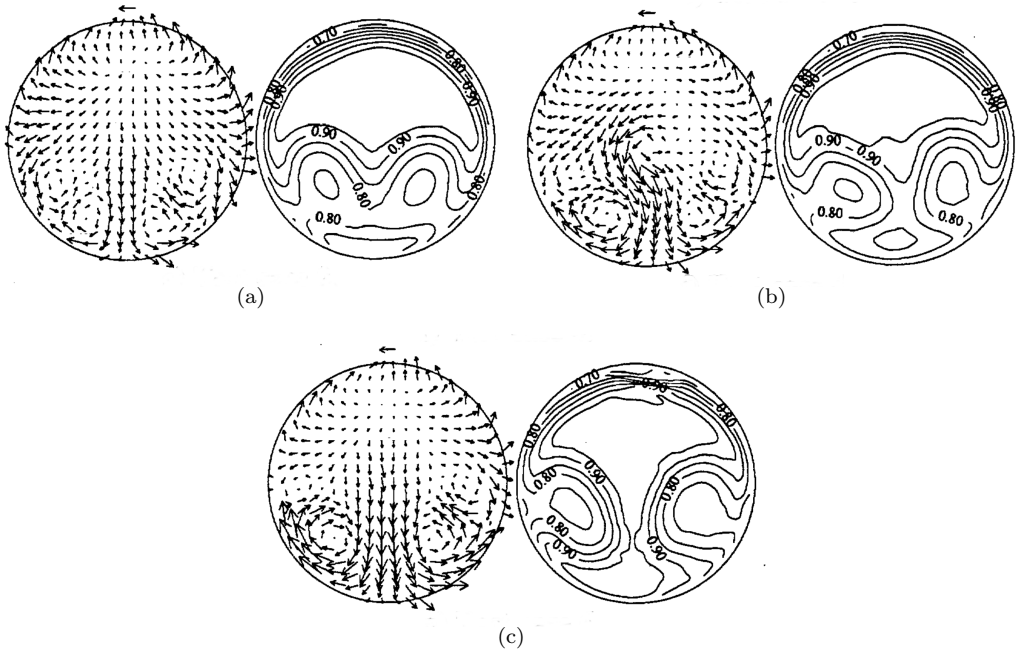

FIGURE 2.29: Measurements of in-plane velocity and total pressure downstream of an s-shaped intake [78], (a): No vortex at inlet to intake, (b): Streamwise vortex ingested at centreline, (c): Streamwise vortex ingested close to surface where induced distortion originates

and total pressure distortion, 2.29(a). When a streamwise vortex was ingested at the intake centreline, there was an increase in the intensity of the swirl distortion and a small improvement in the total pressure distortion 2.29(b). This effect was even stronger when the vortex was ingested close to the surface where the self-generated distortion originates 2.29(c). It was concluded that the streamwise vortex had increased the effectiveness of the flow control vortex generators. Although the total pressure distortion was reduced, the swirl distortion intensity and complexity was increased. It should also be noted that, in light of the findings of Anderson [77] discussed above, the effect may be dependent on the rotation direction of the vortex.

In summary, sub-scale measurements on a conventional aircraft intake have indicated that the inlet flow distortion which results from streamwise vortex ingestion is characterised by low levels of total pressure distortion but notable levels of flow angularity. The total pressure distortion is greatest at low intake velocity ratios, and increases when the vortex was ingested at positions further from the intake centreline as a result of interactions between the vortex flowfield and the intake inner surface boundary layers. Based on prior experience of the response of aircraft engines to total pressure distortion, it is concluded

that the distortion levels measured in the sub-scale tests would be unlikely to provoke engine instability. In a manner similar to the total pressure distortion, the peak flow angularity is greatest during low intake velocity ratio conditions. The available measurements suggest that the peak flow angles reduce when the intake velocity ratio is increased, in a manner which is consistent with inviscid vortex filament theory. However, there is no understanding of the change in flow angularity when the vortex is ingested through the streamtube contraction. Vortex ingestion has also been found to impact the distortion characteristics of complex s-shaped intakes. For a given configuration, there may be a reduction the total pressure distortion levels, with a corresponding increase in the swirl distortion intensity [78].

2.5.2 Response of turbomachinery to streamwise vortices

The preceding section has highlighted that the ingestion of a streamwise vortex can introduce both total pressure and swirl distortion to the intake flow. In this section, the response of the aircraft engine to such distorted intake flow conditions will be reviewed.

The response of a full-scale turbojet engine to the ingestion of a wing-tip vortex was investigated by Mitchell [8]. A streamwise vortex was generated using a tapered wing mounted upstream of the engine, and was ingested through a moveable supersonic intake geometry. The measurements, conducted for intake velocity ratios of between 0.6 and 0.8, demonstrated that the ingestion of the streamwise vortex caused a large reduction in the compressor stability margin, which refers to the proximity of the operating point of the compressor relative to the surge line. The loss in the compressor stability margin was defined in terms of the Loss in Stability Pressure Ratio (LSPR), Eq. 2.52, where P_{av} is the average total pressure, and subsripts "2" and "3" refer to measurements at the compressor face and the compressor exit, respectively. In addition, subscript "V" refers to measurements when the vortex was ingested, and "U" refers to the undistorted intake flow conditions. Note that the parameter LSPR has been computed along a line of constant corrected rotational speed, and represents the change in the compressor pressure ratio at which compressor surge is encountered.

$$LSPR = 1 - \frac{(P_{av,3}/P_{av,2})_V}{(P_{av,3}/P_{av,2})_U} \tag{2.52}$$

The measurements demonstrated that loss in stability margin is dependent on both the vortex centre location at the fan face and the vortex rotation direction relative to the

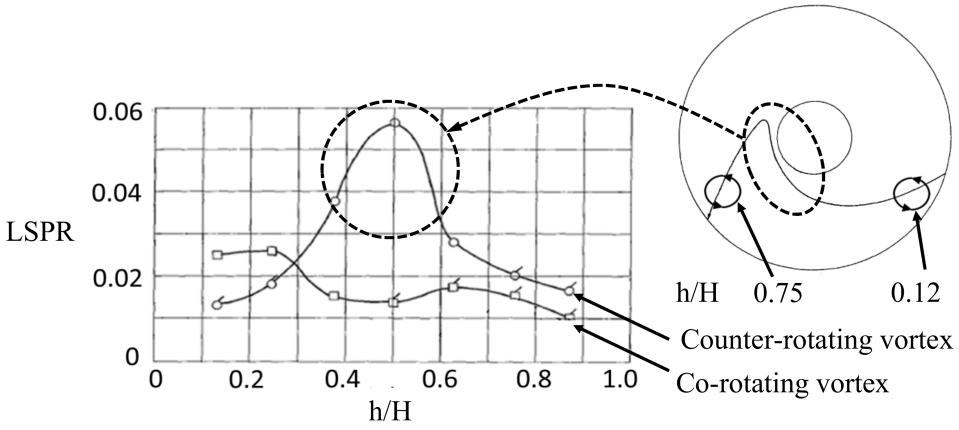

FIGURE 2.30: Loss of stability pressure ratio (LSPR) due to the ingestion of a wing-tip vortex, where h/H indicates the approximate location of the vortex centre relative to the intake lower lip, located at $h/H = 0$ [8]

compressor. The greatest loss in stability occurred when a vortex, rotating in a direction opposite to that of the compressor, was located close to the hub at the compressor face. During such an event, the compressor stall pressure ratio was 33% closer to the nominal operating line when compared to the undistorted surge line [79]. This demonstrates that there is a high risk that an aircraft engine will surge as a result of the ingestion of a streamwise vortex. The intake flow total pressure measured just upstream of the fan face indicated that there was a total pressure loss of approximately 5% of the freestream total pressure confined to the region close to the vortex. Importantly, the loss in stall compressor pressure ratio was up to 28% above the anticipated loss as calculated using the measured total pressure distortion at the engine face, Figure 2.30. The disparity between the measured and estimated loss in stability margin was attributed to the swirl distortion associated with the vortex. This suggests that conventional total pressure distortion descriptors may not be applicable for vortex distortions. As a result, engine sensitivity to swirl distortions may be dramatically underestimated if only the total pressure distortion is used as a measure of the intake flow distortion characteristics. This result also suggests that the swirl distortion plays a more important role than the total pressure distortion in influencing the stability of the compressor.

Similar behaviour has been observed by Meyer et al. [9], who conducted experiments using a low bypass ratio turbojet engine. A delta wing with a variable angle of attack was placed inside the intake duct upstream of the fan location. This produced a twin swirl pattern at the fan face, Figure 2.31(a) and a total pressure distortion pattern which is

similar to that measured in the s-duct configuration of Wendt [78]. The swirl distortion levels were characterised by the fan face average absolute swirl angle $\bar{\tau}$. The total pressure loss inside the vortex cores was approximately 5% of the freestream total pressure, which corresponds to a DC60 level of 0.15. Therefore, based on the total pressure distortion, the compressor response was anticipated to be small. However, the measurements found that the ingestion of the vortices caused a notable reduction in mass flow, total pressure ratio, efficiency, and surge margin. The deterioration in compressor stability margin was greater when the average swirl angle $\bar{\tau}$ was increased, and for higher engine mass flows, Figure 2.31(b).

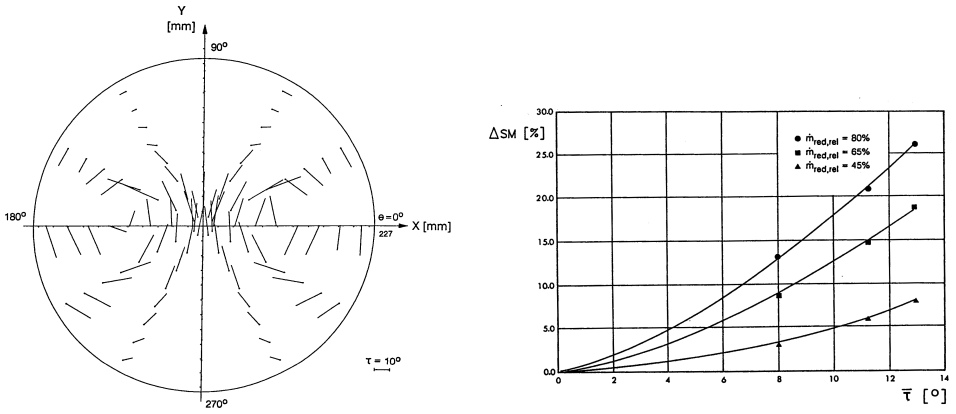

(a) (b)

FIGURE 2.31: Measurements of the impact of counter-rotating streamwise vortices created by a delta wing vortex generator [9], (a): In-plane velocity vectors upstream of engine face, (b): Loss of surge margin as a function of mean absolute swirl angle and engine mass flow

At the highest level of swirl distortion investigated, the average swirl angle at the fan face was 13^o, and the corresponding peak flow angle was approximately 17^o [80]. Under such conditions, it was found that there was a 26% reduction in surge margin, which is a similar value to that measured by Mitchell [8]. In addition, there was a 5% reduction in mass flow, a 4% reduction in compressor total pressure ratio, and a 7% reduction in compressor efficiency. This demonstrates that vortex ingestion not only increases the risk of compressor surge, but it also causes a deterioration in the overall performance of the engine. Importantly, it was found that the compressor surge margin did not have a tolerance to the swirl distortion, and a loss in surge margin was measured even when the average swirl angles were small. The measurements highlight that the turbomachinery response depends on the flow angularity of the intake flow. In the case of a streamwise vortex, the flow angularity is strongly dependent on the size and strength of the vortex,

and is likely to depend on the details of the ingestion process and the initial vortex characteristics prior to ingestion. However, at present, this information cannot be determined for the ingestion of a streamwise vortex, since the details of the ingestion process are not fully understood.

To summarise, it has been found that a streamwise vortex has the potential to notably reduce the performance and operability civil aircraft engines. In particular, losses in surge margin of up to 33% have been measured, with corresponding losses in efficiency, mass flow, and pressure ratio. The turbomachinery response is larger than that anticipated from the measured total pressure distortion, which indicates that the swirl distortion associated with the vortex plays a significant role. The available results suggest that the loss in engine performance is proportional to the flow angularity levels inside the intake flow. Therefore, it is imperative that details of the vortex characteristics following ingestion are known in order to assess the potential impact on the stability and performance of the turbomachinery.

2.5.3 CFD modelling requirements for vortical flows

It has been found in the literature that the simulation of vortical flows using Computational Fluid Dynamics (CFD) is somewhat challenging. For example, in the steady RANS simulations of Egolf et al [81], it was reported that after only two chord lengths downstream of the wing trailing edge, the CFD simulations predicted a vortex peak tangential velocity which was only 40% of the experimental value. This was attributed to the numerical diffusion which was generated in the CFD simulations. For vortical flows, the result is an elevated core radius growth, along with reduced peak tangential velocities and vorticity. A review of the literature has shown that the order of accuracy of the spatial discretisation method, the grid resolution, and the turbulence model, have a significant influence on the level of numerical diffusion.

An important source of numerical diffusion is the numerical discretisation approach. Dacles-Mariani et al.[82] performed RANS simulations of a vortex convecting in a uniform streamwise flow using a 5^{th} order numerical scheme. It was found that between 15 and 20 uniformly-spaced mesh elements were required across the vortex core to obtain a grid independent solution. It was also advised that a streamwise grid spacing of twice that of the in-plane grid resolution should be employed. Similar conclusions were reached by Egolf et al. [81], who concluded that 14 points should define the vortex core when using a 5^{th} order numerical scheme for inviscid simulations of a convecting vortex in a

uniform flow. In addition, it was reported that the mesh resolution requirements could be relaxed if the order of accuracy of the numerical scheme was increased. For example, on a mesh with 7 points in the vortex core, a 9^{th} order numerical scheme produced a peak tangential velocity which was within 5% of the experimental measurements after a convection distance of two wing chord lengths. By comparison, the results using a 3^{rd} order scheme indicated a peak tangential velocity which was 50% of the measured value. However, Spall [83] performed inviscid computations of the convection of a vortex profile using a grid with 15 points in the core, and found that the decay in tangential velocity due to numerical diffusion caused an error of only 10% over two chord lengths. Therefore, it can be concluded that a balance between the mesh quality and the order of accuracy of the numerical scheme is imperative.

It has been found that the turbulence model can produce numerical diffusion which is dominant even when a suitable mesh and numerical scheme is employed. This has been particularly apparent in simulations which use eddy viscosity models. For example, Dacles-Mariani at al [82] found that after less than one chord length from the trailing edge, the magnitude of the velocity at the vortex core radius was only 65% of the experimental value for both 3^{rd} order and 5^{th} order numerical schemes, even with a sufficiently fine mesh in the core region (Figure 2.32(a)). It was noted that the formulation of the turbulence model lead to the generation of large levels of turbulence inside the core [82]. This is in contrast to the experimental measurements, which demonstrated turbulence suppression as a result of the large tangential velocities. This is a common trend for eddy viscosity models, which typically use vorticity in the production terms. To address this issue, an empirical correction function, often referred to as curvature correction [84, 85], was used to mimic the tendency of turbulence suppression in vortex cores. In particular, the production term was modified to include a comparison between the mean strain rate and the vorticity. In this way, the turbulence production levels were minimised in regions where the vorticity is high and the strain rate is low, which is a feature of vortex cores [82]. The correction term successfully suppressed the turbulence in the core, and resulted in considerable improvements in the agreement with the experimental measurements (Figure 2.32(a) and 2.32(b)). The difference between the predicted and measured velocity magnitude in the vortex was reduced to less than 10%.

However, as identified by Dacles-Mariani et al. [82] it may not be possible to correctly capture the flow physics of vortex flows using eddy viscosity models. Experimental data, such as that obtained by Chow et al. [22] and Ramasamy et al. [30], show that the mean strain rate and Reynolds stress tensors are not aligned (Figure 2.33(a) and 2.33(b). The Reynolds stress tensor is rotated by approximately 45^o relative to the mean strain rate

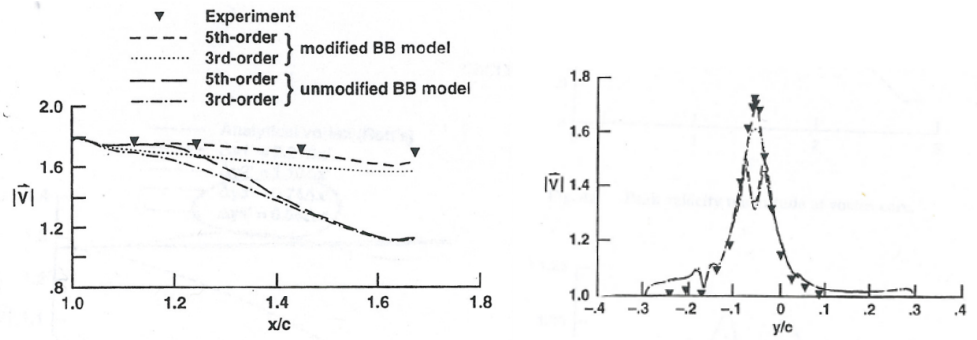

(a) (b)

FIGURE 2.32: Comparison between measured and simulated wing-tip vortex velocity characteristics [82], (a): Velocity magnitude at vortex centre as a function of distance downstream of wing-tip trailing edge, (b): Profile of velocity magnitude through vortex centre at $x/c = 1.24$. $3rd$-order and $5th$-order refer to the order of accuracy of the numerical scheme, unmodified and modified BB model refer to the Baldwin-Barth turbulence model without and with curvature correction, respectively

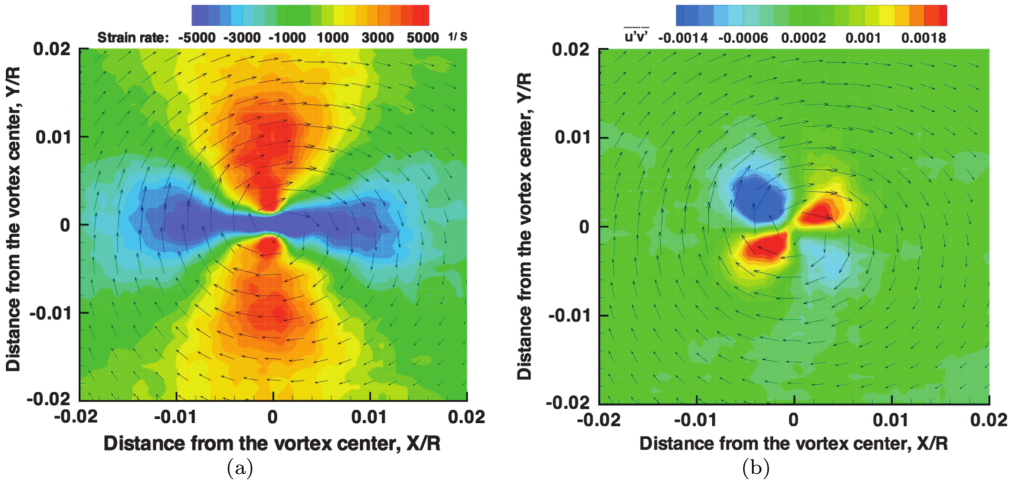

(a) (b)

FIGURE 2.33: Measurements of wing-tip vortex flowfield, (a) Mean in-plane strain rate, (b) Mean in-plane Reynolds stress

tensor. This poses a problem for eddy viscosity models, which employ the Boussinesq assumption to relate the mean strain to the effects of turbulence. The Boussinesq assumption states that the turbulent stress tensor is linearly related to the mean strain rate tensor through a scalar constant known as the eddy viscosity. Therefore, the inherent assumption in all eddy viscosity models is that the turbulent stress tensor is aligned with the mean strain rate tensor. The measurements illustrated in Figures 2.33(a) and 2.33(b) indicate that this is not a valid assumption for vortex flows. As a consequence, the flow

physics of vortex flow cannot be correctly modelled using eddy viscosity models. An alternative is to employ a Reynolds Stress Model (RSM). Wells et al. [84] simulated the wing-tip vortex generation process and near-field behaviour for the case corresponding to Devenport et al. [1]. It was demonstrated that the RSM results were in close agreement with the experimental measurements (Figure 2.34). The eddy viscosity model predicted excessive turbulence levels in the vortex core, which lead to an under-prediction of the peak tangential velocity and an over-prediction of the vortex core radius. It was also found that the use of a curvature-correction model improved the agreement between the simulations and the measurements. However, the curvature-correction results remained inferior to those obtained using an RSM approach.

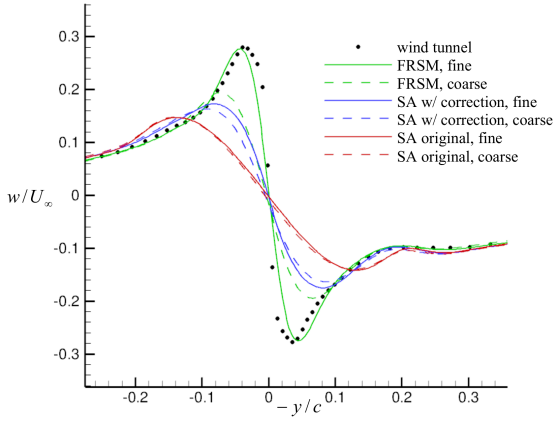

FIGURE 2.34: Comparison between measured and simulated wing-tip vortex tangential velocity profile at $x/c = 4$ downstream of wing trailing edge [84], where FRSM refers to Full Reynolds Stress Model, SA refers to the Spalart-Allmaras turbulence model, "w/correction" refers to simulations which employ the curvature-corrected SA model

To summarise, the literature has highlighted that the results obtained from RANS CFD simulations of vortex flows are very sensitive to modelling approach. Numerical diffusion from the spatial discretisation and the turbulence model typically result in a simulated vortex which features an underpredicted velocity field and an overpredicted size. This may have important implications for vortex ingestion simulations, since the intensity of the inlet flow distortion which results from vortex ingestion may be underestimated. To mitigate the effects of numerical diffusion, it is necessary to maintain a high mesh resolution inside the vortex core to ensure that the velocity gradients are well resolved. It has been found that eddy viscosity simulations are in reasonable agreement with experimental measurements if curvature correction methods are used. However, the particular behaviour of the stress and strain field in the vortex invalidates the assumptions used in the formulation of eddy viscosity models. As a result, higher order turbulence models,

such as Reynolds Stress Models or Large Eddy Simulations, are advocated to capture the vortex flow physics.

2.6 Summary

2.6.1 Existing knowledge pertinent to vortex ingestion

- The risk of ingestion of an externally-generated streamwise vortex is likely to be greatest where the intake capture streamtube is contracting. This occurs during low speed flight and high engine mass flow conditions, where the lift coefficients of various airframe components are likely to be largest, and the aircraft is not operating at the design condition.

- Fundamental theory indicates that a streamwise vortex will undergo intensification in response to a streamwise flow contraction. As a result, the vortex will experience a reduction in core radius, coupled with an increase in peak tangential velocity and streamwise vorticity.

- A small number of experimental studies have addressed the behaviour of streamwise vortices undergoing intensification. Ananthan and Leishman [69] demonstrated that the vortex core radius reduces in response to the strain field imposed by the interaction between the rotor wake and the ground. The evolution of the vortex core radius was successfully modelled using the Squire vortex model coupled with a simple correction based on continuity. Garbeff et al. [70] measured the behaviour of a wing-tip vortex in a mild wind tunnel contraction and found that the vortex peak tangential velocity increased, which is consistent with vortex intensification. However, the core radius did not reduce, as would be expected during vortex intensification. This was attributed to vortex wandering, which often limits the accuracy of point-based measurement methods.

- The ingestion of a streamwise vortex can considerably reduce the engine surge margin. In addition, loss of efficiency, mass flow, which suggests that, even if engine doesn't surge, there is potential for a notable loss of performance, which may occur at critical points in the flight.

- Streamwise vortices consist of very low levels of total pressure distortion, as confirmed by both sub-scale [71, 73] and full-scale measurements [9, 8]. The typical total pressure distortion values are below the levels considered to be an issue for engine stability and performance.

- Engine response is worse than that anticipated from assessments which are based on the total pressure distortion characteristics, which suggests that the swirl distortion is the primary effector. In addition, it has been found that the engine response worsens as the flow angularity inside the intake flow is increased. Measurements of all three velocity components during the vortex ingestion process are therefore required to characterise the flow angularity levels which are attributed to the vortex.

- An ingested streamwise vortex interacts with the induced distortion which is produced inside complex s-shaped intakes. The vortex has the potential to render flow control vortex generators ineffective, which may cause a dramatic increase in the self-generated distortion intensity.

- Care must be taken when simulating vortex flows using RANS CFD simulations. A number of studies, primarily focussed on wing-tip vortex generation and near-field behaviour, have suggested that increased mesh resolution is required inside the vortex core, in conjunction with a high-order numerical scheme. In addition, it has been found that conventional turbulence models used for most engineering studies result in an unrealistic vortex growth rate. This is a symptom an over-prediction of turbulence inside the vortex. Importantly, this may cause an underprediction of the distortion intensity which results from vortex ingestion. Although some correction methods have been used to mitigate the vortex core turbulence levels, the assumptions which are used in the formulation of eddy-viscosity models are not valid in vortex flows. Therefore, simulations using RSMs or LES must be performed to correctly capture the vortex flow physics.

2.6.2 Current deficiencies in knowledge

- There has been no detailed survey of the evolution of the velocity perturbation field or the characteristics of a streamwise vortex in a contracting intake capture streamtube. Thus, there is little knowledge of the characteristics of a vortex once it has been ingested by an intake.

- There is little fundamental understanding of the effect of laminar or turbulent diffusion on the vortex intensification process. However, it is known from wing-tip vortex convection studies that diffusion may have a notable impact on the vortex evolution.

- Prior experimental measurements have considered only a very limited number of cases of vortex intensification. Therefore, there has been no controlled assessment

of the impact of the vortex characteristics or the contraction characteristics on the vortex intensification process.

- Experimental measurements of the impact of streamwise vortices on aircraft engine performance and operability have suggested a strong dependence on the flow angularity levels of the intake flow. Since there is little understanding of the evolution of a streamwise vortex through the intake capture streamtube, it is not possible to estimate the likely vortex characteristics after ingestion. Therefore, an assessment of the likely inlet flow distortion levels is not possible. In addition, it is currently not known which vortex ingestion scenario is likely to produce the highest levels of inlet flow distortion, and so the "worst-case scenario"' has not been identified.

- The behaviour of a streamwise vortex in a uniform flow suggests that full-scale vortices may experience higher levels of diffusion than those at sub-scale. Therefore, the potential scale effects on the vortex ingestion process and the subsequent inlet flow distortion characteristics must be identified.

Chapter 3

Experimental methods

This Chapter provides details of the experimental methods used to obtain quantitative measurements of the behaviour of a streamwise vortex during ingestion. This includes a description of the experimental apparatus, measurement systems and the test matrix. Thereafter, the approach used to post-process the experimental data and to extract the vortex characteristics is described. Finally, an assessment of the experimental uncertainties is provided.

3.1 Sub-scale intake model

A $1/30^{th}$ scale axisymmetric aircraft intake model was employed to generate an intake capture streamtube which is representative of a typical civil aircraft engine, Figure 3.1(a). This intake model has been used in previous studies at on ground vortex ingestion [13] and initial studies on the flow distortion which is caused by the ingestion of streamwise vortices [71, 73]. The intake model consists of an axisymmetric duct with an inner diameter of $D_i = 0.1m$, and an outer diameter of $0.14m$. The intake lip geometry is defined by an ellipse with a major to minor axis ratio of $2:1$.

Boundary layer transition trips consisting of serrated aluminium tape were attached on the inner and outer surfaces of the intake lip. This approach was selected based on prior experimental investigations on the intake geometry which suggested that laminar separation bubbles may occur on the intake lip at the Reynolds numbers of interest in this experimental programme [71]. To facilitate measurements of the flow inside the intake,

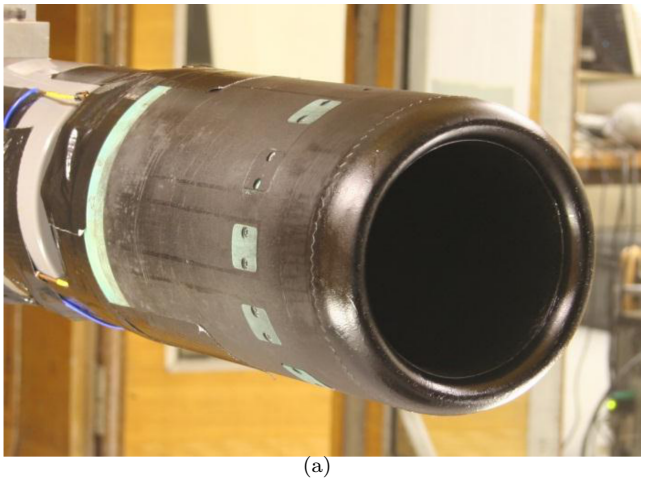

(a)

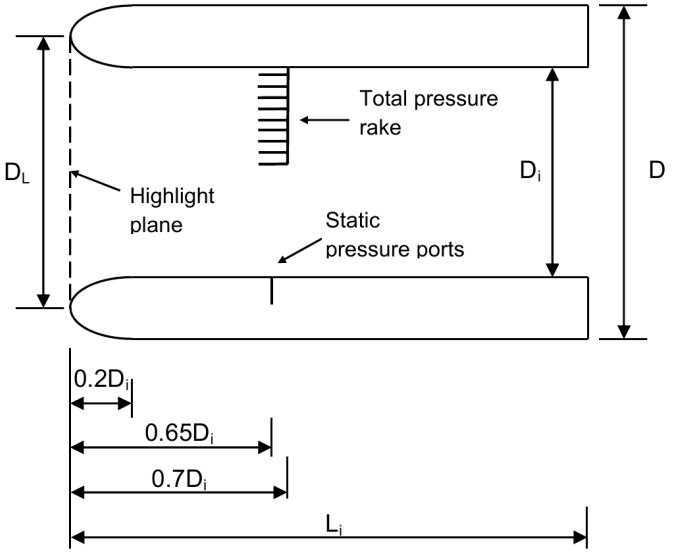

(b)

FIGURE 3.1: Sub-scale intake model, (a): Photograph of intake model, (b): Schematic of intake model with key dimensions (Table 3.1)

TABLE 3.1: Intake model dimensions (Figure 3.1(b))

Property	Value
D (m)	0.14
D_L (m)	0.12
D_i (m)	0.10
L_i (m)	0.254

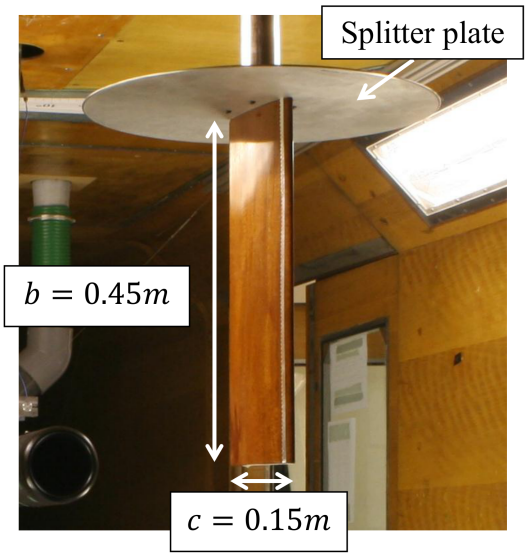

FIGURE 3.2: NACA 0012 semi-span wing and splitter plate

thirty-six equi-spaced static pressure ports are installed on the inner surface at $0.65D_i$ downstream of the highlight plane.

3.2 Vortex generators

An objective in this research is to perform a controlled assessment of the effect of the initial vortex characteristics on the vortex ingestion process. To this end, two different vortex generators were employed to create streamwise vortices of a range of characteristics. This section provides a description of the vortex generators.

The first vortex generator employed in this research was a NACA 0012 semi-span wing, which features a chord of $0.15m$ and a span of $0.45m$, Figure 3.2. A boundary layer transition trip strip was attached at approximately 7% chord on the suction and pressure surfaces to promote a turbulent boundary layer and thus to prevent the formation of laminar separation bubbles. The wing root section was connected to a circular splitter plate with a diameter of $0.45m$ to maximise the strength of the wing-tip vortex and to avoid flow contamination from the support mechanisms. The wing and the splitter plate were connected to a telescopic bar. The connection allowed the wing and the splitter plate to rotate about the spanwise axis of the wing. Therefore, it was possible to control the angle of attack of the wing independently of the telescopic support system.

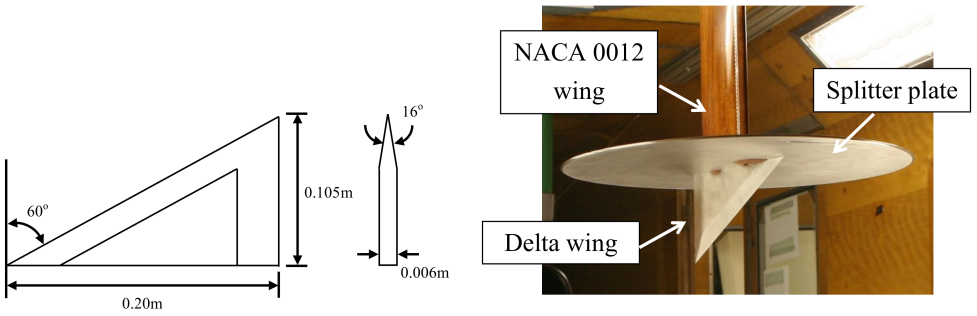

FIGURE 3.3: Semi-span delta wing, (a): Schematic showing dimensions, (b): Photograph of delta wing installed with splitter plate

In addition, a semi-span delta wing was designed for the experimental programme. The vortex generator featured a chord length of $0.20m$, a span of $0.105m$, a sweep-back angle of 60^o, and a maximum thickness of $0.006m$, Figure 3.3(a). The leading and trailing edges of the delta wing were sharp, and were defined with a chamfer half-angle of 8^o. A splitter plate with a diameter of $0.45m$ was attached to the root of the semi-span delta wing to ensure that a single streamwise vortex was generated. The delta wing and splitter plate were designed as a modular attachment to the wing-tip of the NACA 0012 vortex generator, Figure 3.3(b). The angle of attack of the delta wing could be set independently of the NACA 0012 vortex generator. In this way, the NACA 0012 vortex generator could be used as a streamlined strut when the delta wing was in use.

3.3 Wind tunnel configuration

The experimental work was conducted in the $2.4m \times 1.8m$ closed-return low-speed wind tunnel at Cranfield University. The maximum working section velocity is $40ms^{-1}$, and the freestream flow has a typical freestream turbulence level of less than 0.1%.

The intake model was mounted in the centre of the working section (Figure 3.4) and was connected to a $60m^3$ vacuum tank located outside of the wind tunnel using ducting with a $4''$ inner diameter. The streamwise position of the intake highlight plane could be modified using different lengths of ducting. Using this suction system, it was possible to establish a steady flow inside the intake for approximately $20s$ at a maximum Mach number and mass flow of 0.53 and $1.48kgs^{-1}$, respectively. A slide valve was installed in the $4''$ diameter ducting approximately $10D_i$ downstream of the intake model to facilitate control of the intake mass flow. The vortex generator was mounted upstream of the intake

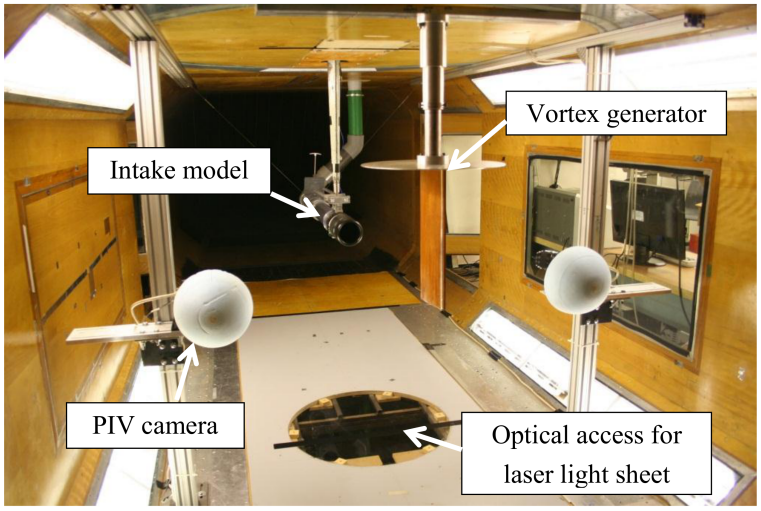

FIGURE 3.4: Photograph of wind tunnel configuration

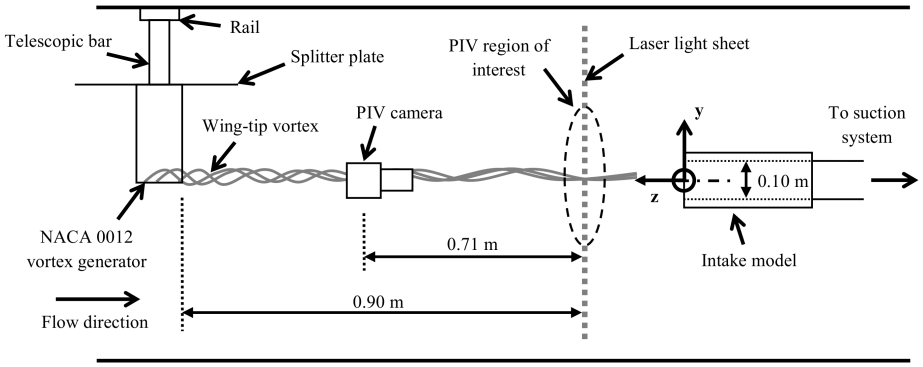

FIGURE 3.5: Schematic showing side-view of wind tunnel configuration. Note that the distance between the intake highlight plane and the laser light sheet was varied during the experiments (see section 3.5 for details)

model such that the trailing edge of the NACA 0012 vortex generator was approximately $11D_i$ upstream of the intake highlight plane. The vortex generator and splitter plate were connected to a telescopic support system and mounting frame (Figure 3.5) which enabled the vortex generator to be translated in the lateral (x) and vertical (y) directions relative to the tunnel centreline axis.

3.4 Measurement systems

The purpose of this research was to measure the evolution of the vortex as it moves through the intake capture streamtube. Previous measurements of convecting streamwise vortices have emphasised that measurements obtained from point-based methods may be contaminated due to wandering [1, 27, 86]. In addition, it has been suggested that streamwise vortices may be sensitive to the presence of probes [16]. Thus, it is apparent that a global, non-intrusive measurement method would be highly suited to measure the vortex ingestion process. In this research, Stereoscopic Particle Image Velocimetry (Stereo PIV) has been employed to obtain quantitative measurements of the 3-component velocity field at various measurement planes inside the intake capture streamtube. As a result, it is possible to quantify the evolution of the vortex inside the intake capture streamtube. It is necessary to employ Stereo PIV to investigate vortex ingestion flows since all three Cartesian velocity components are likely to be large. Consequently, a conventional mono PIV approach would be subject to notable perspective errors which cannot be corrected [87]. In addition, it is desirable to measure the flow angularity which is associated with the vortex to provide an assessment of the likely impact on turbomachinery performance. This section provides details of the Stereo PIV system, as well as the pressure instrumentation which has been employed to establish the experiment conditions.

3.4.1 Stereoscopic Particle Image Velocimetry

Particle Image Velocimetry (PIV) is a global, non-intrusive measurement method which has been successfully employed to obtain quantitative velocity field measurements in a wide range of studies. A digital PIV measurement system consists of a number of components. Firstly, it is necessary to introduce seeding particles into the working section which faithfully follow the motion of the airflow. A high-power laser is then used to illuminate the seeding particles at a particular region of interest. The illuminated particles are then imaged using a bespoke digital camera. To obtain a velocity measurement, the laser illumination and imaging are synchronised in such a way that the two separate images are acquired in very quick succession. Image processing techniques are then employed to determine the displacement of the particles between the two images. With knowledge of the time between the images, it is then possible to evaluate the velocity of the particles. Under the assumption that the particles follow the airflow faithfully, then the particle velocity corresponds to that of the airflow.

It is necessary to use two digital cameras to measure the three-component velocity field at the region of interest. This approach has been employed in this research due to the large in-plane and out-of-plane velocities which are likely to occur in the intake capture streamtube during streamwise vortex ingestion. The characteristics which are often used to define streamwise vortices, such as the core radius and streamwise vorticity, are typically measured on a plane perpendicular to the vortex axis. Therefore, the region of interest was selected to be perpendicular to the streamwise direction.

The laser light sheet was generated using a 200mJ Litron Nano-L dual-pulsed Nd:YAG laser with a wavelength of 532nm and a maximum repetition frequency of 15Hz. The laser beam was transformed into a thin light sheet using a cylindrical plano-concave lens with a focal length $-0.04m$, followed by a cylindrical plano-convex lens with a focal length of $0.1m$. The laser and light sheet optics were installed on an optical breadboard and traverse below the working section with a standoff distance between the optics and the centreline of the working section of approximately $2.3m$. A $0.05m$ diameter mirror was then employed to direct the light sheet into the working section through a Perspex window on the working section floor, which can be observed in Figure 3.4. The light sheet was positioned $0.9m$ downstream of the wing trailing edge and perpendicular to the freestream flow direction (Figure 3.5). This equates to 6 chord lengths downstream of the NACA 0012 wing trailing edge, and 4.5 root chord lengths downstream of the delta wing. At the centre of the working section, the light sheet had a thickness $1.5 \times 10^{-3}m$ and a width of approximately $0.2m$. The seeding fluid consisted of Di-Ethyl-Hexyl-Sebacat (DEHS), which has been identified as a suitable seeding fluid for air measurements [87]. Two PIVTEC PivPart30 seeding generators with Laskin nozzles were used in conjunction with a seeding rake to introduce seeding with a mean particle diameter of $1\mu m$ into the flow upstream of the working section. Two TSI PowerView cameras with a resolution of 4 Mega-pixels were employed, each equipped with $0.105mm$ focal length Micro-Nikkor lenses. The cameras were mounted in side-scatter mode relative to the light sheet, on opposite sides of the working section and upstream of the intake model. The cameras were at an angle of 45^o from the working section centreline axis, and were focussed on a region of interest which was approximately $0.16m$ in width and $0.1m$ in height. The image plane of each camera sensor was tilted relative to the object plane to satisfy the Scheimpflug condition on both cameras. Stereoscopic calibration was facilitated with use of a TSI dual-plane calibration plate. TSI Insight 3G v9.1 was used in conjunction with a TSI LaserPulse 610035 synchronisation unit to control the synchronisation of the laser and the cameras, and to facilitate the image acquisition. The time delay between the first and second PIV frames was selected to ensure that seeding particles translated by no

more than 25% of the light sheet thickness in the streamwise direction. In addition, it was required that the in-plane particle displacements did not exceed 25% of the interrogation window size. In general, it was found that the out-of-plane time delay constraint was more stringent than the in-plane requirements. Prior wing-tip vortex measurements at similar conditions to the current research indicated that a minimum of 100 PIV measurements are required to ensure that the mean vortex characteristics are correctly determined [88]. In this research, a total of 300 PIV measurements for each configuration were acquired to comfortably surpass this requirement. Details of the PIV processing approach, and the subsequent data post-processing techniques, are provided in section 3.6.

3.4.2 Pressure measurements

To characterise the freestream and intake operating conditions, a number of pressure measurements were acquired. The freestream velocity was determined using a Pitot-static probe was installed in the working section. The static and total pressures which were obtained with the Pitot-static probe were measured using a Furness Controls FC-044 differential pressure transducer, which featured a range of 2.5kPa. The flow inside the intake was determined using the pneumatic average of four static pressure ports located at a distance of 0.65Di downstream of the intake highlight plane. The pressure was measured using an Omega PX139-005D4V differential pressure transducer which has a measurement range of 34.4kPa. The total temperature $T_{0,\infty}$ was measured inside the settling chamber of the wind tunnel. Under the assumption of isentropic flow, the intake static pressure p_i was used in conjunction with the freestream total pressure $P_{0,\infty}$ and the total temperature to calculate the mass flow $\dot{m}_i$, the Mach number M_i, and the flow velocity inside the intake W_i. Therefore, it was possible to determine the intake velocity ratio ($VR = W_i/W_\infty$) which characterises the streamtube contraction levels. Details of the approach which has been employed to calculate the flow conditions are given in appendix C. All transducer data was acquired over a sampling period of 5 seconds and at a frequency of 600Hz using LabView with a National Instruments PCI-6255 16-bit DAQ card. Further details of the pressure measurement approach are provided in appendix C

3.5 Test matrix

The experimental part of this research has two main aims. The first is to establish fundamental understanding of the evolution of a streamwise vortex inside a contracting intake capture streamtube. The second aim is to determine how this process changes as

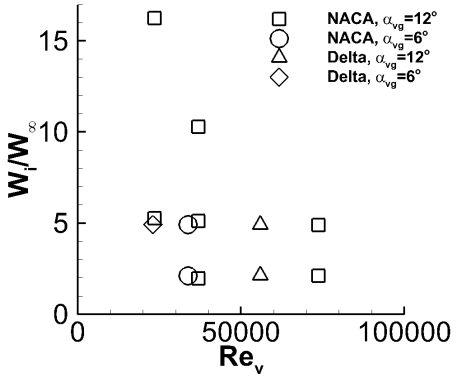

FIGURE 3.6: Vortex ingestion test space showing experimental conditions investigated as a function of vortex Reynolds number (Re_v) and intake velocity ratio (W_i/W_∞)

a function of the intake operating conditions, the initial vortex characteristics prior to ingestion, and the trajectory that the vortex follows through the intake capture streamtube. To this end, vortex ingestion was investigated for a range of intake operating conditions and vortex generator conditions, Figure 3.6. A complete description of the experimental conditions is provided in Table A.1.

To provide a controlled parametric study, the vortices were first ingested into the intake along the intake centreline. In general, the vortex position and trajectory downstream of a wing depends on a number of factors, including the lift coefficient and the freestream velocity [89]. Therefore, it was necessary to adjust the vertical and horizontal position of the wing-tip relative to the intake centreline for each of the vortex generator conditions. This was achieved by inspection of the vortex centre location obtained from initial PIV measurements during the vortex ingestion experiments. Although this procedure was somewhat iterative, the vortex centre position was typically established at a position which is within $0.05D_i$ of the intake centreline.

The first parameter considered in this research was the impact of the intake operating conditions, characterised by the intake velocity ratio $VR = W_i/W_\infty$. A number of intake mass flow conditions were investigated for fixed freestream and vortex generator conditions. In this way, the effect of a change in streamtube contraction levels could be assessed for a given unperturbed streamwise vortex. Intake velocity ratios of between 2.0 and 16.3 were investigated. The corresponding ranges of freestream velocity and intake mass flow were $11.0ms^{-1}$ to $35.4ms^{-1}$, and $0.32kgs^{-1}$ to $1.49kgs^{-1}$ respectively.

The second parameter of interest is the vortex Reynolds number, $Re_v = \Gamma_c/\nu$, where Γ_c is the vortex core circulation and ν is the kinematic viscosity. As discussed in section 2.3,

the rate of vorticity diffusion attributed to turbulence increases with the vortex Reynolds number. Therefore, it is of interest to determine if the vortex ingestion process exhibits a similar dependence on Re_v. The circulation of the wing-tip vortex produced by a wing is strongly linked to the freestream velocity. This can be demonstrated using Kutta-Joukowski theorem (section 2.2.1), such that the vortex total circulation is given by Eq. 3.1.

$$\Gamma_0 = \frac{1}{2} W_\infty c C_L \tag{3.1}$$

For a given vortex generator at a fixed angle of attack, the vortex strength, and thus the vortex Reynolds number, can be increased by means of the freestream velocity. Two approaches have been employed in this research to provide a controlled assessment of the influence of the vortex Reynolds number. Firstly, the NACA 0012 vortex generator was investigated at a fixed angle of attack of $\alpha_{vg} = 12^o$ for freestream velocities of $11.0ms^{-1}$, $17.2ms^{-1}$ and $35.4ms^{-1}$. This produced streamwise vortices with vortex Reynolds numbers of between 2.4×10^4 and 7.4×10^4 (Table A.1). According to Bhagwat and Leishman [50], and as illustrated in Figure 2.17, these vortex Reynolds numbers are in a flow regime where turbulent diffusion is expected to influence the vortex evolution. This range of freestream velocities corresponds to wing chord Reynolds numbers which are between 1.1×10^5 and 3.6×105, and the wing lift coefficient was estimated to be 0.95 using finite wing theory [18]. The intake mass flow for each of the three freestream velocities was controlled in such a way as to maintain an intake velocity ratio of approximately 5.0. Therefore, the streamwise vortices of differing vortex Reynolds numbers will experience the same streamtube contraction characteristics. The second approach used to control the vortex Reynolds number was to reduce the vortex generator lift coefficient, which was facilitated by a reduction in angle of attack from 12^o to 6^o at a fixed freestream velocity of $35.4ms^{-1}$. This corresponded to a lift coefficient reduction from 0.95 to 0.47. Note, therefore, that the change in vortex Reynolds number in this case was independent of the wing chord Reynolds number.

The impact of a change in the vortex generator type was investigated using the delta wing at angles of attack of 12^o and 6^o. This was performed at a freestream velocity of $35.4ms^{-1}$ and an intake velocity ratio of 4.9, Table 1. As such, it is then possible to compare the vortex ingestion process with the conditions investigated with the NACA 0012 vortex generator. The lift coefficients for the delta wing were estimated to be 0.61 and 0.28 for each of the angles of attack, as estimated using the method of Polhamus [90].

Finally, it was unknown if the evolution of a vortex inside the capture streamtube is dependent on the trajectory which the vortex follows. Therefore, the vortex generator was translated laterally by $x/D_i = -0.70$ relative to the vortex generator position required for the centreline ingestion measurements. This off-axis condition was investigated for a subset of the centreline test matrix, Table A.1.

To minimise the complexity of the experimental arrangement, the position of the PIV measurement plane in the working section was fixed and the intake model was translated in the streamwise direction. Using this approach, the measurement plane was located at different streamwise positions inside the capture streamtube. It should be noted that the intake and the capture streamtube were therefore translated relative to the vortex generator. An assumption which is inherent in this experimental approach is that the vortex characteristics undergo little change over the distance translated by the intake model. To assess the validity of this assumption, the Squire model (section 2.3) was used to provide an estimate of the change in unperturbed vortex characteristics over the distance which was translated by the intake. It was found that the wing tip vortex core radius will increase by no more than 2.4%, which is within the measurement uncertainty of the PIV system, and is small in comparison to the change in core radius typically measured during the vortex ingestion process. Furthermore, by using the vortex core radius as an input into the Lamb-Oseen vortex model (Eq. 2.22), the peak tangential velocity and peak streamwise vorticity were estimated to decrease by no more than 2.4% and 4.7% respectively. These values are within the measurement uncertainty of the PIV system (section 3.7), so it can be concluded that translating the intake relative to the PIV measurement plane is likely to have a negligible effect on the vortex ingestion measurements.

The evolution of the vortex within the capture streamtube was measured at PIV planes located at a distance of z/D_i equal to 2.25, 0.80, 0.60, 0.38 and 0.20 upstream of the intake highlight plane. The PIV measurement plane was located at a distance which corresponded to 6 chord lengths downstream of the NACA 0012 trailing edge, and 4.5 chord lengths downstream of the delta wing. Inspection of the PIV measurements for each of the vortex generator conditions indicated that the vorticity contours were axisymmetric and that there were no indications of the wing wake (section 4.1). It was therefore concluded that the vortex roll-up process was complete at the position of the PIV plane. This has been supported using the method of Spreiter and Sacks [19], which estimates that the vortex roll-up process should be complete at approximately 5 chord lengths from the vortex generator trailing edge.

3.6 Stereo PIV data reduction

It is crucial that care is taken to determine a suitable processing and post-processing approach to transform the PIV images into accurate velocity field information. This is particularly true for vortical flows, which feature a number of unique characteristics which may compromise the quality of the PIV measurements. This section provides a description of the processing method which has been employed. Thereafter, details will be given of the approach used to extract the characteristics of the streamwise vortices from the measurements.

3.6.1 PIV processing method

A number of aspects of vortex flows must be considered to maximise the suitability of the PIV processing approach. The vortex flowfield exhibits strong in-plane velocity gradients, and there may be a reduction in seeding density inside the vortex core due to centrifugal action [87]. Both effects can reduce the strength of the PIV correlation peak, increase the measurement uncertainty, and can lead to invalid vectors. It is possible to mitigate the effects of strong in-plane velocity gradients with the use of recursive deformation grid algorithms [91] which have been used successfully in a number of wing-tip vortex measurement studies [88, 92, 30]. The PIV correlation process was performed in Insight 4G using a linear deformation grid method [93] in conjunction with a Gaussian peak engine fit the correlation peak to sub-pixel accuracy. The interrogation windows featured a 50% overlap, an initial window size of 64 pixels (px), and a final window size of 32px. This processing approach produced a vector resolution of approximately 0.01Di or 0.007c. This compares favourably with existing probe-based measurements of wing-tip vortices, which often feature a probe resolution of between 0.002c and 0.03c [17]. The global vector validation strategy consisted of a 16px maximum displacement in the x and y-directions. Furthermore, local vector validation was completed using the universal median test [94] with a non-dimensional tolerance of 3 on a stencil size of 3x3 vectors. In general, the number of invalid vectors was found to be between 1% and 2% for all configurations which have been investigated. Vectors which failed the validation process were replaced with a local mean of 3x3 vectors to ensure the velocity gradients close to the vortex flow were not artificially smoothed. The processing is carried out in an automated fashion to produce the 3-component vector field for each instantaneous measurement.

3.6.2 Calculation of vortex characteristics

A notable feature of wing-tip vortex flows is that the vortex position fluctuates in a random manner [16, 1, 27, 86]. This presents a difficulty for point-based measurements, since the correct position of the vortex centre cannot be determined. The wandering effect causes point-based measurements to over-estimate the vortex core radius [1], and underestimates the peak tangential velocity [1] and streamwise vorticity levels [27]. Therefore, it is necessary to account for the changes in vortex position. This can be achieved using global measurement methods such as PIV, since the vortex position in each instantaneous measurement can be identified before the vortex characteristics are calculated. This approach has been employed in this research,

The 3-component velocity vector fields generated by the PIV processing approach were loaded into Tecplot 360 2010 for post-processing. The Vorticity Disk Method (VDM) [95] has been used to establish the vortex characteristics on each instantaneous PIV measurement. Firstly, the streamwise vorticity field is calculated using the in-plane velocity measurements and a second order differencing scheme. The vortex centre on each instantaneous image is then identified as the location of peak streamwise vorticity. A circular grid with a radius of r_{max} is subsequently placed at the vortex centre, and the flow field is interpolated on to the circular grid using a linear interpolation method. This process is performed for each instantaneous PIV measurement. The data files corresponding to each of the individual circular grids are then loaded into MATLAB. On each instantaneous measurement, the streamwise vorticity is integrated on annuli of increasing radius to generate the circumferentially-averaged circulation profile, $\Gamma(r)$. It is then possible to calculate the circumferentially-averaged tangential velocity profile $V_\theta(r)$ using the expression in Eq. 3.2. Finally, the vortex core radius can be determined from the tangential velocity profile.

$$V_\theta(r) = \frac{\Gamma(r)}{2\pi r} \tag{3.2}$$

The circular zones had a radius of $0.25D_i$ and an approximate radial spatial resolution of $0.002D_i$ or approximately $0.021r_c$ for the NACA 0012 wing-tip vortex in the unperturbed flow. The resolution of the circular zone in the circumferential direction was such that, at the edge of the circular zone ($r = 0.25m$), the resolution in the circumferential direction was equal to the resolution in the radial direction. Note that the circular zone maximum radius corresponded to approximately $r_{max}/r_c = 3$ for the unperturbed vortex measurements. The circular zone size and resolution were selected using a synthetic vortex

velocity field (appendix B). In some cases, the unperturbed vortex core radius increased notably. Therefore, the radius was increased to $0.35D_i$ with a corresponding increase in the circular zone grid resolution to maintain a spatial resolution of approximately $0.002D_i$. The automated processing approach in this research determines the vortex and velocity characteristics for each instantaneous measurement. The average vortex characteristics and flowfield characteristics are subsequently computed. Using this approach, the detrimental effects of wandering have been avoided, since the coordinates of the circular grid are corrected for the instantaneous vortex centre location. It should be emphasised that wandering can have a notable effect on the measurements and, subsequently, the characteristics of the vortex. For example, when the instantaneous vortex position is not accounted for, the peak streamwise vorticity which is approximately 43% lower than the result obtained using the conditional averaging approach (appendix B).

3.7 Measurement uncertainties

An estimate of the measurement uncertainties associated with the PIV processing approach can be determined from the analysis of Raffel et al. [87]. This permits an estimate of the uncertainty contributions from the particle image displacement, particle image diameter, seeding density, quantisation level, and background noise. Furthermore, the experiments and analysis of Van Doorne et al [96] permit an estimation of the registration error due to possible misalignment between the laser light sheet and the camera calibration plate. For a detailed description of the uncertainty calculations, see appendix C. In this work, the overall uncertainty corresponds to 8% of the typical peak tangential velocity and 3% of the out-of-plane velocity. As a result, the uncertainty in peak vorticity is estimated to be 15%, with a concomitant circulation uncertainty of 6%. The core radius measurement uncertainty, dictated by the measurement spatial resolution, was found to be 6%.

The typical uncertainties for the freestream and intake velocity were 1.0% and 3.2% respectively, with a resultant intake velocity ratio uncertainty of 3.4%. The uncertainties were determined using quadrature to combine the transducer measurement error, the calibration error, and the resolution error.

3.8 Summary

This chapter has provided details of the experimental methods employed in this research. A description of the experimental apparatus and measurement techniques has been given. In addition, the experimental variables have been introduced, and an explanation of the approach used to perform controlled parametric studies was provided. Finally, details have been given of the post-processing approach which has been tailored for the unique features of vortical flow.

Chapter 4

Measurements of streamwise vortices in unperturbed flow

It is first necessary to assess the characteristics of the streamwise vortex in the unperturbed freestream flow, prior to entering the intake capture streamtube contraction. To do this, the intake model was removed from the wind tunnel working section to ensure the vortex was contained in a nominally uniform streamwise flow. These measurements provide a reference condition which can be used to quantify the influence of the streamtube contraction on the vortex. In addition, the unperturbed measurements also elucidate certain features of the vortex flow which may subsequently have an influence on the vortex ingestion process. In this chapter, a detailed analysis of the unperturbed vortex at a single condition is performed. A number of configuration parameters have been utilised as part of the vortex ingestion studies. Therefore, the final part of this chapter will establish the influence of the key parameters on the characteristics of the streamwise vortex prior to ingestion.

4.1 Mean vortex characteristics

The conditional-averaging post-processing approach employed in this research (section 3.6.2) collocates each instantaneous velocity field measurement on a common reference frame. In this way, the potentially detrimental effects of wandering can be mitigated (appendix B.1.2).

It is constructive to first consider the results obtained at a single vortex generator configuration. It will then be possible to evaluate how the vortex characteristics change as a function of the key parameters, such as the freestream velocity (W_∞), the vortex generator type, and vortex generator angle of attack (α_{vg}). These parameters will affect the characteristics of the wing-tip vortices, such as the vortex Reynolds number (Re_v) and the core radius (r_c). The measurements acquired for the NACA 0012 vortex generator at an angle of attack of $\alpha_{vg} = 12^o$ and a freestream velocity of $11.0ms^{-1}$ were taken as the reference condition. Therefore, measurements from this configuration are assessed, before the impact of the experimental parameters is elucidated. In the reference configuration, the chord Reynolds number is 1.1×10^5, the vortex Reynolds number is 2.4×10^4, and the PIV measurement plane was located at a distance of $z/c = 5$ downstream of the vortex generator trailing edge (Figure 3.5).

The contours of streamwise vorticity (Figure 4.1(a)) are axisymmetric, and the majority of the streamwise vorticity is contained inside the vortex core (Figure 4.1(b)). Note that there is no evidence of the streamwise vorticity which is attributed to that produced along the trailing edge of the wing (section 2.2.1). The vortex circulation profile (Figure 4.1(c)) rises quickly inside the vortex core, and reaches a non-dimensionalised circulation ($\Gamma_c/W_\infty c$) of 0.21 at the vortex core radius. This value compares favourably with wing-tip vortex measurements at similar conditions. For example, Lee and Pereira [17] measured a non-dimensional core circulation of 0.24 using a NACA 0012 vortex generator at $\alpha_{vg} = 12^o$ and a chord Reynolds number of 3.1×10^5. The circulation profile increases slowly beyond $r/r_c = 1.5$, which indicates that some additional streamwise vorticity is contained in the surrounding flow. Thus, it is clear that the roll-up of vorticity into the vortex core is nearing completion at the streamwise station under investigation in this research. This behaviour is consistent with most wing-tip vortex measurements. For example, the results of Martin et al. [33] suggested that the measured circulation asymptotes towards the total circulation at a radius of approximately $20r_c$ from the vortex centre. As a result, a large region of interest is required to successfully measure the vortex total circulation. It was emphasised by Tung et al. [28] that measurements of the circulation at large radii are increasingly sensitive to small changes in the velocity field, such as those introduced by measurement noise, and it was therefore concluded that the total circulation measurements can be susceptible to error at large radii. In the current research, an increased spatial measurement resolution was favoured over a large region of interest to maximise the number of velocity vectors inside the vortex core. Therefore, the total circulation cannot be determined from the current measurements.

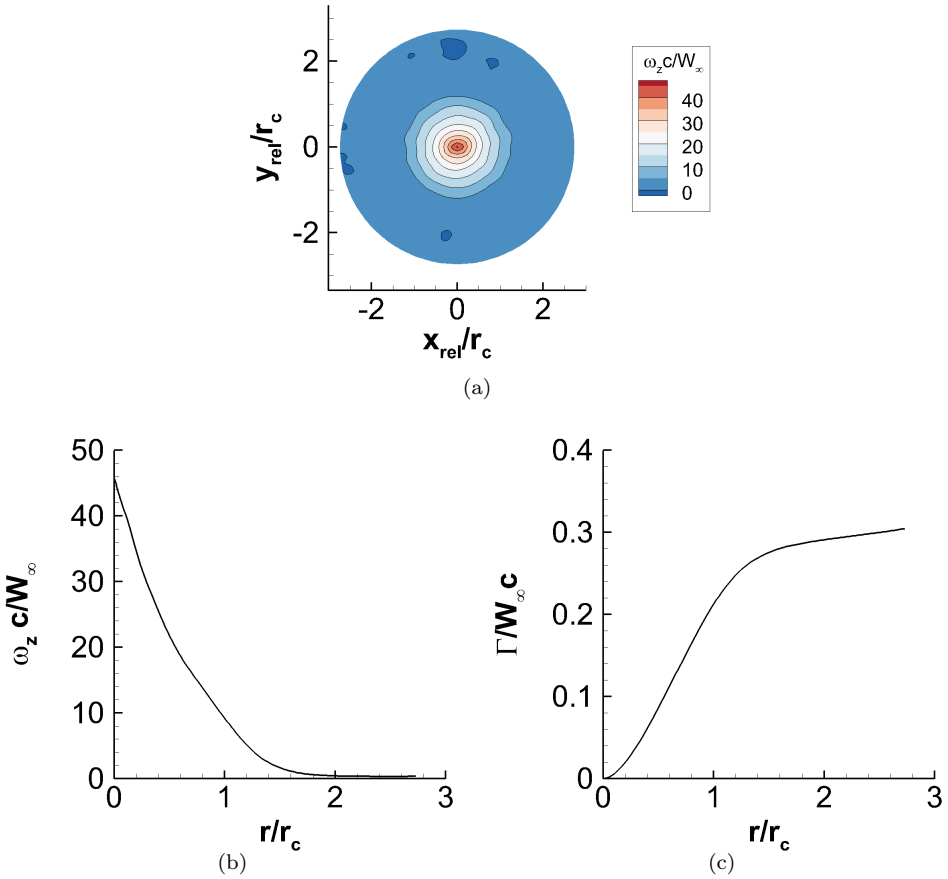

FIGURE 4.1: Unperturbed vortex velocity field measurements, NACA 0012 vortex generator, $Re_c = 1.1\times10^5$, $Re_v = 2.4\times10^4$, where x_{rel} and y_{rel} refer to the x and y coordinates relative to the vortex centre, (a): Streamwise vorticity ($\omega_z c/W_\infty$), (b): Circumferentially-averaged streamwise vorticity profile, ($\omega_z c/W_\infty$) (c): Circumferentially-averaged circulation profile ($\Gamma/W_\infty c$)

The circumferentially-averaged tangential velocity profile (Figure 4.2(a)) is in the form of the characteristic vortex tangential velocity profile (section 2.2.1). The tangential velocity rises in proportion to the distance from the vortex centre and reaches a maximum non-dimensional tangential velocity of $V_\theta/W_\infty = 0.55$ at the vortex core radius of $r_c/c = 0.061$ or $r_c/D_i = 0.092$. Beyond the core radius, the tangential velocity profile merges into a potential vortex type distribution, where the tangential velocity is closely proportional to $1/r$. As discussed in section 2.2.1, there is a close coupling between the tangential and streamwise velocities inside a vortex. As such, a streamwise velocity perturbation relative to the freestream velocity is often measured. Experimental investigations using unswept rectangular wings (such as Lee and Pereira [17]) have confirmed that, at large angles of

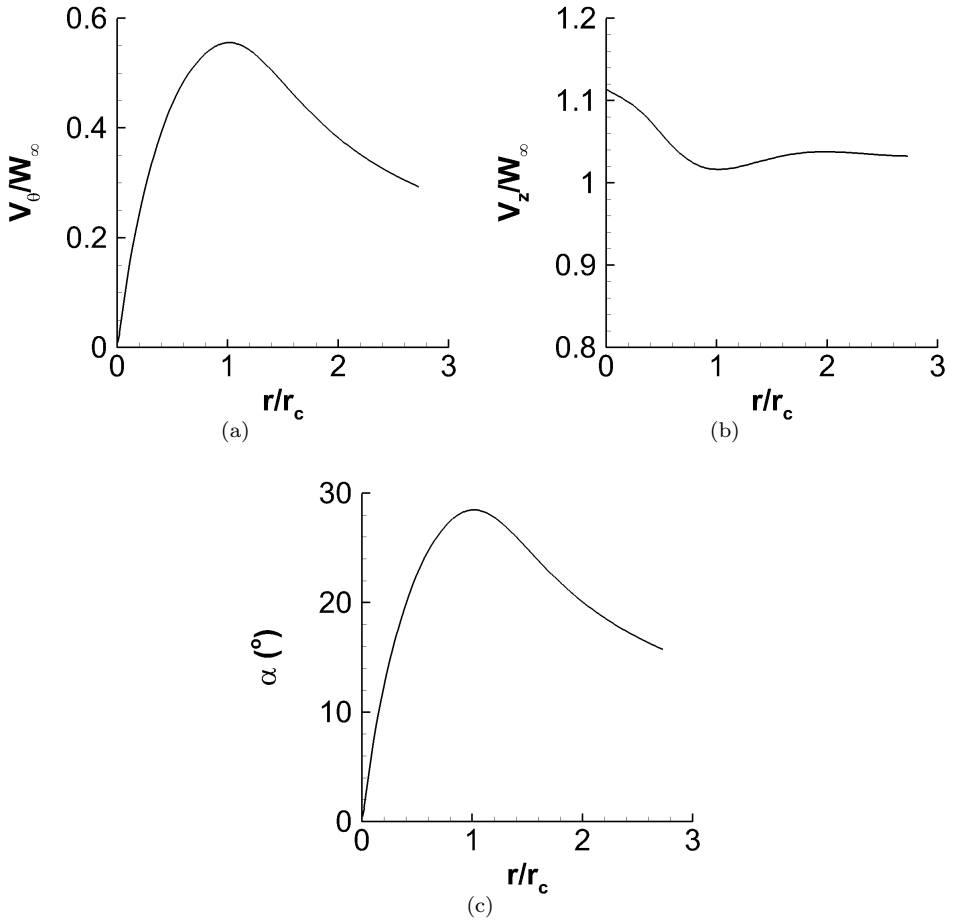

FIGURE 4.2: Unperturbed vortex velocity field measurements, NACA 0012 vortex generator, $Re_c = 1.1 \times 10^5$, $Re_v = 2.4 \times 10^4$, (a): Circumferentially-averaged tangential velocity profile, (V_θ/W_∞), (b): Circumferentially-averaged streamwise velocity profile (V_z/W_∞), (c): Flow angularity profile $(\alpha = tan^{-1}(V_\theta/V_z))$

attack, a streamwise velocity excess will be measured. This is consistent with the streamwise velocity profile measured at the reference condition, Figure 4.2(b), which features a streamwise velocity excess inside the vortex core of approximately 11% of the freestream velocity. The tangential and streamwise velocity profiles can be used to determine the flow angularity (α), which is defined in this research as $\alpha = tan^{-1}(V_\theta/V_z)$. This is an important characteristic for inlet flow distortion studies, since it provides an indication of the deviation of the flow relative to uniform freestream conditions. The combination of the large tangential velocity (Figure 4.2(a)) with the streamwise velocity perturbation (Figure 4.2(b)) produces a large variation of flow angularity across the vortex, Figure 4.2(c). Close to the core radius, the flow angularity reaches a maximum of 28^o. Such flow angles have the potential to produce notable levels of inlet flow swirl distortion if

a wing-tip vortex is ingested by an intake (section 2.5.1). Another parameter which is often used to characterise streamwise vortices is the swirl angle, $\alpha_{sw} = tan^{-1}(V_{\theta,max}/w_c)$, where w_c is the streamwise velocity at the vortex centre. This parameter is of interest since streamwise vortices with a swirl angle of greater than 40^o are susceptible to vortex breakdown [97]. However, the greatest swirl angle measured in this research during unperturbed conditions is approximately 28^o, and so vortex breakdown is not likely in the conditions considered.

In summary, measurements of mean flowfield in the unperturbed flow downstream of the NACA 0012 vortex generator are consistent with existing streamwise vortex measurements in the literature. The vortex flow consists of notable perturbations of in-plane and streamwise velocities relative to the uniform freestream flow, which combine to produce high levels of flow angularity close to the vortex.

4.2 Unsteady vortex characteristics

To provide additional insight into the flow physics of the unperturbed streamwise vortices, the unsteady aspects of the flow have also been investigated. Prior measurements in the literature, such as [22] and [43], indicate the presence of turbulent flow in the vortex core. In addition, wing-tip vortex measurements at the vortex Reynolds numbers of interest in this research suggest that turbulent diffusion plays an important role in the evolution of the vortex [50]. Therefore, it might be expected that both the velocity field and the vortex characteristics measured in this research may feature unsteadiness. The instantaneous snapshots of the streamwise vortex characteristics for the reference unperturbed configuration are given in Figures 4.3(a) to 4.3(e) as a function of the PIV measurement number. As anticipated, the vortex size, peak tangential velocity and core circulation (Figures 4.3(a), 4.3(b) and 4.3(c)) illustrate some degree of unsteadiness. However, it is apparent that the fluctuations are small. For example, the RMS value of the vortex core radius corresponds to 0.2% of the wing chord length, or 2.6% of the mean vortex core radius. Similarly, the peak tangential velocity fluctuations are 0.7% of the freestream velocity, and 1.2% of the mean peak tangential velocity. Finally, the x- and y-coordinates of the vortex centre, Figures 4.3(d) and 4.3(e), show that the vortex experiences fluctuations in position which can be as large as 5% of the wing chord, which corresponds to approximately 82% of the mean vortex core radius. This underlines the importance of employing a post-processing method which captures the instantaneous vortex position before calculating the vortex characteristics.

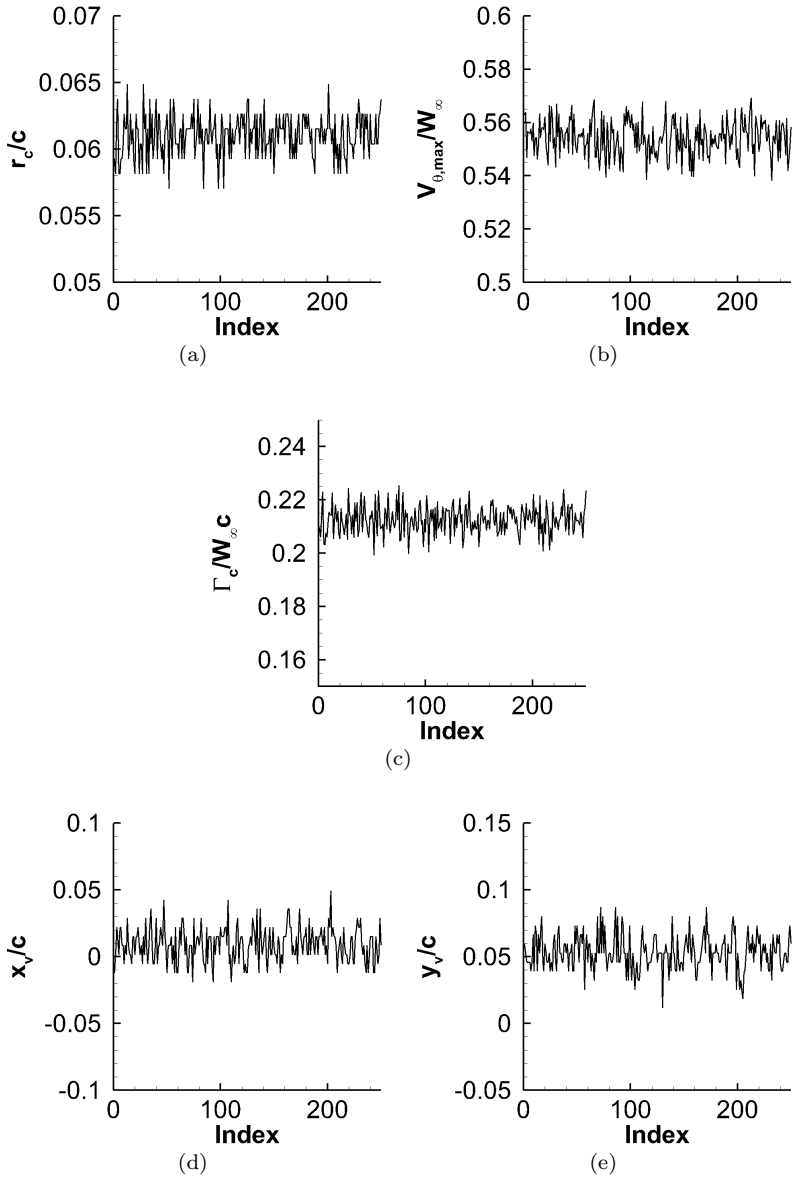

FIGURE 4.3: Instantaneous measurements of streamwise vortex characteristics, NACA 0012, $Re_c = 1.1 \times 10^5$, $Re_v = 2.4 \times 10^4$, (a): Core radius (r_c/c) (b): Peak tangential velocity, ($V_{\theta,max}/W_\infty$), (c): Core circulation ($\Gamma_c/W_\infty c$), (d): Vortex core horizontal location (x_v/c), (e): Vortex core vertical location (y_v/c)

It is also possible to evaluate the unsteadiness of the entire vortex velocity field, since the PIV measurements provide an instantaneous snapshot of the velocity field across the region of interest. The unsteadiness of the velocity field has been computed on the vortex-centred circular zones, so that the unsteadiness values do not contain contributions from wandering. Note that the PIV system employed in this research acquires measurements at a temporal frequency of $7.5Hz$. Therefore, the PIV measurements can contain only a limited, low-frequency portion of the complete turbulence spectrum. In addition, the limited spatial resolution of the PIV measurements restricts the measurement of flowfield variations at length scales smaller than the interrogation region dimensions. Nonetheless, important features of fluctuating velocity field can be extracted and, as will be demonstrated, the PIV measurements demonstrate good agreement with measurements using conventional hot-wire measurement methods.

The measurements at the reference condition suggest that the vortex core is a region of highly turbulent flow, where the turbulence intensity (Figure 4.4(a)) rises to a maximum of approximately 7.9% of the freestream velocity at the vortex centre. This is in agreement with a wide range of wing-tip vortex measurements obtained using hot-wire [45, 26, 22] and LDV [43], which also indicate that the vortex core contains high levels of turbulence. In addition, the current measurements feature a vortex Reynolds number of 2.4×10^4, which is within the regime identified by Bhagwat and Leishman [50] and Ramasamy and Leishman [34] where turbulent diffusion begins to influence the vortex growth rates. It is therefore possible that the rate of vorticity diffusion inside the vortex core, and so the vortex growth rate, will be far greater than if the flow were entirely laminar. Further insight into the unsteady velocity structure can be obtained by considering the RMS of the individual Cartesian velocity components, Figures 4.4(b), 4.4(c) and 4.4(d). The in-plane velocity fluctuations, u_{RMS} and v_{RMS}, are elliptic in shape, with the major axes aligned with the x- and y-coordinate axes, respectively. The current measurements suggest peak values of u_{RMS} and v_{RMS} of 0.1 and 0.08, which is similar to the peak values of 0.15 and 0.16 measured by Chow et al. [23] on a similar wing-tip geometry at $z/c = 0.7$ and $Re_c = 4.6 \times 10^6$. Clearly, the current measurements have been acquired at a station further downstream of the wing ($z/c = 6$) and at a chord Reynolds number which is an order of magnitude smaller ($Re_c = 1.1 \times 10^5$), which may explain the quantitative differences in the RMS values. Nonetheless, the current measurements are in good qualitative agreement, and the unsteadiness levels are of the same order of magnitude. In-plane normal stress contours with an elliptic shape were also measured by Chow et al. [22] and Ramasamy et al. [30], and were also observed in the simulations conducted by Zeman [48]. Such a contour pattern indicates that the in-plane normal stresses are not isotropic [22].

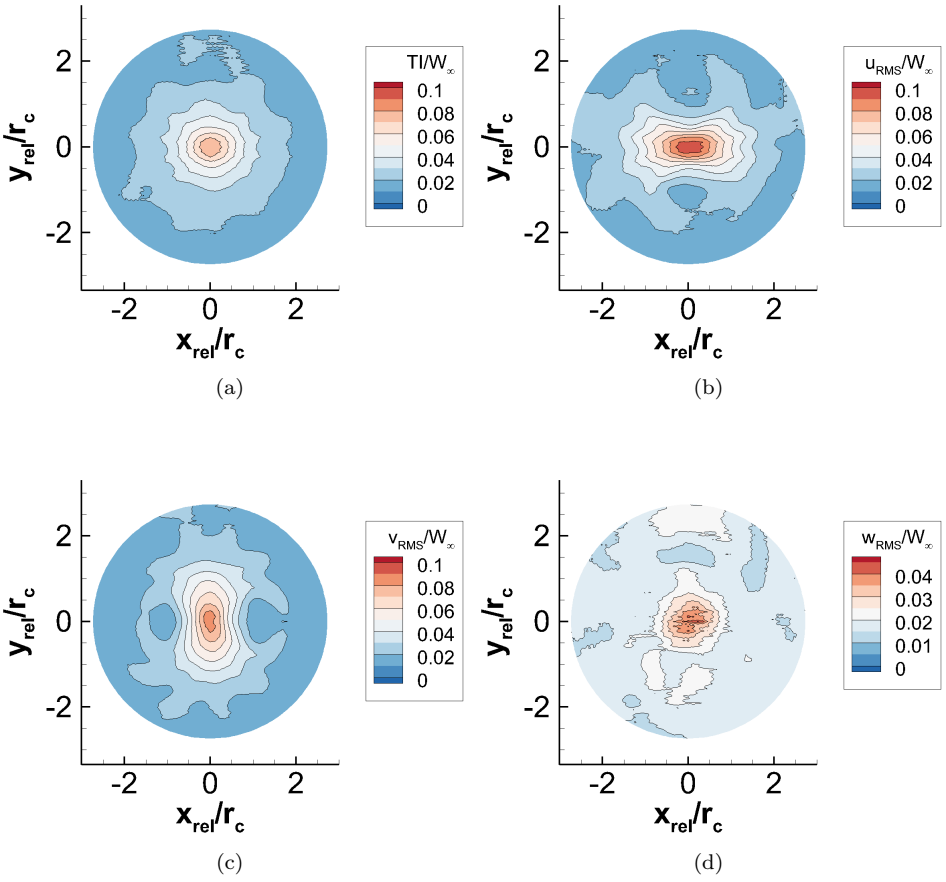

FIGURE 4.4: Conditionally-averaged velocity fluctuations, NACA 0012 vortex generator, $Re_c = 1.1 \times 10^5$, $Re_v = 2.4 \times 10^4$, (a): Mean Turbulence Intensity (TI/W_∞, $TI = \left(\sqrt{\frac{1}{3}(u'^2 + v'^2 + w'^2)}\right)$) (b): Mean x-component velocity fluctuations (u_{RMS}/W_∞), (c): Mean y-component velocity fluctuations (v_{rms}/W_∞), (d): Mean z-component velocity fluctuations (w_{rms}/W_∞)

It was demonstrated by Chow et al. [23] that this stress anisotropy arises as a result of an imbalance in the turbulence production inside the vortex core, such that the radial normal stresses ($V_{r,RMS}$) become greater than the tangential normal stresses ($V_{\theta,RMS}$). This characteristic can also be observed in the current measurements, Figures 4.5(a) and 4.5(b), which demonstrate that the radial normal velocity fluctuations measured beyond the vortex centre are larger than the tangential normal velocity fluctuations. Finally, the streamwise velocity fluctuations (Figure 4.4(d)) are circular in shape with a maximum located close to the vortex centre. This is also in agreement with previous wing-tip vortex measurements [1, 23].

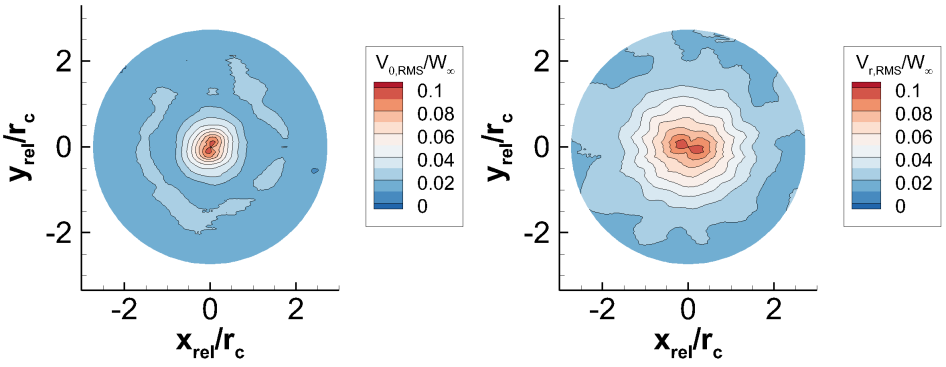

FIGURE 4.5: Conditionally-averaged velocity fluctuations, NACA 0012 vortex generator, $Re_c = 1.1\times10^5$, $Re_v = 2.4\times10^4$, (a): Circumferential velocity fluctuations ($V_{\theta,RMS}/W_\infty$) (b): Radial velocity fluctuations ($V_{r,RMS}/W_\infty$)

In addition to the turbulent normal stresses, it is also possible to use the current measurements to obtain information on the Reynolds stresses. The mean in-plane Reynolds stresses ($u'v'/W_\infty^2$), Figure 4.6(b)) are rotated by 45^o relative to the mean in-plane strain rate ($S_{x,y}c/W_\infty$), Figure 4.6(a)), in the direction opposite to the rotation direction of the vortex. This characteristic has been observed in various experimental measurements [23, 22] and vortex simulations [48], and is a consequence of the anisotropic normal stresses [23].

A strong link between the in-plane and out-of-plane fluctuations is illustrated in the $u'w'/W_\infty^2$ and $v'w'/W_\infty^2$ contours, Figures 4.6(c) and 4.6(d), respectively. The stress levels are of a similar magnitude to the in-plane Reynolds stresses seen in Figure 4.6(b). An analysis of the out-of-plane strain terms cannot be conducted, since the single-plane Stereo PIV measurement technique used in this research cannot resolve the streamwise gradients at a given measurement plane position. Nonetheless, it is possible to refer to existing wing-tip vortex measurements to explain the $u'w'$ and $v'w'$ patterns which have been observed in Figures 4.6(c) and 4.6(d). Chow et al. [22] found that the Cartesian out-of-plane Reynolds stresses both featured a two-lobed structure, as observed in the current measurements. The positive lobes of $u'w'$ is rotated by approximately 45^o from the negative y-axis, and the positive lobe of $v'w'$ is rotated by approximately 30^o from the positive x-axis. Chow et al. [23] suggested that this turbulent structure is a result of the streamwise velocity perturbation, and indicates that turbulence is acting to diminish the magnitude of the streamwise velocity excess. Thus, it is apparent that the out-of-plane characteristics of the vortex flow may contribute an additional source of turbulent

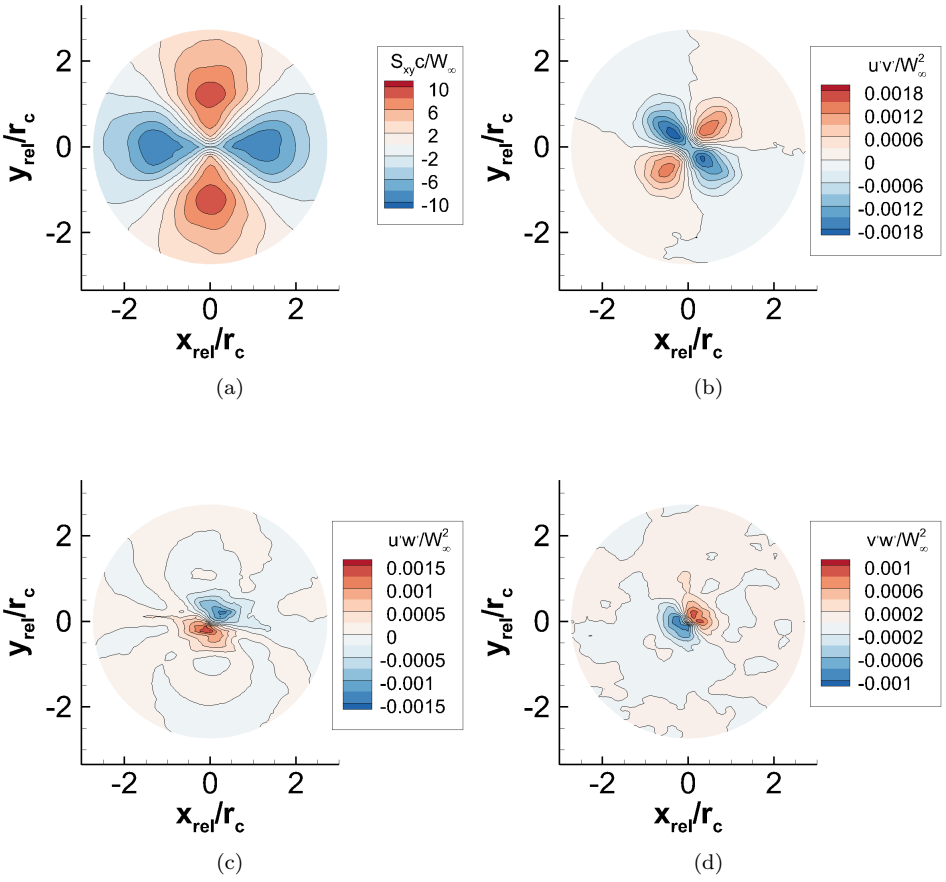

FIGURE 4.6: Conditionally-averaged velocity fluctuations, NACA 0012 vortex generator, $Re_c = 1.1 \times 10^5$, $Re_v = 2.4 \times 10^4$, (a): Mean in-plane strain rate ($S_{xy}/W_\infty c$), (b): Mean Reynolds stress ($u'v'/W_\infty^2$), (c): Mean Reynolds stress ($u'w'/W_\infty^2$), (d): Mean Reynolds stress ($v'w'/W_\infty^2$). N12 and N6 refer to the NACA 0012 vortex generator at $\alpha_{vg} = 12^o$ and 6^o, respectively. D12 and D6 refer to the delta wing vortex generator at $\alpha_{vg} = 12^o$ and 6^o, respectively

diffusion in the vortex flow. This has been investigated in this research by employing different vortex generator configurations and vortex generator types (section 3.5).

The unsteadiness characteristics obtained from the current PIV measurements are in good agreement with wing-tip vortex turbulence measurements which are available in the literature, despite the limited spatial and temporal resolution of the measurements. In particular, the measurements have successfully captured features of the normal and Reynolds stresses which have been observed in other wing-tip vortex measurements. The current PIV measurements can provide important insight into the turbulent characteristics of the unperturbed vortex. It has been found that the reference streamwise vortex consists

of highly turbulent flow inside the vortex core. As a result, the wing-tip vortex flow may experience diffusion rates which are higher than those attributed to laminar viscosity alone. An important objective of the vortex ingestion studies will be to determine if the turbulent fluctuations have an effect on the evolution of the streamwise vortex during the ingestion process.

4.3 Influence of vortex generator conditions

In the preceding section, a detailed analysis was presented for the wing-tip vortex characteristics measured downstream of the NACA 0012 vortex generator at a chord Reynolds number of 1.1×10^5. A range of vortex generator conditions have been considered as part of the vortex ingestion measurements (Tables 4.1 and A.1). The purpose of this section is to elucidate the details of the vortex characteristics downstream of the vortex generators as a function of the chord Reynolds number, the vortex generator type, and the vortex generator angle of attack. In this way, it will be possible to identify the key features of the vortex prior to entering the intake capture streamtube contraction.

TABLE 4.1: Vortex characteristics for unperturbed freestream flow

VG	α_{vg}	$Re_c = \frac{W_\infty c}{\nu}$	$Re_v = \frac{\Gamma_c}{\nu}$	$\frac{r_c}{D_i}$	$\frac{\Gamma_c}{W_\infty D_i}$	$\frac{\omega_{z,max} D_i}{W_\infty}$	$\frac{\omega_{z,av} D_i}{W_\infty}$
0012	12^o	1.1×10^5	2.4×10^4	0.092	0.319	30.34	12.11
0012	12^o	1.7×10^5	3.7×10^4	0.087	0.318	38.77	13.44
0012	12^o	3.6×10^5	7.4×10^4	0.082	0.307	48.80	14.66
0012	6^o	3.6×10^5	3.4×10^4	0.065	0.143	27.83	10.97
Delta	12^o	4.7×10^5	5.6×10^4	0.111	0.236	22.24	6.05
Delta	6^o	4.7×10^5	2.3×10^4	0.061	0.098	22.36	8.41

4.3.1 Chord Reynolds number

The impact of the vortex generator chord Reynolds number was investigated using the NACA 0012 vortex generator at an angle of attack of 12^o. freestream velocities of $11.0ms^{-1}$, $17.2ms^{-1}$, and $35.4ms^{-1}$ were investigated, Table A.1, which correspond to chord Reynolds numbers of 1.1×10^5, 1.7×10^5 and 3.6×10^5. This approach successfully produced a controlled increase in the vortex Reynolds number from 2.4×10^4 to 7.4×10^4

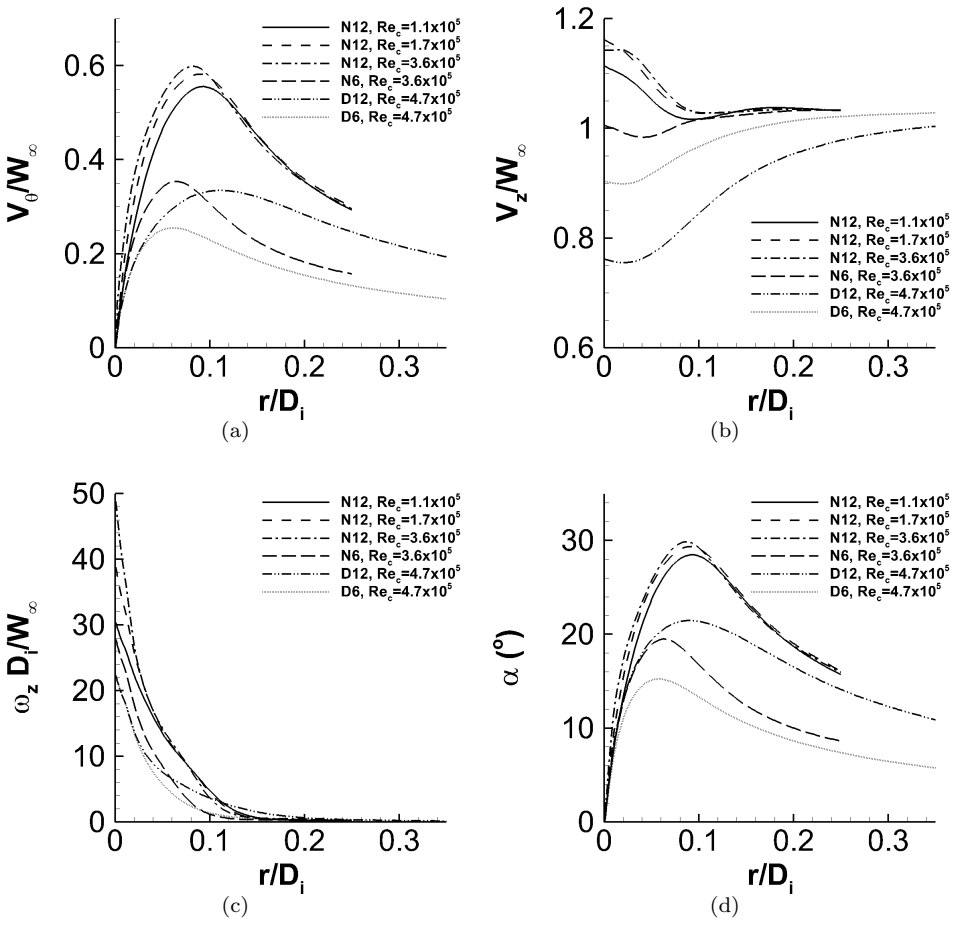

FIGURE 4.7: Unperturbed vortex velocity field measurements, (a): Circumferentially-averaged tangential velocity profile, (V_θ/W_∞), (b): Circumferentially-averaged streamwise velocity profile (V_z/W_∞), (c): Circumferentially-averaged streamwise vorticity profile $(\omega_z c/W_\infty)$, (d): Circumferentially-averaged flow angularity profile $(\alpha = tan^{-1}(V_\theta/V_z))$

when the chord Reynolds number was increased from 1.1×10^5 to 3.6×10^5 (Table 4.1). There is also an 8% increase in the peak tangential velocity normalised by the freestream velocity, an 11% reduction in the vortex core radius, Figure 4.7(a), and a 61% increase in the peak normalised streamwise vorticity, Figure 4.7(c). This Reynolds number dependence may be explained from the observations of Zhou et al. [27], who suggested that an increase in the chord Reynolds number causes a thinner wake to be produced by the wing. As a consequence of the reduced wake thickness, the vortex roll-up process is of a greater intensity, which results in the smaller vortex core radius, increased normalised peak tangential velocity and increased peak streamwise vorticity as reported in Table 4.1. The streamwise velocity, however, does not illustrate a strong dependence on the chord

Reynolds number, and features a streamwise velocity excess of between 11% and 16% across the range of chord Reynolds numbers tested (Figure 4.7(b)). The peak flow angle indicates only a weak dependence on the chord Reynolds number, and increases from 28^o at $Re_c = 1.1 \times 10^5$ to 30^o at $Re_c = 3.6 \times 10^5$ (Figure 4.7(d)). This is a result of a small increase in the ratio (V_θ/V_z) which, in turn, is due to the small increase in $V_{\theta,max}$ (Figure 4.7(a)) coupled with little change in the normalised streamwise velocity profile, Figure 4.7(b).

The increase of chord Reynolds number at a constant angle of attack successfully produced a large increase in the vortex Reynolds number, with a corresponding rise in the peak streamwise vorticity. However, when normalised by the freestream velocity, there were only small changes in the normalised tangential and streamwise velocity profiles. As a result, the peak flow angle remained close to 30^o for all chord Reynolds numbers considered.

4.3.2 Vortex generator type

A second approach which was used to vary the unperturbed vortex characteristics was to employ a delta wing in place of the NACA 0012 vortex generator. This was investigated at a freestream velocity of $35.4ms^{-1}$ and an angle of attack of 12^o. For this configuration, the chord Reynolds number was 4.7×10^5, and the measurement plane was located at a distance of $4.5c$ downstream of the delta wing trailing edge. Note that the delta wing was mounted at the same distance upstream of the intake as the NACA 0012 vortex generator. However, because the delta wing features a larger chord than the NACA 0012 vortex generator, the non-dimensional distance z/c is reduced for the delta wing.

The delta wing vortex features a core vortex Reynolds number of 5.6×10^4, which is 24% lower than that of the NACA 0012 vortex generator Table 4.1. A number of reasons contribute to this difference. Firstly, the lift generation mechanisms for delta wings and rectangular wings differ, since delta wing aerodynamics are strongly influenced by the leading edge vortices [18]. The lift coefficient of the delta wing is estimated to be 0.61, compared to the lift coefficient of 0.95 for the NACA 0012 vortex generator (section 3.5). In addition, the delta wing features a planform area which is 16% of the NACA 0012 vortex generator. The delta wing vortex features a 33% larger core radius, with a 45% lower peak tangential velocity and a 55% lower peak streamwise vorticity (Figures 4.7(a) and 4.7(c)). The streamwise velocity profile of the delta wing vortex consists of a deficit of 24% relative to the freestream velocity, Figure 4.7(b), which is notably different from the

16% streamwise velocity excess measured on the NACA 0012 vortex. This qualitatively agrees with the comparable delta wing measurements of Wang et al. [98], who measured a streamwise velocity deficit of 20% at a distance of half a chord length downstream of the wing trailing edge. It was suggested that the streamwise velocity deficit was caused when low-momentum, high-turbulence fluid produced at the trailing edge of the wing which was entrained into the vortex. The peak flow angularity associated with the delta wing vortex reaches 22^o, Figure 4.7(d), which is notably lower than the peak angle of 30^o measured for the NACA 0012 vortex at the same freestream condition.

A comparison between the vortices produced by the delta wing and NACA 0012 vortex generators at a fixed freestream condition confirm that the characteristics of the streamwise vortex are strongly dependent on the vortex generation source. In comparison to the wing-tip vortex produced by the NACA 0012 vortex generator, the delta wing vortex features a reduced vortex Reynolds number, peak tangential velocity, peak streamwise vorticity, and peak flow angle. In addition, the delta wing vortex features a streamwise velocity deficit, which is in contrast to the excess measured on the NACA 0012 wing-tip vortex. Thus, it will be possible to assess the effect of the streamwise velocity perturbation on the vortex ingestion process.

4.3.3 Angle of attack

Prior studies have shown that the vortex weakens when the angle of attack is reduced, with a reduced peak tangential velocity, core radius, streamwise velocity perturbation and streamwise vorticity [17, 1, 29, 99]. Therefore, the final approach used to vary the characteristics of the unperturbed vortices was to reduce the vortex generator angle of attack. The current measurements agree with the trends reported in the literature. When the angle of attack of the NACA 0012 vortex generator is reduced from 12^o to 6^o, there is a reduction of the peak tangential velocity and streamwise vorticity (Figures 4.7(a) and 4.7(c)) of 40% and 43% respectively at a chord Reynolds number of 3.6×10^5. The streamwise velocity perturbation reduces from an excess of approximately $0.16W_\infty$ to a small deficit of $0.05W_\infty$ (Figure 4.7(b)). The measurements also indicate a 21% smaller vortex core radius, and a swirl angle which reduces from 30^o to 15^o, Figure 4.7(d). In addition, the vortex Reynolds number reduced from 7.4×10^4 to 3.4×10^4. This reduction in Reynolds number is independent of the chord Reynolds number, which will permit isolation of any important differences with the results obtained in the previous section, where increases in the vortex Reynolds number were coupled with the chord Reynolds number.

Compared to the measurements at $\alpha_{vg} = 12^o$, the vortex generated by the delta wing at an angle of attack of 6^o exhibits a 24% lower peak tangential velocity (Figure 4.7(a)), a 58% lower core circulation, and a 45% smaller core radius. Furthermore, the peak flow angularity which reduces from 21^o to 15^o (Figure 4.7(d)). Interestingly, at this condition a velocity deficit of 9% of the freestream velocity was measured, (Figure 4.7(b)). This agrees with the near-field measurements of Wang et al. [98], who also found that the streamwise velocity deficit associated with the delta wing vortex was reduced at lower angles of attack. The peak streamwise vorticity (Figure 4.7(c) and Table 4.1) remains unchanged with the reduction in angle of attack. This is unexpected, since the measurements of the NACA 0012 wing-tip vortex indicated that the peak streamwise vorticity reduced in proportion to the angle of attack. One possible explanation is that, at higher angles of attack, the wake generated at the trailing edge of the delta wing higher levels of turbulence. In such a scenario, it is possible that the rate of vorticity diffusion inside the vortex core is increased. Therefore, as the vortex convects from the wing to the PIV measurement plane, the peak vorticity will reduce more rapidly than that experienced in the vortex at a lower angle of attack.

It has been found that the primary effect of a reduction in the vortex generator angle of attack is a corresponding reduction in the vortex Reynolds number. This is coupled with a reduced vortex core radius, peak tangential velocity, peak streamwise vorticity, and streamwise velocity perturbation. A degree of nonlinearity was observed in the case of the delta wing vortex, which featured little change in the streamwise vorticity when the angle of attack was reduced. It was suggested that the rate of vorticity diffusion inside the vortex core may be substantially greater at higher angles of attack.

4.3.4 Unsteadiness of vortex characteristics and velocity field

In this section, the effect of the change in vortex generator conditions on the unsteadiness of the vortex characteristics and the velocity field unsteadiness is discussed.

The unsteadiness of the vortex characteristics can be expressed in terms of the RMS value of the fluctuations about the mean value, Table 4.2. The NACA 0012 vortex generator results indicate that the unsteadiness levels of the core radius and core circulation are independent of the chord Reynolds number, and remain less than 1% when normalised using the freestream velocity and the intake inner diameter. The peak tangential velocity unsteadiness increases by 45% between chord Reynolds numbers of 1.1×10^5 to 3.6×10^5. In addition, the wandering levels, indicated by x_v/c and y_v/c, increase by approximately

TABLE 4.2: RMS unsteadiness of unperturbed vortex characteristics

VG	α_{vg}	$Re_c = \frac{W_\infty c}{\nu}$	$Re_v = \frac{\Gamma_c}{\nu}$	$\frac{r_{c,RMS}}{D_i}$	$\frac{V_{\theta,max,RMS}}{W_\infty}$	$\frac{\Gamma_{c,RMS}}{W_\infty D_i}$	$\frac{x_{v,RMS}}{D_i}$	$\frac{y_{v,RMS}}{D_i}$
0012	12^o	1.1×10^5	2.4×10^4	0.0024	0.0069	0.0081	0.019	0.020
0012	12^o	1.7×10^5	3.7×10^4	0.0027	0.0077	0.0096	0.018	0.018
0012	12^o	3.6×10^5	7.4×10^4	0.0023	0.010	0.0086	0.022	0.023
0012	6^o	3.6×10^5	3.4×10^4	0.0026	0.0062	0.0058	0.022	0.026
Delta	12^o	4.7×10^5	5.6×10^4	0.0186	0.017	0.033	0.031	0.028
Delta	6^o	4.7×10^5	2.3×10^4	0.0113	0.015	0.016	0.037	0.034

15%. A reduction in the NACA 0012 angle of attack from 12^o to 6^o has little effect on the unsteadiness associated with the vortex core radius or the vortex position. However, there is a clear reduction in the peak tangential velocity and core circulation unsteadiness of 38% and 33%, which suggests that the unsteadiness associated with these parameters is strongly influenced by the details of the vortex generation process.

The delta wing vortex characteristics features notably higher levels of unsteadiness than those measured for the NACA 0012 wing-tip vortex at both $\alpha_{vg} = 12^o$ and 6^o. For example, at an angle of attack of 12^o and a freestream velocity of $35.4ms^{-1}$, the delta wing vortex core radius, peak tangential velocity and core circulation unsteadiness are, respectively, 5.8 times, 1.7 times and 3.8 times greater than those measured on the NACA 0012 wing-tip vortex at the same freestream velocity. There is a similar order of magnitude increase in the RMS unsteadiness levels for an angle of attack of 6^o. These results suggest that the delta wing vortex generation process features greater levels of unsteadiness in comparison to the NACA 0012 vortex generator. The wandering levels at both angles of attack, however, are similar in magnitude for both vortex generators.

The contours of normalised turbulence intensity (TI/W_∞), Figures 4.8(a) to 4.8(f), indicate that the peak velocity unsteadiness levels occur at the vortex centre for all configurations. The peak turbulence intensity almost doubles when the chord Reynolds number of the NACA 0012 vortex generator is increased from 1.1×10^5 to 3.6×10^5 (Figures 4.8(a) to 4.8(c)). This rise in velocity unsteadiness is consistent with the rise in peak tangential velocity unsteadiness reported in Table 4.2. However, the increase in Re_c has little effect on the velocity unsteadiness beyond $r/r_c = 2$, where TI/W_∞ is approximately 0.02 for all chord Reynolds numbers.

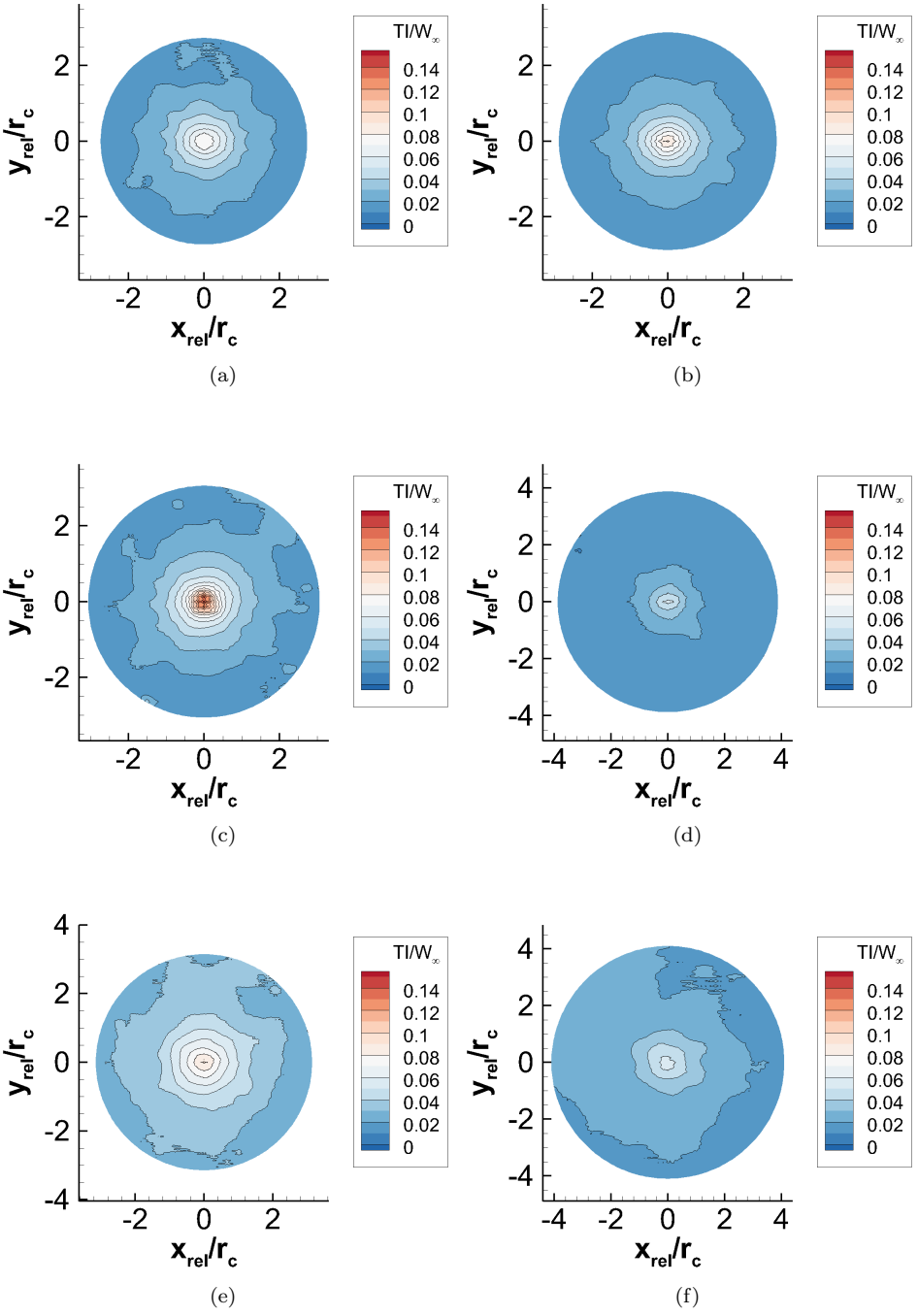

FIGURE 4.8: Unperturbed vortex measurements, Turbulence Intensity (TI/W_∞), (a): NACA 0012, $\alpha_{vg} = 12^o$, $Re_c = 1.1 \times 10^5$, (b): NACA 0012, $\alpha_{vg} = 12^o$, $Re_c = 1.7 \times 10^5$, (c): NACA 0012, $\alpha_{vg} = 12^o$, $Re_c = 3.6 \times 10^5$, (d): NACA 0012, $\alpha_{vg} = 6^o$, $Re_c = 3.6 \times 10^5$, (e): Delta, $\alpha_{vg} = 12^o$, $Re_c = 4.7 \times 10^5$, (f): Delta, $\alpha_{vg} = 6^o$, $Re_c = 4.7 \times 10^5$

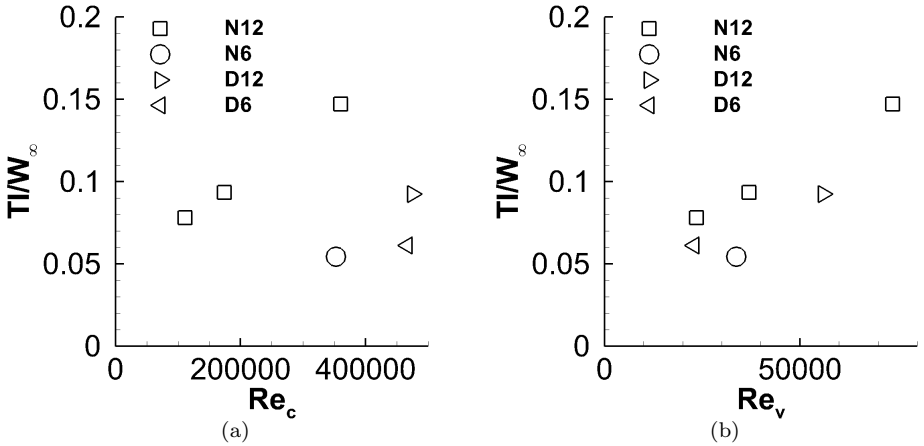

FIGURE 4.9: Unperturbed vortex measurements, turbulence intensity at vortex centre (TI/W_∞), (a): As a function of Re_c, (b): As a function of Re_v
, where N and D refer to the NACA 0012 and delta wing vortex generators, and 6 and 12 refer to the vortex generator angle of attack.

Therefore, the effect of an increase in the chord Reynolds number is to increase the intensity of the velocity fluctuations of the flow inside and immediately surrounding the vortex core, which will cause an increase in the turbulent diffusion levels inside the vortex core. When the angle of attack of the NACA 0012 vortex generator is reduced from 12^o to 6^oat a constant chord Reynolds number, there is a corresponding reduction in the velocity unsteadiness levels inside the core, Figures 4.8(d). This result demonstrates that the peak velocity unsteadiness levels are not simply a function of chord Reynolds number, as observed in Figure 4.9(a). Instead, a closer correlation is obtained when the peak turbulence intensity is plotted as a function of the vortex Reynolds number, Figure 4.9(b). The peak levels of velocity unsteadiness measured in the delta wing vortices (Figures 4.8(e) and 4.8(f)) are lower than the counterparts measured on the NACA 0012 vortex generator (Figures 4.8(c) and 4.8(d)). For example, the peak turbulence intensity for the delta wing at $\alpha_{vg} = 12^o$ is 37% lower than that measured with the NACA 0012 vortex generator at the same condition. This is perhaps unexpected, since the unsteadiness associated with the vortex characteristics, Table 4.2, is notably higher for the delta wing vortex. A possible explanation is that the delta wing velocity unsteadiness (Figure 4.8(e)) is distributed over a larger area when compared to the NACA 0012 results Figure 4.8(c). Therefore, the velocity unsteadiness levels at the core radius are higher for the delta wing vortex, which will cause comparatively larger fluctuations in the vortex characteristics which are measured there, such as the core radius and peak tangential velocity. In a similar fashion to the NACA 0012 measurements, the delta wing peak turbulence intensity values appear

to show a stronger correlation with the vortex Reynolds number (Figure 4.9(b)) than the chord Reynolds number (Figure 4.9(a)). This further supports the assertion that the turbulence levels are influenced by a number of factors, including the chord Reynolds number, and the details of the vortex generation process.

4.4 Summary

The purpose of this chapter was to establish the characteristics of the vortices measured downstream of the vortex generators in the absence of the intake capture streamtube. It was found that the unperturbed vortex is characterised by perturbations of in-plane and out-of-plane velocities relative to the freestream flow. The in-plane velocity perturbation produces large variations of flow angularity close to the vortex. Based on prior measurements of the impact of a vortex on engine performance, the magnitude of the flow angles in this research may have a detrimental effect on intake and fan performance. An assessment of the unsteadiness of the unperturbed vortex has also been conducted. The vortex characteristics, such as size and core circulation, feature small fluctuations. However, the measurements indicate that the vortex has high levels of velocity unsteadiness inside the core. A comparison between the current measurements and hot-wire measurements in the literature has been performed. It was found that the velocity unsteadiness levels and characteristics are in good qualitative agreement with measurements using conventional hot-wire methods at similar vortex generation conditions. The vortices which have been investigated in this section feature notable levels of velocity unsteadiness inside the vortex core. This suggests that the evolution of the vortex may be characterised by rates of vorticity diffusion which are higher than that attributed to laminar diffusion alone. Finally, a controlled parametric study of the vortex generator configuration demonstrated that the mean and unsteady characteristics of the generated vortex are influenced by the vortex generator chord Reynolds number, angle of attack, and vortex generator type. Therefore, using a range of vortex generator configurations, it will be possible to identify if the vortex ingestion process is sensitive to the characteristics of the vortex prior to ingestion.

Chapter 5

Measurements of streamwise vortex ingestion

The limited number of vortex ingestion measurements which are available in the literature suggest that a streamwise vortex can cause notable levels of inlet flow distortion inside an aircraft intake [8, 71, 73]. However, the characteristics of the vortex inside the intake, and so its effect on the flow distortion levels, will be strongly dependent on the details of the ingestion process. Therefore, it is necessary to establish fundamental understanding of how the vortex evolves as it passes from the unperturbed upstream flow into the intake. For the first time, a detailed parametric study of streamwise vortices in a streamtube contraction has been conducted. The first part of this chapter analyses a datum vortex ingestion configuration. The features of the capture streamtube velocity field are assessed, and a detailed analysis of the vortex evolution is given. This focuses on both the mean vortex characteristics and aspects of the flow unsteadiness. Thereafter, the results of the controlled parametric study are presented. This focuses on the impact of a change in the streamtube contraction levels and the impact of the initial characteristics of the streamwise vortex in the unperturbed flow. Finally, the parametric study is concluded with an assessment of the impact of the vortex ingestion trajectory.

5.1 Analysis of vortex ingestion flowfield

The purpose of this section is to characterise the flowfield associated with a vortex passing through an intake capture streamtube. Firstly, the characteristics of the intake capture

streamtube are established as a function of the distance from the intake highlight plane. This is followed by an analysis of the response of the streamwise vortex to the streamtube contraction, in terms of the time-averaged vortex characteristics and velocity field. Finally, the unsteady features of the vortex ingestion process are analysed to provide further insight into the dominant flow physics.

In this section, the analysis will be performed of the measurements obtained for the NACA 0012 vortex generator at an angle of attack of $\alpha_{vg} = 12^o$ and a freestream velocity of $17.2ms^{-1}$. At this condition, the chord and vortex Reynolds numbers correspond to 1.7×10^5 and 3.7×10^4 respectively. The vortex was ingested along the centreline of an intake capture streamtube with a velocity ratio of $W_i/W_\infty = 5.1$. For this configuration, the diameter of the capture streamtube far upstream of the intake corresponds to $D_\infty/D_i = 2.3$.

5.1.1 Intake capture streamtube velocity field

It is first of interest to elucidate the details of the streamwise velocity field (w/W_∞) intake capture streamtube. The normalised streamwise velocity contours (w/W_∞), Figure 5.1(a), suggest that the perturbation associated with the intake is negligible at $z/D_i = 2.25$ upstream of the highlight plane. This is further supported by inviscid CFD simulations (appendix B.2) which confirm that the streamwise velocity at $z/D_i = 2.25$ is equal to $1.043W_\infty$ at this intake velocity ratio (VR=5.1).

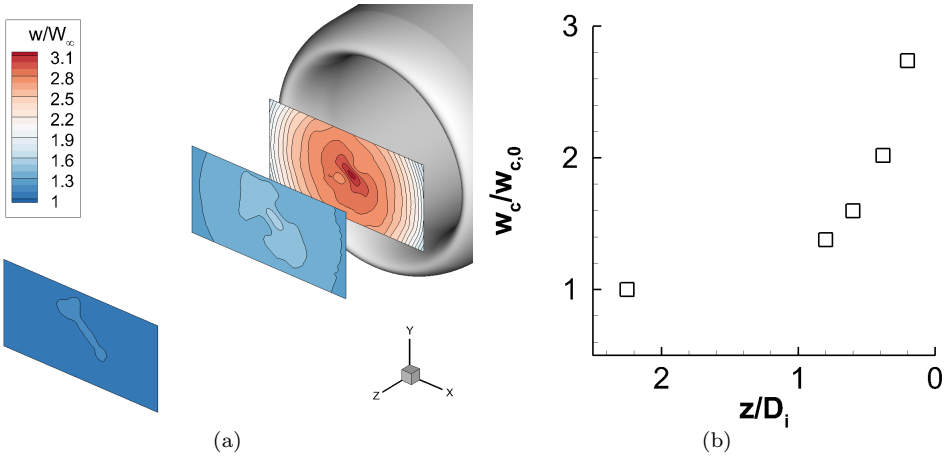

FIGURE 5.1: Contours of streamwise velocity component (w/W_∞) at $z/D_i = 2.25$, 0.80 and 0.20 upstream of the intake highlight plane, NACA 0012 vortex generator, $Re_c = 1.7 \times 10^5$, $Re_v = 3.7 \times 10^4$

Therefore, it is appropriate to consider the vortex at $z/D_i = 2.25$ as the unperturbed vortex condition. The effects of the streamtube contraction become apparent at $z/D_i = 0.80$, after which the flow undergoes an intense acceleration to approximately three times the freestream velocity at $z/D_i = 0.20$. The flow reaches a velocity of $w/W_\infty = 3.2$ at $z/D_i = 0.20$. Therefore, the flow velocity continues to increase downstream of $z/D_i = 0.20$. The inviscid CFD simulations confirm that the contraction process is complete inside the intake, at a position which is approximately $1.0D_i$ downstream of the intake highlight plane (appendix B.2).

An important feature which can be observed in the streamwise velocity contours is that the streamwise velocity is not uniform across the streamtube cross-section. Instead, the streamwise velocity reaches a maximum at the centre of the streamtube, and diminishes with distance from the centreline axis. For example, at a given distance from the intake highlight plane (z/D_i), a fluid element at the streamtube centreline will experience greater contraction levels than a fluid element located at some distance from the centreline. This may have a notable influence on the vortex evolution inside the streamtube contraction, and has been analysed in detail in section 5.2.4.

5.1.2 Vortex characteristics

An understanding of the behaviour of the vortex flow inside the streamtube contraction can be obtained with reference to the circumferentially-averaged profiles of tangential velocity (V_θ/W_∞), streamwise velocity (V_z/W_∞), streamwise vorticity ($\omega_z D_i/W_\infty$) and flow angularity ($\alpha = tan^{-1}(V_\theta/V_z)$), Figures 5.2(a) to 5.3, where D_i is the intake inner diameter, and W_∞ is the freestream velocity.

As the vortex approaches the intake highlight plane, there is a notable increase in the peak tangential velocity, and a corresponding reduction in the vortex core radius, Figure 5.2(a). For example, between $z/D_i = 2.25$ and $z/D_i = 0.20$, the peak tangential velocity increases by 52%, and the vortex core radius reduces by 35%. Note that these changes are greater than the measurement uncertainties at these conditions, which correspond to 5% and 6% for the change in peak tangential velocity and core radius, respectively. There is also a large increase in streamwise velocity (Figure 5.2(b)), which has already been observed in Figure 5.1(a). The observed behaviour of the vortex is consistent with vortex intensification. Some important details can be identified in the streamwise velocity profiles, Figure 5.2(b). Firstly, the initial streamwise velocity perturbation inside the vortex core, which is approximately equal to $0.16W_\infty$, is small in comparison to the overall

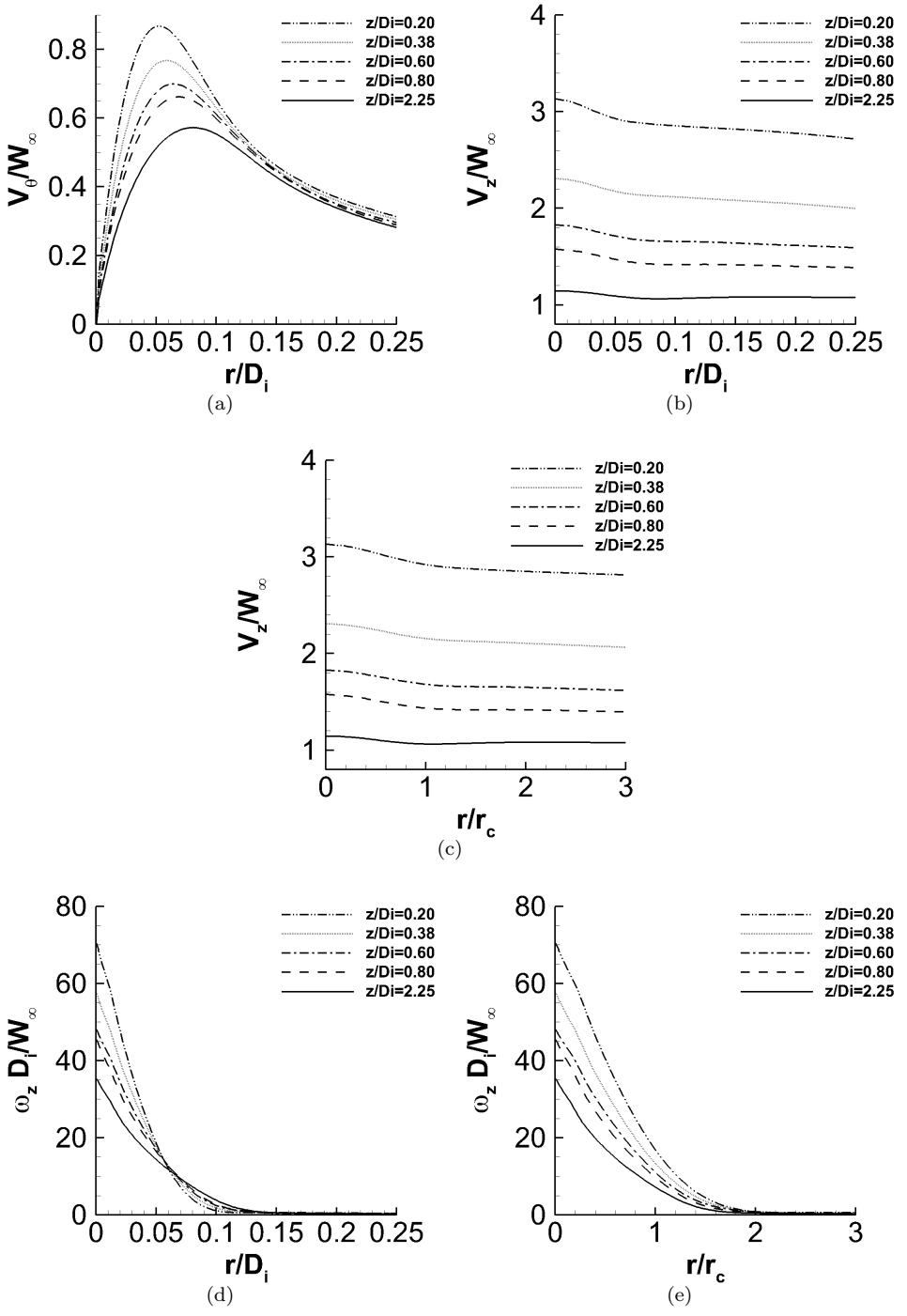

FIGURE 5.2: Circumferentially-averaged profiles of vortex perturbation field, NACA 0012 vortex generator, $Re_c = 1.7\times10^5$, $Re_v = 3.7\times10^4$, (a): Tangential velocity (V_θ/W_∞), (b): Streamwise velocity (V_z/W_∞) as a function of r/D_i, (c): Streamwise velocity (V_z/W_∞) as a function of r/r_c, (d): Streamwise vorticity ($\omega_z D_i/W_\infty$) as a function of r/D_i, (e): Streamwise vorticity ($\omega_z D_i/W_\infty$) as a function of r/r_c

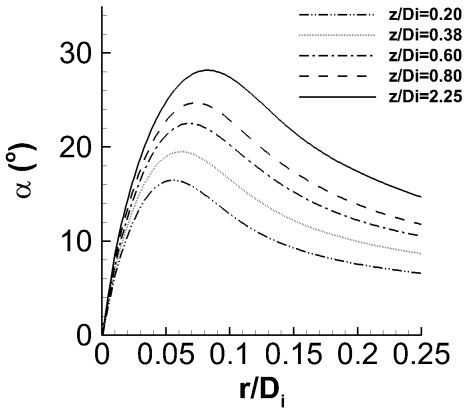

FIGURE 5.3: Circumferentially-averaged profiles of vortex flow angle distribution ($\alpha = tan^{-1}(V_\theta/V_z)$), NACA 0012 vortex generator, $Re_c = 1.7 \times 10^5$, $Re_v = 3.7 \times 10^4$

increase in streamwise velocity of the surrounding capture streamtube flow. In addition, the magnitude of the streamwise velocity perturbation remains small throughout the contraction process. For example, at $z/D_i = 2.25$, the ratio of the centreline streamwise velocity to the streamwise velocity at the core radius is 7%. At $z/D_i = 0.20$, this ratio is unchanged. This is in contrast to the results from the Batchelor model in section 2.4.1 for a similar contraction and unperturbed vortex as the measurements in Figures 5.2(a) to 5.2(e). In particular, the Batchelor model indicated that the streamwise velocity inside the vortex core should increase at a rate which is greater than that in the flow which surrounds the vortex (Figures 2.21(b) and 2.22), and should result in a streamwise velocity at the vortex centre which is approximately 10% greater than the surrounding flow (Figure 2.21(b)). However, it should be noted that the Batchelor model assumes that the streamwise velocity perturbation forms from an initially uniform streamwise velocity distribution, which is not the case in the current measurements. Furthermore, the Batchelor model assumes that the flow is inviscid, which may not be an appropriate assumption. As the streamwise velocity perturbation inside the vortex core is increased, there are additional out-of-plane velocity gradients, which are likely to be diffused under the action of viscosity. A final observation is that the streamwise velocity perturbation is largely confined to the vortex core (Figure 5.2(c)). Beyond the vortex core, the streamwise velocity gradually reduces with distance from the vortex centre, which is a result of the non-uniform streamtube streamwise velocity profile, as identified in Figure 5.1(a).

As anticipated, the streamwise vorticity (Figure 5.2(d)) also experiences a large increase when the vortex moves through the streamtube contraction. For example, the peak streamwise vorticity doubles between $z/D_i = 2.25$ and $z/D_i = 0.20$. The surrounding

streamwise vorticity also convects inwards during the contraction due to the reduction in the vortex core radius. When displayed as a function of r/r_c (Figure 5.2(e)), it is clear that the vorticity intensification takes place for all of the streamwise vorticity contained in the flow.

The evolution of the flow angularity distribution during the contraction process is of particular interest, since this parameter provides an indication of the swirl distortion levels which may be experienced by the aircraft engine once inside the intake. An important observation from the flow angle distributions (Figure 5.3) is that the peak flow angle reduces while the vortex moves through the contraction. At $z/D_i = 2.25$, the peak flow angle corresponds to 28.2^o, which reduces to 16.5^o at $z/D_i = 0.20$. This behaviour can be explained with reference to the tangential and streamwise velocity profiles. The increase in streamwise velocity during the contraction is greater than that observed in the tangential velocity. As a result, the ratio V_θ/V_z becomes smaller, which causes a corresponding reduction in the flow angularity ($\alpha = tan^{-1}(V_\theta/V_z)$). This is a particularly important result, since the effect of the streamtube contraction is to reduce the swirl distortion levels attributed to the vortex. In the presence of a streamtube contraction, the peak flow angles inside the intake will be notably lower than those measured upstream of the intake and prior to ingestion.

5.1.3 Comparison with theory

The preceding results indicate that, as the streamwise vortex moves through the contracting intake capture streamtube, the vortex experiences a large change in characteristics in a manner consistent with vortex intensification. It is then of interest to compare the measured vortex intensification levels with fundamental vortex theory. In this way, it will be possible to identify important flow physics which impact the vortex intensification process. Furthermore, the comparison will establish understanding of whether the dynamics of a vortex inside a streamtube contraction can be modelled adequately using fundamental theory.

In section 2.4.1, it was demonstrated that an approximate model for vortex intensification could be derived from vortex filament theory, assuming that the flow is inviscid, incompressible, and barotropic. The flow contraction was defined as a change in mean streamwise velocity, for example, from the freestream velocity (W_∞) to another streamwise velocity (w), where details of the transition in velocity are not considered. From continuity, the radius of the vortex filament will change from $r_{f,0}$ to r_f, Eq. 5.1.

$$\frac{r_f}{r_{f,0}} = \sqrt{\frac{W_\infty}{w}} \tag{5.1}$$

From this expression, it is possible to determine relationships for the vortex peak tangential velocity and peak streamwise vorticity (section 2.4.1). If the streamwise vortex is considered as a vortex tube of initial core radius $r_{c,0}$, then a change in streamwise velocity from w to W_∞ will result in a reduced core radius of r_c, Eq. 5.2.

$$\frac{r_c}{r_{c,0}} = \sqrt{\frac{W_\infty}{w}} \tag{5.2}$$

Batchelor [62] demonstrated that Eq. 5.2 is strictly valid only when the vortex has an infinitesimal cross-sectional area. In the case of a vortex with a finite core radius, it was shown that there is a coupling between the streamwise and tangential velocity fields. This coupling causes an additional streamwise pressure gradient inside the vortex core, which amplifies the effect of the flow contraction and causes an even greater change in the vortex core radius compared to that given in Eq. 5.2. This effect is a function of the flow contraction levels, and the initial core radius and average vorticity of the vortex. Therefore, the validity of Eq. 5.2 for application in the current measurements depends on the strength of the coupling effect, and can be assessed using the Batchelor model (section 2.4.1). The numerical results obtained in section 2.4.1 illustrated that the vortex core streamwise velocity (w_c) is no more than 10% greater than the streamwise velocity of the flow surrounding the vortex. Therefore, it can be concluded that the measured value of $w_c/w_{c,0}$ is a close representation of the capture streamtube contraction levels surrounding the vortex. In addition, it was found that the additional streamwise pressure gradient inside the vortex core produced a core radius which is 2% smaller than that given by vortex filament theory. Therefore, this effect is expected to be small for the measured configuration. On this justification, vortex filament theory can be employed with the vortex core streamwise velocity ratio ($w_c/w_{c,0}$) to estimate the theoretical change in the vortex core radius (Eq. 5.3), average streamwise vorticity (Eq. 5.4), and peak tangential velocity (Eq. 5.5).

$$\frac{r_c}{r_{c,0}} = \sqrt{\frac{w_{c,0}}{w_c}} \tag{5.3}$$

$$\frac{\omega_{z,av}}{\omega_{z,av,0}} = \frac{w_c}{w_{c,0}} \tag{5.4}$$

$$\frac{V_\theta}{V_{\theta,0}} = \sqrt{\frac{w_c}{w_{c,0}}} \tag{5.5}$$

In addition, the peak streamwise vorticity can be estimated by considering the vortex filament located at the vortex centre, and is given in Eq. 5.6.

$$\frac{\omega_{z,max}}{\omega_{z,max,0}} = \frac{w_c}{w_{c,0}} \tag{5.6}$$

Finally, the peak flow angularity can be estimated as given in Eq. 5.7.

$$\frac{tan(\alpha_{max})}{tan(\alpha_{max,0})} = \sqrt{\frac{w_{c,0}}{w_c}} \tag{5.7}$$

The expressions given in Eqs. 5.3 to 5.7 can be utilised to evaluate the measured vortex intensification levels. It will also be possible to assess of the suitability of vortex filament theory to capture the flow physics of the vortex inside the streamtube contraction. The comparison between the measurements and the vortex filament model has been conducted using the vortex core radius ($r_c/r_{c,0}$), peak tangential velocity ($V_{\theta,max}/V_{\theta,max}$), peak streamwise vorticity ($\omega_{z,max}/\omega_{z,max,0}$), core average streamwise vorticity ($\omega_{z,av}/\omega_{z,av,0}$), and peak flow angularity ($tan(\alpha_{max})/tan(\alpha_{max,0})$).

In agreement with the trends observed in the streamwise velocity profiles (Figure 5.2(b)), the streamwise velocity at the vortex centre ($w_c/w_{c,0}$) increases notably as the vortex approaches the intake highlight plane, Figure 5.4(a). At $z/D_i = 0.20$, the streamwise velocity reaches a value of $2.7w_{c,0}$. Note that the maximum velocity magnitude measured in this configuration is $56.1ms^{-1}$, which corresponds to a Mach number of 0.16. Therefore, it can be concluded that the effects of compressibility are be negligible.

The change in the vortex core radius ($r_c/r_{c,0}$), Figure 5.4(b), is in good agreement with the values which have been estimated from the vortex filament theory (Eq. 5.3), and the differences between the model results and the measurements are smaller than the experimental uncertainty. The change in peak tangential velocity ($V_{\theta,max}/V_{\theta,max,0}$) for $w_c/w_{c,0} < 2.0$ is close to the vortex intensification results from the vortex filament model (Figure 5.4(c)). When the contraction levels are greater than 2.0, the measured peak tangential velocity values begin to deviate from those estimated by the vortex filament model. The change in peak streamwise vorticity ($\omega_{z,max}/\omega_{z,max,0}$) and core average vorticity ($\omega_{z,av}/\omega_{z,av,0}$), however, are consistently lower than the results which have been

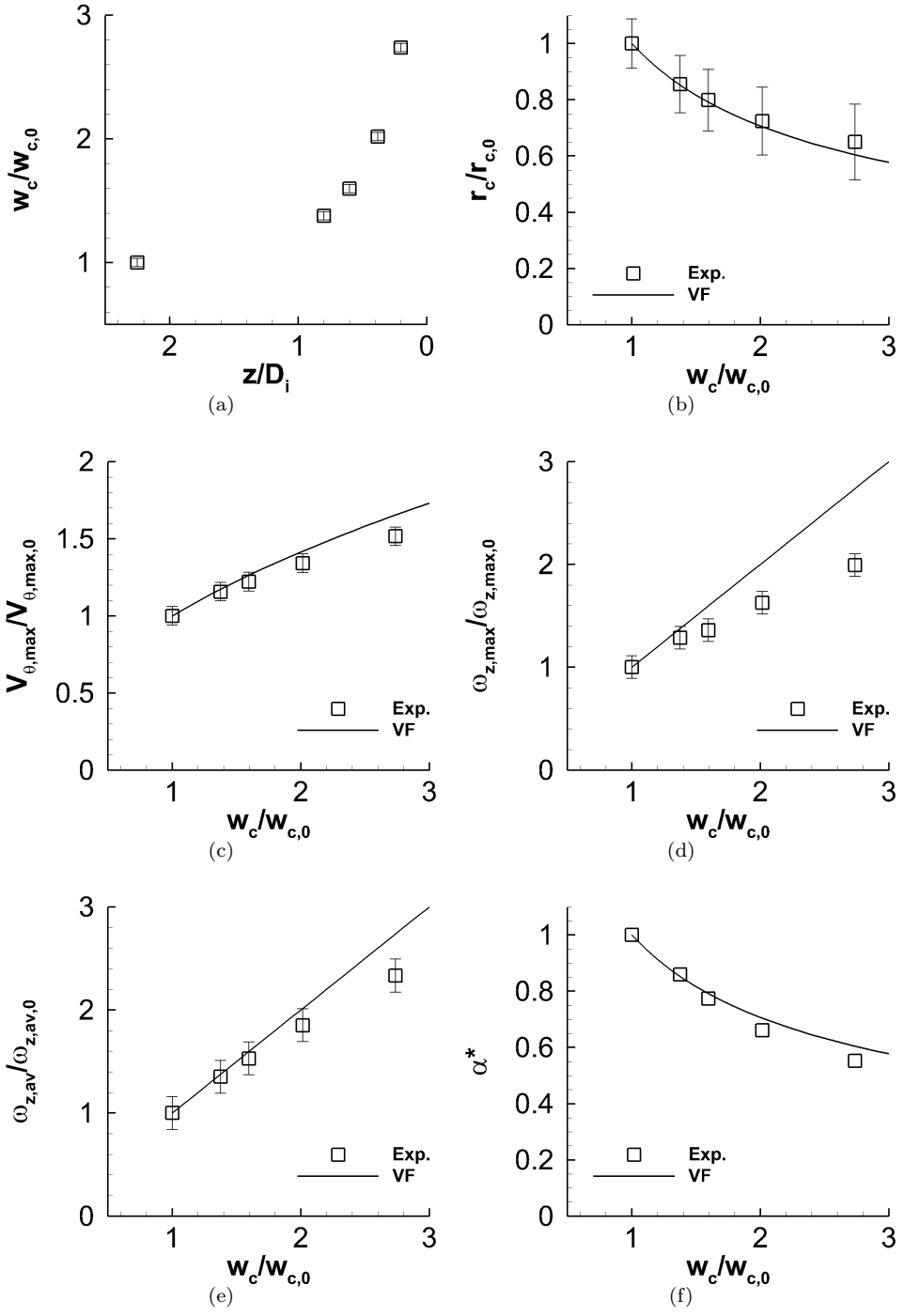

FIGURE 5.4: Change in vortex characteristics during centreline ingestion, NACA 0012 vortex generator, $Re_c = 1.7 \times 10^5$, $Re_v = 3.7 \times 10^4$, VR=5.1, (a): Streamwise velocity at vortex centre ($w_c/w_{c,0}$), (b): Core radius ($r_/r_{c,0}$), (c): Peak tangential velocity ($V_{\theta,max}/V_{\theta,max,0}$), (d): Peak streamwise vorticity ($\omega_{z,max}/\omega_{z,max,0}$), (e): Average core streamwise vorticity ($\omega_{z,av}/\omega_{z,av,0}$), (f): Peak flow angle ($\alpha^* = tan(\alpha_{max})/tan(\alpha_{max,0})$). Note that VF corresponds to vortex filament theory (Eqs. 5.3 to 5.7)

obtained from the vortex filament model (Figures 5.4(d) and 5.4(e)). Finally, in a manner similar to the core radius and peak tangential velocity measurements, the peak flow angles (Figure 5.4(f)) are in good agreement with the vortex filament theory for $(w_c/w_{c,0})$ of less than 2.0. At higher contraction levels, the measured peak flow angles are somewhat lower than theory. This is a consequence of the aforementioned peak tangential velocity levels, which are lower than anticipated from vortex filament theory.

Further insight into the behaviour of the vortex characteristics in Figures 5.4(b) to 5.4(e) can be provided with reference to the change in the vortex core circulation $(\Gamma_c/\Gamma_{c,0})$, Figure 5.5. In particular, the vortex core circulation remains constant during the intensification process, to within experimental uncertainty. Therefore, the destruction, or dissipation, of vorticity inside the vortex core is negligible. The Lamb-Oseen model demonstrates the behaviour of a vortex where the core circulation is constant, but vorticity diffusion takes place as a result of viscosity. It was shown in section 2.3 that the diffusion is characterised by an increase in the vortex core radius, coupled with reductions in the peak tangential velocity and peak streamwise vorticity. Importantly, the change in vorticity is notably larger than the changes in the core radius and peak tangential velocity, since the diffusion effects are greatest in the regions where the velocity gradients are largest [16]. This knowledge can be used to aid the interpretation of the evolution of the vortex characteristics which has been observed in Figures 5.4(b) to 5.4(e). The peak streamwise vorticity does not increase to the levels which are anticipated from vortex filament theory. Thus, vorticity at the vortex centre is subject to notable diffusion levels, which act in opposition to the vortex intensification process. This effect of viscosity is consistent with the vorticity equation (Eq. 2.23), which indicates that the diffusion caused by viscosity acts in opposition to the vorticity intensification process. The average vorticity in the vortex core (Figure 5.4(e)) also illustrates behaviour which is consistent with vorticity diffusion, although the effects are less pronounced than that observed at the vortex centre. Therefore, it can be concluded that the effects of vorticity diffusion are not uniform throughout the vortex core. Instead, the impact of diffusion is greatest at the vortex centre, and has a reduced influence at greater radii inside the vortex. This also explains why the change in vortex core radius and peak tangential velocity (Figures 5.4(b) and 5.4(c)) are in good agreement with the inviscid model. It should be reminded that the measurements of the streamwise vortex prior to the streamtube contraction (sections 4.3.4 and 4.3.4) found that there are notable levels of velocity unsteadiness inside the vortex core. Turbulent diffusion is known to accelerate the diffusion of vorticity inside vortex cores [50], so it can be concluded that turbulent diffusion may also contribute to the differences between the measurements and the vortex filament model. These turbulent diffusion levels are

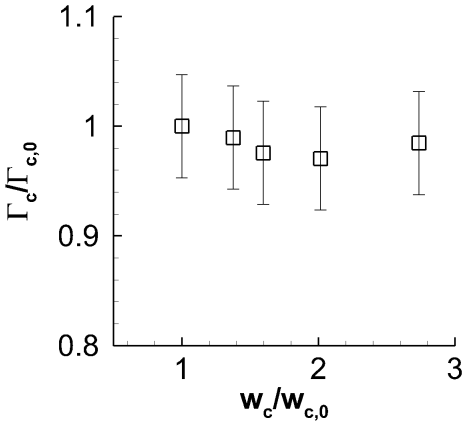

FIGURE 5.5: Change in vortex core circulation ($\Gamma_c/\Gamma_{c,0}$) as a function of change in streamwise velocity at vortex centre ($w_c/w_{c,0}$), NACA 0012 vortex generator, $Re_c = 1.7 \times 10^5$, $Re_v = 3.7 \times 10^4$

known to be a function of the vortex Reynolds number [50, 51]. Furthermore, the details of the streamwise velocity perturbation have an influence on the turbulence levels inside the vortex [46, 23]. Consequently, it is anticipated that the differences between the vortex filament model and the measured vortex characteristics will depend on the initial characteristics of the vortex, prior to the streamtube contraction.

5.1.4 Unsteadiness measurements

Previous wing-tip vortex measurements have demonstrated that the turbulent diffusion can dramatically increase the growth rates experienced by a vortex in a uniform streamwise flow [21, 54, 50]. The wing-tip vortices investigated in this research feature notable levels of turbulent fluctuations inside the vortex core (sections 4.2 and 4.3.4). Therefore, it is of interest to identify the unsteady nature of the vortex characteristics and the velocity field during the vortex intensification process. Note that the unsteadiness characteristics have been obtained using the conditional-averaging approach (section 3.6.2). Therefore, the effects of wandering have been removed, and the measurements contain the unsteadiness in the velocity field for a reference frame whose origin is located at the vortex centre.

During vortex intensification, the unsteadiness associated with the vortex core radius (Figure 5.6(a)) and the vortex location (Figures 5.6(d) and 5.6(e)) is damped. This is a direct result of the flow contraction, which appears to have a stabilising effect on the unsteadiness of the in-plane spatial characteristics. However, the unsteadiness associated with

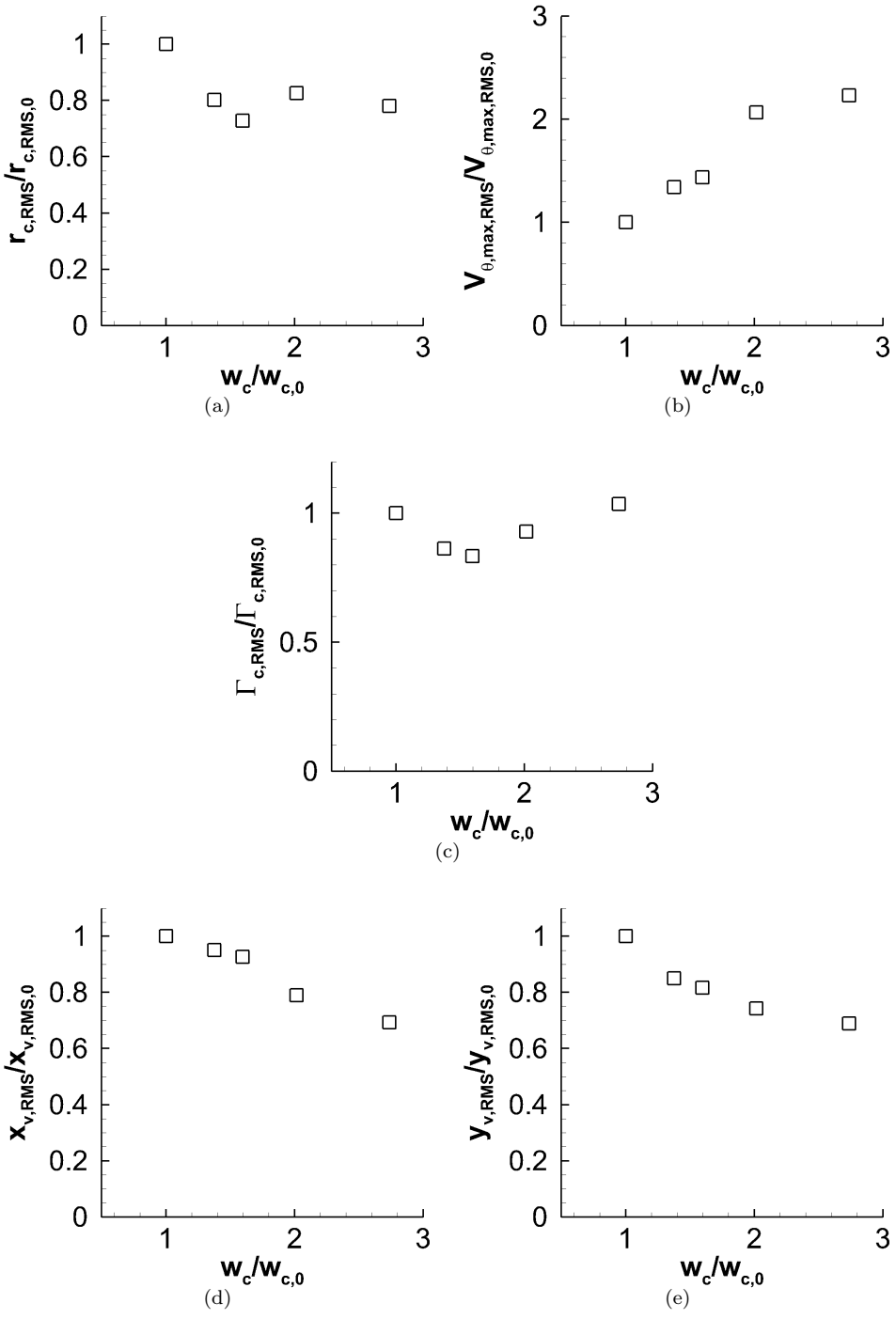

FIGURE 5.6: Unsteadiness of vortex characteristics during centreline ingestion as a function of contraction levels $w_c/w_{c,0}$, NACA 0012 vortex generator, $Re_c = 1.7 \times 10^5$, $Re_v = 3.7{\times}10^4$, VR=5.1, (a): Core radius ($r_{c,RMS}/r_{c,RMS,0}$), (b): Peak tangential velocity ($V_{\theta,RMS}/V_{\theta,RMS,0}$), (c): Core circulation ($\Gamma_{c,RMS}/\Gamma_{c,RMS,0}$), (d): Vortex core horizontal location ($x_{v,RMS}/x_{v,RMS,0}$), (e): Vortex core vertical location ($y_{v,RMS}/y_{v,RMS,0}$)

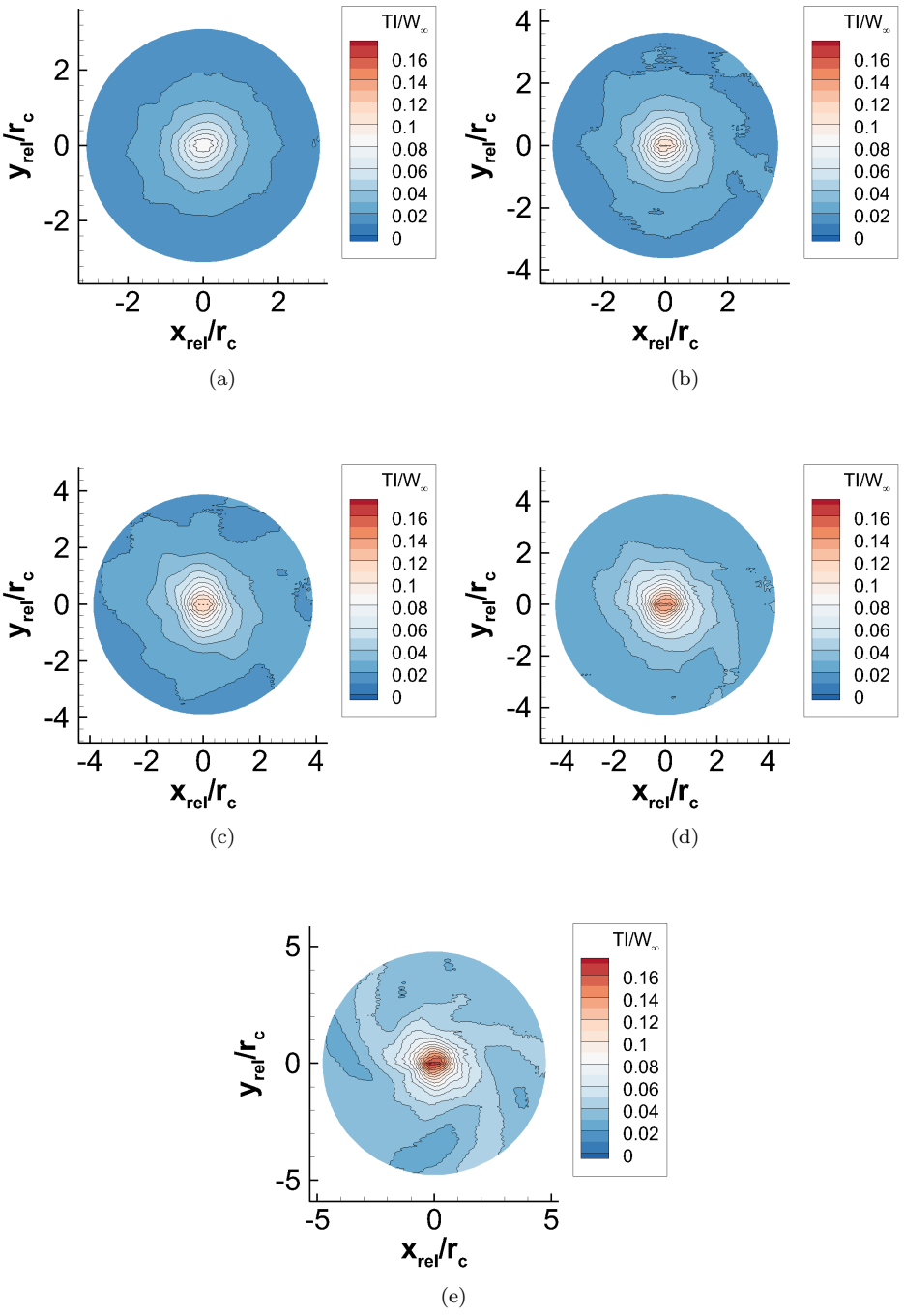

FIGURE 5.7: Turbulence intensity contours (TI/W_∞), NACA 0012 vortex generator, $Re_c = 1.7 \times 10^5$, $Re_v = 3.7 \times 10^4$, VR=5.1, as a function of distance from the intake highlight plane, (a): $z/D_i = 2.25$, (b): $z/D_i = 0.80$, (c): $z/D_i = 0.60$, (d): $z/D_i = 0.38$, (e): $z/D_i = 0.20$

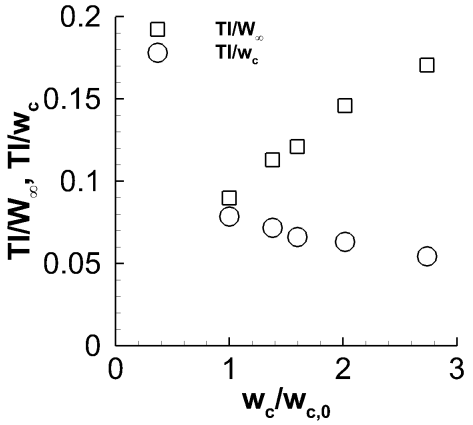

FIGURE 5.8: Turbulence intensity at vortex centre (TI/W_∞) and (TI/w_c) as a function of local streamtube contraction levels, NACA 0012 vortex generator, $Re_c = 1.7 \times 10^5$, $Re_v = 3.7 \times 10^4$, VR=5.1

the peak tangential velocity (Figure 5.6(b)) and the core circulation (Figure 5.6(c)) grows during the intensification process. The fact that the peak tangential velocity unsteadiness increases is an indication that the unsteadiness associated with the vortex velocity field also rises. This is confirmed in the contours of turbulence intensity (TI/W_∞), Figures 5.7(a) to 5.7(e). The peak turbulence intensity is located at the vortex centre throughout the intensification process, and increases steadily from a value of $0.09W_\infty$ at $z/D_i = 2.25$ to $0.17W_\infty$ at $z/D_i = 0.20$ (Figure 5.8). This result demonstrates that, like the mean velocities, the mean unsteadiness of the flow also rises during intensification. When normalised by the local streamwise velocity at the vortex centre, it is apparent that the velocity fluctuations are damped relative to the surrounding flow (Figure 5.8). However, the unsteadiness levels clearly suggest that the vortex core remains a highly turbulent region during intensification, and thus it is likely that turbulent diffusion may play an important role in defining the evolution of the vortex characteristics.

5.1.5 Summary

The measurements at a single vortex ingestion configuration have highlighted a number of important features pertaining to the intake capture streamtube flow and the vortex evolution. The intake capture streamtube is characterised by an intense streamwise contraction, which takes place over a distance of approximately one intake diameter upstream of the highlight plane. Further upstream of the intake, the effect of the streamtube contraction is negligible.

Measurements of a streamwise vortex which was ingested along the intake centreline have demonstrated that the vortex experiences notable levels of vortex intensification due to the streamtube contraction. The intensification process results in a reduction of the vortex core radius, with a corresponding rise in the vortex peak tangential velocity, peak streamwise vorticity, and core average vorticity. As anticipated from fundamental theory (section 5.1.3), the peak flow angularity is damped during the contraction process. This is a promising result with regards to the inlet flow distortion levels which result from vortex ingestion.

Vortex filament theory was employed to obtain an estimate of the theoretical vortex intensification levels for the measured streamtube contraction levels. It was found that, at low contraction levels, the measured vortex intensification levels were in good agreement with the inviscid, incompressible vortex filament theory. When the streamtube contraction levels increase, however, the vortex characteristics deviate from those anticipated from theory. In particular, the measured vortex has a greater core radius, with comparatively lower peak tangential velocity, peak streamwise vorticity, core streamwise vorticity, and peak flow angles. It has been suggested that viscous and turbulent diffusion may play an important role during vortex intensification, and may be the source of the differences between fundamental theory and the measurements. The likeliness of turbulent diffusion is supported by the notable levels of velocity fluctuations measured inside the vortex core prior to, and during, vortex intensification.

5.2 Effect of principal parameters

The analysis of a single vortex ingestion configuration has identified a number of key research questions which must be addressed. Firstly, it has been found that the vortex intensification levels observed in the experimental data are in good agreement with fundamental filament theory for low contraction levels. It is hypothesised that the effects of laminar and turbulent diffusion may become increasingly apparent when the contraction levels are further increased. Therefore, it is of interest to evaluate the impact of a change in the streamtube contraction levels. This aspect is investigated in section 5.2.1. Secondly, the results indicate that the vortex core is a turbulent region and, as such, turbulent diffusion may be of importance. Wing-tip vortex studies have suggested that the turbulent diffusion levels increase with the vortex Reynolds number [42, 50]. Therefore, it is necessary to identify if a change in the vortex Reynolds number has an impact the vortex intensification process. In a similar light, it is possible that the vortex intensification

process is dependent on other details of the unperturbed vortex. This will investigated using the measurements with the delta wing vortex. Finally, the current measurements have shown that the contraction levels at a given streamwise plane are not uniform across the streamtube cross-section. This may have an influence on the evolution of the vortex as it passes through the streamtube contraction, and has been investigated in the final part of this section.

5.2.1 Streamtube contraction levels

To determine the impact of the streamtube contraction levels on the evolution of the vortex inside the intake capture streamtube, the intake velocity ratio (VR) has been varied using the intake mass flow at a constant freestream velocity (section 3.5). Three intake velocity ratios (VR=2.0, 5.1 and 10.3) have been considered for a freestream velocity of $17.2ms^{-1}$. The NACA 0012 vortex generator was employed at an angle of attack of 12^o to create a streamwise vortex which was positioned at the intake centreline. At these conditions, the chord Reynolds number was 1.7×10^5, and the vortex Reynolds number was 3.7×10^4 (Table A.1). Note that the unperturbed streamwise vortex characteristics were therefore fixed during these measurements, since only the intake flow conditions were varied to produce the change in streamtube contraction levels.

As expected, the streamwise velocity ratio at the vortex centre ($w_c/w_{c,0}$) is strongly dependent on the intake velocity ratio, Figure 5.9(a). At a given distance upstream of the intake highlight plane (z/D_i), the value of $w_c/w_{c,0}$ increases in proportion to the intake velocity ratio. This is simply a result of the increased contraction levels inside the capture streamtube. For an intake velocity ratio of 10.3, the streamwise velocity ratio at $z/D_i = 0.20$ reaches a value of 4.1. The velocity magnitude at this measurement plane reaches approximately $93ms^{-1}$. This corresponds to a Mach number of 0.27, which indicates that the effect of compressibility is likely to be small for the conditions considered.

The measured vortex characteristics (Figures 5.9(b) to 5.9(f)) suggest that the vortex experiences notable levels of vortex intensification in response to the flow contraction. This is consistent with the results presented in the preceding section. It is interesting to note that the vortex characteristics in Figures 5.9(b) to 5.9(f), which have been measured for streamtube contractions of VR=2.0, 5.1 and 10.3, follow a single curve as a function of ($w_c/w_{c,0}$). This result is perhaps not anticipated, since the strain rates at a particular value of z/D_i depend on the intake velocity ratio. For example, in Figure 5.9(a), the strain rate $\Delta w_c/\Delta z$ is notably larger for VR=10.3 when compared to VR=2.0. Therefore, for a

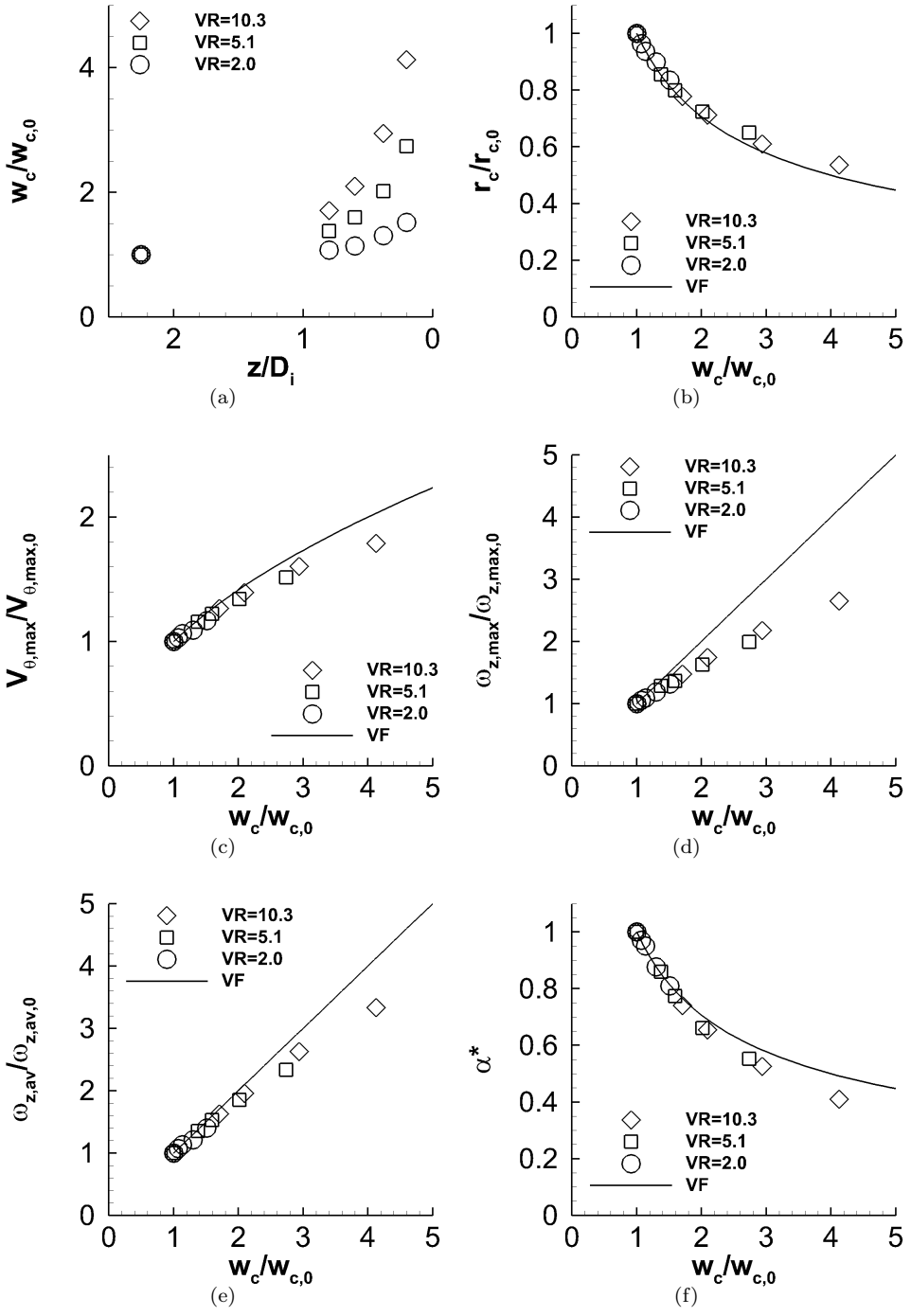

FIGURE 5.9: Vortex characteristics during centreline ingestion, NACA 0012 vortex generator, $Re_c = 1.7 \times 10^5$, $Re_v = 3.7 \times 10^4$, as a function of intake velocity ratio (VR), (a): Streamwise velocity at vortex centre ($w_c/w_{c,0}$), (b): Core radius ($r_/r_{c,0}$), (c): Peak tangential velocity ($V_{\theta,max}/V_{\theta,max,0}$), (d): Peak streamwise vorticity ($\omega_{z,max}/\omega_{z,max,0}$), (e): Average core streamwise vorticity ($\omega_{z,av}/\omega_{z,av,0}$), (f): Peak flow angle ($\alpha^* = tan(\alpha_{max})/tan(\alpha_{max,0})$). Note that VF corresponds to vortex filament theory (Eqs. 5.3 to 5.7)

given unperturbed vortex ingested along the intake centreline, it appears that the vortex intensification levels are strongly dependent on the total streamwise strain ($w_c/w_{c,0}$), rather than the particular details of the streamwise strain rate distribution.

The peak flow angles (Figure 5.9(f)) are inversely proportional to the local streamtube contraction levels for a wide range of intake velocity ratios. This is an important result in terms of the potential inlet flow distortion levels which result from the ingestion of a vortex. In particular, this result demonstrates that the peak flow angles inside an intake are likely to be smallest during high velocity ratio conditions, since $w_c/w_{c,0}$ will also be large. If the intake velocity ratio is reduced, then the peak flow angles will increase. Therefore, for a given unperturbed vortex, the risk of a loss of engine performance due to the ingestion of a vortex is likely to be greatest where the intake velocity ratio is low. An example of such a condition is during the rotation and climb-out phases of flight.

The vortex measurements for an intake velocity ratio of 5.0 (section 5.1) indicated that the measured levels of vortex intensification were in good agreement with vortex filament theory where $w_c/w_{c,0}$ was less than 2.0. At higher contraction levels, the measurements began to deviate from theory, and suggested that the vortex had undergone lower levels of intensification than was anticipated from theory. This trend is also observed across the range of intake velocity ratios investigated in Figures 5.9(b) to 5.9(f). For example, at $w_c/w_{c,0} = 2.0$, the changes in the vortex core radius and peak tangential velocity are 3% higher and 4% lower than anticipated from vortex filament theory. In addition, the increase in peak streamwise vorticity obtained from the measurements is 12% smaller than the vortex filament result. Such differences are small, and close to measurement uncertainty. When the contraction levels further increase, there is a corresponding rise in the differences between the measurements and vortex filament theory. These differences are of a similar magnitude for the vortex core radius, peak tangential velocity, and peak flow angularity (Figures 5.9(b), 5.9(c) and 5.9(f)). It is interesting to note that the average streamwise vorticity (Figure 5.9(e)) is in closer agreement with the theory than the peak streamwise vorticity (Figure 5.9(d)), which demonstrates that the levels of vorticity intensification at the vortex centre are lower than that which has been experienced on average throughout the vortex core. This is a result of the effects of vorticity diffusion. At the vortex centre, the vorticity levels and velocity gradients are at the maximum in the vortex flowfield, and so the intensity of vorticity diffusion is expected to be large. At the core radius, the vorticity levels are notably lower (for example, as demonstrated in Figure 5.2(e)), so the diffusion of vorticity is less intense. Consequently, it can be concluded that the intensity of vorticity diffusion is a function of radius, and is strongest at the vortex centreline axis. On average across the vortex core, however, diffusion has a smaller effect

on the intensification process, and so parameters which have been calculated at the vortex core radius are in good agreement with the inviscid vortex filament theory.

The vortex measurements at a range of intake velocity ratios have shown that vortex ingestion along the intake centreline is characterised by inviscid, incompressible vortex intensification where the local streamwise contraction levels are less than 2.0. At greater contraction levels, the measured levels of vortex intensification are lower than the levels anticipated from vortex filament theory. The behaviour is consistent with the effects of laminar and turbulent diffusion (section 2.3). In addition, there is a clear dependence on the total streamwise strain experienced by the vortex, since the difference between theory and the measurements increases monotonically with $w_c/w_{c,0}$. The measurements indicate that the peak flow angles are damped by the streamtube contraction, with an additional damping due to diffusion. Therefore, for a given unperturbed vortex, the peak flow angularity is inversely proportional to the intake velocity ratio. An important conclusion from this result is that the impact of a streamwise vortex on an aircraft engine is likely to be greatest if vortex ingestion occurs during low intake velocity ratio conditions, such as those experienced at the end-of-runway phase of flight.

5.2.2 Vortex Reynolds number

The literature review has highlighted that the vortex Reynolds number ($Re_v = \Gamma_c/\nu$) has a marked influence on the evolution of wing-tip vortices in uniform streamwise flows 2.3. In particular, measurements have demonstrated that an increase in the vortex Reynolds number produces a corresponding rise in the rate at which vorticity is diffused inside the vortex core. There have been no prior studies of the impact of the vortex Reynolds number on vortex intensification. This lack of understanding will be addressed in this section by means of a controlled parametric study on the vortex Reynolds number of the vortex prior to entering the streamtube contraction.

The study on the influence of the vortex Reynolds number was conducted at an intake velocity ratio of approximately 5.0 for all conditions. As detailed in section 3.5, the vortex Reynolds number was controlled using the freestream velocity and the angle of attack of the vortex generator. Using the NACA 0012 vortex generator, vortex Reynolds numbers of between 2.4×10^4 and 7.4×10^4 were obtained for an angle of attack of 12^o (Table 4.1). To better illustrate the change in unperturbed vortex characteristics, a reference vortex Reynolds number of $Re_{v,0} = 2.4 \times 10^4$ has been chosen. Therefore, the vortex Reynolds numbers which have been investigated can be expressed as $Re_{v,0}$, $1.6Re_{v,0}$ and

$3.1Re_{v,0}$, respectively. The second approach which was employed was to reduce the vortex generator angle of attack from 12^o to 6^o at a constant freestream velocity of $35.3ms^{-1}$. This produced a wing-tip vortex with a vortex Reynolds number of 3.4×10^4, or $1.4Re_{v,0}$. Importantly, using this approach, it is possible to determine the role of the vortex Reynolds number for a fixed chord Reynolds number.

The change in the streamwise velocity at the vortex centre (Figure 5.10(a)) shows only a weak dependence on the vortex Reynolds number, such that the value of $w_c/w_{c,0}$ increases by 14% when Re_v is reduced from $3.1Re_{v,0}$ to $Re_{v,0}$. The evolution of the vortex core radius and the peak flow angularity (Figures 5.10(b) and 5.10(f)) are unaffected by the change in vortex Reynolds number, meanwhile the peak tangential velocity and average core vorticity (Figures 5.10(c) and 5.10(e)) show only a small increase at a given $w_c/w_{c,0}$ when Re_v is reduced from $3.1Re_{v,0}$ to $Re_{v,0}$. However, in contrast, the peak streamwise vorticity reduces monotonically as the value of Re_v is increased (Figure 5.10(d)). In a manner similar to the trends reported in the preceding section, the measured values of $omega_{z,av}/\omega_{z,av,0}$ are in good agreement with vortex filament theory, whereas the peak vorticity values are notably lower than theory. In addition, the agreement between the measured and theoretical values of $\omega_{z,max}/\omega_{z,max,0}$ worsens as the vortex Reynolds number increases. This behaviour indicates that the rate of vorticity diffusion increases with Re_v, which reduces the measured value of $(\omega_{z,max}/\omega_{z,max,0})$ for a given $w_c/w_{c,0}$. There are two likely factors which contribute to this behaviour. Firstly, the unperturbed measurements indicated that the intensity of the velocity fluctuations inside the vortex core, prior to entering the streamtube contraction, increase with the vortex Reynolds number (section 4.3.4). Therefore, the rise in turbulent momentum transfer accelerates the rate of vorticity diffusion inside the vortex core, and the subsequent vortex intensification levels are lower than anticipated from inviscid theory. A second factor which must be considered is that the change in vortex Reynolds number also affects the value of the vortex core radius and peak streamwise vorticity prior to intensification. For example, for the case corresponding to $Re_{v,0}$, the vortex core radius is $r_c/D_i = 0.092$, and the peak streamwise vorticity is $\omega_z D_i/W_\infty = 30.3$ (Table 4.1). When the vortex Reynolds number is increased to $3.1Re_{v,0}$, the vortex core radius reduces to $r_c/D_i = 0.082$, and the peak streamwise vorticity increases to $\omega_z D_i/W_\infty = 48.8$, indicating that the vorticity levels are higher and are concentrated over a smaller region. This is reflected in a rise of the vortex core average vorticity $(\omega_{z,av})$ from 3.8 to 10.9. Therefore, as the vortex Reynolds number is increased, the intensity of vorticity diffusion inside the vortex core and prior to the flow contraction is elevated. As a result, during intensification, the strength of the diffusion process relative to the intensification process is greater, which will undoubtedly increase

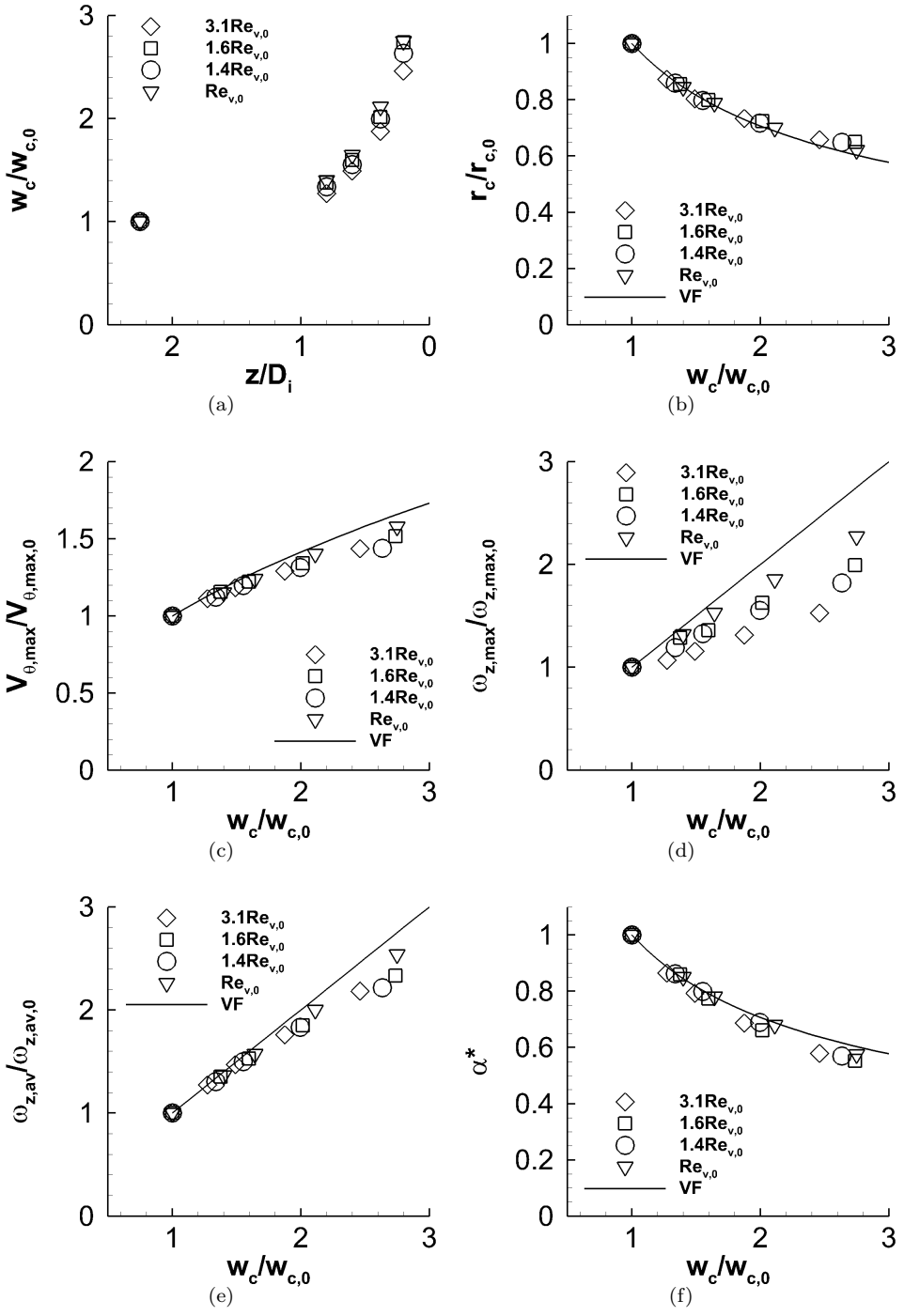

FIGURE 5.10: Vortex characteristics during centreline ingestion, NACA 0012 vortex generator, as a function of vortex Reynolds number (Re_v), where $Re_{v,0} = 2.4 \times 10^4$ (a): Streamwise velocity at vortex centre ($w_c/w_{c,0}$), (b): Core radius ($r_/r_{c,0}$), (c): Peak tangential velocity ($V_{\theta,max}/V_{\theta,max,0}$), (d): Peak streamwise vorticity ($\omega_{z,max}/\omega_{z,max,0}$), (e): Average core streamwise vorticity ($\omega_{z,av}/\omega_{z,av,0}$), (f): Peak flow angle ($\alpha^* = tan(\alpha_{max})/tan(\alpha_{max,0})$). Note that VF corresponds to vortex filament theory (Eqs. 5.3 to 5.7)

the differences between the measured vortex intensification levels and the inviscid model. Importantly, the effect of these elevated diffusion levels is most apparent at the vortex centre, and is less evident for parameters which have been measured at the core radius.

It can be concluded that, over the range of conditions investigated, the vortex Reynolds number does not have a notable effect on the evolution of the vortex core radius, peak tangential velocity or peak flow angle during intensification, and all three parameters are in close agreement with vortex filament theory. However, the results indicate that the vorticity inside the vortex core is subject to increased diffusion rates when the vortex Reynolds number is increased. This is thought to be a result of a rise in the vortex flow turbulence levels prior to the contraction, as well as an increase in the average core vorticity.

5.2.3 Vortex type

In the preceding sections, the intensification process was investigated for wing-tip vortices generated by the NACA 0012 vortex generator. As outlined in section 4.3, the streamwise vortex created by the delta wing vortex generator has notably different features from the NACA 0012 wing-tip vortices. The purpose of this section is to determine if these features have an impact on the vortex intensification process.

There is a notable variation in the streamwise velocity at the vortex centre (Figure 5.11(a)) between the different vortex types. For example, at an angle of attack of 12^o and a freestream velocity of $35.4ms^{-1}$, the NACA 0012 wing-tip vortex attains a value of $w_c/w_{c,0}$ of 2.46 at $z/D_i = 0.20$. In comparison, the delta wing vortex core flow reaches a streamwise velocity $w_c/w_{c,0}$ of 3.23. This is unexpected, since the streamtube contraction levels are identical for both cases. The reason for the differences lies in the dynamics of the vortex core flow. From the Batchelor model (section 2.4.1), the sensitivity of the flow inside the vortex core to the streamtube contraction is proportional to kr_c (Figure 2.22), where $k = 2\omega_{av}/w_c$. Using the unperturbed vortex characteristics, the values of kr_c for the NACA 0012 and delta wing vortex generators at $\alpha_{vg} = 12^o$ are estimated to be 2.4 and 1.34 respectively. Thus, based on the Batchelor model, the delta wing vortex is expected develop a smaller streamwise velocity perturbation than the NACA 0012 wing-tip vortex. Instead, the reason for the differences can be explained by considering the one-dimensional Euler equation for a streamline along the vortex centre, Eq. 5.8, where ρ is the density, p is the static pressure, and z is the streamwise ordinate.

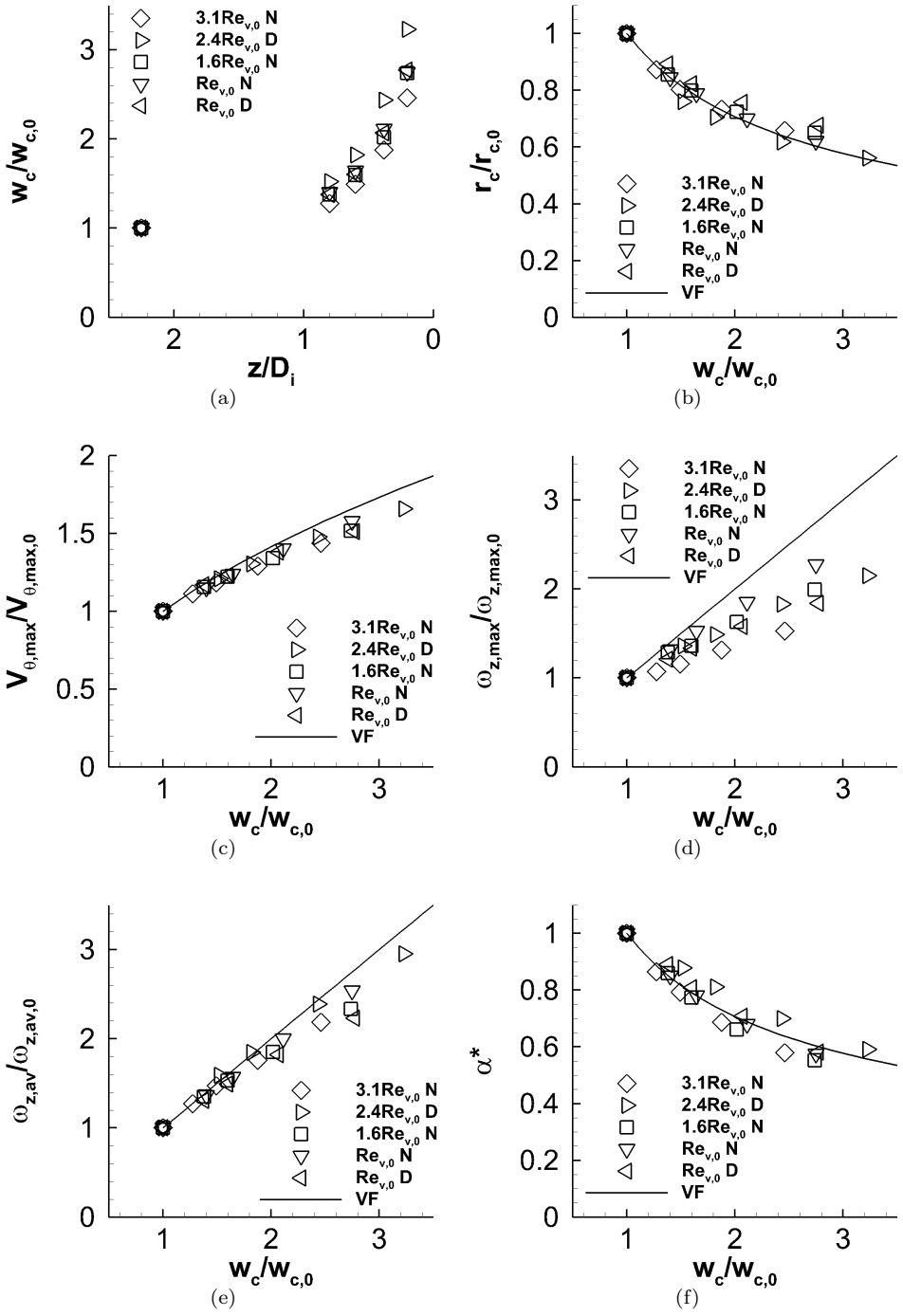

FIGURE 5.11: Vortex characteristics during centreline ingestion, NACA 0012 and delta wing vortex generators, VR=4.9, (a): Streamwise velocity at vortex centre ($w_c/w_{c,0}$), (b): Core radius ($r_/r_{c,0}$), (c): Peak tangential velocity ($V_{\theta,max}/V_{\theta,max,0}$), (d): Peak streamwise vorticity ($\omega_{z,max}/\omega_{z,max,0}$), (e): Average core streamwise vorticity ($\omega_{z,av}/\omega_{z,av,0}$), (f): Peak flow angle ($\alpha^* = tan(\alpha_{max})/tan(\alpha_{max,0})$). Note that VF corresponds to vortex filament theory (Eqs. 5.3 to 5.7). N12 and N6 refer to the NACA 0012 vortex generator at $\alpha_{vg} = 12^o$ and 6^o, respectively. D12 and D6 refer to the delta wing vortex generator at $\alpha_{vg} = 12^o$ and 6^o, respectively

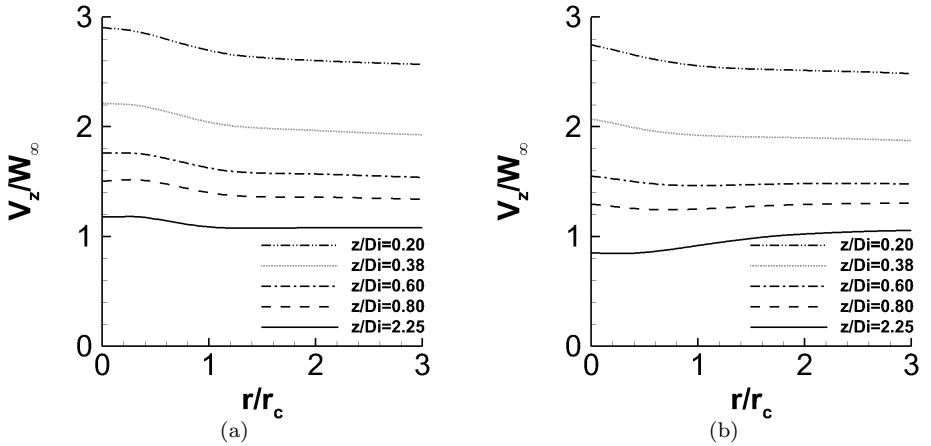

FIGURE 5.12: Circumferentially-averaged streamwise velocity profiles (V_z/W_∞) (a): NACA 0012 wing-tip vortex, $Re_c = 3.6 \times 10^5$, $Re_v = 7.4 \times 10^4$, (b): Delta wing vortex, $Re_c = 4.7 \times 10^5$, $Re_v = 5.6 \times 10^4$

$$\frac{dw_c}{dz} = -\frac{1}{\rho w_c}\frac{dp}{dz} \tag{5.8}$$

It is assumed that the flow is incompressible, and that the vortex centre is at the centre of the intake capture streamtube. At a given streamwise position z, the fluid will experience a favourable pressure gradient dp/dz due to the streamtube contraction. An important difference between the NACA 0012 and delta wing vortices is the nature of the streamwise velocity perturbation prior to the streamtube contraction (Figures 5.12(a) and 5.12(b)). The NACA 0012 wing-tip vortex features a streamwise velocity of $1.16W_\infty$, whereas the delta wing vortex features a streamwise velocity perturbation of $0.75W_\infty$. Therefore, when compared to the NACA 0012 wing-tip vortex, the value of the right hand side of Eq. 5.8 is larger for the delta wing, since the initial value of w_c is smaller. As a result, Eq. 5.8 suggests that a vortex with a streamwise velocity deficit will experience a greater increase in $w_c/w_{c,0}$ than that experienced by a vortex with a streamwise velocity excess, as observed in Figure 5.11(a). Despite the notable differences in the streamwise velocity profile evolution, the vortex core radius, peak tangential velocity, average core vorticity, and flow angularity measurements (Figures 5.11(b), 5.11(c), 5.11(e) and 5.11(f)) are similar for both the NACA 0012 and delta wing vortices. In agreement with the trends reported in sections 5.2.1 and 5.2.2, the values of $\omega_z/\omega_{z,0}$ are notably lower than the average core vorticity (Figure 5.11(d)). The maximum values of $\omega_{z,max}/\omega_{z,max,0}$ vary depending on the initial vortex characteristics, prior to entering the streamtube contraction. In the

preceding section, it was demonstrated that as the vortex Reynolds number increases, the maximum value of $\omega_z/\omega_{z,0}$ for a particular $w_c/w_{c,0}$ reduces.

However, the delta wing vortex measurements do not agree with this trend. For example, consider the measurements for the NACA 0012 and delta wing vortices which both feature a vortex Reynolds number of $Re_v = Re_{v,0}$. The maximum value of $\omega_{z,max}/\omega_{z,max,0}$ of the delta wing vortex is 39% lower than the NACA 0012 vortex with the same vortex Reynolds number. The unperturbed measurements (Table 4.1) show that the delta wing vortex has a core average vorticity which is 2.2 times that of the NACA 0012 wing-tip vortex. Therefore, the streamwise vorticity inside the delta wing vortex is concentrated over a smaller area compared to the NACA 0012 wing-tip vortex. As a consequence, prior to entering the streamtube contraction, the intensity of the vorticity diffusion process at the vortex centre is greater for the delta wing vortex. A result of this is that, inside the streamtube contraction, the intensification levels at the centre of the delta wing vortex are lower than the NACA 0012 vortex, due to elevated levels of diffusion. As detailed in sections 5.2.1 and 5.2.2, this effect is local to the centre of the vortex, and the parameters at the vortex core radius do not show the same trends. In addition, the maximum values of $\omega_{z,max}/\omega_{z,max,0}$ observed in Figure 5.11(d) are inversely proportional to the unperturbed values of average core vorticity (Table 4.1). This indicates that the average vorticity inside the vortex core is an important parameter which defines the level of diffusion which is experienced at the vortex centre during intensification.

It has been found that the evolution of the vortex core radius, peak tangential velocity, and peak flow angularity, are not affected by a change in the unperturbed vortex type. However, the streamwise vorticity characteristics depend on the characteristics of the vortex prior to intensification. It has been found that diffusive effects become increasingly apparent when the vortex average vorticity is increased. In the presence of a strong streamwise velocity deficit, the vortex core fluid experiences a greater acceleration in streamwise velocity than that experienced by the core fluid of a vortex with a streamwise velocity excess. This out-of-plane perturbation resulted in peak flow angles which were larger than anticipated by vortex filament theory.

5.2.4 Vortex ingestion trajectory

In section 5.1.1, it was shown that the intake capture streamtube velocity profile is not uniform. Instead, the maximum streamwise velocity is located at the centreline, and there are large in-plane velocities at the edge of the streamtube when close to the intake

highlight plane. This may have an impact on the evolution of the vortex as it passes through the streamtube contraction. To assess this effect, the position of the streamwise vortex in the upstream flow, relative to the intake centreline, was varied. To achieve this, the vortex generator was translated laterally in the working section, such that the vortex was in a position corresponding to $x/D_i = -0.70$ from the intake centreline. This was conducted using the NACA 0012 vortex generator at an angle of attack of 12^o, and chord Reynolds numbers of 1.1×10^5 and 1.7×10^5. The two freestream velocities resulted in intake velocity ratios of 16.3 and 10.3 respectively. Note that the vortex position upstream of the intake, for each of the intake velocity ratios, corresponds to a position which is 37% and 47% of the streamtube radius from the intake centreline.

The streamwise velocity ratio $w_c/w_{c,0}$, Figure 5.13(a), is consistently lower than the centreline counterparts for both intake velocity ratios. This appears to be a direct consequence of the non-uniform contraction levels which have been measured across the streamtube cross-section (Figure 5.1(a)). This feature indicates that the off-axis vortex, at a particular z/D_i, experiences locally lower streamtube contraction levels. Between $z/D_i = 0.60$ and $z/Di = 0.20$, the difference between the off-axis and centreline values of $w_c/w_{c,0}$ for VR=16.3 reduces from 24% to 11%, which indicates that the flow on the off-axis trajectory has experienced a greater strain rate over this region upstream of the intake. Note that the values of $w_c/w_{c,0}$ for the centreline and off-axis measurements are expected to reach approximately the same value inside the intake, since the intake velocity ratio is the same for both cases. An important aspect which must be determined, therefore, is if the vortex intensification process is affected by the differing strain rates.

All measured vortex characteristics (Figures 5.13(b) to 5.13(f)) show that there is little dependence on the vortex trajectory when the streamwise velocity ratio $w_c/w_{c,0}$ is less than 3.0. However, at greater contraction levels, the vortex intensification levels experienced by the vortex on the off-axis trajectory are closer to the vortex filament theory than those measured on the centreline. For example, at $z/D_i = 0.20$, the vortex ingested along the off-axis trajectory has an 11% smaller core radius, with peak values of tangential velocity and streamwise vorticity which are 18% and 30% higher than the centreline measurements. Note that the off-axis measurements in Figures 5.13(a) to 5.13(f) have not been corrected for the fact that the vortex axis is tilted relative to the measurement plane. It is estimated from the measurements that the tilt of the vortex axis does not exceed 24^o. A correction for the tilt of the vortex axis would result in off-axis vortex characteristics which are closer to the vortex filament theory. However, the magnitude of the change in vortex characteristics is likely to be small. For example, Burley et al. [100] obtained measurements of the wing-tip vortex which was produced by a four-bladed

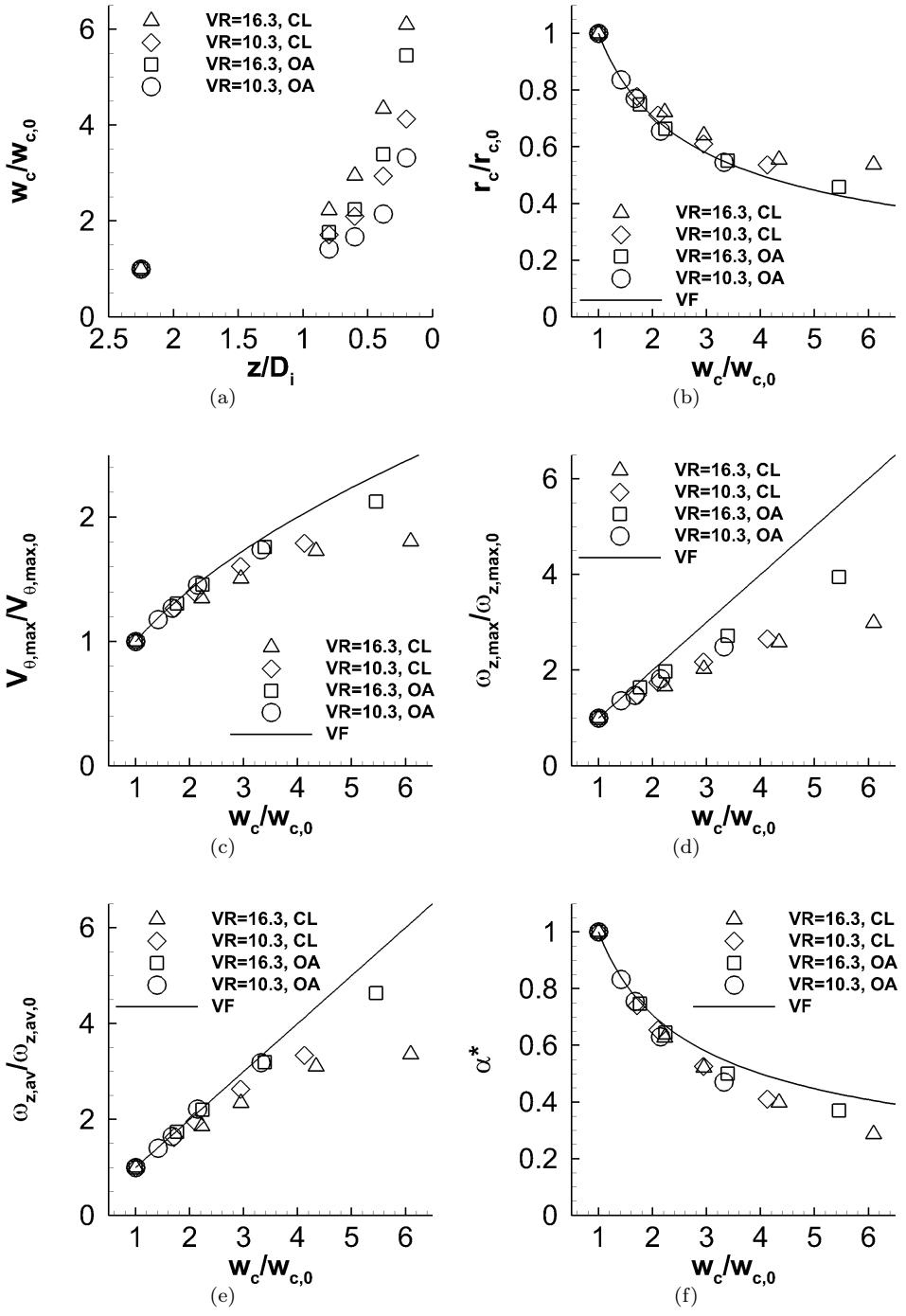

FIGURE 5.13: Vortex characteristics, NACA 0012 vortex generator, VR=5.1, for centreline (CL) and off-axis (OA) ingestion trajectories, (a): Streamwise velocity at vortex centre ($w_c/w_{c,0}$), (b): Core radius ($r_/r_{c,0}$), (c): Peak tangential velocity ($V_{\theta,max}/V_{\theta,max,0}$), (d): Peak streamwise vorticity ($\omega_{z,max}/\omega_{z,max,0}$), (e): Average core streamwise vorticity ($\omega_{z,av}/\omega_{z,av,0}$), (f): Peak flow angle ($\alpha^* = tan(\alpha_{max})/tan(\alpha_{max,0})$). Note that VF corresponds to vortex filament theory (Eqs. 5.3 to 5.7)

helicopter rotor. The blades were of a NACA 23012 section, with a radius and a chord of 2m and 0.121m, respectively. The measurements were acquired for a chord Reynolds number of 1.76×10^6 in an open jet wind tunnel facility. It was demonstrated that a vortex axis tilt of 32^o resulted in an overestimation of the vortex core radius by 18%, and an underestimation of the peak tangential velocity of 10%. These values are close to the measurement uncertainty in the current research, and it can thus be concluded that the effect of vortex axis tilt is likely to have a negligible effect on the trends which are reported in Figures 5.13(a) to 5.13(f).

The off-axis ingestion measurements suggest that along the off-axis trajectory, the vortex has experienced greater levels of vortex intensification, and the effects of diffusion are smaller. Consider the vortex ingested along the intake centreline for VR=16.3. As the streamwise velocity ratio increases (Figure 5.13(a)), the vortex undergoes intensification, and there is a corresponding rise in the effect of diffusion which becomes increasingly apparent as the value of $w_c/w_{c,0}$ increases. However, on the off-axis trajectory, the increase in $w_c/w_{c,0}$ takes place over a far smaller distance (z/D_i). During intensification, as the vorticity levels increase, there is a corresponding rise in the rate of vorticity diffusion. It is hypothesised that the differing strain rates for the centreline and off-axis trajectories (Figure 5.13(a)) have an impact on the balance between the vorticity intensification and vorticity diffusion processes. In particular, the increase in vorticity produces a corresponding rise in the vorticity diffusion levels, which subsequently acts in opposition to further increases in vorticity due to intensification. Therefore, if flow contraction process takes place gradually, the diffusive effects will become more apparent than if the contraction is rapid.

It has been demonstrated that, at low contraction levels, the vortex trajectory inside the streamtube contraction has no effect on the vortex intensification process. However, as the contraction levels increase, the vortex ingested along an off-axis trajectory undergoes greater levels of intensification than those measured along the intake centreline, for a given streamtube contraction. Furthermore, the off-axis vortex intensification levels are closer to vortex filament theory than the centreline counterpart. It was found that the time scale associated with the flow contraction reduces with distance from the intake centreline, which appears to reduce the effect of diffusion. It can be concluded that the highest levels of flow angularity will be measured when the vortex is ingested at the edge of the intake capture streamtube, since the damping effects of diffusion are least. As a result, it can be hypothesised that the highest levels of flow angularity inside the intake will occur when a vortex is ingested along an off-axis trajectory.

5.3 Summary

This chapter has been focussed on the results from the detailed study on the behaviour of a streamwise vortex inside a contracting intake capture streamtube. As anticipated, the vortex undergoes notable levels of vortex intensification in response to the flow contraction. This is characterised by a reduction in the vortex core radius, coupled with increases in the vortex peak tangential velocity, peak streamwise vorticity, and average core vorticity. At large intake velocity ratio conditions, the peak flow angularity which is associated with the vortex is damped by the contraction. Therefore, the largest levels of flow angularity will occur at low intake velocity ratio conditions, such as those experienced during end-of-runway operations. The loss of stability and performance of the aircraft engine is likely to increase with the levels of flow angularity inside the intake flow [9], and so vortex ingestion during low velocity ratio conditions will present the greatest risk to aircraft engine operation.

An extensive parametric study was conducted to elucidate the details of the flow physics associated with vortex intensification. An inviscid vortex filament model was employed to quantitatively assess the levels of vortex intensification which have been obtained in the measurements. It was demonstrated that the evolution of the vortex characteristics which are defined at the edge of the vortex core, such as the peak tangential velocity and the peak flow angle, are in good agreement with the line vortex model for contraction levels $w_c/w_{c,0}$ of less than 2.0. However, it has been found that vorticity diffusion takes place inside the vortex core. Subsequently, the increase in vorticity inside the vortex core is less than anticipated from fundamental theory. The effects of vorticity diffusion are greatest at the vortex centre, and increase with the vortex Reynolds number and the initial vorticity levels inside the vortex, prior to the flow contraction. The dependence on the vortex Reynolds number demonstrates that turbulent diffusion offers a notable contribution to the overall vorticity diffusion levels. It has also been demonstrated that the streamwise velocity perturbation inside the vortex core has an impact on the vortex intensification process. Finally, for a given streamtube contraction, a streamwise vortex is subject to lower levels of vorticity diffusion when the vortex trajectory is some distance from the intake centreline. As a consequence, the vortex undergoes greater levels of intensification, and the corresponding peak flow angles are higher than those which are obtained when the vortex is ingested along the intake centreline. It can therefore be concluded that the off-axis ingestion scenario is one which presents the greatest risk to the stability and performance of an aircraft engine.

Chapter 6

Vortex ingestion simulations

It is of great interest to conduct studies using Computational Fluid Dynamics (CFD) to assess the nature of vortex ingestion on aircraft engines. For example, CFD can be employed to evaluate the likely airframe configurations and flight conditions which may result in the ingestion of a vortex. In addition, simulations can uncover the potential impact that such a vortex can have on the performance and operability of the intake and the engine. Furthermore, CFD simulations are not subject to the same limitations as experimental measurements, and can easily be employed to investigate a wide range of realistic geometries and configurations at full-scale Reynolds numbers. However, the results obtained from such studies can only be considered as reliable if the CFD simulations are known to capture the correct flow physics of vortices. Unfortunately, there is little prior research in the literature which identifies the correct approach to simulate vortex ingestion using CFD. To address this lack of understanding, detailed investigations have been conducted to establish a validated CFD approach for vortex ingestion studies. The studies have permitted the identification of the mesh characteristics, turbulence model, and inlet boundary conditions which are required to correctly simulate the vortical flows which are of interest for vortex ingestion studies. Thereafter, the CFD approach is validated by means of the measurements from the sub-scale vortex ingestion studies of chapter 5. Finally, the approach is extended for use at full-scale conditions which, crucially, provides a method to elucidate the impact of vortex ingestion on full-scale aircraft engines.

6.1 Modelling requirements for vortex simulations

Before details of the CFD modelling requirements for vortex ingestion can be identified, it is first necessary to consider the approach which may be taken to simulate the ingestion of an externally-generated streamwise vortex by an aircraft intake. Although there are no prior examples of such simulations in the literature at present, some important lessons can be obtained from the simulations of other intake flow configurations in which vortex ingestion takes place. Examples include ground vortices [101] and vortices generated on the fuselage in the proximity of the engine [14]. In both examples, the vortex generation process has been included in the simulations of the intake flow and, in some cases, components of the aircraft engine [14]. However, these simulations feature a number of limitations. Firstly, large computational domains are required, with a large number of mesh cells in order to correctly resolve the vortex generation and evolution processes in the external flowfield. This can force a compromise in terms of mesh resolution in critical parts of the CFD domain, such as the intake boundary layers [14], and can subsequently limit the accuracy of the results. Furthermore, in such simulations, the range of vortex characteristics and flowfield configurations is generally constrained by the fixed geometry. As an alternative, it may be possible to avoid simulating the vortex generation process, and instead to prescribe the vortex flowfield as an inlet boundary condition to a domain which contains only the intake. This approach has been favoured in this research. Importantly, the complexity and the size of the computational domain can be reduced, and it may be possible to increase the mesh resolution in other key areas, such as the intake boundary layer or components of the aircraft engine. In addition, the characteristics of the vortical distortion, such as the vortex size and strength, may be controlled parametrically using the boundary conditions to provide vital information on the sensitivity of aircraft engines to vortical distortions.

A review of the literature has demonstrated that it can be challenging to correctly capture the flow physics of vortices using CFD. For example, the results from the wing-tip vortex simulations of Egolf et al. [81] highlighted that the wing-tip vortex diffused rapidly after a short distance. This was particularly evident in the peak tangential velocity, which was approximately 40% of the value which was obtained from experimental measurements. This notable difference was attributed to numerical diffusion. A range of wing-tip vortex studies using CFD (notably [81, 82, 102, 85, 84]) have demonstrated the wing-tip vortices may be excessively diffused as a result of numerical diffusion, and that the impact of numerical diffusion is dependent on the order of accuracy of the numerical scheme the grid resolution in the vortex core, and the choice of turbulence model (section 2.5.3). This

numerical diffusion may present a notable difficulty for vortex ingestion simulations. If the vortex is subject to excessively large levels of numerical diffusion, then the correct behaviour of the vortex during ingestion will not be captured. As a consequence, the intensity of the vortical flow inside the intake, and so the inlet flow distortion levels, will be underpredicted. To simulate vortex ingestion in the correct manner, it is therefore necessary to identify CFD modelling guidelines which will minimise the numerical diffusion levels. Simulations of an isolated vortex in a freestream flow have been performed to provide a quantitative assessment of the sensitivity of the vortex evolution to the details of the mesh characteristics, turbulence model, and boundary conditions. In this section, description of the vortex convection simulations will be provided. This includes the details of the test case, the CFD domain details, the mesh characteristics, the boundary conditions, and the numerical model.

6.1.1 Test case details

The evolution of the wing-tip vortex is validated using existing wing-tip vortex measurements which are available in the literature. Wing-tip vortex measurements were acquired by Devenport et al. [1] using a similar wing geometry, at comparable conditions to the current experimental dataset as highlighted in Table 6.1.

TABLE 6.1: Comparison of vortex generation conditions considered in current research and in Devenport et al. [1]

	Current measurements	Devenport et al. [1]
VG section	NACA 0012	NACA 0012
b (m)	0.45	0.879
c (m)	0.15	0.203
$AR = b/c$	3.0	4.3
α_{vg} (^{o})	12	5
x/c	6	4
Re_c	1.1 - 3.6$\times 10^5$	5.3×10^5
Re_v	2.4 - 7.4$\times 10^4$	3.4×10^4
r_c/c	0.054-0.061	0.037
M	0.03-0.10	0.13

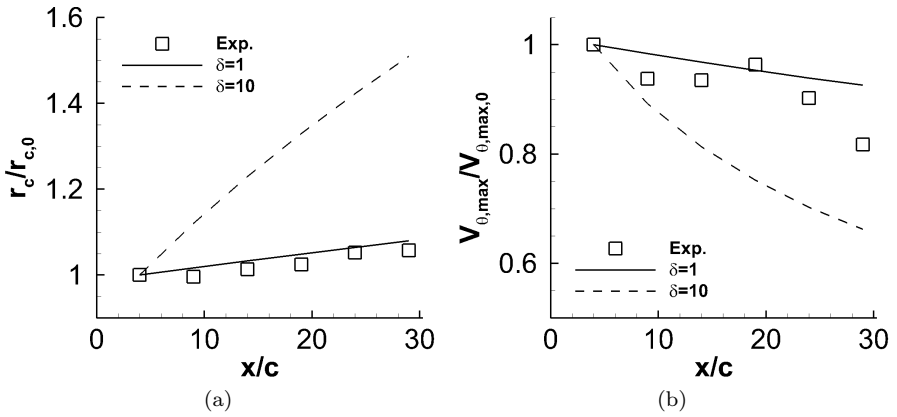

FIGURE 6.1: Experimental measurements and Squire model results for wing-tip vortex characteristics downstream of a semi-span vortex generator, as a function of x/c, (a): Vortex core radius ($r_c/r_{c,0}$), (b) Vortex peak tangential velocity ($V_{\theta,max}/V_{\theta,max0}$)

Note the similarities in the vortex Reynolds numbers. At this value of Re_v, the vortex diffusion rates will be characterised by an apparent diffusion coefficient, δ, (section 2.3) with a value of between 1 and 10 (Figure 2.17). The measured vortex core radius features a growth rate which is very close to the laminar growth rate given by the Squire model with $\delta = 1$, Figure 6.1(a), and the evolution of the peak tangential velocity lies between $\delta = 1$ and $\delta = 10$ (Figure 6.1(b)). Therefore, the experimental measurements are consistent with the trends which have been reported in the literature [50], and so it can be concluded that the test case is suitable as a means to establish CFD guidelines.

The measurements from the Devenport test case which have been employed to generate the inlet boundary conditions have been acquired at $x/c = 4$ downstream of the wing trailing edge, which is two chord lengths closer to the trailing edge of the wing than the current experimental measurements (Table 6.1). However, the characteristics of the vortex perturbation field are expected to be similar for both cases, since the measurements have both been acquired in the near field of the wing, where the vortex roll-up process is well underway (section 2.2. Note that the measurements in the Devenport test case were acquired in a Cartesian axis system where the x-axis corresponds to the streamwise axis. In the current research, the z-axis has been employed as the streamwise axis. The Devenport test case simulations thus employ the x-axis as the streamwise axis.

6.1.2 CFD methods

6.1.2.1 Mesh characteristics

Prior studies [82, 81, 83] have demonstrated that the in-plane and out-of-plane mesh resolutions inside the vortex core have a strong effect on the evolution of the vortex. Therefore, it is desirable to establish a meshing approach which permits a controlled parametric study on the mesh resolution inside the vortex core. The simulation consists of an isolated vortex whose axis is aligned with the streamwise direction. Therefore, a suitable approach is to generate a CFD domain which places the vortex at the streamwise centreline axis of the domain. A Cartesian mesh has been generated using ICEM 12.1, and features symmetry boundaries which are parallel to the streamwise direction and at a suitable distance from the vortex centre (Figure 6.2(a)). The domain is completed with inlet and outlet boundaries which are perpendicular to the flow direction. A length of $100r_c$ from the vortex centreline to the symmetry boundary was employed. This is expected to be sufficiently large to avoid potential interactions between the vortex and boundaries. For example, Ragab and Sreedhar [46] found that a distance of $30r_c$ from the vortex centreline to the domain boundaries is sufficient. The extent of the CFD domain in the streamwise direction was selected to be a length of 11.3c, where c is the wing chord length. This distance encapsulates three of the experimental measurement points in the Devenport dataset (Figure 6.1(a)). Therefore, the vortex characteristics extracted from the CFD simulations can be compared with two measurement points.

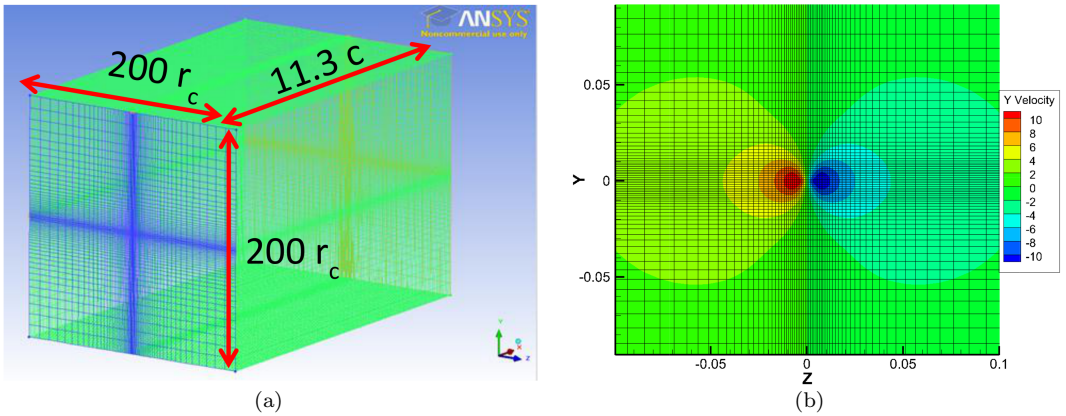

(a) (b)

FIGURE 6.2: Characteristics of mesh employed for isolated vortex convection simulations, (a): CFD domain dimensions, (b): Mesh characteristics on a plane perpendicular to the streamwise direction and vortex axis (Y-Z axis)

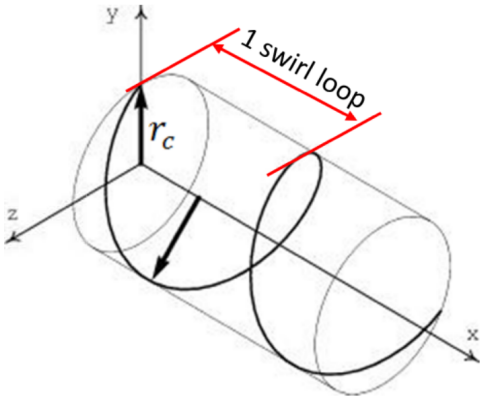

FIGURE 6.3: Definition of a swirl loop

The in-plane mesh topology features a region of constant spacing which spans the vortex core diameter in the vertical and horizontal directions, Figure 6.2(b). Note that the edge of this region corresponds to the node located at the vortex core radius. Using this approach, the number of elements in the vortex core could be controlled. Beyond the vortex core radius, the mesh element dimensions increase at an expansion ratio of 1.2. The streamwise mesh resolution was defined using the concept of a vortex swirl loop, Figure 6.3, which corresponds to the helical path taken by a particle at the vortex core radius convecting at the freestream velocity. The time taken for a single swirl loop, t_{sl}, can be approximated using the initial values of the vortex core radius ($r_{c,0}$), the peak tangential velocity ($V_{\theta,max,0}$), as given in Eq. 6.1. It is thus possible to employ the streamwise velocity (W_∞) to compute the streamwise distance which corresponds to a swirl loop, Eq. 6.2. The streamwise mesh resolution was thus defined as the number of mesh elements contained in the pitch of the vortex swirl loop.

$$t_{sl} = \frac{2\pi r_{c,0}}{V_{\theta,max,0}} \tag{6.1}$$

$$x_{sl} = W_\infty t_{sl} \tag{6.2}$$

6.1.2.2 Boundary conditions

As an alternative to simulating the vortex generation process, all vortex simulations in this research feature suitable inlet plane boundary conditions to implement the perturbation

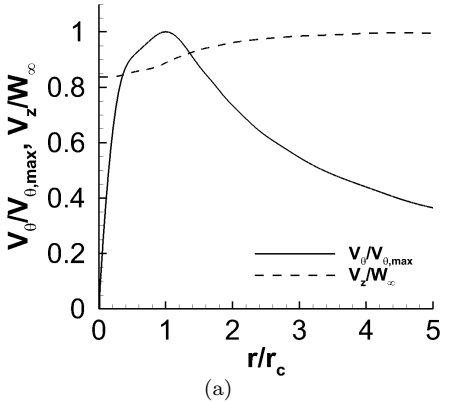

(a)

FIGURE 6.4: Tangential and streamwise velocity profiles employed to define the velocity boundary conditions at the inlet plane of the CFD domain

field of a known vortex. There are a number of approaches in which the vortex perturbation field can be obtained. Firstly, the vortex flowfield at a particular plane perpendicular to the vortex axis can be extracted from experimental measurements. Alternatively, it is possible to extract the vortex flowfield from the results of a CFD simulation which includes the vortex generation process. Another possible approach is to employ a vortex model, such as the Vatistas vortex model [103, 50], to generate the vortex velocity field. However, for this test case, the experimental measurements obtained by Devenport et al. [1] are available for use [104].

As described in section 6.1.1, the measurements at $x/c = 4$ downstream of the wing trailing edge have been employed to generate the inlet boundary conditions. Inspection of the measurements revealed that the wing-tip vortex at $x/c = 4$ is approximately axisymmetric. Thus, the circumferentially-averaged tangential and streamwise velocity profiles from this streamwise location (Figure 6.4(a)) were selected to define the inlet boundary conditions. A cubic spline interpolation approach was employed in MATLAB to interpolate the experimental grid points, with a spatial resolution of 0.0015m ($0.2r_c$), onto a grid of resolution 0.0001m ($0.013r_c$). The velocity profiles were then interpolated onto the grid nodes on the inlet plane of the CFD domain.

Note that the experimentally-measured velocity profiles extended from the vortex centre to a distance of approximately $r/r_c = 40$ from the vortex centre. The domain width and height corresponded to $100r_c$ from the vortex centre (section 6.1.2.1), and it was therefore necessary to extrapolate the velocity profiles to the edges of the CFD domain. An exponential function curve fit was employed define a continuous distribution of V_θ. The measured streamwise velocity perturbation reduced quickly with distance from the vortex

centre, such that the vortex streamwise velocity was approximately equal to the freestream velocity for radii greater than $r/r_c = 4$. Thus, a constant value of $V_z = W_\infty$ was enforced beyond the experimental data at $r/r_c = 40$. The boundary profiles were subsequently prescribed as Cartesian velocity components on the inlet boundary plane. Note that a compressible inlet boundary profile formulation was not required for this case, since the experimental measurements, and the corresponding vortex convection simulations, were conducted at a freestream flow Mach number of 0.13.

In addition to the velocity distributions, it is also necessary to prescribe details of the mean turbulent flow at the inlet boundary. However, it was noted that vortex wandering may have resulted in an over-measurement of in-plane velocity unsteadiness [1]. Therefore, it is not possible to employ the in-plane turbulence measurements with confidence to prescribe turbulence profiles as part of the inlet plane turbulence boundary conditions. However, based on a wandering correction method, it was concluded that the vortex core may contain low levels of turbulence. Therefore, it was deemed appropriate to apply uniform turbulence boundary conditions which correspond to the measured freestream turbulence intensity of $TI = 0.1\%$. This is a simplifying assumption, since wing-tip vortices often feature profiles of turbulence inside the vortex core [23, 43]. Note that the implications of this choice of turbulence boundary condition are addressed in section 6.1.3.2. To complete the definition of the turbulence boundary conditions, an eddy viscosity ratio of $\nu_t/\nu = 1.0$ was employed. This value was selected since the measurements from this test case [1] suggest that the flow at the centre of the vortex features low levels of turbulence. Note, however, that turbulent flow was reported at greater radii inside the vortex, and in the surrounding flow, so the use of a turbulent viscosity ratio of zero is not appropriate.

The domain outlet boundary consisted of a uniform static pressure outlet condition. The static pressure corresponded to the freestream static pressure of the unperturbed freestream flow. The outlet plane featured a uniform turbulence profile which consisted of a turbulence intensity of 0.1% and an eddy viscosity ratio of 1.0.

6.1.2.3 Numerical approach and convergence strategy

The vortex convection simulations were conducted using a density-based, cell-centred, implicit RANS numerical model implemented in FLUENT 12.1. The objective was to employ a commercial CFD package to provide a validated approach which can be used both for fundamental studies of vortex intensification, and for engineering studies of vortex ingestion. Therefore, a RANS-based turbulence modelling approach was favoured. A

3^{rd} order MUSCL discretisation scheme was employed in conjunction with Roe's flux difference splitting to evaluate the convective fluxes and the turbulence equations. Finally, the gradient and derivative terms were computed using a least squares approach. The solution convergence was evaluated using the scaled residuals of the equations of continuity, momentum, energy, and the relevant turbulence equations for the chosen turbulence model. All simulations featured a typical scaled residual of less than 10^{-7}. In addition, the total circulation, as calculated on the outlet plane of the CFD domain, was monitored to ensure that the streamwise vortex characteristics had also achieved convergence.

6.1.3 Results

In this section, the results of the vortex convection simulations are presented. Note that, in all simulations, the vortex characteristics have been extracted using the Vorticity Disk Method (section 3.6.2) with a circular zone radius of $r_{max}/r_c = 3$ and a spatial resolution of $0.027r_c$. Unless stated otherwise, simulations have been conducted using the $k-\omega$ SST turbulence model.

6.1.3.1 Impact of mesh resolution

Notable levels of numerical diffusion can result if the mesh resolution inside the vortex core is not sufficient (section 2.5.3). As a consequence, the evolution of the vortex will not be captured correctly in the simulations. It is therefore necessary to establish guidelines for the minimum number of mesh elements which should resolve the vortex core region. To do this, a controlled parametric study on the in-plane and streamwise mesh resolution inside the vortex core was conducted. The in-plane and out-of-plane mesh resolutions were varied independently such that their influence on the vortex convection process can be ascertained.

The in-plane mesh resolution has been characterised in terms of the number of uniformly-spaced mesh elements which define the vortex core diameter when evaluated in the x- and y-directions from the vortex centre. In-plane mesh resolutions of 4, 8, 16, 20 and 32 elements were investigated with a constant streamwise mesh resolution of 15 mesh elements per swirl loop. This streamwise resolution is confirmed to be sufficient by the studies conducted later in this section, and is further supported by Dacles-Mariani et al. [82], who employed a resolution of approximately 20 mesh elements per swirl loop for wing-tip vortex generation simulations. As detailed in section 6.1.2.2, the inlet boundary velocity profiles were interpolated to the grid nodes. This approach provided the most

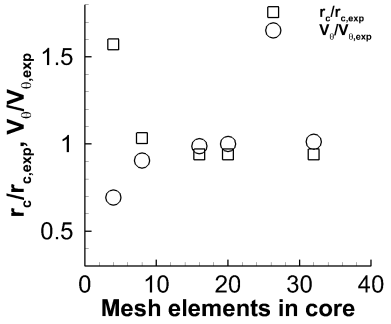

FIGURE 6.5: Influence of the in-plane mesh resolution on the vortex characteristics predicted by the CFD solver at the inlet plane of the CFD domain, $k-\omega$ SST model

consistent way of ensuring that the peak tangential velocity and core radius of the vortex, as provided to FLUENT, were constant for all mesh resolutions. The profiles were subsequently interpolated on to the inlet plane of the given vortex convection mesh using a least-squares method which is implemented in the FLUENT profile reader [105]. However, it is acknowledged that, due to the large velocity gradients which are attributed to the vortex flowfield, a cell-centred solver may not be able to establish the correct flowfield at the inlet boundary. Therefore, it was first necessary to evaluate the vortex characteristics which have been extracted from the inlet plane of the converged CFD solution. This has been achieved by evaluating the vortex core radius ($r_c/r_{c,exp}$) and the peak tangential velocity ($V_{\theta,max}/V_{\theta,max,exp}$) as a function of the in-plane mesh resolution (Figure 6.5), where subscript "exp" refers to the value which defined the inlet boundary condition profiles. When the vortex core is defined by 4 mesh elements, the vortex which is obtained at the inlet boundary features a core radius which is 57% larger and a peak tangential velocity which is 31% lower than the prescribed values. Therefore, it is apparent that the CFD solver is unable to resolve the vortex boundary conditions in a correct manner at such low mesh resolutions. As the mesh resolution is increased, the characteristics of the vortex at the inlet boundary quickly converge towards the values which were prescribed in the inlet profiles. In particular, the results (Figure 6.5) demonstrate that a minimum of 16 mesh elements are required inside the vortex core in order to capture the correct vortex core radius and peak tangential velocity to within 5% of the prescribed value.

It is anticipated that the streamwise mesh resolution has an influence on the evolution of the vortex characteristics as it convects. Therefore, the vortex characteristics, in terms of the core radius, peak tangential velocity, peak streamwise vorticity, and total circulation, (Figures 6.6(a) to 6.6(d)), have been extracted at a number of streamwise planes. Note that subscript "0" refers to the value at the inlet plane of the CFD domain. The

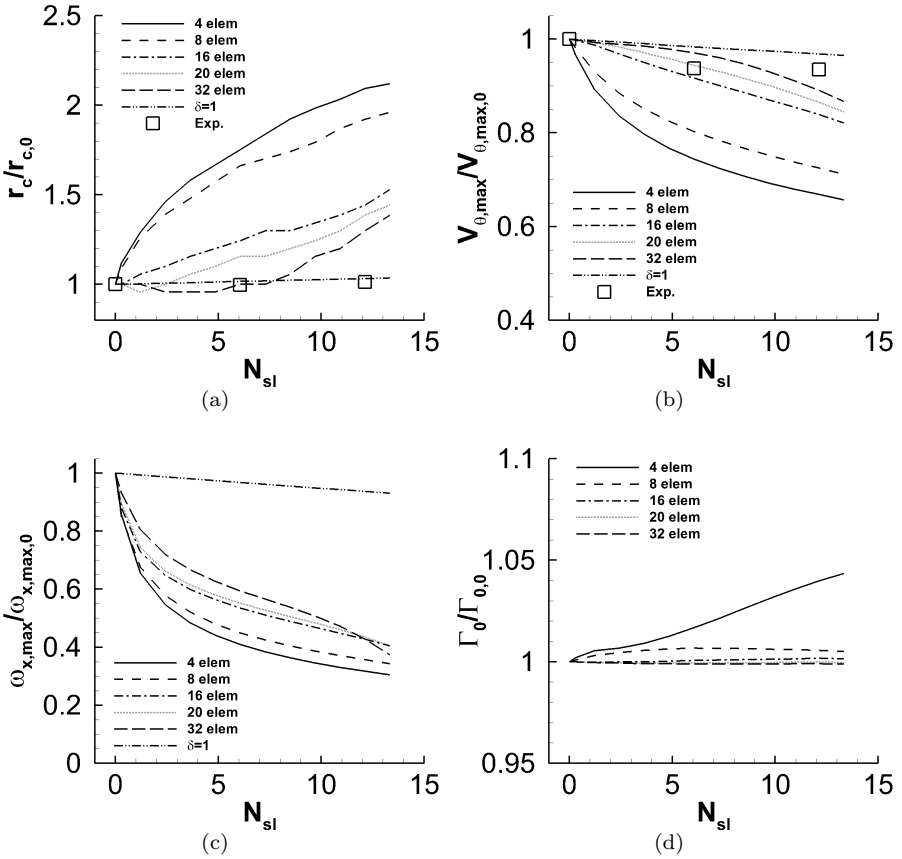

FIGURE 6.6: Evolution of vortex characteristics during convection as a function of the number of vortex swirl loops (N_{sl}), influence of the number of in-plane mesh elements employed to resolve the vortex core diameter, $k-\omega$ SST model, (a): Vortex core radius ($r_c/r_{c,0}$), (b) Vortex peak tangential velocity ($V_{\theta,max}/V_{\theta,max0}$), (c): Vortex peak streamwise vorticity ($\omega_{z,max}/\omega_{z,max0}$), (d): Vortex total circulation ($\Gamma_0/\Gamma_{0,0}$)

streamwise distance has been expressed as the number of swirl loops ($N_{sl} = t/t_{sl}$), where $t = x/W_\infty$, and t_{sl} is given in Eq. 6.1.

The vortex characteristics which have been extracted from the CFD simulations show that the vortex evolution is strongly dependent on the in-plane mesh resolution. For a mesh resolution which consists of 4 elements across the vortex core, the vortex core radius increases notably as the vortex convects (Figure 6.6(a)). For example, after approximately 12 swirl loops, the vortex core radius is 1.98 times the value prescribed at the inlet plane, which corresponds to a core radius which is 3.23 times larger than the experimental measurement. Similarly, the vortex peak tangential velocity (Figure 6.6(b)) and the peak streamwise vorticity (Figure 6.6(c)) reduce dramatically to 67% and 32% of the value at the inlet boundary. The results demonstrate that the vortex has undergone notable levels

of diffusion during convection. The intensity of the diffusion process is evidently greater than that observed in the experimental measurements of core radius (Figure 6.6(a)) and the peak tangential velocity (Figure 6.6(b)). Interestingly, the total circulation of the vortex increases as the vortex convects in the flow, Figure 6.6(d). This behaviour violates conservation of angular momentum, and demonstrates that the CFD solver cannot capture the correct flow physics for such a low mesh resolution. When the mesh resolution inside the vortex core is increased, there is a corresponding reduction in the diffusion rates. For example, when the in-plane mesh resolution is increased from 4 to 16 mesh elements, the vortex core radius reduces from 198% to 144% of the value prescribed at the inlet plane. A further increase in the mesh resolution to 32 elements results in vortex growth rates which are close to those measured in the experiments for N_{sl} of less than 6 (Figures 6.6(a) and 6.6(b)). However, over greater convection distances, the CFD simulations indicate greater levels of vortex growth than that which is observed in the experimental measurements.

It is also necessary to determine the impact of the streamwise mesh resolution on the vortex convection process. Dacles-Mariani et al. [82] stated that, for wing-tip vortex generation simulations, the in-plane mesh resolution has a stronger effect on the vortex evolution than the out-of-plane mesh resolution. It was recommended that the out-of-plane mesh resolution should be 1.35 times that of the in-plane mesh spacing, which corresponds to approximately 20 mesh elements per vortex swirl loop. However, little detail was given to the sensitivity of the vortex evolution to different out-of-plane mesh resolutions. Therefore, streamwise mesh resolutions of 5, 10, 15 and 30 elements in each vortex swirl loop were investigated. The vortex characteristics (Figures 6.7(a) to 6.7(d)) indicate that the vortex diffusion process does not behave in a monotonic fashion with changes in the streamwise mesh resolution. Instead, the vortex evolution is unchanged when the number of streamwise mesh elements is increased from 10 to 30. However, when the mesh resolution is reduced to 5 elements per swirl loop, the vortex experiences a rapid diffusion process. It is therefore apparent that, at sufficiently low streamwise mesh resolutions, the flow physics of the vortex convection process cannot be captured correctly.

The vortex convection simulations have demonstrated that, although it was not possible to obtain close agreements between the experimental measurements and the results which have been extracted from the CFD simulations, acceptable results can be obtained for an in-plane mesh resolution of 16 elements. In addition, it was demonstrated that a minimum of 10 mesh elements should be employed to resolve the streamwise distance corresponding to a single vortex swirl loop.

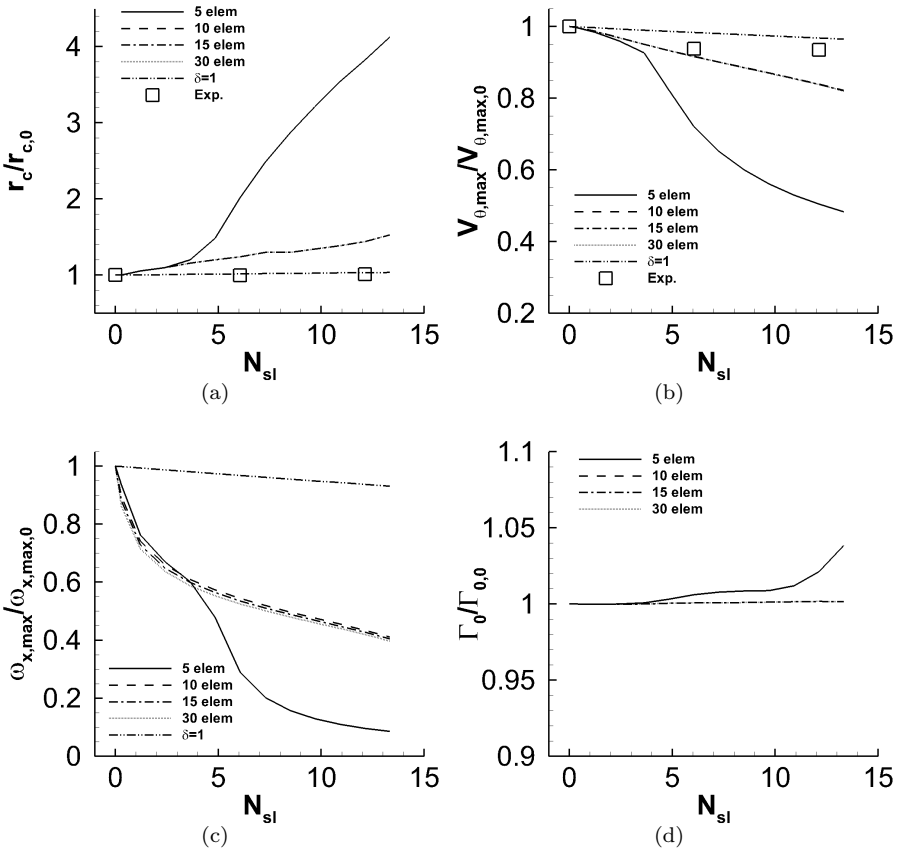

FIGURE 6.7: Evolution of vortex characteristics during convection as a function of the number of vortex swirl loops (N_{sl}), influence of the number of out-of-plane mesh elements employed to resolve the distance corresponding to one vortex swirl loop, $k-\omega$ SST model, (a): Vortex core radius ($r_c/r_{c,0}$), (b) Vortex peak tangential velocity ($V_{\theta,max}/V_{\theta,max0}$), (c): Vortex peak streamwise vorticity ($\omega_{z,max}/\omega_{z,max0}$), (d): Vortex total circulation ($\Gamma_0/\Gamma_{0,0}$)

6.1.3.2 Impact of turbulence model

A number of CFD studies of wing-tip vortex generation and evolution in the near field have demonstrated that the agreement between the simulation results and experimental measurements is strongly dependent on the choice of turbulence model [82, 81, 102, 85, 84]. A common result which has been reported in these studies is that the turbulence model can produce large levels of turbulence inside the vortex core, which results in a vortex which is more diffused that the experimental measurements suggest [82]. However, there have been few prior studies which assess the impact of turbulence modelling on wing-tip vortex convection simulations. Therefore, studies have been conducted using the Spalart-Allmaras (SA), $k-\epsilon$ and $k-\omega$ SST eddy-viscosity models which are available in FLUENT

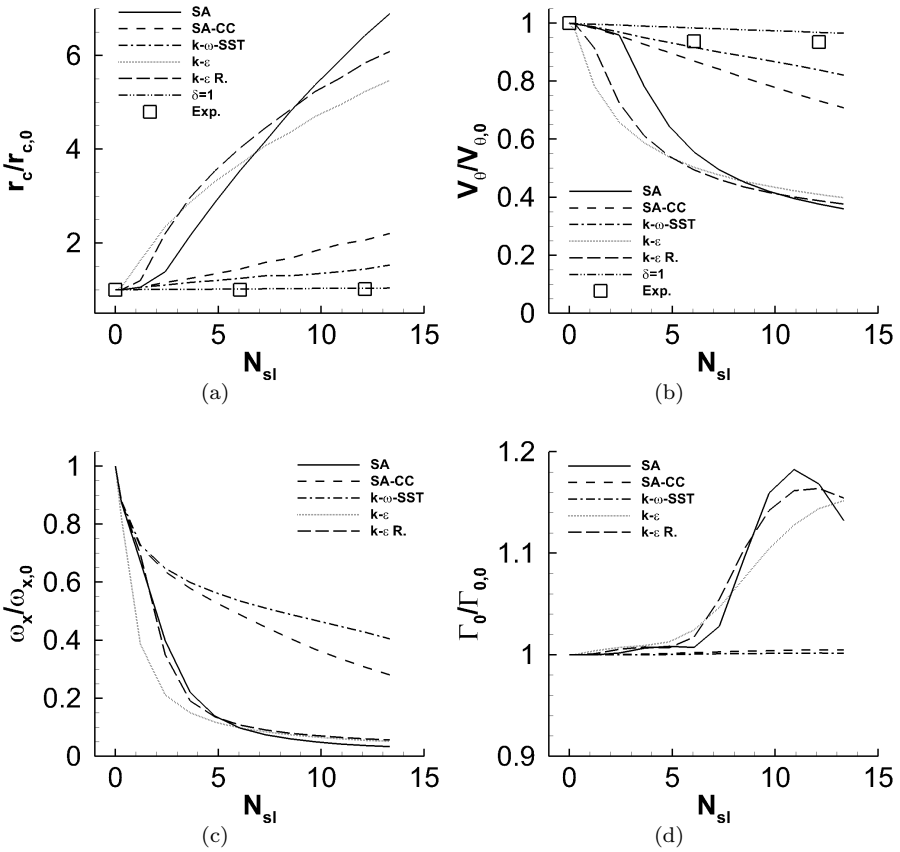

FIGURE 6.8: Evolution of vortex characteristics during convection as a function of the number of vortex swirl loops (N_{sl}), influence of the choice of eddy-viscosity turbulence model, (a): Vortex core radius ($r_c/r_{c,0}$), (b) Vortex peak tangential velocity ($V_{\theta,max}/V_{\theta,max0}$), (c): Vortex peak streamwise vorticity ($\omega_{z,max}/\omega_{z,max0}$), (d): Vortex total circulation ($\Gamma_0/\Gamma_{0,0}$)

12.1. In addition, the "modified" SA model and the Realizable $k-\epsilon$ turbulence models were also investigated. These models feature modifications to the original SA and $k-\epsilon$ turbulence models to offer improved performance for vortical flows [106]. The modified SA model is of particular interest, since the model features an ad-hoc correction to the turbulence production formulation was introduced to improve the agreement between experimental measurements and CFD results of wing-tip vortex flow [82]. It is therefore desirable to investigate if such turbulence models offer an improvement for the vortical flows of interest in this research. In all cases, in-plane and out-of-plane mesh resolutions of 16 and 15 mesh elements, respectively, have been employed.

The evolution of the vortex characteristics during the convection process demonstrates a strong dependence on the turbulence model. In all cases, the vortex core radius grows

at a rate which is faster than the experimental measurements (Figure 6.8(a)). Similarly, the reduction in peak tangential velocity is consistently greater than the measurements suggest (Figure 6.8(b)), and there is a notable reduction in the peak streamwise vorticity at the vortex centre (Figure 6.8(c)). The results obtained using the $k-\omega$ SST model are in the closest agreement with the experimentally-measured vortex core radius and peak tangential velocity (Figures 6.8(a) and 6.8(b)), which are, respectively, 34% greater and 11% lower than the experimental measurements after approximately 12 swirl loops. However, the Spalart-Allmaras, $k-\epsilon$ and $k-\epsilon$ Realizable turbulence models produce excessive levels of vortex growth. For both turbulence models, the vortex core radius (Figure 6.8(a)) is almost 6 times the measured vortex core radius after 12 swirl loops. The turbulent viscosity at the vortex centre, ν_t/ν, for each of the turbulence models demonstrate that the turbulence levels inside the vortex core vary considerably between different models, and that the SA and $k-\epsilon$ turbulence models result in the greatest levels of turbulence inside the vortex core (Figure 6.9). For example, in the case of the SA turbulence model, the turbulent viscosity levels are two orders of magnitude larger than those observed in the $k-\omega$ SST results. This behaviour provides an explanation for the differences in the vortex characteristics which have been presented in Figures 6.8(a) to 6.8(d). In particular, where turbulence production rates are greatest, the vortex flow experiences the high levels of turbulence and thus the diffusion levels are elevated. It should be emphasised that the turbulence production levels are typically small for wing-tip vortices [43], and are only augmented when a large streamwise velocity perturbation exists [23, 46]. In the case under consideration for the current vortex convection studies, the streamwise velocity perturbation is small, and turbulence production is expected to be low [1]. Thus, the notable increase in turbulence inside the vortex core which is observed in Figure 6.9 suggests that the turbulence models do not capture the correct behaviour of the vortex turbulence field. The Spalart-Allmaras turbulence model, for example, uses the vorticity tensor to compute the turbulent production. As a result, the turbulence levels quickly rise inside the vortex core where the vorticity levels are greatest. The turbulence levels are reduced by several orders of magnitude when the modified SA model is employed (Figure 6.9). This is reflected in the evolution of the vortex characteristics (Figures 6.8(a) to 6.8(d)), which are closer to the experimental measurements than those of the standard SA model. Nonetheless, the modified SA model remains inferior to the $k-\omega$ SST turbulence model.

A feature of the turbulent flow in wing-tip vortices is the presence of anisotropic turbulent stresses [23, 30], which can be observed in a Cartesian coordinate system as a misalignment between the mean in-plane Reynolds stresses and the mean in-plane strain

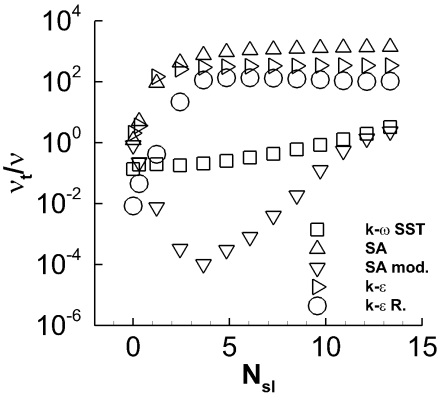

FIGURE 6.9: Evolution of eddy viscosity ratio at the vortex centre (ν_t/ν) for different turbulence models, as a function of the number of swirl loops (N_{sl}), $k-\omega$ SST model

rates (section 4.2). This presents a problem for eddy viscosity turbulence models, which employ the Boussinesq assumption to determine the turbulence levels in the simulated flow. A fundamental requirement for the Boussinesq assumption to be valid is that the Reynolds stress tensor is aligned with the mean strain rate tensor. Clearly, this is not a valid assumption for the vortical flows of interest in this research and, as a consequence, it is not possible for EV turbulence models to capture the flow physics of vortices. This limitation is a contributing factor to the limited agreement between the CFD simulations and the experimental measurements shown in Figures 6.8(a) and 6.8(b). It is necessary to determine if a second-moment closure turbulence model can be employed in favour of the eddy viscosity models. The results from RSM simulations of wing-tip vortex generation have reported far closer agreement with experimental results in comparison to eddy-viscosity models [84]. Thus, simulations using the wing-tip vortex convection test case were performed by Stankowski [107] under the direction of and in collaboration with this Doctoral research. It is important to note that the simulation mesh, numerical model, and boundary conditions, were identical to those employed for the eddy-viscosity model simulations. The Linear Pressure Strain (LPS) RSM model was selected. The RSM simulations were initialised using the solution from the converged $k-\omega$ SST simulations to ensure that the simulations achieved a converged solution. In-plane mesh resolutions of 16 and 32 elements were investigated, with a streamwise mesh resolution of 15 mesh elements per swirl loop. For an in-plane mesh resolution of 16 mesh elements, the vortex core radius and peak tangential velocity results (Figures 6.10(a) and 6.10(b)) obtained using the RSM simulations are close to those of the $k-\omega$ SST model. When the mesh resolution is increased to 32 elements across the vortex diameter, the simulated vortex diffusion rates are in excellent agreement with the experimental measurements. For example, after 12

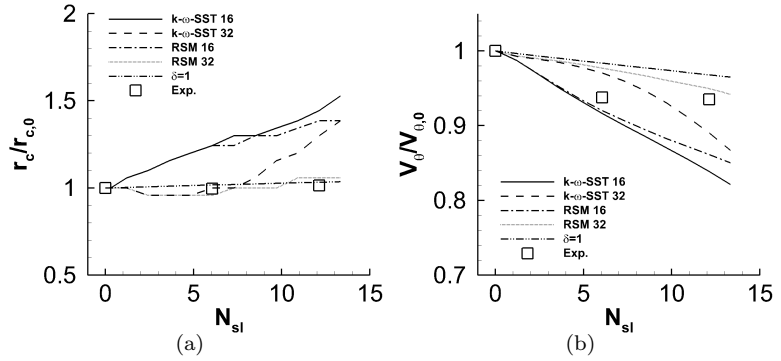

FIGURE 6.10: Evolution of vortex characteristics during convection as a function of the number of vortex swirl loops (N_{sl}), influence of in-plane mesh resolution for $k-\omega$ SST and RSM LPS turbulence models, (a): Vortex core radius ($r_c/r_{c,0}$), (b) Vortex peak tangential velocity ($V_{\theta,max}/V_{\theta,max0}$)

swirl loops from the inlet plane, the vortex obtained from the RSM simulation features a core radius and peak tangential velocity which are within 3% of the measured values. The results therefore demonstrate that the laminar-like vortex diffusion levels which have been obtained in the experiments can be obtained using an RSM simulation with a sufficiently high mesh resolution. In addition, it should be reminded that for shorter convection distances ($N_{sl} < 6$), it is possible to achieve satisfactory agreement with the experimental measurements with use of 16 mesh elements across the vortex diameter.

Additional insight into the vortex flow physics can be obtained in the details of the vortex turbulence characteristics, such as the normal turbulent stress profiles at $N_{sl} = 6$, Figure 6.11(a).

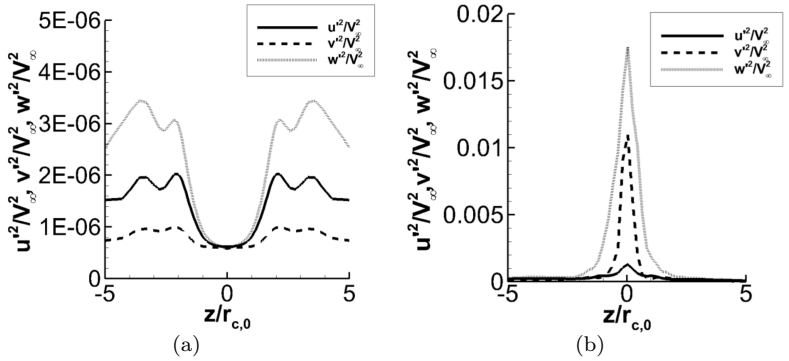

FIGURE 6.11: Cartesian turbulence profiles, evaluated perpendicular to the vortex axis and through the vortex centre, (a): Results from the RSM LPS simulations, (b): Experimental measurements

There are some notable discrepancies from the experimental data. In particular, the simulations feature turbulence levels which are several orders of magnitude lower than that observed in the experiments. The experimental measurements of v'^2 and w'^2 in Figure 6.11(b) may be excessively large as a result of wandering [1]. However, the out-of-plane turbulence terms are essentially unaffected by wandering [1], and so the measurements can be used with confidence. On this basis, the CFD simulations feature turbulence levels which are two orders of magnitude lower than the experiments. An important conclusion which can be reached is that, in the RSM simulations, the initially uniform turbulence boundary conditions do not develop into the anticipated profiles which are observed in Figure 6.11(b), and the turbulence levels which are prescribed at the inlet plane are not self-sustained in the vortex flow. In fact, this is consistent with experimental measurements [43] and simulations [46], which demonstrate that the turbulence production levels are small in the absence of large streamwise velocity perturbations. Thus, despite the promising agreement between the simulated and measured vortex diffusion characteristics (Figures 6.10(a) and 6.10(b)), it is apparent that potentially important features of the vortex flow have not been captured in the simulations. Therefore, it is necessary to address an approach to ensure that the correct turbulence characteristics are simulated. This will is the focus of the following section.

6.2 Turbulence boundary conditions for vortex simulations

An important conclusion from the preceding section is that additional simulations must be performed to identify the turbulence boundary condition requirements which correctly initiate the turbulence field at the CFD inlet plane. Details of the turbulence field can be obtained from CFD simulations of the vortex generation process, or from experimental measurements. Unfortunately, the in-plane turbulence measurements which are available for the test case in the preceding section are likely to be impacted by wandering. Therefore, it is not possible to use the measurements to develop valid turbulence boundary conditions. It was concluded that the experimental measurements obtained in this research for the unperturbed wing-tip vortices should be used as a basis to develop an approach for defining turbulence boundary conditions. This is appropriate since the measurements do not include the effects of wandering and, in addition, are in good agreement with the findings reported in the literature (section 4.2). The purpose of this section is to present the development of an approach which can be used to prescribe appropriate turbulence boundary conditions in conjunction with a vortex of known characteristics.

6.2.1 Test case details

The test case which has been employed consists of the wing-tip vortex generated by the NACA 0012 vortex generator at an angle of attack of $\alpha_{vg} = 12^o$ and a chord Reynolds number of 1.7×10^5. The characteristics of the wing-tip vortex, measured at a distance of $z/c = 6$ downstream of the wing trailing edge, are given in Table 4.1. Note that the chord and vortex Reynolds numbers are similar to those of the test case which was investigated in section 6.1.1. As demonstrated by Iversen [42] and Bhagwat and Leishman [50], the vortex Reynolds number is a key parameter which characterises the evolution of wing-tip vortices as they convect downstream of the wing. The test cases feature similar vortex Reynolds numbers and vortex generator characteristics, so it is anticipated that the diffusion levels experienced by the vortices during convection should also be similar.

In section 3.5, it was noted that the PIV configuration which was employed in this research did not permit the translation of the PIV measurement plane. Therefore, it was not possible to acquire vortex convection measurements for the unperturbed wing-tip vortices which were investigated in this research. As a consequence, the vortex convection simulations for this test case cannot be directly validated with experimental measurements. However, it is known that the Squire vortex model provides a good description of the evolution of the vortex characteristics for a wide range of wing-tip vortex flows [50]. Therefore, it is possible to use the Squire vortex model to evaluate the evolution of the wing tip vortex for this test case.

6.2.2 CFD methods

6.2.2.1 Mesh characteristics

The CFD domain for the present studies features similar characteristics as those employed in the Devenport studies (section 6.1.3). In particular, the Cartesian mesh featured extents of $200r_c$ in the x- and y-directions, which minimises the interaction between the streamwise vortex and the symmetry boundaries which have been employed at the far field boundaries. The CFD domain features a length of $10c$ in the streamwise direction, which corresponds to approximately 15 vortex swirl loops. To minimise the effects of numerical diffusion during the simulations, the guidelines which have been established in section 6.1.2.1 have been employed. It was found that the vortex diffusion characteristics were in good agreement with the experimental measurements when 32 mesh elements were used to resolve the vortex core diameter. Therefore, the mesh employed for the test case in this section also

featured a mesh resolution of 32 elements. In addition, the mesh featured 16 elements in the streamwise distance associated with a single swirl loop.

6.2.2.2 Boundary conditions

The inlet boundary conditions for the test case outlined in section 6.2.1 have been generated using experimental measurements which have been obtained in the unperturbed vortex measurements in chapter 4. The conditionally-averaged Stereoscopic PIV measurements have been employed to ensure that the experimental data are not corrupted by the effects of wandering. The data is defined on a circular zone which features a maximum radius of approximately $r/r_c = 3$ from the vortex centre, Figure 6.12. The CFD inlet plane features a width and height of $200r_c$, so the experimental data must be extrapolated in the radial direction to provide boundary profiles which encapsulate the entire CFD inlet plane. As illustrated in Figure 6.12, the streamwise velocity profile is approximately equal to the freestream velocity (W_∞). Therefore, the value of V_z at $r/r_c = 3$ was applied for all inlet plane points beyond $r/r_c = 3$.

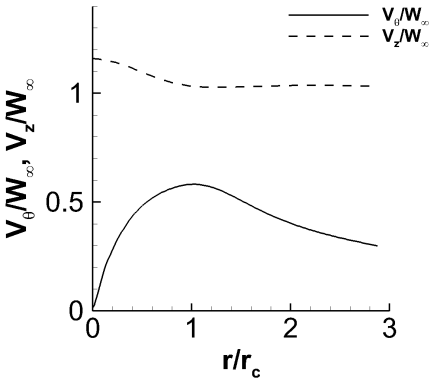

FIGURE 6.12: Tangential and streamwise velocity profiles employed to define the velocity boundary conditions at the inlet plane of the CFD domain

The circumferentially-averaged tangential velocity profile can be derived from the circulation distribution by means of Eq. 6.3. To implement this approach, it is necessary to prescribe a profile for $\Gamma(r)$ for $r/r_c > 3$. Experimental measurements, for example, Tung et al. [28] and Martin et al. [33], demonstrate that the value of $\Gamma(r)$ increases only slowly for $r/r_c > 2$, and is approximately constant beyond $r/r_c = 10$. Therefore, it is assumed in this research that the circulation is constant beyond the circular zone, and is equal to the value of $\Gamma(r)$ at the circular zone edge. Importantly, the gradient of the circulation profile ($\partial\Gamma^2/\partial r$) remains non-negative throughout the flow. This condition is necessary

to avoid the potential for centrifugal instabilities to be generated in the flow, as given by Rayleigh's stability criterion [53].

$$V_\theta(r) = \frac{\Gamma(r)}{2\pi r} \tag{6.3}$$

In general, the turbulence boundary conditions required for RSM simulations consist of the turbulent kinetic energy (k), the turbulent dissipation rate (ϵ), the mean normal stresses (u'^2, v'^2, w'^2), and the mean Reynolds stresses ($u'v', v'w', u'w'$). All such components, with the exception of ϵ, can be extracted directly from the experimental measurements. To obtain ϵ, it is possible to employ Eq. 6.4 in conjunction with the turbulent kinetic energy profile and a suitable value of the turbulence length scale, l [106]. Note that C_μ=0.09. Similarly, it is possible to define profiles of the specific dissipation (ω) using Eq. 6.5 [106].

$$\epsilon = (C_\mu^{0.75})k^{1.5}/l; \tag{6.4}$$

$$\omega = k^{0.5}/((C_\mu^{0.25})l); \tag{6.5}$$

Little information is available in the literature to define a suitable value of the turbulence length scale, and so an objective of the present study is to identify the most appropriate value for the vortices under investigation. An important feature of the turbulence field in wing-tip vortices is the presence of non-isotropic, non-axisymmetric turbulence components, such as the in-plane normal stresses and Reynolds stresses (Figures 6.13(a) and 6.13(b)). To preserve the details of the turbulence characteristics, the conditionally-averaged circular zone, instead of a circumferential average, has been employed to generate the turbulence boundary conditions. In this way, the highly non-axisymmetric normal stresses and Reynolds stresses can be preserved. Experimental measurements [1] suggest that, beyond the vortex core and the wing wake, the turbulence characteristics quickly reduce to values similar to freestream turbulence. Therefore, for $r/r_c > 3$, the turbulence components are scaled to produce an overall turbulence intensity of approximately 0.1%, which is representative of the typical freestream turbulence levels in a typical low-speed wind tunnel.

Valuable insight into the requirements for turbulence boundary conditions can be provided by assessing the sensitivity of the vortex convection simulations to the details which are provided in the turbulence boundary conditions. Three different turbulence

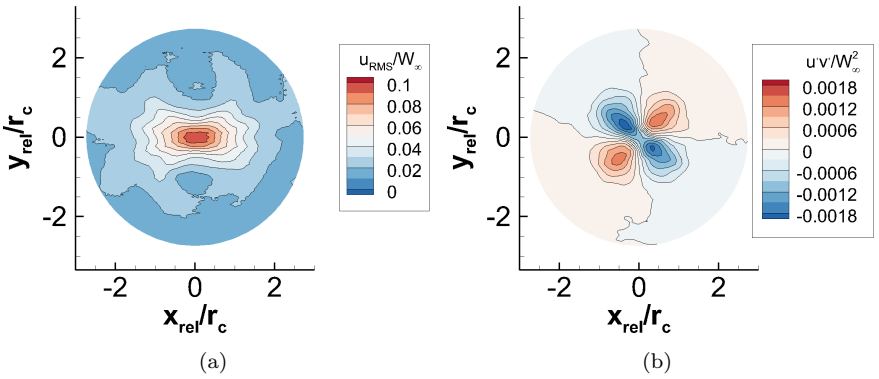

FIGURE 6.13: Velocity unsteadiness measurements obtained from the NACA 0012 wing-tip vortex measurements in the unperturbed freestream, (a) In-plane normal stress ($u'u'/W_\infty^2$), (b): In-plane Reynolds stress ($u'v'/W_\infty^2$)

boundary condition strategies have therefore been investigated. The first corresponds to turbulence boundary conditions which have been generated using all of the required turbulence components for RSM simulations, namely, the profiles of turbulent kinetic energy (k), turbulent dissipation (ϵ), the normal stresses (u'^2, v'^2, w'^2) and the Reynolds stresses ($u'v', u'w', v'w'$). As discussed in section 6.2.3, this approach was found to give good agreement between the CFD results and the trends reported in the literature. The second strategy consists of providing only the profiles of k and ϵ. In such a scenario, the turbulent stresses at the inlet boundary are assumed to be isotropic, and are evaluated internally by FLUENT using the turbulent kinetic energy profile [106]. The final boundary condition strategy consists of uniform inlet turbulence levels across the entire inlet plane, where the turbulence levels are prescribed as the values obtained at the centre of the unperturbed vortex. As such, the turbulent kinetic energy k/W_∞^2 is equal to 0.013, which corresponds to a turbulence intensity of TI/W_∞=0.093. Note that this value is two orders of magnitude larger than those prescribed at the inlet plane of the Devenport test case simulations which were reported in section 6.1.3. The corresponding profiles of turbulent dissipation were computed using a turbulence length scale of $0.1r_c$.

In a manner similar to the Devenport test case, the vortex boundary conditions were interpolated linearly on to the CFD inlet plane mesh (section 6.1.2.2). The outlet plane boundary condition consisted of a uniform static pressure distribution with a value corresponding to the freestream static pressure. Finally, the far-field domain boundaries which are parallel to the vortex axis were defined with a symmetry boundary condition.

6.2.2.3 Numerical model and convergence strategy

The vortex convection simulations in this section were performed using the same numerical model and convergence strategy as those employed for the Devenport test case (section 6.1.2.3).

6.2.3 Impact of turbulence model

In section 6.1.3.2, it was demonstrated that choice of the turbulence model has a strong effect on the ability of the CFD solver to correctly simulate the evolution of an isolated vortex. Importantly, it was asserted that eddy-viscosity models are unable to correctly capture the evolution of the vortex characteristics, and that it is necessary to assess the behaviour of the vortex characteristics and the turbulence properties when suitable inlet boundary conditions are prescribed. There is little information on suitable length scales for wing-tip vortex flows. However, Baldwin et al [108] employed a length scale of $l = 0.1r_c$ at the inlet boundary for wing-tip vortex convection simulations. Therefore, a turbulence length scale of $l = 0.1r_c$ has been employed to define the inlet boundary profiles of ϵ and ω for the RSM and $k-\omega$ SST simulations, respectively. Note that the Linear Pressure Strain (LPS) pressure strain model has been employed for the RSM simulations. Preliminary studies demonstrated that the choice of pressure strain model had little effect on the evolution of the vortex mean characteristics [107].

When appropriate turbulence boundary conditions are employed, the vortex evolution in the $k-\omega$ SST simulations (Figures 6.14(a) to 6.14(c)) is characterised by large levels of diffusion. For example, after $N_{sl} = 11$, the simulated vortex core radius is 2.2 times the value anticipated from the Squire vortex model with $\delta = 1$ (Figure 6.14(a)). Instead, the vortex diffusion characteristics are close for $\delta = 60$, which is notably larger than anticipated from the experimental measurements available in the literature. The intense diffusion levels which have been observed in this test case are a result of the prescription of the turbulence profiles on the inlet boundary. In contrast, the results from the RSM simulation, demonstrate that the vortex core radius (Figure 6.14(a)) and peak tangential velocity (Figure 6.14(b)) evolve in a manner which is close to the laminar trend given by the Squire model.

When appropriate turbulence boundary conditions are prescribed, $k-\omega$ SST turbulence model produces unrealistic vortex diffusion characteristics. In contrast, the correct evolution of the vortex characteristics is obtained using the RSM approach in conjunction with

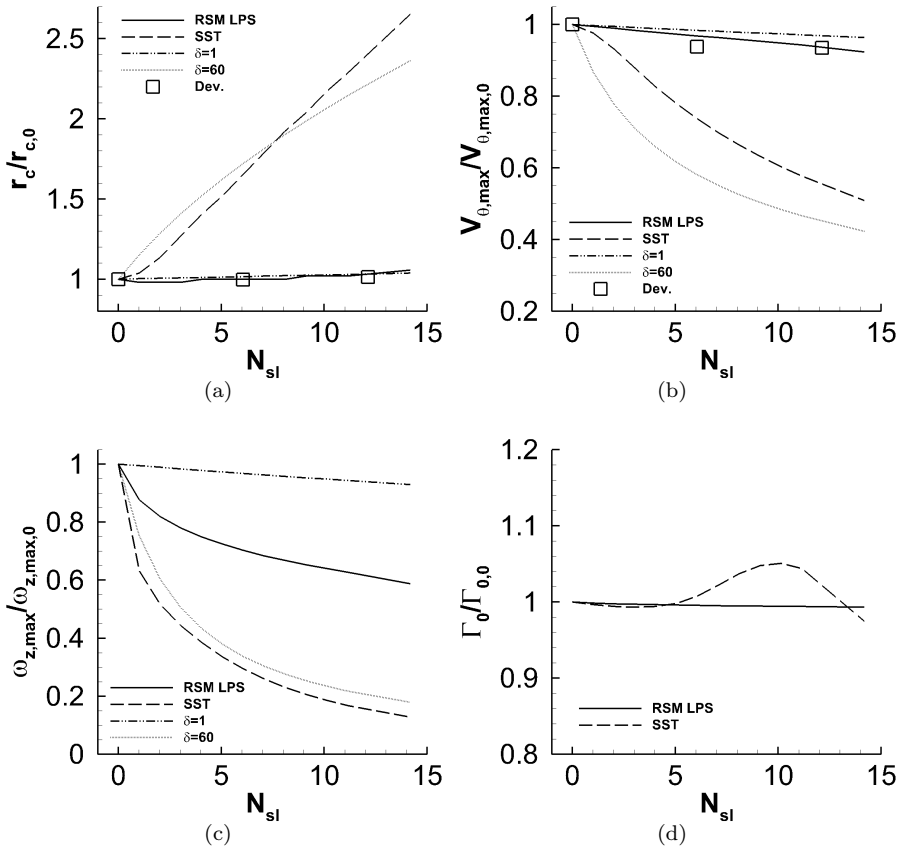

FIGURE 6.14: Evolution of vortex characteristics during convection as a function of the number of vortex swirl loops (N_{sl}), experimental measurements employed to define turbulence boundary condition profiles, $k-\omega$ SST and RSM LPS turbulence models, (a): Vortex core radius ($r_c/r_{c,0}$), (b) Vortex peak tangential velocity ($V_{\theta,max}/V_{\theta,max0}$), (c): Vortex peak streamwise vorticity ($\omega_{z,max}/\omega_{z,max0}$), (d): Vortex total circulation ($\Gamma_0/\Gamma_{0,0}$). Note that Dev. refers to the wing-tip vortex measurements of Devenport et al. [1]

suitable turbulence boundary conditions. Therefore, it can be concluded that EV models such as the $k-\omega$ SST model result in a vortex diffusion process which is excessively rapid, and it is necessary to employ second-moment closure turbulence models to investigate the flows of interest for vortex ingestion.

6.2.4 Analytical turbulence BC profiles

The preceding section has demonstrated that RSM simulations, in conjunction with suitable turbulence boundary conditions, can correctly capture the evolution of the vortex

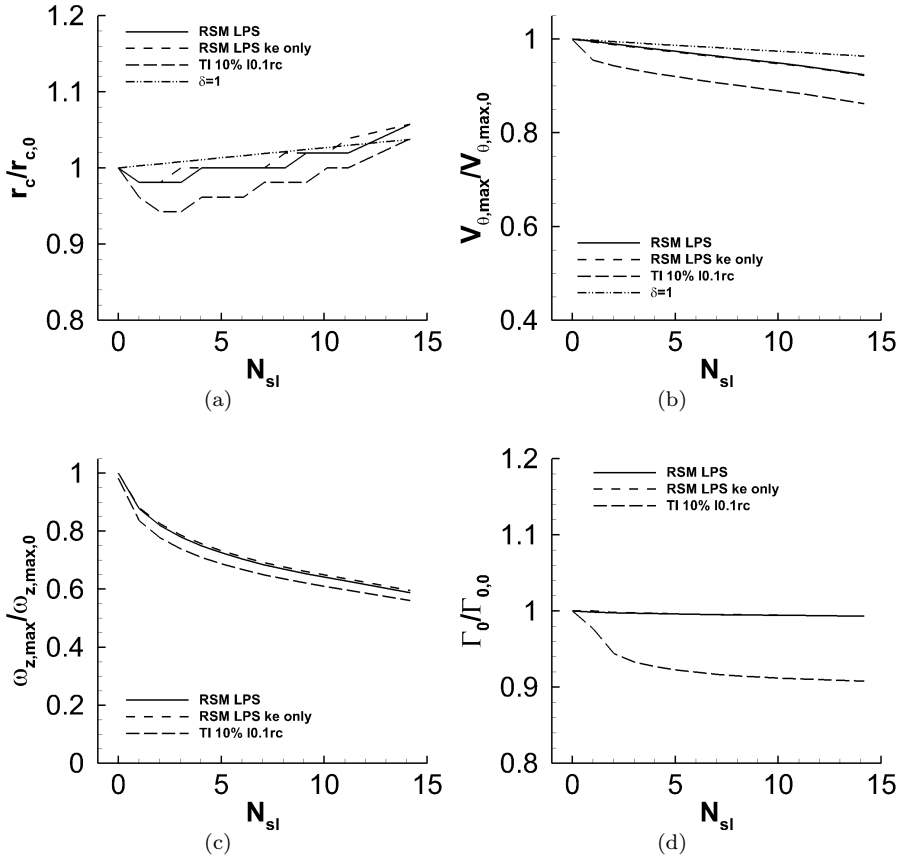

FIGURE 6.15: Evolution of vortex characteristics during convection as a function of the number of vortex swirl loops (N_{sl}), sensitivity of vortex characteristics to the turbulence components defined at the inlet boundary, RSM LPS model, (a): Vortex core radius ($r_c/r_{c,0}$), (b) Vortex peak tangential velocity ($V_{\theta,max}/V_{\theta,max0}$), (c): Vortex peak streamwise vorticity ($\omega_{z,max}/\omega_{z,max0}$), (d): Vortex total circulation ($\Gamma_0/\Gamma_{0,0}$)

flow. However, in general, detailed measurements of the turbulent stresses and turbulent kinetic energy may not be available for cases of interest for vortex ingestion studies. One possible approach is to produce suitable turbulence boundary conditions using an analytical or semi-empirical approach. It is necessary to evaluate which turbulence components are required to correctly initialise the vortex flow. Thereafter, it will be possible to identify suitable analytical profiles which can be employed to approximate the nature of the turbulence profiles which have been measured experimentally.

Firstly, it is of interest to determine if the vortex convection process is affected when only the profiles of k and ϵ are prescribed. The evolution of the vortex core radius (Figure 6.15(a)), peak tangential velocity (Figure 6.15(b)), peak streamwise vorticity (Figure 6.15(c)), and total circulation (Figure 6.15(d)) are unchanged in comparison to the

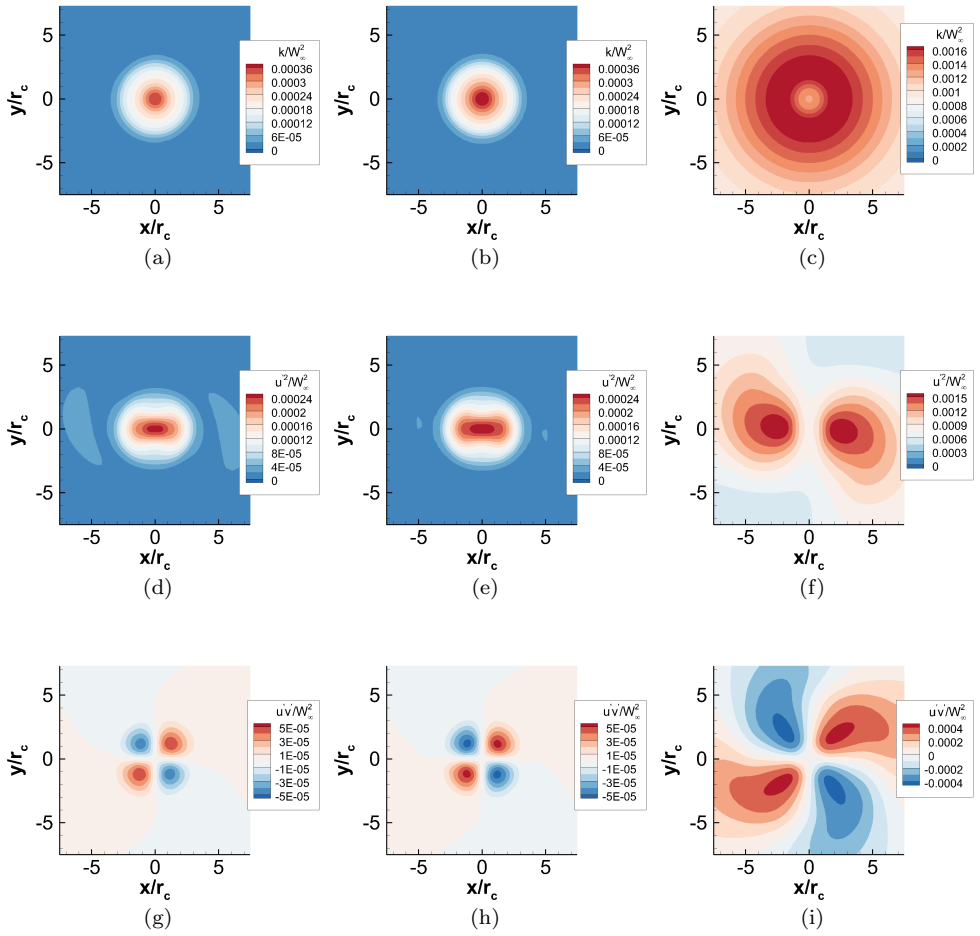

FIGURE 6.16: Contours of turbulence characteristics obtained from RSM LPS simulations, $N_{sl} = 6$, (a), (d) and (g): All turbulence components prescribed, (b), (e) and (h): Profiles of k and ϵ prescribed, turbulent stresses computed from k, (c), (f) and (i): Uniform turbulence boundary conditions comprising a turbulence intensity of $TI = 10\%$ and uniform turbulence length scale $l = 0.1r_c$

case where all turbulence components are prescribed. However, when uniform turbulence boundary conditions are employed, the vortex undergoes a strong adjustment after the inlet boundary which results in a rapid reduction in the vortex core radius, peak tangential velocity, and total circulation. This behaviour is not consistent with the trends which have been observed thus far in the vortex convection simulations. Therefore it is clear that that such uniform turbulence profiles are not appropriate as a method of initialising the turbulence characteristics of the vortex.

Further insight into the evolution of the vortex flow can be obtained using the contours

of selected turbulence characteristics at a distance of $N_{sl} = 6$ downstream of the inlet plane, Figures 6.16(a) to 6.16(i). When the complete set of turbulence characteristics are provided in the inlet boundary conditions, the peak turbulent kinetic energy remains at the vortex centre (Figure 6.16(a)), and the characteristic turbulence anisotropy is preserved, as indicated by the elliptic u'^2 contours (Figure 6.16(d)). Finally, as anticipated, the in-plane Reynolds stresses feature the characteristic four-lobed pattern (Figure 6.16(g)). Interestingly, when only the profiles of k and ϵ are prescribed, the vortex develops almost identical turbulence profiles (Figures 6.16(b), 6.16(e), and 6.16(h)) as those for the case when all components were prescribed. When uniform turbulence boundary conditions are prescribed, the peak turbulent kinetic energy is located outside of the vortex core (Figure 6.16(c)), and the mean in-plane and Reynolds stresses (Figures 6.16(f) and 6.16(i)) feature notably different structures to the other simulations. In addition, the turbulence contours observed in Figures 6.16(c) do not resemble the experimental measurements (Figures 6.13(a) and 6.13(b)), so it can be concluded that it is not appropriate to define the turbulence boundary conditions in terms of uniform turbulence profiles.

Inspection of the circumferentially-averaged turbulent kinetic energy profile (k/k_{max}) reveals that the profile can be closely approximated with a Gaussian curve fit, Figure 6.17. Note that the profile corresponds to the measurements from the NACA 0012 wing-tip vortex at an angle of attack of $\alpha_{vg} = 12^o$, for a vortex Reynolds number of 3.7×10^4 and a chord Reynolds number of 1.7×10^5. The equation for the Gaussian profile is given by Eq. 6.6, where k_{max} is the peak turbulent kinetic energy, k_∞ is the turbulent kinetic energy at a large distance from the vortex, and r is the distance from the vortex centre. In addition, the parameter c can be determined from Eq. 6.7, where the constant FWHM in Eq. 6.7 corresponds to the Full Width at Half Maximum value of the Gaussian profile

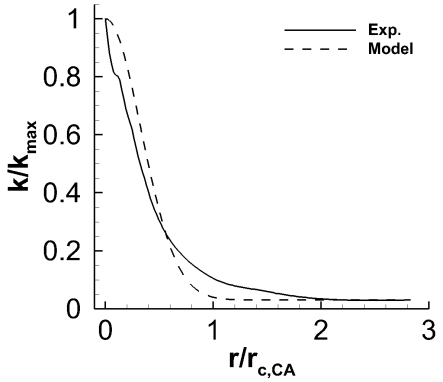

FIGURE 6.17: Gaussian curve fit of turbulent kinetic energy (k/k_{max}) profile obtained from PIV measurements, as a function of distance from the vortex centre (r/r_c)

[109]. In particular, the value of FWHM is equal to a radius corresponding to the value of $k = k_{max}/2$ as determined from the experimental profile of k (Figure 6.17). To complete the definition of the turbulence boundary conditions, Eq. 6.4 has been employed to calculate the profile of the turbulent dissipation rate.

$$k(r) = k_\infty + (k_{max} - k_\infty)\, e^{-r^2/2c^2} \tag{6.6}$$

$$c = \frac{FWHM}{2\ln 2} = \frac{0.366 r_c}{2\ln 2} \tag{6.7}$$

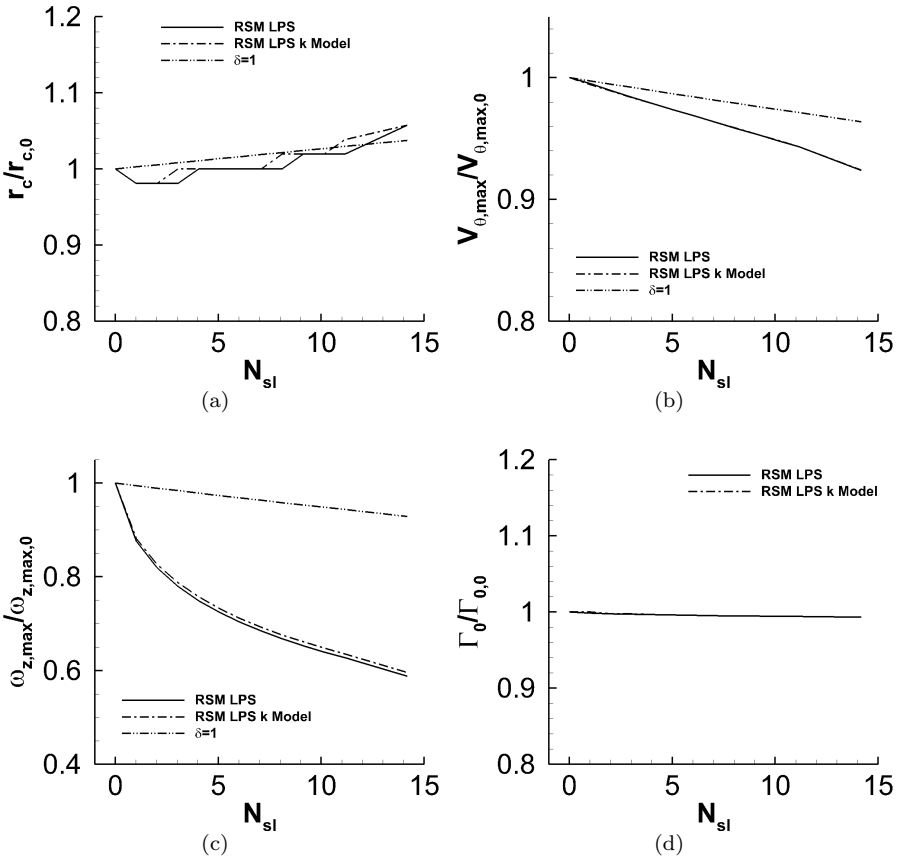

FIGURE 6.18: Evolution of vortex characteristics during convection as a function of the number of vortex swirl loops (N_{sl}), sensitivity of vortex evolution to method employed to define vortex turbulence boundary conditions, complete boundary conditions using experimental measurements (RSM LPS), boundary conditions using model for turbulent kinetic energy profile (RSM LPS k model), (a): Vortex core radius ($r_c/r_{c,0}$), (b) Vortex peak tangential velocity ($V_{\theta,max}/V_{\theta,max0}$), (c): Vortex peak streamwise vorticity ($\omega_{z,max}/\omega_{z,max0}$), (d): Vortex total circulation ($\Gamma_0/\Gamma_{0,0}$)

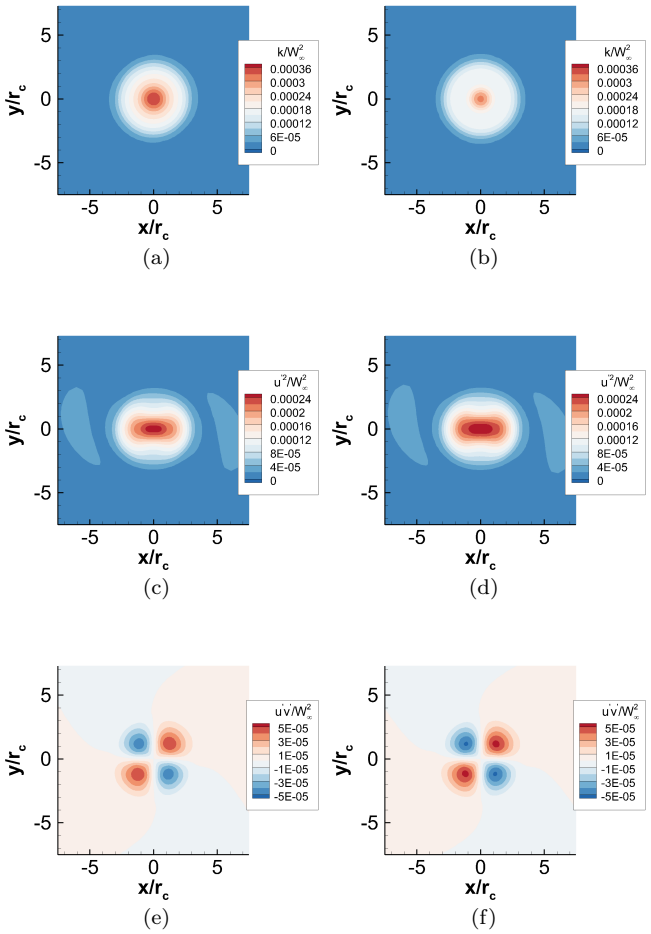

FIGURE 6.19: Contours of turbulence characteristics obtained from RSM LPS simulations, $N_{sl} = 6$, (a), (c) and (e): All turbulence components prescribed, (b), (d) and (f): Profiles of k and ϵ prescribed using model for turbulent kinetic energy (Eq. 6.6), turbulent stresses computed from k

The results from the vortex convection simulations, Figures 6.18(a) to 6.18(d) demonstrate that the vortex evolution for the simulation with the boundary conditions model are almost identical to those where the boundary conditions were prescribed directly from the experimental measurements. Therefore, the correct vortex diffusion characteristics can be captured when a simple analytical model for the turbulence boundary conditions is employed.

The contours of the turbulence characteristics after 6 vortex swirl loops from the inlet boundary, Figures 6.19(a) to 6.19(f), also indicate that the analytical turbulence profile captures the expected turbulence levels and characteristics. In particular, turbulence

anisotropy is correctly developed as the vortex convects, which results in elliptic normal stress contours (Figure 6.19(b)), in addition to the correct four-lobed in-plane Reynolds stress contours (Figure 6.19(f)). Therefore, it can be concluded that suitable turbulence profiles can be generated using an analytical profile for the turbulent kinetic energy. This provides an approach to generate appropriate turbulence boundary conditions for vortical flow where experimental measurements of the turbulence profiles are not available. In section 6.4.2.3, this method is generalised for use with sub-scale and full-scale vortex ingestion simulations for which no prior details of the velocity or turbulence fields are available.

6.2.5 Impact of turbulence length scale

A final parameter which is used to define the turbulence boundary conditions is the turbulence length scale, which represents the typical size of the turbulent eddies contained in the flow [110]. The prescription of the turbulence length scale at the inlet plane permits a description of the k and ϵ profiles at the inlet plane, as required for RSM simulations using FLUENT [105]. The vortex convection simulations which have been presented in the preceding sections have been performed using a turbulence length scale of $0.1r_c$ to define the turbulence field at the inlet boundary. It is necessary to establish the most appropriate turbulence length scale for use in vortex convection simulations. In addition, the sensitivity of the vortex convection simulations to the value of turbulence length scale should be assessed. Thus, length scales of $0.01r_c$, $0.1r_c$, $1.0r_c$ and $10r_c$ have been investigated. In addition, based on the simulations of Baldwin et al. [108], Iversen [42] proposed a turbulent vortex model which featured a turbulence length scale which increases linearly with distance from the vortex centre, Eq. 6.8, where $\alpha_I = 0.01854$.

$$l = \alpha_I r \tag{6.8}$$

The evolution of the vortex characteristics (Figures 6.20(a) to 6.20(d)) is surprisingly insensitive to the change in turbulence length scale from $l = 0.01r_c$ to $1r_c$. However, when the turbulence length scale is increased to $l = 10r_c$, there is a corresponding increase in the diffusion levels experienced by the vortex. As a consequence, the vortex features a core radius which is approximately 10% larger than that observed in the simulations where the turbulence length scale is between $0.01r_c$ and $1r_c$. It is also necessary to consider the evolution of the vortex turbulence field. To obtain a quantitative assessment of the

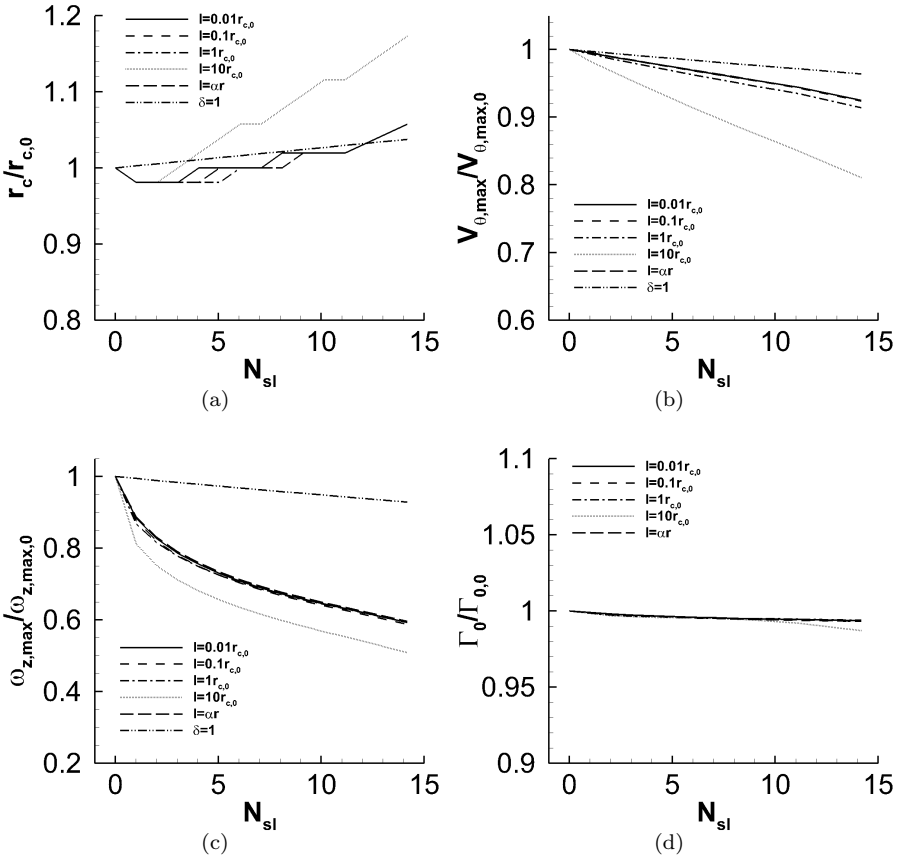

FIGURE 6.20: Evolution of vortex characteristics during convection as a function of the number of vortex swirl loops (N_{sl}), sensitivity of vortex evolution to turbulence length scale at inlet boundary (l), (a): Vortex core radius ($r_c/r_{c,0}$), (b) Vortex peak tangential velocity ($V_{\theta,max}/V_{\theta,max0}$), (c): Vortex peak streamwise vorticity ($\omega_{z,max}/\omega_{z,max0}$), (d): Vortex total circulation ($\Gamma_0/\Gamma_{0,0}$)

streamwise development of the turbulence characteristics, measurements of the out-of-plane velocity fluctuations at the vortex centre (w_{rms}) have been extracted from Chow et al. [23], Devenport et al. [1] and Han et al. [43]. It should be noted that, in contrast to the in-plane turbulence measurements, the out-of-plane turbulence measurements are only weakly affected by wandering [1]. The experimental measurements have been presented alongside the values of w_{rms} obtained from the CFD simulations (Figure 6.21(a)).

In all cases, the turbulence decay rates observed in the CFD simulations just downstream of the inlet plane are notably greater than the experimental measurements suggest. Beyond $N_{sl} = 2$, the turbulence length scale has a measurable effect on the turbulence decay characteristics. The greatest decay rates occur for a length scale of $l = \alpha r$. As the length

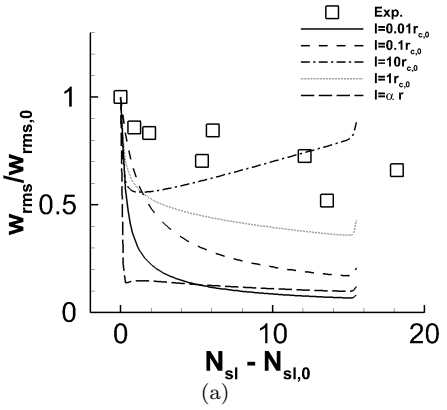

(a)

FIGURE 6.21: Evolution of streamwise turbulent stress the vortex centre ($w_{rms}/w_{rms,0}$), as a function of the number of swirl loops (N_{sl}), influence of turbulence length scale. Simulation results have been compared with the experimental measurements of [43, 23, 1]

scale is increased, the agreement between the CFD results and the experimental measurements improves. At $l = 10r_c$, however, the turbulence levels increase with downstream distance, which is not consistent with the measurements. It can therefore be concluded that a turbulence length scale of $1r_c$ provides the most suitable boundary condition to capture the evolution of the vortex turbulence characteristics.

6.2.6 Summary of requirements

An extensive study has been undertaken to identify the correct approach to model streamwise vortices using CFD. Simulations have been conducted of an isolated wing-tip vortex contained in a uniform streamwise flow. Experimental measurements of the wing-tip vortex characteristics have been employed to evaluate the CFD simulation results. As anticipated, the evolution of the vortex as it convects inside the CFD domain is strongly dependent on the mesh resolution. A minimum of 16 mesh elements, measured on a plane perpendicular to the vortex streamwise axis, are required across the vortex core diameter. For lower mesh resolutions, the vortex was subject to excessive levels of diffusion, which resulted in a vortex which was larger and of a lower intensity than measured experimentally. In addition, it was found that a minimum of 10 mesh elements are required to resolve the streamwise distance which corresponds to a single vortex swirl loop.

A range of RANS turbulence models have also been investigated. It was demonstrated that single-equation and two-equation eddy viscosity (EV) turbulence models provide only limited agreement with the experimental measurements. The fundamental assumptions

which are used in the formulation of eddy viscosity models are invalid for the streamwise vortices of interest for vortex ingestion studies, which means that such models are unable to correctly simulate the vortex flow physics. As a consequence, second moment closure models, in the form of Reynolds Stress Models, are required. However, the RSM simulations demonstrated that correct turbulence characteristics inside the vortex do not result when uniform turbulence boundary conditions are prescribed at the inlet. Instead, it is necessary to prescribe appropriate turbulence boundary conditions. A sensitivity study found that suitable profiles of turbulent kinetic energy (k) and turbulent dissipation rate (ϵ) are sufficient to initialise the turbulence field at the CFD inlet boundary. These profiles can be prescribed in the form of a Gaussian curve, the coefficients of which have been determined from the sub-scale, unperturbed, wing-tip vortex measurements obtained in this research. It was found that this boundary conditions approach produced results which were in excellent agreement with the results obtained using experimental measurements to define the turbulence boundary conditions.

The CFD modelling requirements developed herein ensure that the effects of numerical diffusion on vortex ingestion simulations can be minimised, and allow the flow physics wing-tip vortices to be correctly modelled in CFD. The guidelines will therefore be applied to investigate vortex ingestion, which is the focus of the remainder of this chapter.

6.3 Sub-scale vortex ingestion

In the previous section, a series of guidelines were developed to allow vortical flows to be simulated correctly using CFD. The guidelines can now be applied to investigate vortex ingestion flows, as detailed in this section. Firstly, the guidelines are utilised to perform sub-scale vortex ingestion simulations at the conditions which have been investigated experimentally in chapter 5. In this way, the first validated CFD approach for vortex ingestion will be established. This section therefore provides a description of the vortex ingestion test case, the CFD domain, the boundary conditions, and the numerical model. The results from the CFD simulations are then evaluated using the sub-scale vortex measurements which were reported in chapter 5.

6.3.1 Test case

In chapter 5, the measurements from a wide range of configurations of streamwise vortex ingestion were analysed. The experiments investigated a number of intake flow conditions and initial vortex characteristics to identify the dominant flow physics and vortex characteristics which occur when a vortex is ingested. The experimental measurements have shown that the vortex Reynolds number (Re_v), the vortex core average vorticity ($\omega_{z,av}$), and the streamtube contraction levels ($w_c/w_{c,0}$), are the most important parameters which define the evolution of the vortex as it is ingested. In particular, it was found that important diffusion effects take place when $w_c/w_{c,0}$ is greater than 2. Therefore, a configuration with a large intake velocity ratio has been selected. The test case consists of the ingestion of the NACA 0012 wing-tip vortex along the intake centreline. The vortex was generated at a chord Reynolds number of 1.7×10^5 and at a vortex generator angle of attack of 12^o. At this condition, the vortex featured a vortex Reynolds number of 2.4×10^4. The intake velocity ratio (W_i/W_∞)is equal to 10.3, such that the intake Mach number and mass flow are $M_i = 0.56$ and $\dot{m}_i = 1.467 kgs^{-1}$, respectively. Therefore, this test case is appropriate to evaluate if it is possible to capture the important diffusion processes which have been measured in chapter 5.

6.3.2 CFD methods

6.3.2.1 Intake geometry and mesh characteristics

The aircraft intake geometry which has been employed in the sub-scale studies corresponds to the intake model which was investigated in the experimental vortex ingestion measurements (section 3.1). The mesh was generated in the research of Stankowski [107] in collaboration with this research. The intake is embedded inside a Cartesian mesh domain (Figure 6.22(a)) which extends $25D_i$ in the vertical and horizontal directions, and $15D_i$ in the streamwise direction. Therefore, the domain edges are located at a distance of $12.5D_i$ from the intake centreline. The intake highlight plane is located at a streamwise distance of $8D_i$ downstream of the intake highlight plane to avoid interactions between the perturbation field of the intake and the inlet boundary conditions.

The blocking strategy consisted of a C-grid around the intake surfaces to maintain appropriate mesh quality around the intake lip and to control the intake boundary layer resolution, Figure 6.22(b). An O-grid topology was employed close to the intake centreline to ensure that the Cartesian domain can transition smoothly into the C-grid surrounding the

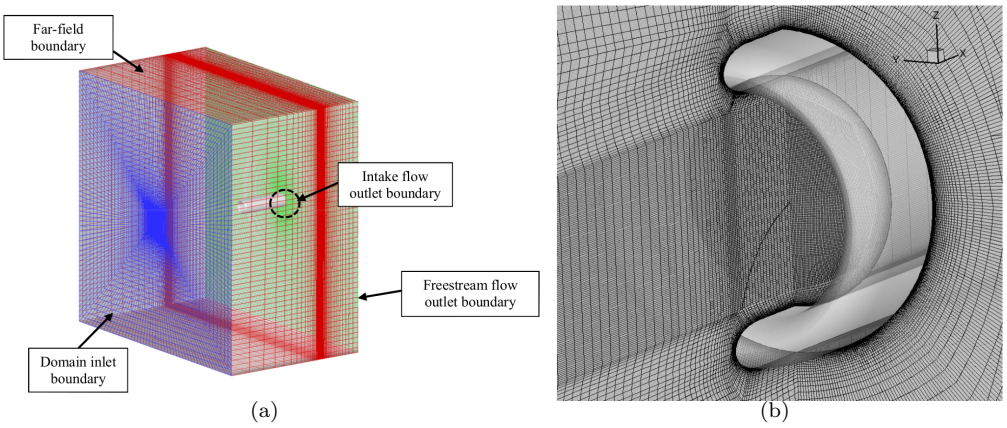

FIGURE 6.22: Sub-scale vortex ingestion simulation domain (a): Domain details, (b): Details of mesh close to intake

circular intake geometry. For the vortex and freestream conditions described in section 6.3.1, a single vortex swirl loop is approximately 0.1m. Therefore, the vortex is expected to convect a distance of 10 swirl loops from the inlet plane to the intake highlight position. It is apparent from the results of section 6.1.3.1, such as Figure 6.6(a), that the vortex may experience unrealistic levels of vorticity diffusion if the mesh is not of a sufficient resolution. Thus, the central rectilinear block features a region of increased mesh resolution. In this way, it was possible to ensure that a minimum of 16 mesh elements were used to resolve the vortex core diameter at the inlet plane. At $z/D_i = 0.20$, the mesh resolution ensured that 12 mesh elements resolved the vortex core. This estimate is based on the measured value of r_c from the experiments (section 5.2.1). In addition, the streamwise mesh resolution consisted of 15 mesh elements in the streamwise distance which corresponds to a single swirl loop. In this way, it is anticipated that numerical diffusion as a result of the mesh characteristics will be small. With reference to Figure 6.20(a), the vortex core radius is expected to grow by no more than 10% from the value at the inlet boundary. The intake boundary layer mesh resolution was sufficiently high to ensure that the value of y^+ is no greater than 1, and the domain consisted of approximately 7.2×10^6 mesh elements. Further details of the mesh characteristics can be obtained in [107].

6.3.2.2 Boundary conditions

The approach used in section 6.1.2.2 has been employed to prescribe the vortex on the inlet boundary of the CFD domain. In particular, the boundary conditions have been defined using the conditionally-averaged velocity and turbulence fields. For the vortex ingestion

simulations, however, it is necessary to prescribe compressible inlet boundary conditions, due to the presence of large sub-sonic Mach numbers inside the intake (section 6.3.1). Distributions of flow direction ($\vec{d}$), total pressure (P_0), and total temperature (T_0), are therefore required, in addition to appropriate turbulence boundary conditions. The flow direction $\vec{d} = (d_x, d_y, d_z)$ is computed by normalising the Cartesian velocity components (V_x, V_y, V_z) by the corresponding velocity magnitude $|\mathbf{V}|$, Eq. 6.9. Note that, similar to the convection simulations, the Cartesian velocity components have been derived from the circumferentially-averaged profiles of V_θ and V_z which have been obtained in the unperturbed flow measurements (chapter 4).

$$\begin{aligned} d_x &= \frac{V_x}{|\mathbf{V}|} \\ d_y &= \frac{V_y}{|\mathbf{V}|} \\ d_z &= \frac{V_z}{|\mathbf{V}|} \end{aligned} \tag{6.9}$$

It is assumed that the total pressure distribution can be obtained using Bernoilli's equation, Eq. 6.10, where p is the static pressure, and ρ_∞ is the density in the freestream. To apply Eq. 6.10, it is assumed that the freestream flow associated with the unperturbed vortex is incompressible. This is valid for the vortical flows considered in this research since the Mach number of the flow does not exceed $M = 0.10$.

$$P_0 = p + \frac{1}{2}\rho_\infty |\mathbf{V}|^2 \tag{6.10}$$

Note that total pressure loss inside the vortex core has been neglected. This has been justified on the basis that the wing-tip vortex measurements of Chow et al. [23] have indicated that the total pressure loss in the extended near field of the wing is approximately 1% of $P_{0,\infty}$. Therefore, the total pressure loss for wing-tip vortices is small, and it is therefore appropriate to consider it negligible. The vortex flowfield generally features a static pressure distribution as a consequence of the large tangential velocities which occur inside the vortex (section 2.2.1), which can be approximated by integrating the radial momentum equation, Eq. 6.11. Note that V_θ is the circumferentially-averaged tangential velocity profile which is used to generate the in-plane velocity field. The resulting static

pressure perturbation can then be superimposed on the surrounding uniform static pressure field which is attributed to the freestream flow, and subsequently forms an input to the calculation of the total pressure distribution in Eq. 6.10.

$$\frac{\partial p}{\partial r} = \rho \frac{V_\theta^2}{r} \tag{6.11}$$

There is little information on the temperature profiles inside a wing-tip vortex. However, the total temperature field has been assumed to be constant. In addition, Mayer and Powell [111] acquired numerical solutions to the steady, axisymmetric Navier-Stokes equations applied to an isolated streamwise vortex, and found that the static temperature perturbation was zero for an incompressible flow. At a Mach number of 0.5, the vortex featured a static pressure of $T/T_\infty = 0.80$. These results are consistent with the findings of Aboelkassem and Vatistas [112], which demonstrated analytically that the static temperature at the vortex centre is approximately $0.83T_\infty$ for a Mach number of 0.4. It is therefore concluded that, for incompressible flow, the static temperature perturbation is also negligible.

To complete the definition of the inlet boundary conditions, the turbulence boundary conditions were prescribed using the turbulent kinetic energy, normal stresses, and Reynolds stresses, obtained from the experimental measurements. Thus, the same method as that employed in section 6.2.4 has been used to create the turbulence profiles at the inlet plane. A turbulence length scale of $l = 1r_c$ has been employed, based on the findings of section 6.2.5. Therefore, it was possible to compute the distributions of turbulent dissipation rate or specific dissipation, using Eqs. 6.4 and 6.5, depending on the choice of turbulence model.

A symmetry boundary condition has been employed on the far-field boundaries which are parallel to both the intake axis and the freestream direction. The outlet boundary which is located external to the intake flow was defined using the freestream static pressure, coupled with a turbulence intensity and length scale of 5% and $1r_c$, respectively, for the turbulence boundary conditions. Note that the freestream static pressure has been defined using the static pressure which was measured using the Pitot-static probe. The flow inside the intake was defined using the experimental measurements of static pressure, along with the mass flow which was calculated from the static pressure levels. In FLUENT 12.1, it is possible to specify a desired mass flow in conjunction with the static pressure [106]. The solver performs incremental changes on the static pressure at the outlet to satisfy a mass flow of $1.467 kgs^{-1}$ which was calculated from the experimental measurements.

6.3.2.3 Turbulence modelling

The vortex convection simulations in sections 6.1.3.2 and 6.2.4 demonstrated notable differences between the results obtained with eddy-viscosity and RSM turbulence models. It was shown that it is necessary to employ an RSM to correctly simulate the vortex as it convects in a uniform freestream flow. It is therefore of great interest to evaluate the performance of eddy-viscosity and RSM models for vortex ingestion simulations. In particular, it will be possible to determine if the unsuitability of eddy-viscosity models for vortical flows has a detrimental effect on simulations of engineering interest. To this end, the $k-\omega$ SST turbulence model has been employed, in addition to the Linear Pressure Strain RSM model.

6.3.2.4 Numerical scheme and convergence strategy

The simulations were performed using the steady, implicit, density-based solver implemented in FLUENT 12.1, in a manner which is similar to the vortex convection simulations as detailed in section 6.1.2.3. However, in contrast to the convection simulations, convergence could only be achieved using a strategy where the numerical scheme is modified during the iterative convergence process. The convergence strategy was different for the $k-\omega$ SST and RSM simulations. For the $k-\omega$ SST turbulence model, the simulation was initialised using uniform freestream conditions, in conjunction with a CFL number of 1 and 1^{st}-order upwind numerical scheme for continuity, momentum, and turbulence equations. After 500 iterations, the CFL number was increased to 2, and the numerical scheme was changed to the 2^{nd}-order upwind scheme. After a further 500 iterations, the 3^{rd}-order MUSCL numerical scheme was employed, and a CFL number of 5 was selected. Following an additional 1500 iterations, the intake static pressure and target mass flow conditions were prescribed, and iterations were continued by progressively increasing the CFL number to 20. Approximately 20000 iterations in total were required to achieve satisfactory convergence. In general, the continuity residuals reached a value of $10^{-}4$, the momentum residuals achieved a value of 10^{-3}, and the turbulence equation residuals were of the order 10^{-6}.

For the simulations which employed the RSM turbulence model, it was necessary to initialise the simulations from the converged $k-\omega$ SST results using a CFL number of 5. In addition, a 1^{st}-order upwind numerical scheme was employed for all eight turbulence equations for the first 6000 iterations. The numerical scheme was then changed to the 2^{nd}-order upwind scheme, and the simulations were continued for a further 3000 iterations.

The CFL number was then increased to 10 for 3000 iterations, before a final increase to 20. Convergence was typically achieved after a total of 15000 iterations, at which the continuity and momentum residuals attained values of 10^{-5} and 10^{-3}. In addition, the turbulence terms converged at approximately 10^{-7}. Note that successful convergence could not be obtained using the 3^{rd}-order MUSCL discretisation scheme for the turbulence terms. Instead, the 2^{nd}-order upwind method was employed for these equations.

6.3.3 Results

6.3.3.1 Vortex characteristics

To assess the results obtained from the $k-\omega$ SST and RSM simulations, the vortex characteristics have been normalised using two approaches. The first is to normalise the vortex characteristics using the intake diameter D_i and the freestream velocity W_∞. Using this approach, it is possible to evaluate the evolution of the vortex characteristics as the vortex convects from the inlet plane of the CFD domain, inside the intake capture streamtube, and inside the intake. The second approach is to normalise the vortex characteristics for each case by their respective values at $z/D_i = 2.25$. This approach, which was employed in chapter 5 to analyse the experimental measurements, will allow an assessment of the vortex intensification levels which have been obtained in the simulations.

The streamwise velocity at the vortex centre (w_c/W_∞), vortex core radius (r_c/D_i), peak tangential velocity ($V_{\theta,max}/W_\infty$, peak streamwise vorticity ($\omega_{z,max}D_i/W_\infty$), core circulation ($\Gamma_c/W_\infty D_i$), and peak flow angularity (α_{max}) are shown in Figures 6.23(a) to 6.23(f). The values of w_c/W_∞ (Figure 6.23(a)) as the vortex convects from the inlet plane towards the intake at $z/D_i = 0$ are similar for both turbulence models. Furthermore, the results from the CFD simulations are in good agreement with the experimental measurements during the streamtube contraction process. In particular, between $z/D_i = 2.25$ and $z/D_i = 0.20$, the differences between the simulated and experimental values of w_c/W_∞ reduce from 16% to 6% for the $k-\omega$ SST model, and from 6% to zero for the RSM simulations. The results in Figure 6.23(a) also demonstrate that the intake perturbation field has little effect at $z/D_i = 2.25$. For example, the RSM simulation results indicate that the value of w_c/W_∞ at $z/D_i = 2.25$ is only 4% greater than the value at the inlet plane of the CFD domain. This provides further evidence that it was appropriate in chapter 5 to consider the vortex characteristics at $z/D_i = 2.25$ as the unperturbed values prior to contraction inside the capture streamtube.

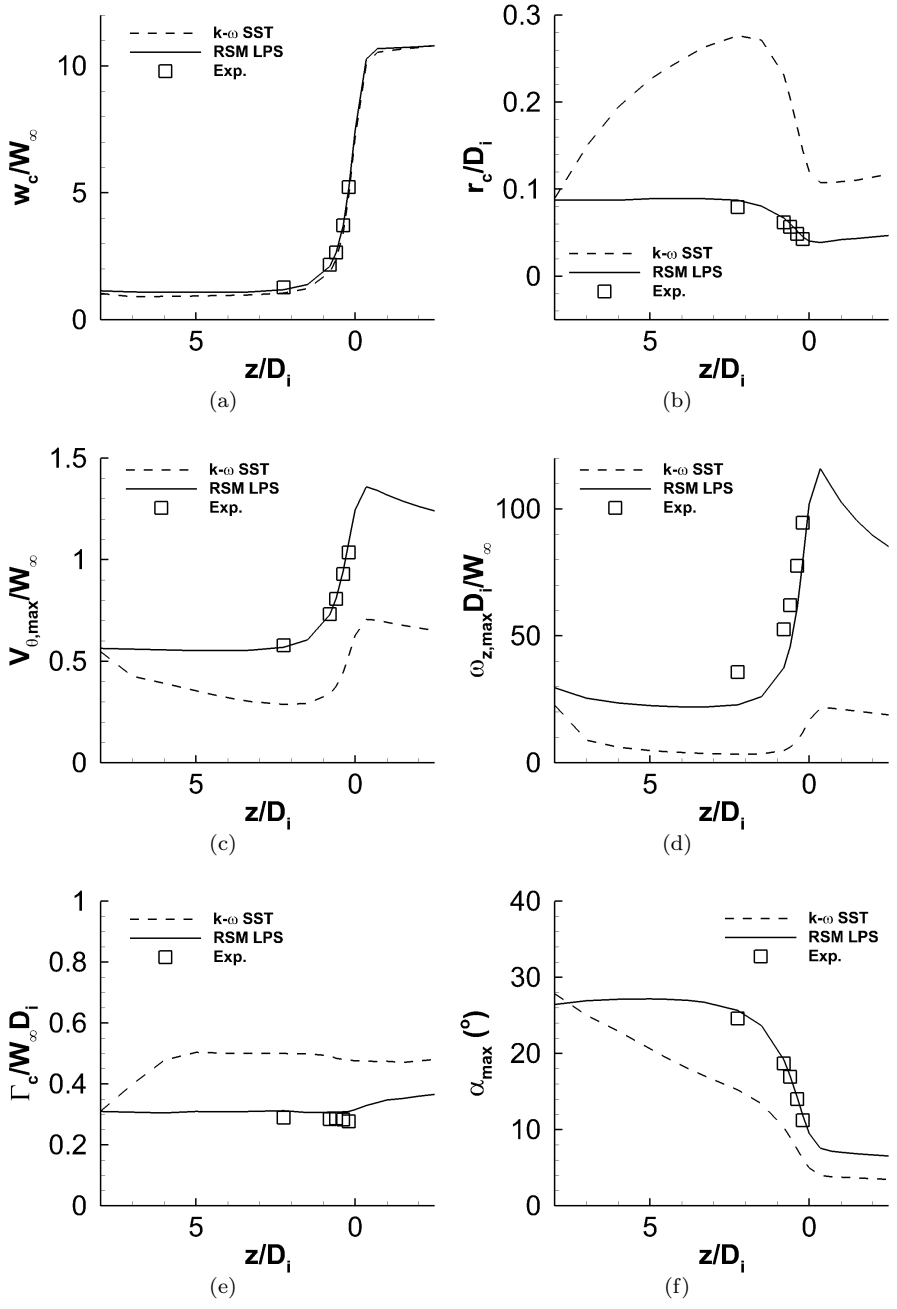

FIGURE 6.23: Evolution of vortex characteristics during ingestion as a function of distance from the intake highlight plane (z/D_i), vortex characteristics normalised by intake inner diameter (D_i) and freestream velocity (W_∞), $Re_v = 3.4 \times 10^4$, VR=10.3, (a): Vortex core radius (r_c/c), (b) Vortex peak tangential velocity ($V_{\theta,max}/W_\infty$), (c): Vortex peak streamwise vorticity ($\omega_{z,max}D_i/W_\infty$), (d): Vortex core circulation ($\Gamma_c/W_\infty D_i$), (e): Vortex peak flow angularity (α_{max})

The evolution of the vortex core radius (Figure 6.23(b)), peak tangential velocity (Figure 6.23(c)) and peak streamwise vorticity (Figure 6.23(d)) indicates that the vortex in the $k-\omega$ SST simulations is subject to notable levels of diffusion between the inlet plane and the beginning of the streamtube contraction at approximately $z/D_i = 2.25$. In particular, the vortex grows to a maximum of 3.06 times the value of r_c prescribed at the inlet plane, with a peak tangential velocity and peak streamwise vorticity which are only 53% and 15% of the inlet plane values. In contrast, the RSM simulations feature very low levels of vorticity diffusion, such that r_c/D_i and $V_{\theta,max}/W_\infty$ are equal to the values prescribed at the inlet plane, and $\omega_{z,max}D_i/W_\infty$ has reduced by 23%. The contrasting results between the two turbulence modelling approaches provides a clear indication of the limitations of using eddy viscosity turbulence models for vortex simulations, since the mesh characteristics and turbulence models are identical for both cases. These limitations are also apparent in the core circulation values, Figure 6.23(e), which increase by 62% in the initial stages of the convection process, that is, between the inlet plane and $z/D_i = 5$. In contrast, the vortex obtained in the RSM simulations features a constant core circulation during the convection phase, which is consistent with experimental measurements [1].

The large diffusion levels which have been obtained upstream of the intake for the $k-\omega$ SST simulations has a notable influence on the subsequent vortex intensification process. The vortex in the $k-\omega$ SST is larger than the experimental measurements, and the values of peak tangential velocity, peak streamwise vorticity, and peak flow angularity, are substantially under-estimated. As a consequence, the vortex intensification process is not captured correctly using the $k-\omega$ SST model. Meanwhile, the results from the RSM simulations are in good agreement with the experiments for the range of z/D_i positions which were measured experimentally. In particular, the difference between the simulations and the measurements is less than 10% for the vortex core radius, 5% for the peak tangential velocity, and 6% for the peak flow angularity. However, the peak vorticity levels which have been obtained from the RSM simulations feature a larger difference from the experimental measurements. At $z/D_i = 2.25$, the vortex in the RSM simulations features a peak vorticity which is 64% of the value obtained in the experiments. This appears to be a result of vorticity diffusion takes place as the vortex convects from the inlet plane to the intake. During the intensification process, the differences between the simulations and the measurements improves, such that the simulated streamwise vorticity at $z/D_i = 0.20$ is 84% of the measured value.

The results from the RSM simulation show that peak vorticity is most challenging characteristic to capture in the correct manner. As the vortex convects from the inlet plane towards the intake, there is a notable reduction in the peak vorticity (Figure 6.23(d)).

In contrast, the parameters which are evaluated at the core radius, such as the vortex core radius, peak tangential velocity, and core circulation (Figures 6.23(b), 6.23(c) and 6.23(e)) undergo little change during the same convection process. This result shows that vorticity diffusion is strongest at vortex centre, and has a smaller impact on the vortex flowfield beyond the vortex centreline. A similar result was obtained in the analysis of the experimental measurements of vortex intensification in chapter 5. Therefore, it is clear from the results of the CFD simulations that, similar to the intensification process, the effect of vorticity diffusion is not uniform across the vortex core. Subsequently, during the vortex intensification process, the characteristics from the RSM simulations which have been evaluated at the core radius are in very good agreement with the experimental measurements. Although the initial value of the peak streamwise vorticity is lower than the experimental measurements at $z/D_i = 2.25$, the evolution of the peak vorticity in the streamtube contraction is in good agreement with the measurements. Thus, the results from the CFD simulations are consistent with the findings from the analysis of the experimental measurements in chapter 5.

A similar result was obtained in the analysis of the vortex ingestion measurements. In particular, it was found that the parameters which have been measured at the vortex core radius are in good agreement with the vortex filament model, whereas diffusion has an impact on the peak vorticity at the vortex centre

The results in Figures 6.23(a) to 6.23(f) demonstrate the likely issues of using eddy viscosity turbulence models for vortex simulations. Firstly, it is not possible to capture the evolution of the vortex while it convects in the flow upstream of the intake. As a consequence, the vortex at the beginning of the intensification process does not feature the correct characteristics. The second issue is that, since the vortex intensification levels are not correct, simulations with an eddy-viscosity model are likely to result in misleading inlet flow distortion characteristics. For example, at $z/Di = -1.0$, the peak flow angularity as given by the $k-\omega$ SST model is only 53% of the value given by the RSM simulations. This may have a notable impact on the conclusions which are obtained from inlet flow distortion studies. Consequently, the inlet flow distortion characteristics for this vortex ingestion case have been investigated in section 6.3.3.2.

Given the excellent agreement between the RSM simulation results and the experimental measurements, it is possible to conclude that the CFD approach which has been employed is suitable for vortex ingestion simulations. It is therefore possible to use the simulation results to obtain additional understanding of the vortex ingestion process in the flow downstream of the experimental measurement planes. The evolution of w_c/W_∞ (Figure

6.23(a)) indicates that the flow continues to contract from $z/D_i = 0.20$ to approximately $z/D_i = -0.75$. Thus, the contraction process is complete downstream of the intake highlight plane, after which there is a very slow rise in w_c/W_∞. As the flow moves along the intake, it is anticipated that the boundary layers will grow in thickness. Therefore, the gradual increase in blockage will produce a small increase in velocity, as observed in Figure 6.23(a). Inside the intake, the vortex features a peak flow angularity of approximately 7^o, which is notably smaller than the flow angularity associated with the unperturbed vortex. The evolution of the vortex characteristics (Figures 6.23(b) to 6.23(d) and Figure 6.23(f)) between $z/D_i = 0.20$ and $z/D_i = -0.75$ is consistent with vortex intensification. After w_c/W_∞ stabilises inside the intake, the vortex evolves in a manner consistent with vorticity diffusion, such that there is an increase in the r_c/D_i, coupled with a reduction in $V_{\theta,max}$ and $\omega_{z,max}$. The diffusion rates are greater than those experienced in the flow upstream of the intake. This is anticipated, since the gradients of vorticity inside the vortex are greater after intensification, so the diffusion due to laminar and turbulent momentum transfer will be more intense. In addition, due to smaller vortex core radius (Figure 6.23(b)), the number of mesh elements which resolve the vortex core has also reduced from 16 mesh elements in the freestream flow to approximately 8 to 10 mesh elements inside the intake. Thus, the levels of mesh related numerical diffusion are expected to have increased. This reduced in-plane mesh resolution is likely to be the cause for the 18% increase in the vortex core circulation as the vortex enters the intake flow, since a similar effect has been observed in the vortex convection simulations when the in-plane mesh resolution is low (Figure 6.6(d)).

6.3.3.2 Distortion characteristics

The vortex characteristics in the preceding section demonstrated that the vortex undergoes a notable transformation from the unperturbed freestream flow to inside the intake. There is a need to assess the corresponding intake flow distortion levels which result from the ingestion of a vortex. To do this, the intake flow has been extracted at $z/D_i = -0.70$ downstream of the intake highlight plane. This axial location inside the intake is representative of the position of the aerodynamic interface plane for civil aircraft engines [72]. The contours of normalised total pressure ($P_0/P_{0,\infty}$) and flow angularity (α) have been extracted for both the $k-\omega$ SST and RSM simulations, Figures 6.24(a) to 6.24(d).

For both turbulence models, the total pressure contours (Figures 6.24(a) and 6.24(b)) demonstrate that there is little total pressure loss inside the vortex core, and the primary source of total pressure loss inside the intake flow is attributed to the intake boundary

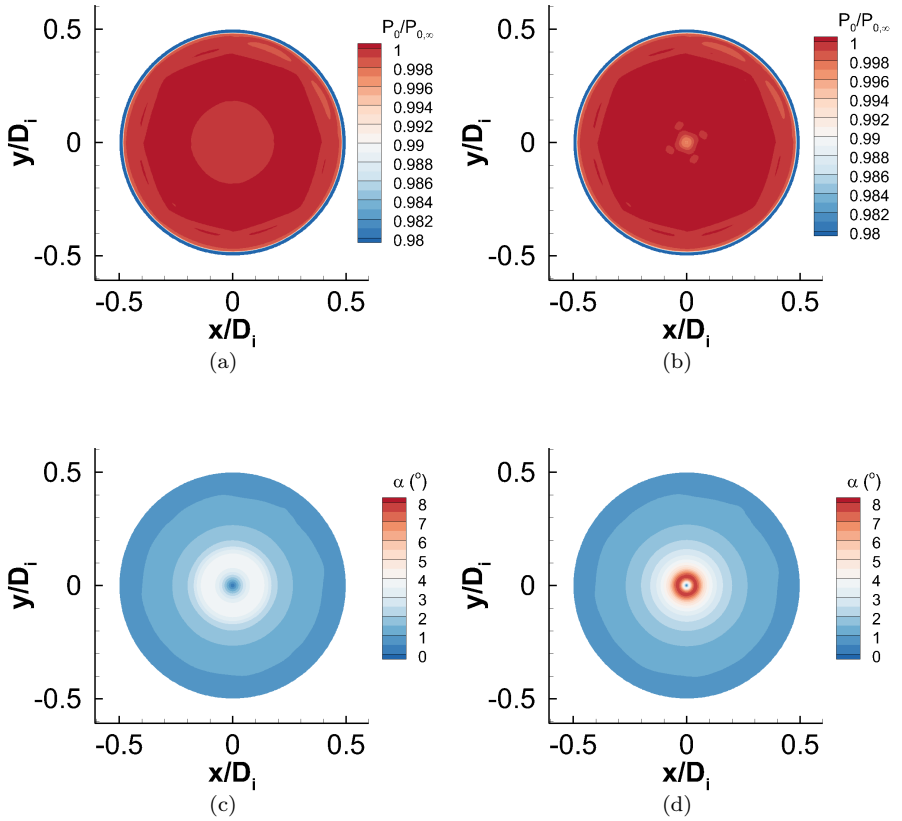

FIGURE 6.24: Inlet flow distortion characteristics at $z/D_i = -0.70$ downstream of the intake highlight plane, $Re_v = 3.7 \times 10^4$, VR=10.3, vortex ingested along intake centreline, (a): Total pressure contours ($P_0/P_{0,\infty}$), $k-\omega$ SST, (b) Total pressure contours ($P_0/P_{0,\infty}$), RSM LPS, (c): Flow angularity ($\alpha = tan^{-1}(V_\theta/w)$, $k-\omega$ SST, (d): Flow angularity ($\alpha = tan^{-1}(V_\theta/w)$, RSM LPS

layers. For example, in the RSM simulations, the total pressure loss at the vortex centre corresponds to $0.997P_{0,\infty}$, which is clearly small. This is in qualitative agreement with the sub-scale experimental measurements obtained by Talwar [71] and Hodjatzadeh [73], who reported similar total pressure loss levels.

The total pressure distortion levels, expressed in terms of the DC60 distortion coefficient (Table 6.2), are also negligible. However, the vortex imparts measurable levels of flow angularity across the intake flow, Figures 6.24(c) and 6.24(d), in the form of a bulk flow rotation in the positive direction about the streamwise axis. The peak flow angularity levels are strongly dependent on the turbulence model. A maximum of 3.9^o is obtained for the $k-\omega$ SST simulations, which is half of the value which was observed in the RSM simulations. This difference is a result of the excessive numerical diffusion levels which

TABLE 6.2: Distortion descriptors for sub-scale vortex ingestion, $Re_v = 3.7 \times 10^4$, VR=10.3, vortex ingested along intake centreline, $k-\omega$ SST and RSM turbulence models

	$k-\omega$ SST	RSM (LPS)
DC60	9.30E-04	8.50E-04
SC60	4.46E-05	3.51E-05
SI (^{o})	1.4409	1.5249

were observed in the results of section 6.3.3.1. This notable difference in results is not reflected in the swirl distortion descriptors, Table 6.2. The SC60 coefficient, which is of the order of 10^{-5}, indicates very low levels of swirl distortion. This is expected since the flow consists of an axisymmetric bulk swirl. This result highlights that the SC60 parameter is not appropriate to evaluate the swirl distortion levels when the vortex is ingested close to the intake centreline. A third parameter which can be used to quantify the inlet flow distortion levels is the swirl intensity (SI) [113], Eqs. 6.12 to 6.14, where $\alpha(\theta)_i$ is the swirl angle as a function of circumferential position θ_i along ring i evaluated at a constant radius.

$$SI = \frac{SS_i k \times \theta_i^+ + |SS_i^-| \times \theta_i^-}{360} \tag{6.12}$$

$$SS_i^+ = \frac{1}{\theta_i^+} \int_{\theta_i^+} \alpha(\theta)_i d\theta_i \tag{6.13}$$

$$SS_i^- = \frac{1}{\theta_i^-} \int_{\theta_i^-} \alpha(\theta)_i d\theta_i \tag{6.14}$$

The swirl intensity parameter (SI) corresponds to 1.44^o and 1.53^o for the $k-\omega$ SST and the RSM simulations, which shows that there is only a small increase in this parameter between the two turbulence modelling approaches. The small increase in SI may be attributed to the fact that although the vortex in the RSM simulations features greater in-plane swirl velocities, the vortex is smaller, and so the largest in-plane velocities cover a smaller area of the intake flow that the vortex flow obtained from the $k-\omega$ SST simulations. This is consistent with the previous observations that the flow contraction has a damping effect on the distortion associated with the vortex. Note that the distorted

flow inside complex s-shaped intakes can be characterised by SI values of between 6 and 12 [113], which demonstrates that the swirl distortion levels which have been obtained in the sub-scale simulations moderate in comparison to the distortions which are measured inside complex intake geometries. Despite the low levels of the distortion descriptors, it should be emphasised that even small levels of flow angularity in the intake flow are sufficient to impact the performance of an aircraft engine. For example, given an average flow angularity of only 2^o, a loss in surge margin of approximately 2.5% was measured by Meyer et al. [9]. In addition, the distortion descriptors provide a mass-averaged description of the entire intake flow. It is possible that the response of an aircraft engine may be more closely linked to the maximum flow angularity values in small areas of the intake flow, such as in the immediate vicinity of the hub.

Overall, the inlet flow distortion characteristics which have been determined from the CFD simulations are consistent with the limited number of experimental measurements of the flow distortion which results from vortex ingestion. Therefore, the CFD method which has been developed herein provides a method to investigate a range of vortex ingestion scenarios.

6.4 Scale effects

The sub-scale vortex convection and ingestion simulations have been used to establish an approach to simulate vortex ingestion using CFD. This has been possible due to the availability of sub-scale wing-tip vortex measurements in the literature and, crucially, the first comprehensive experimental investigation of vortex ingestion. This CFD method has been used in the previous section to provide new insight into the evolution of a sub-scale wing-tip vortex as it enters into a sub-scale intake. Of course, engineering investigations of vortex ingestion are concerned with full-scale configurations, for which there is currently very little understanding. Thus, it is necessary to employ the validated CFD method to investigate vortex ingestion at full-scale. Two important objectives will be achieved. Firstly, wing-tip vortex measurements have demonstrated that the vortex evolution is strongly dependent on the vortex Reynolds number, which generally increases from sub-scale to full-scale. It is consequently important to establish if similar trends are prevalent during vortex ingestion. Thus, the full-scale vortex ingestion simulations will establish fundamental understanding of the effect of scale on vortex intensification flow physics. Secondly, using a realistic aircraft intake geometry, it will also be possible to characterise the likely inlet flow distortion characteristics during vortex ingestion at representative conditions.

In this section, the details of the CFD approach are provided. This includes the intake geometry, the mesh characteristics, the boundary conditions approach, and the numerical scheme. Then, the test matrix is described, which identifies the intake conditions and vortex characteristics which are investigated. Finally, the results of the CFD simulations are analysed.

6.4.1 Test matrix

It is necessary to determine representative conditions for the vortex ingestion simulations. In particular, suitable unperturbed vortex characteristics, freestream conditions, and intake flow conditions, must be identified. To do this, it is constructive to consider a possible future engine-airframe configuration which is likely to be susceptible to vortex ingestion, such as the medium-sized civil airliner shown in Figure 6.25.

This configuration is of similar dimensions to current single-aisle civil airliners, such as the Boeing 757, and features rear-mounted engines and canards at the forebody of the aircraft. For such a configuration, there is a risk that the canard wing-tip vortex will enter the capture streamtube of the intake. As discussed in the Introduction, the risk of vortex ingestion is likely to be greatest during end-of-runway operations, such as the rotation phase of the take-off run. For this category of aircraft, a rotation velocity of $70ms^{-1}$ is appropriate. Under take-off conditions, a representative civil aircraft engine will feature an intake flow Mach number of 0.47, and a corresponding flow velocity of $W_i = 145ms^{-1}$. Therefore, at rotation, the intake velocity ratio $VR = W_i/W_\infty$ is equal to 2.1. To estimate the characteristics of the canard wing-tip vortex, it is necessary to prescribe the canard dimensions. Possible future airliner configurations with canards were investigated by Strohmeyer and Seubert [114]. The canards which were investigated featured a surface area of between 10% and 23% of the primary wing area. Thus, a

FIGURE 6.25: Possible future civil airliner with rear-mounted engines and canards [3]

value of 15% was selected as a suitable, first-order approximation to the area of the canards on the conceptual aircraft configuration in Figure 6.25. The wing area of the Boeing 757-200, corresponding to $35m^2$ was taken to be representative of the conceptual aircraft wings. Thus, the canard area was found to be $5.25m^2$. The canard geometry was assumed to consist of an unswept, rectangular wing, with an aspect ratio of 5[114], which results in a canard chord and semi-span of 2.65m and 6.6m. To obtain an estimate for representative values for the size and strength of a canard wing-tip vortex, it has been assumed that the canard wing consists of a NACA 0012 section with a rectangular wing-tip. It is then possible to estimate the wing-tip vortex characteristics using the wing-tip vortex measurements which have been obtained in this research. A suitable approach is to consider the worst-case in terms of the vortex characteristics, where the vortex strength is greatest. This takes place at the maximum lift coefficient [17]. The current experimental measurements were acquired close to the maximum lift coefficient of the NACA 0012 vortex generator (section 3.5), and are thus appropriate to be used to estimate the canard vortex characteristics. In section 4.3, the non-dimensional vortex core circulation and core radius (Table 4.1) correspond to $\Gamma_c/W_\infty c = 0.205$ and $r_c/c = 0.545$, respectively. Note that these values correspond to the NACA 0012 wing-tip vortex at an angle of attack of 12^o, and a chord Reynolds number of 3.6×10^5. This angle of attack is unlikely to be attained during normal aircraft operation, but represents the condition where the lift coefficient, and so the vortex strength, is greatest [17]. It is acknowledged that, during normal aircraft operation, the control surfaces of an aircraft do not operate at large incidences or close to the maximum lift coefficient. However, such a condition can be considered as the worst-case in terms of the possible characteristics of the vortex which is generated by the canard, since the vortex strength is greatest. Based on the preceding values, for a chord length of 2.65m and a freestream velocity of $70ms^{-1}$, the vortex core circulation and core radius are, respectively, $40.74m^2s^{-1}$ and 0.144m. The core circulation corresponds to a vortex Reynolds number of 2.7×10^6, which is two orders of magnitude greater than the values associated with the vortices which were investigated experimentally in chapter 4. It is also of interest to consider a vortex ingestion scenario at a lower freestream velocity, prior to the rotation phase. As the freestream velocity is reduced, there is a corresponding increase in the intake velocity ratio (W_i/W_∞) since the intake flow velocity is typically constant throughout the take-off run [2]. Therefore, the capture streamtube contraction levels are increased, which will result in a corresponding rise in the vortex intensification levels (section 5.2.1). The measurements of the wing-tip vortex in the unperturbed flow demonstrate that the non-dimensional circulation and core radius ($\Gamma_c/W_\infty c$ and r_c/c) increase by less than 5% when the freestream velocity was reduced from $35.3ms^{-1}$ to $11.0ms^{-1}$ (Table 4.1). Therefore,

TABLE 6.3: Full-scale and sub-scale vortex ingestion configurations

Scale	Full-scale	Sub-scale	Full-scale	Sub-scale
VR (W_i/W_∞)	2.1	2.1	4.9	4.9
W_i	145	74.5	145	74.5
W_∞	75	35.4	32	15.2
M_i	0.47	0.22	0.47	0.22
Γ_c/W_iD_i	0.108	0.146	0.046	0.063
r_c/D_i	0.055	0.082	0.055	0.082
Re_v	2.7×10^6	7.3×10^4	1.2×10^6	3.1×10^4
Re_c	1.3×10^7	3.5×10^5	5.6×10^6	1.5×10^5

as a first-order approximation, it is appropriate to consider $\Gamma_c/W_\infty c$ and r_c/c as constant values. An intake velocity ratio of 4.9 was selected, which corresponds to a freestream velocity of $32ms^{-1}$. Therefore, at this freestream velocity, the vortex Reynolds number is 1.2×10^6 (Table 6.3).

Sub-scale simulations have also been conducted assuming an intake inner diameter (D_i) and vortex generator chord of 0.1m and 0.15m, respectively. These values correspond to the intake and vortex generator geometries which were investigated in the sub-scale vortex ingestion experiments of chapter 5. The sub-scale and full-scale simulations feature identical intake velocity ratios to ensure the simulated vortex experiences the same flow contraction characteristics. Thus, for a VR of 2.1, the intake velocity and freestream velocity are $74.5ms^{-1}$ and $35.4ms^{-1}$, respectively. This condition was investigated experimentally in chapter 5. To achieve an intake velocity ratio of 4.9, the freestream velocity is reduced to $15.2ms^{-1}$. Thus, using the sub-scale values of D_i and c, the vortex Reynolds numbers for the two sub-scale freestream velocities are 7.3×10^4 and 3.1×10^4.

Based on the scaling approach which has been employed, it is interesting to note that the vortex core radius and core circulation, when normalised by the intake diameter and intake flow velocity, are very similar for the sub-scale and full-scale simulations. For example, for an intake velocity ratio of 2.1, Γ/W_iD_i is equal to 0.108 and 0.146 for the full-scale and sub-scale conditions, respectively. In addition, the core radii are 0.06 and 0.08. This result indicates that, despite the large differences in the absolute values of the vortex characteristics, the scaling approach has ensured that the vortex perturbation field, relative to the intake flow, is similar for both scales.

6.4.2 CFD Methods

6.4.2.1 Intake geometry

The geometry for an modern, high-bypass ratio civil aircraft engine has been created [115]. The intake geometry, Figure 6.26, included a representative diffusion section, and a non-rotating spinner. The fan diameter D_i is 2.61m, and the hub to tip ratio is 0.3. Finally, the fan face is located at a distance of approximately $0.5D_i$ downstream of the intake highlight plane.

6.4.2.2 Mesh characteristics

The sub-scale simulations were performed using the mesh which was detailed in section 6.3.2.1. Using a similar approach to the sub-scale simulations, the full-scale intake was placed inside a Cartesian domain, Figure 6.27. The Cartesian domain extended a distance of $12.5D_i$ in the x- and y-directions from the intake centreline. In addition, the inlet boundary was located at a distance of $5D_i$ upstream of the intake highlight plane, and the domain extended $10D_i$ domain downstream of the intake highlight plane.

Close to the intake centreline axis, a refined Cartesian mesh was employed to maintain a suitable mesh resolution in the location of the vortex. In accordance with the findings from

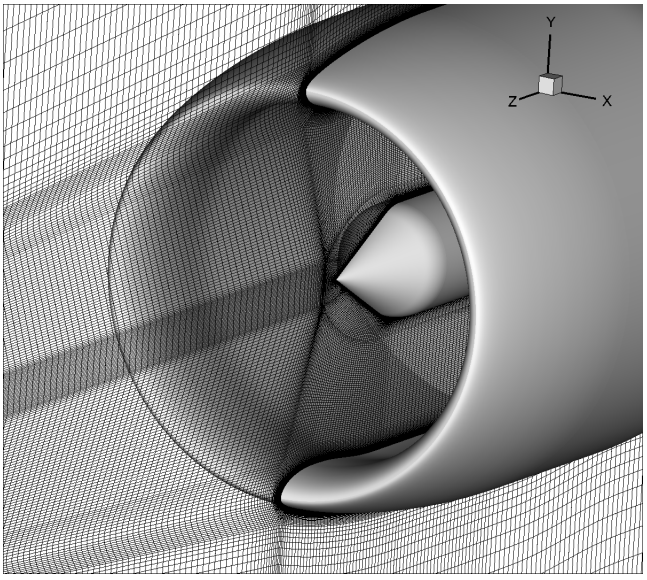

FIGURE 6.26: Details of intake geometry for full-scale vortex ingestion simulations

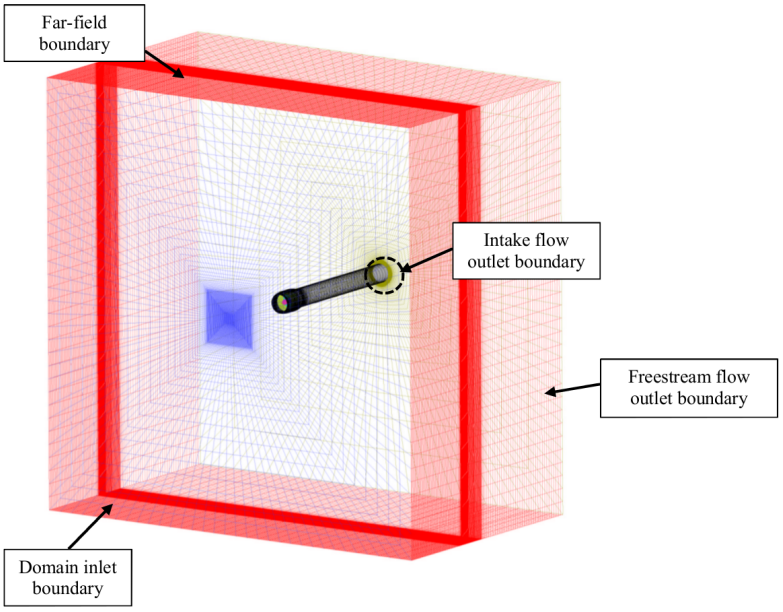

FIGURE 6.27: Details of the CFD domain employed for full-scale vortex ingestion simulations

the vortex convection simulations, a resolution of 32 elements per vortex core diameter was employed. In addition, 16 mesh elements were employed to resolve a single vortex swirl loop. Using this approach, it was possible to minimise the effects of grid related numerical diffusion. The domain consisted of approximately 7×10^6 mesh elements.

6.4.2.3 Boundary conditions

The flow conditions which have been selected in section 6.4.1 for investigation have not been measured experimentally. Thus, to generate the appropriate vortical inlet boundary conditions, it necessary to employ models for the vortex perturbation field. The Vatistas vortex model [103] has been found to provide a good description of the vortex tangential velocity profile [50]. The tangential velocity distribution, as a function of the vortex core radius, total circulation, and distance from the vortex centre, is given by Eq. 6.15 , where n is an integer. It has been found that n=1 is suitable for ground vortices [72], meanwhile n=2 is more appropriate for wing-tip vortices [50]. Thus, a value of n=2 has been selected to define the inlet boundary conditions in this research. Expressions for the streamwise and radial velocity distributions for wing-tip vortices were developed by Bhagwat and Leishman [50], as given in Eq. 6.16 and 6.17. The parameter A is equal to the integral of the streamwise momentum perturbation associated with the vortex [116],

and z is the distance downstream of the wing trailing edge. The sub-scale experimental measurements have demonstrated that a streamwise velocity perturbation of 15% greater than the freestream velocity is measured at the conditions of interest. It is assumed that the vortex boundary conditions are at a distance of $z/c = 6$. Therefore, for the sub-scale and full-scale configurations, it is possible to evaluate the values of A and z which are required for Eq. 6.16 and 6.17.

$$V_\theta(r) = \frac{\Gamma_0}{2\pi}\left[\frac{r}{(r_c^{2n} + r^{2n})^{\frac{1}{n}}}\right] \tag{6.15}$$

$$V_z(r,z) = V_\infty - \frac{A}{z}\left[1 - \frac{r^2}{(r_c^{2n} + r^{2n})^{\frac{1}{n}}}\right] \tag{6.16}$$

$$V_r(r,z) = -\frac{Ar}{2z^2}\left[1 - \frac{r^2}{(r_c^{2n} + r^{2n})^{\frac{1}{n}}}\right] \tag{6.17}$$

In a manner similar to the sub-scale vortex ingestion simulations, the static and total pressure distributions have been computed under the assumption of incompressible flow, with no total pressure loss. An exact solution for the static pressure exists [103], as given in Eq. 6.18

$$p = p_\infty + \frac{\pi\rho}{4}\left[\frac{\Gamma_0}{2\pi r_c}\right]^2\left[\frac{2}{\pi}tan^{-1}\left(\frac{r}{r_c}\right)^2 - 1\right] \tag{6.18}$$

Therefore, using Bernoulli's theorem, it is possible to calculate the total pressure distribution, Eq. 6.19.

$$p_0 = p + \frac{1}{2}\rho\left(V_\theta^2 + V_r^2 + V_z^2\right) \tag{6.19}$$

Equations 6.15 to 6.19 were used to generate the flow direction and total pressure distributions on the CFD inlet plane for the freestream conditions and vortex characteristics which are given in Table 6.3. A MATLAB script was employed to calculate r using the mesh node positions on the inlet plane, and to calculate the corresponding perturbation field at each node location. This perturbation field was then imported into FLUENT using the Profile loader.

The vortex convection simulations in section 6.2.4 highlighted that appropriate turbulence boundary conditions must be prescribed in conjunction with the vortex velocity and pressure fields. However, there is a dearth of measurements of wing-tip vortices at full-scale in the literature to guide the definition of the boundary conditions for the full-scale simulations. In section 6.2.4, a model for the turbulent kinetic energy (k) profile was developed. It was shown the model could be used successfully to initialise the turbulence field inside the vortex. A required input for the model is the maximum turbulent kinetic energy, k_{max}/W_∞^2. A value of $k/W_\infty^2 = 0.013$ was employed. However, in section 4.3.4, it was shown that the turbulence intensity TI/W_∞, and thus the turbulent kinetic energy, increases as a function of the vortex Reynolds number and the chord Reynolds number. Further insight can be provided from Figures 6.28(a) and 6.28(b), which show the Cartesian turbulence components ($u_{rms}/W_\infty, v_{rms}/W_\infty, w_{rms}/W_\infty$) as a function of the vortex and chord Reynolds numbers. The Cartesian components for the sub-scale measurements increase linearly with the vortex Reynolds number and the chord Reynolds number. The measurements of Chow et al. [23] have also been included. These measurements have been acquired at a vortex Reynolds number of 1.5×10^6, which is the same order of magnitude as the conditions to be investigated in the full-scale simulations (Table 6.3). In particular, the values of u_{rms}/W_∞, v_{rms}/W_∞, and w_{rms}/W_∞, are similar to the levels which were measured at sub-scale for $Re_v = 7.4 \times 10^4$.

It is not possible to develop a trend for the turbulence components as a function of Re_v and Re_c due to the lack of data which is available in the literature to populate Figures 6.28(a) and 6.28(b). However, the trend which is indicated in Figures 6.28(a) and 6.28(b)

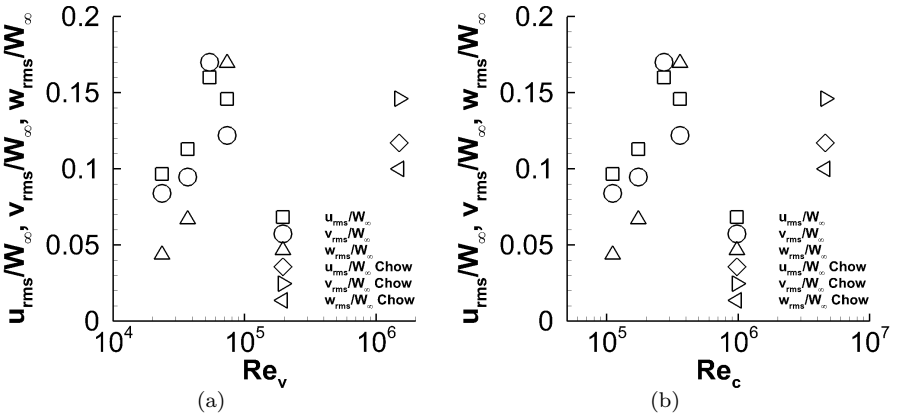

FIGURE 6.28: Experimental measurements of Cartesian components of turbulence at vortex centre (u_{rms}/W_∞,v_{rms}/W_∞,w_{rms}/W_∞) as a function of (a): vortex Reynolds number (Re_v), (b): wing chord Reynolds number (Re_c)

is that the turbulence intensity does not continue to increase in proportion to Re_c and Re_v but, instead, stabilises at a value of between $0.10W_\infty$ and $0.15W_\infty$. Based on this result, it can therefore be concluded that the turbulence levels which have been measured using the PIV measurements at a vortex Reynolds number of 7.4×10^4 provide a suitable representation of the likely levels at full-scale. At this condition, a turbulent kinetic energy of k_{max}/W_∞^2=0.032 was measured, and was thus specified in Eq. 6.6 to generate the turbulent kinetic energy distribution for the full-scale vortex cases. In addition, a length scale of $l = 1r_c$ has been employed to produce distributions of the turbulent dissipation rate (Eq. 6.4).

6.4.2.4 Numerical scheme

Steady simulations were conducted using the same as that employed in the sub-scale validation. In particular, a $3rd$-order MUSCL scheme was used for the continuity and momentum equations, and a 2^{nd}-order upwind model was utilised for the turbulence terms. In the full-scale simulations, the Green-Gauss node-based method [106] was employed for the calculation of the gradients of the fluxes, since this method was found to provide better convergence characteristics than the least-squares approach [115].

Iterative convergence was achieved using a similar convergence strategy to the sub-scale vortex ingestion simulations 6.3.2.4. The RSM simulations were initiated from converged $k - \omega$ SST results using a CFL number of 5. The continuity and momentum equations were solved using the 3^{rd}-order MUSCL discretisation scheme, and a 1^{st}-order upwind numerical scheme was employed for all eight turbulence equations for the first 1000 iterations. The numerical scheme was then changed to the 2^{nd}-order upwind scheme, and the simulations were continued for a further 1000 iterations. The 3^{rd}-order MUSCL scheme was then implemented, and the CFL number was then progressively increased to 60 such that convergence was typically achieved after a total of 10000 iterations. All equations converged with residuals of 10^{-12}.

6.4.3 Results

The purpose of the full-scale simulations is to identify the influence of scale on the vortex ingestion process. Thus, the analysis in this section is focussed first on the evolution of the vortex as it undergoes intensification. This will establish fundamental understanding of the vortex flow physics at realistic vortex Reynolds numbers. Thereafter, the inlet flow

distortion characteristics will be assessed to determine the likely effects of vortex ingestion on a realistic, full-scale aircraft engine.

6.4.3.1 Vortex characteristics

To evaluate the evolution of the sub-scale and full-scale vortices, the vortex centre velocity ($w_c/w_{c,0}$), core radius ($r_c/r_{c,0}$), peak tangential velocity ($V_{\theta,max}/W_\infty$), peak streamwise vorticity ($\omega_{z,max}D_i/W_\infty$), have been extracted and normalised by the value at $z/D_i = 2.25$. In addition, the peak flow angularity (α_{max}) has been calculated.

The evolution of $w_c/w_{c,0}$, Figure 6.29(a), demonstrates that the streamtube contraction levels are almost identical for the sub-scale and full-scale cases which have been investigated. This is expected, since the intake velocity ratio features the same value for both scales. In addition, it is clear that the streamtube contraction characteristics for a simple intake model are similar to those obtained for a realistic aircraft geometry. The change in vortex core radius (Figure 6.29(b)), peak tangential velocity (Figure 6.29(c)), and peak streamwise vorticity (Figure 6.29(d)) indicate that the full-scale and sub-scale vortex intensification process is very similar in nature. One aspect which must be investigated is the rate at which vorticity diffusion takes place for the sub-scale and full-scale simulations. This is investigated in chapter 7.

6.4.3.2 Inlet flow distortion

The simulations of vortex ingestion for the sub-scale validation test case (section 6.3.3.2) highlighted that the inlet flow during vortex ingestion consisted of a bulk swirl distortion coupled with low levels of total pressure distortion. A similar assessment of the inlet flow distortion characteristics has been performed for the full-scale and sub-scale vortex ingestion simulations. Note that the measurement plane on the full-scale simulations has been positioned at $z/D_i = 0.55$, which corresponds to the approximate location of the engine fan face [115].

The total pressure loss contours for the sub-scale cases (Figures 6.30(a) and 6.30(b)) are consistent with the findings in section 6.3.3.2, since the total pressure loss is less than $0.01P_{0,\infty}$ at the vortex centre, and the intake boundary layer is the greatest source of total pressure loss throughout the intake flow. The total pressure loss at the vortex centre is 0.994 for VR=2.1, and is 0.999 for VR=4.9, so it can be concluded that the change in streamtube contraction levels has little influence on the loss levels inside the vortex core.

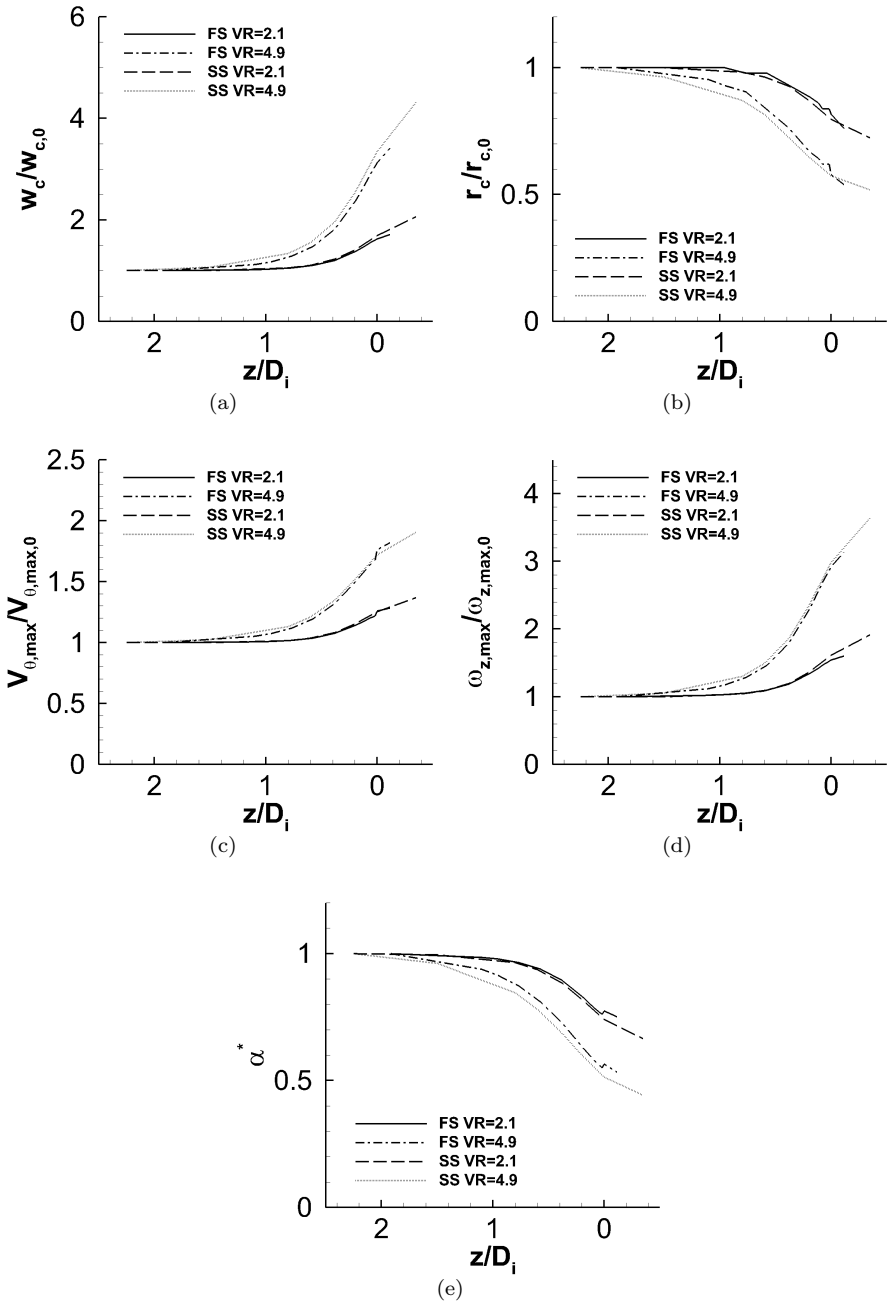

FIGURE 6.29: Evolution of vortex characteristics during ingestion as a function of distance from the intake highlight plane (z/D_i), vortex characteristics normalised by intake inner diameter (D_i) and freestream velocity (W_∞), $Re_v = 3.4 \times 10^4$, VR=2.1 and 4.9, (a): Streamwise velocity at vortex centre ($w_c/w_{c,0}$), (b): Vortex core radius ($r_c/r_{c,0}$), (c) Vortex peak tangential velocity ($V_{\theta,max}/V_{\theta,max,0}$), (d): Vortex peak streamwise vorticity ($\omega_{z,max}/\omega_{z,max,0}$), (e): Vortex peak flow angularity (α_{max})

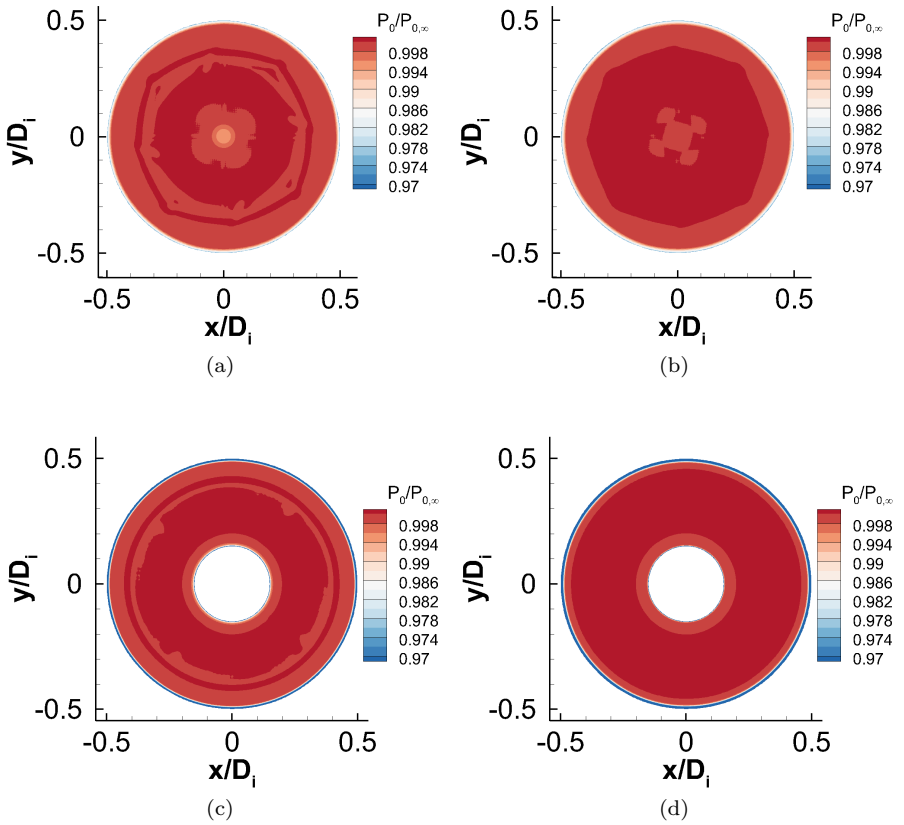

FIGURE 6.30: Total pressure loss contours ($P_0/P_{0,\infty}$) at $z/D_i = -0.55$ downstream of the intake highlight plane for full-scale simulations and $z/D_i = -0.70$ for sub-scale simulations, (a): Sub-scale, VR=2.1, (b) Sub-scale, VR=4.9, (c): Full-scale, VR=2.1, (d): Full-scale, VR=4.9

This is consistent with the experimental measurements of Talwar [71] and Hodjatzadeh [73]. The full-scale simulations (Figures 6.30(c) and 6.30(d)) demonstrate that the total pressure loss at the fan-face is characterised by loss which is adjacent to both the intake casing and the spinner. For VR=2.1, The loss levels in the fluid at the spinner and the casing consist of a minimum of 0.897 and 0.915, respectively. Since the vortex has been ingested along the intake centreline axis, then the vortex wraps around the spinner as it moves through the intake. Thus, the total pressure loss which is surrounding the spinner can be attributed to both the spinner boundary layer loss and the loss associated with the vortex core. When the intake velocity ratio is increased to 4.9, the minimum values of total pressure at the spinner and the casing are 0.893 and 0.912. Therefore, the differences in the flow distortion characteristics between the two intake VR conditions are small. This is reflected in the DC60 values, Table 6.4, which are equal to 1.64 and 1.58 for VR=2.1

TABLE 6.4: Full-scale and sub-scale inlet flow distortion characteristics

Scale	Sub-scale	Full-scale	Sub-scale	Full-scale
VR	2.1	2.1	4.9	4.9
DC60	6.00×10^{-3}	1.52×10^{-3}	6.10×10^{-3}	1.47×10^{-3}
SC60	9.81×10^{-4}	2.22×10^{-5}	3.57×10^{-4}	1.76×10^{-5}
SI_{av} (^{o})	6.51	3.73	2.95	1.65

and VR=4.9, respectively. It is apparent that a slightly greater DC60 has been obtained for VR=2.1 as a result of the marginally greater levels of loss adjacent to the spinner. The DC60 values, similar to the sub-scale simulations, are approximately constant for both intake velocity ratios. Importantly, the DC60 levels are of the order 10^{-3}, which corresponds to negligible levels of total pressure distortion.

The contours of flow angle for the sub-scale simulations (Figures 6.31(a) and 6.31(b)) demonstrate that the flow consists of notable levels of swirl distortion. In particular, the vortex results in a bulk swirl flowfield, where the peak flow angle reaches 19.9^o for VR=2.1, and 12.7^o for VR=4.9. It should be reminded that the peak flow angles in the unperturbed flow are identical for both intake velocity ratios, and the differences are simply a result of the different streamtube contraction levels. In particular, the experimental measurements (chapter 5) and the corresponding analysis demonstrated that the peak flow angles are inversely proportional to the streamtube contraction levels. As discussed in section 6.3.3.2, the SC60 distortion descriptor does not provide an accurate reflection of the swirl distortion levels in the intake flow. This result is also evident for the sub-scale simulations in this section, since the SC60 parameter corresponds to 9.8×10^{-4} and 3.7×10^{-4} for VR=2.1 and 4.9 (Table 6.4). The value of SI, however, provides a better representation of the notable levels of swirl inside the intake flow. For intake velocity ratios of 2.1 and 4.9, SI corresponds to 6.5^o and 3.0^o. Limited information which is available in the open literature suggests that the distortion which occurs inside complex s-shaped intakes can be characterised by SI values of between 4 and 11 [113]. The distortion which results from such intake designs is known to have a marked impact on the performance of aircraft engines, and so it can be concluded that the swirl distortion levels which have been measured from the sub-scale simulations do indicate the potential for a loss in aircraft engine performance. At full-scale conditions, the peak flow angle corresponds to 6.2^o for an intake velocity ratio of 2.1 (Figure 6.31(c)). This value is notably lower than that observed in the equivalent sub-scale simulation (Figure 6.31(a)), where

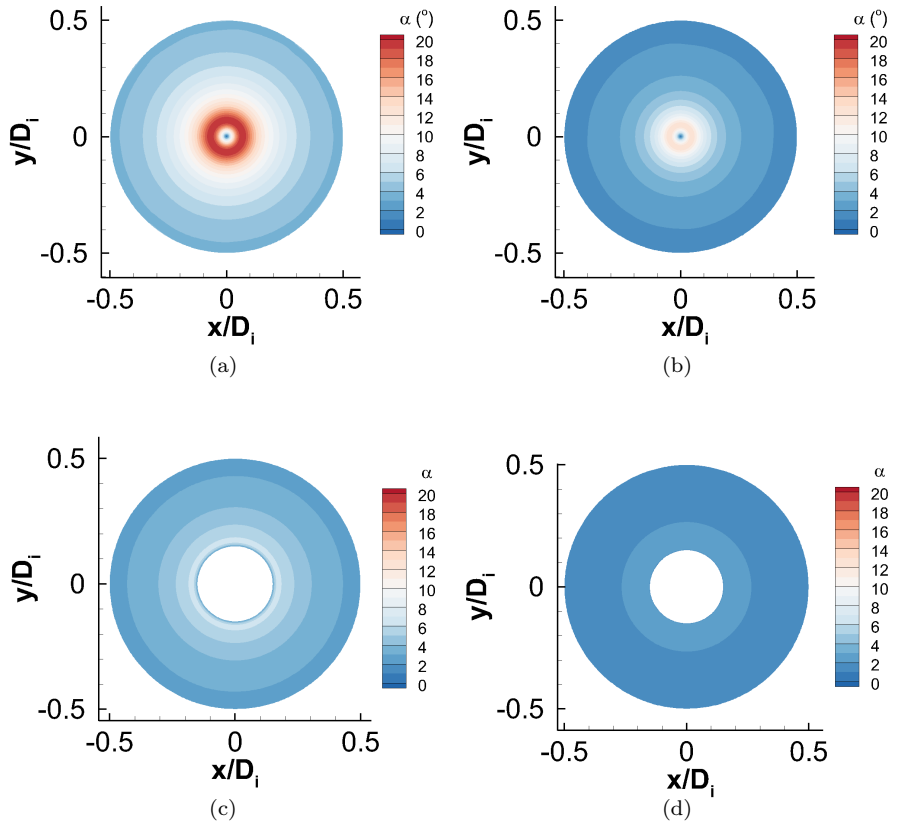

FIGURE 6.31: Flow angularity contours (α) at $z/D_i = -0.55$ downstream of the intake highlight plane for full-scale simulations and $z/D_i = -0.70$ for sub-scale simulations, (a): Sub-scale, VR=2.1, (b) Sub-scale, VR=4.9, (c): Full-scale, VR=2.1, (d): Full-scale, VR=4.9

the peak flow angle was 19.9^o. The vortex characteristics (Figure 6.29(b) to 6.29(e)) show that the characteristics of sub-scale and full-scale vortices are very similar throughout the contraction process upstream of the intake highlight plane. Therefore, the differences arise inside the intake. As the vortex wraps around the spinner, the vortical flow is forced radially outward from the intake centreline. To conserve angular momentum, there must be a corresponding reduction in the tangential velocity of the vortex. Furthermore, the contours of streamwise velocity inside the intake (Figure 6.32) demonstrate that, close to the spinner, the flow undergoes an acceleration as it moves through the intake. As a consequence, in the flow surrounding the spinner, the ratio V_θ/w_c is expected to reduce, which will produce a net reduction in α. Similar conclusions can be reached for the results obtained at an intake velocity ratio of 4.9 (Figure 6.31(d)).

It should be emphasised that the low DC60 and SC60 values which have been reported

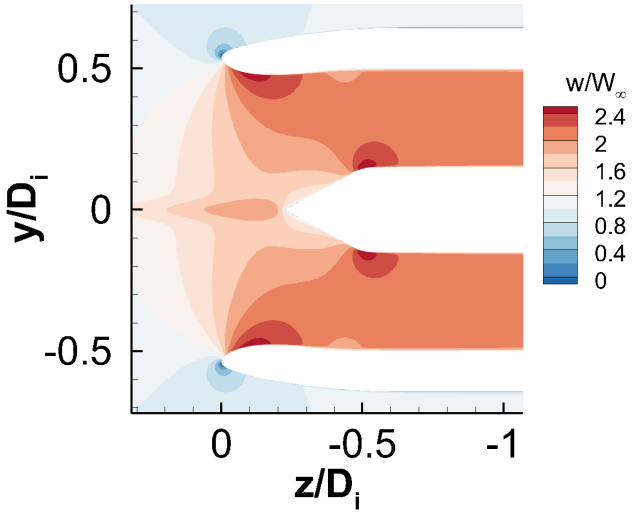

FIGURE 6.32: Contours of streamwise velocity (w_c/W_∞) on symmetry plane $x = 0$

in Table 6.4 are a consequence of the fact that the distortion characteristics inside the intake are axisymmetric (Figures 6.30(a) to 6.31(d)). The CFD approach which has been developed in this research have been employed by Heimbucher [115] and Pernod [117] to investigate the inlet flow distortion levels which result from the ingestion of a vortex at various locations inside the intake capture streamtube relative to the intake centreline. Vortex strengths of $\Gamma^* = \Gamma_0/W_i D_i$ of 0.29, 0.47 and 0.95 were investigated with a vortex core radius $r_c^* = r_c/D_i$ of 0.29. The vortex size and strengths have been selected to represent possible canard wing-tip vortices [117]. Note, therefore, that the vortices simulated by Pernod [117] feature the same order of magnitude of vortex strength as those considered in the full-scale studies in this research (Table 6.3). However, the vortex core radius in the freestream is 5.3 times larger than the current simulations. Importantly, the values of DC60, SC60 and SI increase as the vortex ingestion position is moved from the intake centreline to 30% and 60% of the intake capture streamtube radius, Figures 6.33(a), 6.33(b) and 6.33(c). The distortion levels are notably higher than the values which are obtained when the vortex is ingested at the intake centreline. For example, the DC60 values range between 0.02 and 0.14 for ingestion at 90% of the intake capture streamtube radius. In addition, SC60 descriptors lie within the range of 0.073 and 0.28. These values are of the same order as those which are known to induce engine instability [76]. Similarly, the SI values, which range from 3.9^o to 12.6^o when the vortex is ingested along the intake centreline (Figure 6.33(c)), are of a similar order to the SI values which have been measured on complex s-shaped intakes [113]. Consequently, it can be concluded

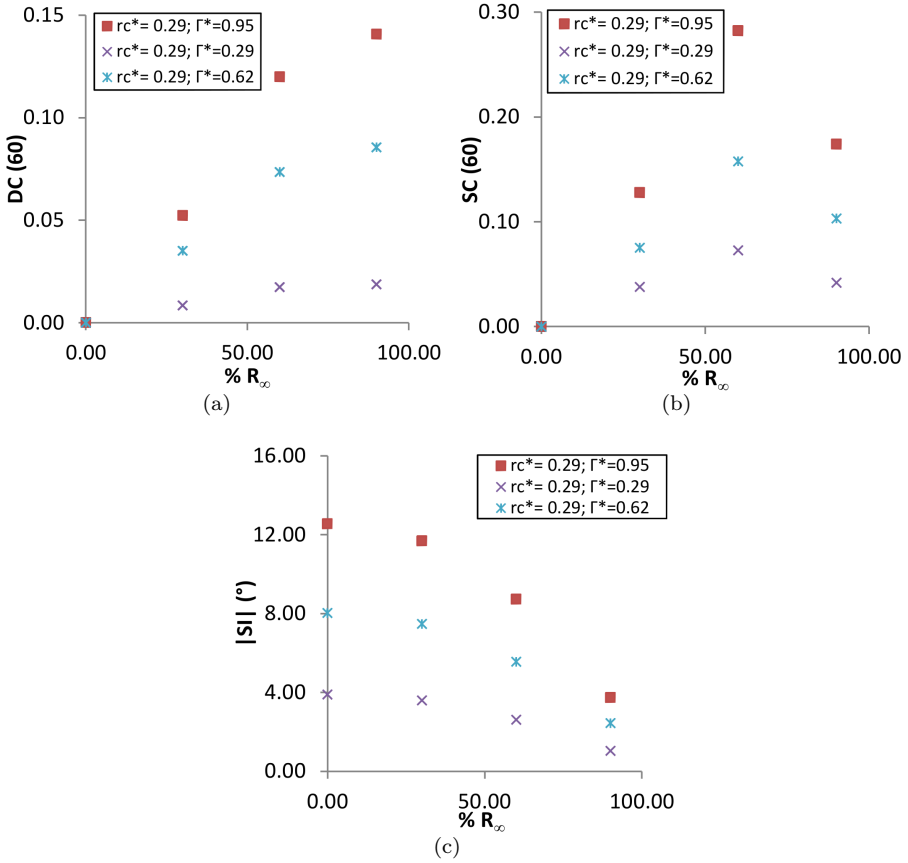

FIGURE 6.33: Inlet flow distortion characteristics at $z/D_i = -0.55$ downstream of the intake highlight plane for full-scale simulations, VR=1.71, influence of vortex strength (Γ^*) and distance of vortex centre location from intake centreline axis ($\%R_\infty$), where R_∞ is the radius of the intake capture streamtube far upstream of the intake, figures from [117], (a): DC60, (b): SC60, (c): SI

that the distortion levels which result from the ingestion of representative canard wing-tip vortices have the potential to induce a loss of engine stability and performance.

The sub-scale and full-scale simulations of vortex ingestion have demonstrated that the inlet flow total pressure distortion is dominated by the total pressure loss inside the intake boundary layers, which is very low. The primary difference which was observed between the sub-scale and full-scale simulations is the presence of is presence of additional total pressure loss at the spinner surface in the full-scale simulations. Importantly, the total pressure loss attributed to vortex is small on both scales. This result is in agreement with previously reported measurements of sub-scale and full-scale vortex ingestion flows. Furthermore, total pressure distortion levels across intake flow are unaffected by an increase in intake velocity ratio. As anticipated, swirl distortion characteristics are dependent

on intake velocity ratio. Swirl distortion levels are lower for full-scale simulations than sub-scale simulations. The primary reason is the presence of the spinner, which causes a reduction in tangential velocity coupled with an increase in streamwise velocity, the overall effect of which is to reduce the peak swirl angles. Therefore, sub-scale simulations in the absence of the spinner will over-estimate the swirl distortion characteristics. Nevertheless, full-scale simulations indicate swirl intensity values have the potential to impact the performance of an aircraft engine.

6.5 Summary

Simulations have been performed using Computational Fluid Dynamics (CFD) to identify the correct approach to simulate vortex ingestion. An important feature of this work is that the intake is simulated in isolation, and the streamwise vortex is prescribed as a boundary condition upstream of the intake. A review of the literature has identified that it can be particularly challenging to simulate wing-tip vortices using CFD. The results from wing-tip vortex simulations have demonstrated that the agreement with experimental results can be poor, and is strongly dependent on the details of the mesh characteristics and the turbulence modelling approach. Few studies have elucidated the requirements for simulating an isolated wing-tip vortex, as required in this research. Additionally, there is little prior knowledge of the correct CFD approach for simulating vortex ingestion flows. Studies have been performed in this research to address this lack of knowledge.

Wing-tip vortex convection simulations were first conducted to evaluate the impact of the mesh resolution on the ability of the CFD solver to capture the vortex convection process. The evolution of the vortex characteristics was assessed using experimental measurements which are available in the literature. It was demonstrated that notable levels of numerical diffusion can result when the in-plane and out-of-plane mesh resolution is insufficient. As a consequence, the vortex diffuses rapidly, and the agreement with the experimental measurements is poor. Using the vortex convection results, it has been possible to establish the required mesh resolution to ensure that mesh-related numerical diffusion is minimised.

The CFD simulations have shown that eddy-viscosity turbulence models are inappropriate for simulating vortex convection and vortex ingestion flows. A notable result is that commonly-used eddy-viscosity models, such as the Spalart-Allamras and $k-\omega$ SST models, over-predict the rate at which the wing-tip vortex diffuses. This is a result of large levels of turbulence inside the vortex core which are generated by the turbulence model.

Eddy-viscosity models rely on the Boussinesq assumption, which states that the turbulence and strain rate tensors are aligned. The experimental measurements which have been obtained in this research, in agreement with those in the literature, show that the Boussinesq assumption is not appropriate for the vortex flows. As a result, turbulence models which employ the Boussinesq assumption are unable to capture the flow physics associated with vortices. The vortex convection simulations demonstrated that the vortex evolution is in good agreement with the experimental measurements when a Reynolds Stress Model (RSM) is employed. A key requirement for RSM simulations is that appropriate turbulence profiles must be prescribed at the inlet boundary condition. This research has demonstrated that it is necessary to prescribe profiles of the turbulent kinetic energy (k) and the turbulent dissipation rate (ϵ), in conjunction with a turbulence length scale of $l = 1r_c$. The sub-scale wing-tip vortex measurements (chapter 4) measurements have thus been utilised to create an analytical profile for the turbulent kinetic energy. In this way, it is possible to prescribe suitable turbulence boundary conditions when the vortex turbulence characteristics are not known a priori.

Simulations were also performed using a sub-scale vortex ingestion case which was investigated in the experimental programme. It was found that agreement between the experimental measurements and the results obtained with the $k - \omega$ SST turbulence model were poor. In particular, the vortex experiences notable levels of diffusion prior to the contraction process. However, the details of the vortex intensification process from the RSM simulations are in very good agreement with the experimental measurements. It is therefore concluded that RSM simulations, in conjunction with appropriate turbulence boundary conditions, are imperative for vortex intensification and vortex ingestion simulations. When applied to full-scale vortex ingestion flows, it has been found that the notable distortion levels arise from the ingestion of a typical canard wing-tip vortex.

Chapter 7

Synthesis and discussion

In the preceding chapter, it was demonstrated that the vortex intensification process can be subject to notable levels of diffusion. It was demonstrated, using the wide range of configurations which have been investigated in this research, that the diffusion levels are strongly dependent on the streamtube contraction levels, the details of the vortex prior to the streamtube contraction, and the trajectory the vortex follows inside the streamtube. Importantly, it was shown that, under certain conditions, a simple vortex filament model is not appropriate for modelling the evolution of a vortex inside a streamtube contraction. The purpose of this chapter is to detail the development of a semi-empirical model which can capture the effects of diffusion on the vortex as it undergoes intensification. Such a model will permit the development of understanding of the fundamental flow physics surrounding the diffusion process. In addition, a semi-empirical model will provide a validated approach to estimate the characteristics of a vortex following ingestion. This will provide invaluable information which can be used to evaluate the likely inlet flow distortion features which result from the ingestion of a streamwise vortex.

7.1 Semi-empirical model

The experimental measurements obtained in this research show that, for local streamtube velocity ratios ($w_c/w_{c,0}$) of greater than 2, vorticity diffusion plays a role in vortex intensification. It was found that diffusion has a measureable influence on the vortex characteristics, and it was demonstrated that the vortex undergoes less intensification than anticipated from vortex filament theory. The differences between the measurements and vortex filament theory were greatest when the vortex was ingested along the intake

centreline, and when the local streamtube contraction levels are large. Under such conditions, a model based on inviscid, incompressible theory does not adequately capture the evolution of the vortex inside the streamtube contraction, and it is therefore desirable to obtain a model for the effects of diffusion. The purpose of this section is to describe the implementation of a semi-empirical model which captures the diffusion process which takes place during vortex intensification.

7.1.1 Model formulation

In order to implement a model for vortex diffusion, it is useful first to consider the evolution of a vortex in a uniform streamwise flow. An example of this case is a wing-tip vortex which, following generation, will convect downstream of the wing. As discussed in section 2.3, vorticity diffusion results in a gradual increase in the vortex core radius, coupled with a reduction in the vortex peak tangential velocity. The rate at which the vortex diffuses has been found to depend on a number of factors, including the vortex Reynolds number and the streamwise velocity perturbation. It has been found that the Squire vortex model (Eq. 2.22) provides a good description of the vortex diffusion process, through the use of an empirical parameter defined as the apparent diffusion coefficient, δ is selected empirically to match the vortex growth rates with experimental measurements. A value of δ of more than 1 suggests that the vortex growth rate exceeds that attributed to laminar viscosity alone. A number of important aspects of the vortex diffusion process can be identified from the Squire vortex model. Consider a vortex of a given strength and a fixed initial core radius $r_{c,0}$. The growth of the vortex core radius as a function of time is therefore increased when δ increases, as illustrated qualitatively in Figure 7.1(a) for small values of time t. In addition, the vortex experiences a reduction in peak tangential velocity (Figure 7.1(b)) and peak streamwise vorticity (Figure 7.1(c)). As a result, δ can be considered as a measure of the strength of the diffusion process, such that an increase in δ represents an increase in the rate of diffusion. A second feature of vortex diffusion is that, as the initial vortex core radius reduces, for a given value of δ, the diffusion rates increase (Figure 7.1(d)). Thus, when the vortex size reduces, the rates of diffusion increase, and the increase in the vortex core radius per unit time is greater.

In this research, an approach is sought to implement the Squire vortex model as a diffusion correction to the vortex filament model. It has been demonstrated in the preceding paragraph that, using the Squire vortex model, the vortex diffusion process between two points in space can be characterised in terms of the time the vortex takes to convect between the points, plus a semi-empirical function of the vortex Reynolds number which

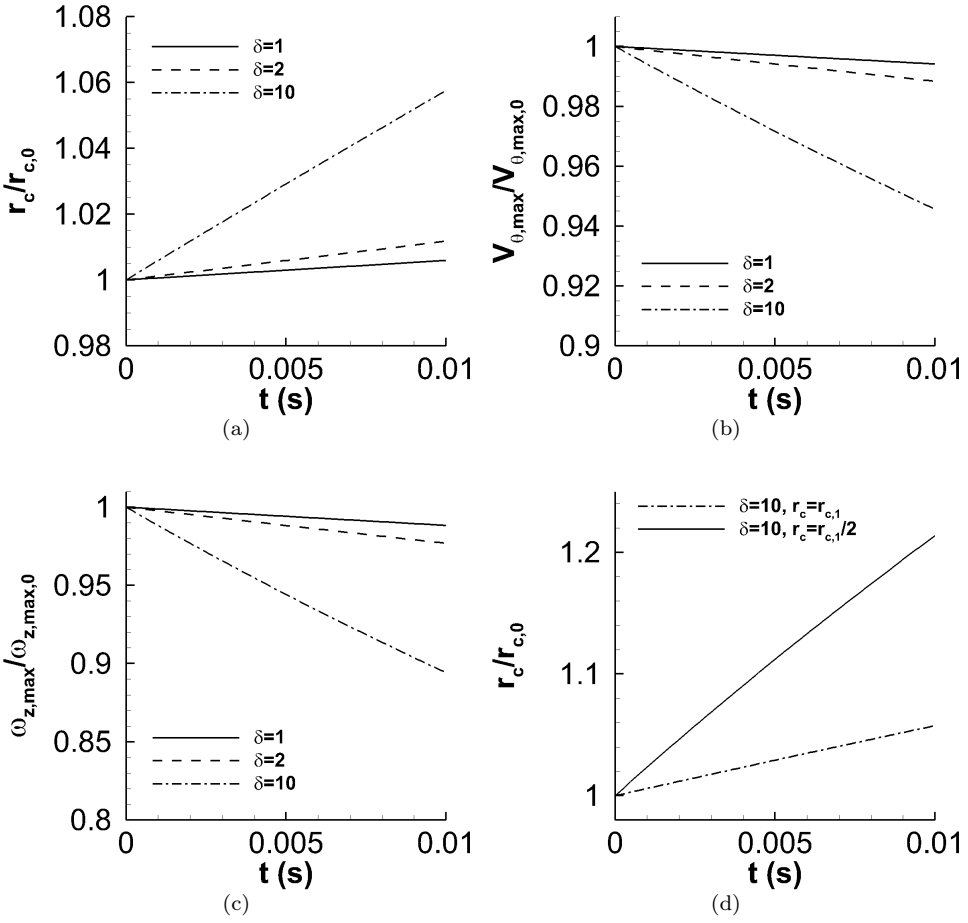

FIGURE 7.1: Evolution of streamwise vortex characteristics from the Squire vortex model Eq. 2.22, as a function of the apparent diffusion coefficient (δ) and time (t) for small values of t, (a): Vortex core radius ($r_c/r_{c,0}$), (b): Peak tangential velocity ($V_{\theta,max}/V_{\theta,max,0}$), (c): Peak streamwise vorticity ($\omega_{z,max}/\omega_{z,max,0}$), (d): Influence of initial core radius ($r_{c,1}$) on evolution of vortex core radius ($r_c/r_{c,0}$)

specifies the contribution of turbulent diffusion. A similar approach has been employed by Ananthan and Leishman [69]. A schematic of the approach developed in this research is given in Figure 7.2(a). Consider a streamwise vortex with an initial core radius of $r_{c,1}$ measured upstream of the streamtube contraction, where the freestream velocity is W_∞. It is assumed that the streamwise velocity perturbation inside the vortex is small at plane 1, so that $w_{c,1} = W_\infty$. At some point inside the streamtube contraction, the streamwise velocity has increased to w_2, and the core radius has reduced to ($r_{c,2}$). It is assumed that the effect of the coupling between the tangential and streamwise velocity fields is small, so that the streamwise velocity at the vortex centre remains approximately equal to that of the flow surrounding the vortex. The current experimental measurements have

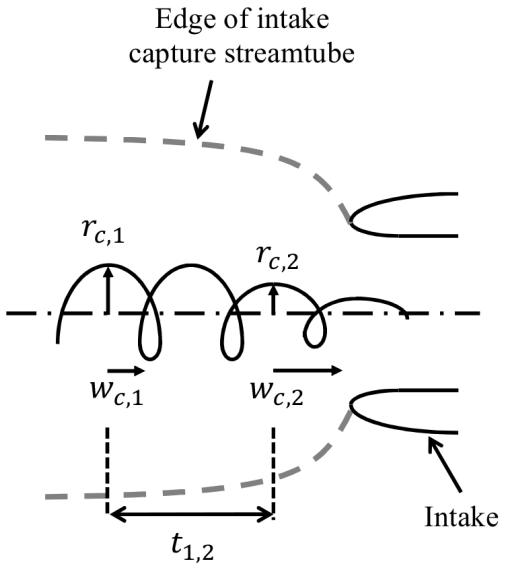

FIGURE 7.2: Schematic of intake flowfield and definitions for vortex intensification and diffusion models

demonstrated that this is a valid assumption where the streamwise velocity perturbation is small. Thus, in the absence of viscous or turbulent diffusion, the core radius $r_{c,2}$ is equal to the initial core radius ($r_{c,1}$) plus a change in core radius which is a result of inviscid, incompressible vortex filament intensification ($\Delta r_{c,VF}$). This can be calculated using Eq. 7.1 and, as anticipated, will produce a negative change in core radius for a contracting flow.

$$\Delta r_{c,VF} = r_{c,1}\sqrt{w_{c,1}/w_{c,2}} - r_{c,1} = r_{c,1}\left(\sqrt{w_{c,1}/w_{c,2}} - 1\right) \tag{7.1}$$

$$r_{c,2} = r_{c,1} + \Delta r_{c,VF} + \Delta r_{c,D} \tag{7.2}$$

It was demonstrated in chapter 5 that this relationship is appropriate where $w_c/w_{c,0}$ is less than approximately 2. However, at greater contraction levels, there is a gradual increase in the difference between the vortex filament model and the measurements. It was hypothesised that such differences between the measurements and the vortex filament result are caused by diffusion, and can be denoted $\Delta r_{c,D}$. Therefore, the vortex core radius can be determined using the combination of the vortex filament result, and the change in core radius due to diffusion, Eq. 7.2. The approach which has been proposed in this

research is to employ the Squire model (Eq. 2.22) to determine the value of $\Delta r_{c,D}$. Using the Squire vortex model, the change in core radius due to diffusion is given by Eq. 7.3, where δ_i is the apparent diffusion coefficient for vortex intensification. Note that, as expected, the diffusive contribution produces a positive change in core radius, which is in opposition to intensification.

$$\Delta r_{c,D} = \sqrt{r_{c,1}^2 + 4\alpha_l \delta_i \nu t_{1,2}} - r_{c,1} \tag{7.3}$$

In addition to the initial core radius $r_{c,1}$, there are two important inputs in to Eq. 7.3. The first is the convection time between the two points in the contraction ($t_{1,2}$). This can be calculated easily with knowledge of the streamtube velocity field in space. Once the vortex core radius, with the diffusion correction, is known for plane 2 using Eq. 7.2, the change in the vortex core radius ($r_{c,2}/r_{c,1}$) can be calculated (Eq. 7.3). This value can be considered to be the change in the vortex filament radius, corrected for diffusion. This change can then be used to determine the change in vortex filament properties, in a manner similar to the inviscid vortex filament theory which was detailed in section 2.4.1. In particular, the change in vortex core radius provides expressions for the vortex core average vorticity (Eq. 7.5), the peak streamwise vorticity (Eq. 7.6), and the peak flow angularity Eq. 7.7. To derive Eqs. 7.4 to 7.7, it is assumed that the core circulation of the vortex is constant. This is a valid assumption, since the measurements have shown that the changes in the vortex core circulation during intensification are smaller than the measurement uncertainty.

$$\frac{V_{\theta,max,2}}{V_{\theta,max,1}} = \frac{r_{c,1}}{r_{c,2}} \tag{7.4}$$

$$\frac{\omega_{z,av,2}}{\omega_{z,av,1}} = \left(\frac{r_{c,1}}{r_{c,2}}\right)^2 \tag{7.5}$$

$$\frac{\omega_{z,max,2}}{\omega_{z,max,1}} = \left(\frac{r_{c,1}}{r_{c,2}}\right)^2 \tag{7.6}$$

$$\alpha^* = \frac{(V_{\theta,max}/w_c)_2}{(V_{\theta,max}/w_c)_1} \tag{7.7}$$

A crucial input into the diffusion correction is the apparent diffusion coefficient (δ), the value of which is currently not known for vortex intensification flows. Note that Ananthan and Leishman [69], who used a similar approach to model helicopter rotor wake intensification, assumed that the apparent diffusion coefficient is constant and depends only on the vortex Reynolds number as given in Eq. 2.21. However, there has been no attempt to determine directly the value of δ during the intensification process, or to assess whether the value remains constant as a function of the vortex intensification levels.

7.1.2 Calculation of the apparent diffusion coefficient

The modelling approach selected in this research is to use the Squire vortex model to apply a diffusion correction to the vortex filament model. This requires a priori knowledge of the apparent diffusion coefficient. The purpose of this section is to evaluate the required value or trend for δ_i to permit the application of the Squire vortex model. This will complete the details required for a diffusion-corrected vortex filament model.

It is necessary to determine the behaviour of the apparent diffusion coefficient δ_i between two planes inside the streamtube contraction, denoted plane 1 and plane 2, (Figure 7.2(a)). Plane 1 corresponds to the measurements at $z/D_i = 2.25$, at which it is assumed that the vortex characteristics are equal to the unperturbed state. An expression for δ_i can then be derived by stating that the difference between the measured vortex core radius ($r_{c,2}$) and the core radius calculated from vortex filament theory ($r_{c,2,VF}$) is equal to the contribution from diffusion ($\Delta r_{c,D}$). Thus, the Squire vortex model can be employed to apply a correction to the vortex filament theory result. If we select the difference between the measurement and the vortex filament result ($r_{c,2} - r_{c,2,VF}$) as amount by which diffusion will cause the vortex core radius to increase during the time between the two measurement planes, then it is possible to express the Squire model as Eq. 7.8.

$$r_{c,1} + (r_{c,2} - r_{c,2,VF}) = \sqrt{r_{c,1}^2 + 4\alpha_l \delta_i \nu t_{1,2}} \tag{7.8}$$

In a manner consistent with the inviscid vortex filament model which was used to aid the analysis in the preceding chapter, the vortex filament theory here is implemented using the measured streamwise velocity at the vortex centre $w_{c,2}/w_{c,1}$. It is then possible to rearrange Eq. 7.8 to obtain an expression for the apparent diffusion coefficient (Eq. 7.9).

$$\delta_i = \frac{\left(r_{c,1} + r_{c,2} - r_{c,2,VF}\right)^2 - r_{c,1}^2}{4\alpha_l \nu t_{1,2}} \tag{7.9}$$

The convection time $t_{1,2}$ can be determined using the measured profile of the streamwise velocity w_c as a function of the distance travelled by the vortex (z). Inherent in this calculation is the assumption that the streamwise velocity at the vortex centre (w_c) is approximately equal to that of the surrounding flow. Therefore, the assumption that $t = z/W_\infty$ is valid, as required for the Squire vortex model (Eq. 2.21). In this research, $t_{1,2}$ was calculated using Simpson's Rule applied to the discrete measurements of w_c at each of the measurement planes.

The values of the δ_i have been calculated for the wide range of vortex ingestion configurations which have been investigated in this research. The analysis of the experimental measurements, conducted in chapter 5, found that the vortex undergoes lower levels of intensification than anticipated from vortex filament theory. The differences between the vortex filament model and the measurements increased in proportion to the local streamtube contraction levels. It was concluded that diffusion which results from laminar and turbulent momentum transfer was the likely cause of this trend. To provide further insight into this behaviour, the values of δ_i has been calculated for the NACA 0012 wing-tip vortex with a vortex Reynolds number of $Re_v = 3.7 \times 10^5$ for the case where the vortex has been ingested along the intake centreline. Note that three intake velocity ratios (VR), corresponding to 2.0, 5.1 and 10.3, have been investigated to produce a wide range of streamtube contraction levels. Wing-tip vortex convection measurements suggest that a value of δ_i of the order 10^1 is appropriate for the vortices measured in this research. Similar values have been calculated from the current experimental measurements (Figure 7.3), which range from close to zero for low contraction levels, to a maximum of 13 at

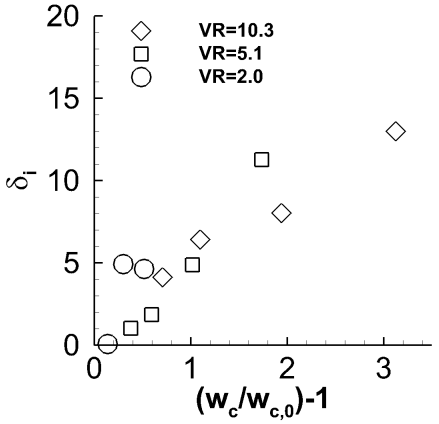

FIGURE 7.3: Apparent diffusion coefficient (δ_i) as a function of local streamwise velocity ratio ($w_c/w_{c,0}$-1) for intake velocity ratios of VR=10.3, 5.1 and 2.0, $Re_c = 1.7 \times 10^5$, $Re_v = 3.7 \times 10^4$, centreline ingestion

$w_c/w_{c,0}-1$ of 3.1. A value of $\delta_i = 0$ is expected at $w_c/w_{c,0}-1$=0, since this corresponds to the unperturbed condition. A negative value of δ_i was obtained at the lowest $w_c/w_{c,0}-1$. Inspection of Eq. 7.9 shows that such a value of δ_i occurs when the measured change in r_c is of a greater magnitude than that anticipated from vortex filament theory. It is likely that the low contraction levels, coupled with the measurement uncertainty on r_c, are the cause of the negative value. The calculated values of δ_i confirm that the impact of diffusion becomes greater as the contraction levels rise. This result also suggests that the rate of diffusion increases during the vortex intensification process. For example, when ($w_c/w_{c,0}$-1) is less than 1, the diffusion rates are small and close to the rates observed in laminar vortex diffusion. As a result, the impact of diffusion is also small, and the vortex characteristics are in close agreement with vortex filament theory. At greater contraction levels, however, the apparent diffusion coefficient increases to a value of 13 at ($w_c/w_{c,0}$-1)=3.1, which indicates that there has also been a corresponding rise in the diffusion rates. This increase can be attributed to two factors. Firstly, the vorticity levels inside the vortex core rise substantially during intensification, as demonstrated by the peak and average core streamwise vorticity measurements (Figures 5.8(d) and 5.8(e)). Therefore, even in the presence of purely laminar flow, one can expect an increase in the levels of diffusion inside the vortex core. In addition, the current measurements suggest that the turbulence levels inside the vortex core are large. Therefore, it is likely that turbulent diffusion also contributes to the increase in δ_i observed in the measurements.

The behaviour of the apparent diffusion coefficient as a function of the vortex Reynolds number, and for an even greater range of contraction levels than Figure 7.3, is shown in Figure 7.4(a). The data presented in Figure 7.4(a) corresponds to the results extracted from all of the NACA 0012 vortex generator configurations where the vortex was ingested along the intake centreline. It is clear from the wide range of conditions that the vortex diffusion rates increase as a function of the contraction levels. In addition, for a given ($w_c/w_{c,0}$-1), δ_i is somewhat sensitive to the initial characteristics of the vortex, prior to intensification. For example, at ($w_c/w_{c,0}$-1) of approximately 1.8, the value of δ_i increases from 3 to 11 when the vortex Reynolds number increases from $Re_v = Re_{v,0}$ to $Re_v = 1.6Re_{v,0}$. However, further increases in Re_v do not produce a corresponding rise in δ_i. This behaviour does not agree with the conclusions of Bhagwat and Leishman [50] who found that, for vortex Reynolds numbers of above 10^4, the value of δ_i increases monotonically with Re_v. It was concluded that the turbulent diffusion levels increased with the vortex Reynolds number due to a rise in the turbulence levels inside the vortex core. It should be noted that the experimental data which was analysed by Bhagwat and Leishman [50] comprised a far greater range of vortex Reynolds numbers than that considered in

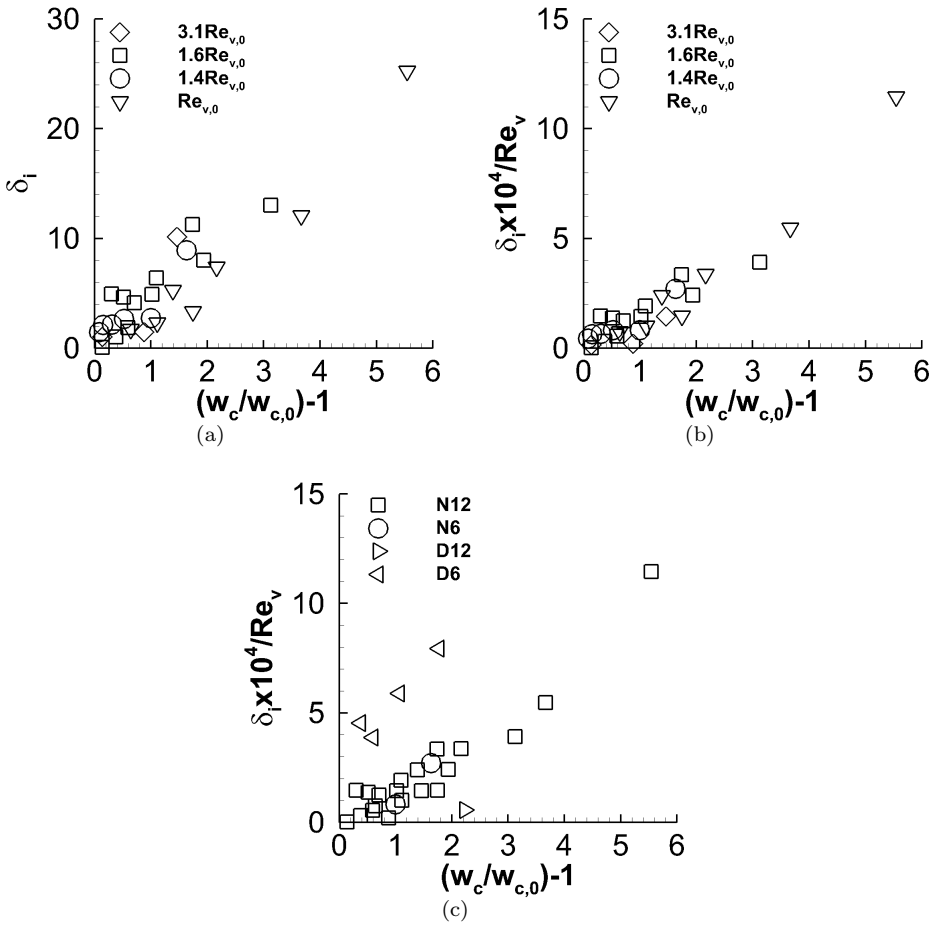

FIGURE 7.4: Apparent diffusion coefficient (δ_i) as a function of local streamwise velocity ratio ($w_c/w_{c,0}$-1), centreline ingestion, (a): Influence of vortex Reynolds number Re_v, where $Re_{v,0} = 2.4 \times 1{-}4$, (b): Influence of vortex Reynolds number Re_v, δ_i normalised by vortex Reynolds number ($\delta_i \times 10^4/Re_v$), (c): Influence of vortex type, where N and D refer to the NACA 0012 vortex generators, 12 and 6 refer to vortex generator angles of attack (α_{vg}) of 12^o and 6^o, respectively, δ_i normalised by vortex Reynolds number ($\delta_i \times 10^4/Re_v$)

this research. It is therefore likely that the differences in δ_i between $Re_v = Re_{v,0}$ and $Re_v = 3.1Re_{v,0}$ cannot easily be detected. Interestingly, there is a notable reduction in scatter when δ_i is normalised by the vortex Reynolds number ($\delta_i \times 10^4/Re_v$), Figure 7.4(b). Such behaviour confirms that δ_i increases approximately linearly with Re_v across the range of conditions which have been investigated in this research. This result is in agreement with the model for the apparent diffusion coefficient proposed by Squire [49] (Eq. 2.21), as well as the conclusions of Bhagwat and Leishman [50]. The link between the apparent diffusion coefficient and the vortex Reynolds number demonstrated in Figure

7.4(b) shows that, for a given streamtube contraction, the diffusion levels experienced by a vortex will increase with the vortex Reynolds number, due to an increase in the turbulent diffusion levels.

Further insight to the behaviour of δ_i can be provided by including the delta wing vortex measurements, Figure 7.4(c). It is clear that the delta wing vortex measurements do not conform with Eq. 2.21. In particular, only a single positive value of δ_i has been obtained for the delta wing vortex with a vortex Reynolds number of $2.4Re_{v,0}$. As observed in section 5.2.3, the delta wing vortex core radius is smaller than that anticipated from vortex filament theory at four of the five measurement planes, which means that a negative value of δ_i is obtained (Eq. 7.9). The single value of δ_i lies below the NACA 0012 wing-tip vortex trend, which indicates that the diffusion rates experienced by the vortex are lower than that observed on the NACA 0012 vortices at similar contraction levels and vortex Reynolds numbers. This also appears to be a consequence of the effect of the large out-of-plane velocity deficit. Further differences from the NACA 0012 wing-tip vortex trend have been observed in the values of δ_i/Re_v calculated for the delta wing vortex of vortex Reynolds number $Re_{v,0}$. In particular, the values lie some distance above the trend obtained from the NACA 0012 wing-tip vortex data, which demonstrates that the delta wing vortex features diffusion rates which are larger than anticipated at this vortex Reynolds number. Clearly, the vortex Reynolds number is not the only parameter which influences the diffusion rates experienced by the vortex.

In the previous chapter, the importance of Re_v was hypothesised from the behaviour of the changes in the peak streamwise vorticity ($\omega_{z,max}/\omega_{z,max,0}$) and the average vorticity ($\omega_{z,av}/\omega_{z,av,0}$). It is therefore promising that a similar dependence on Re_v has been found in δ_i, since this parameter has been calculated using the vortex core radius. The influence of Re_v on the change in the vortex core radius ($r_c/r_{c,0}$) is not apparent when plotted as a function of $w_c/w_{c,0}$ (for example, Figure 5.9(a)). The reason can be explained with reference to the NACA 0012 wing-tip vortex measurements, for vortex Reynolds numbers of $Re_{v,0}$, $1.6Re_{v,0}$ and $3.1Re_{v,0}$. Recall that the freestream velocity was used to control the control the vortex Reynolds number, and the intake mass flow was varied to maintain an approximately constant intake velocity ratio. Therefore, the convection time between the measurement planes $t_{1,2}$ decreases as the vortex Reynolds number is increased. From Eq. 2.22, the total effect of diffusion between two planes is proportional to both the convection time and the value of δ_i. At a vortex Reynolds number of $Re_{v,0}$, the value of δ_i is the lowest of the three cases (Figure 7.4(a)), and the convection time, for example, between $z/D_i = 2.25$ and $z/D_i = 0.20$ is approximately 0.0109s. When the vortex Reynolds number is increased to $3.1Re_{v,0}$, there is a corresponding rise in δ_i, but the convection

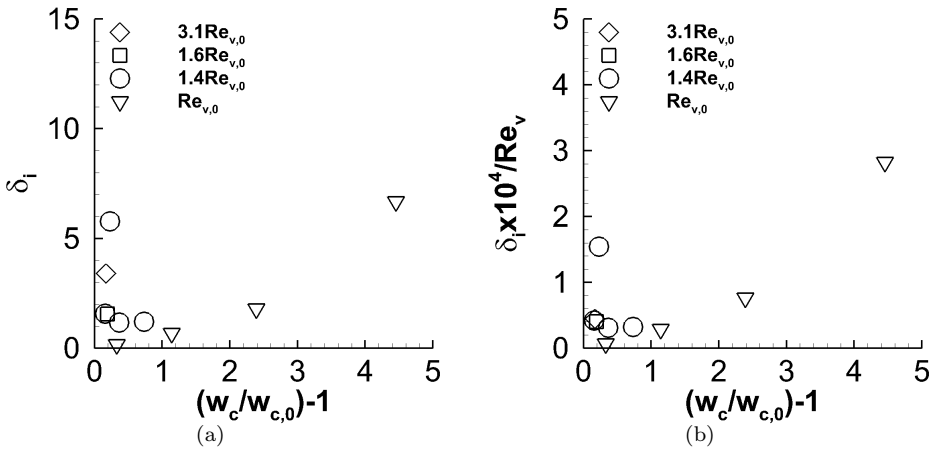

FIGURE 7.5: Apparent diffusion coefficient (δ_i) as a function of local streamwise velocity ratio ($w_c/w_{c,0}$-1), centreline ingestion, (a): Influence of vortex Reynolds number Re_v, where $Re_{v,0} = 2.4 \times 1{-}4$, (b): Influence of vortex Reynolds number Re_v, δ_i normalised by vortex initial average vorticity ($\delta_i \times 10^4/Re_v$)

time between the same two measurement planes reduces to 0.0035s. As a consequence, the overall effect of diffusion on the change in core radius is similar, and there is little difference between the measured values of $r_c/r_{c,0}$ for the different vortex Reynolds numbers.

It was demonstrated in section 5.2.4 that the differences between the vortex filament model and the measured vortex characteristics reduced when the vortex was ingested along an off-axis trajectory relative to the intake centreline. Therefore, it was concluded that the effects of diffusion were smaller along such a trajectory. A number of important points can be identified from the corresponding values of δ_i, Figure 7.5(a). Firstly, in agreement with the centreline measurements (Figure 7.4(a)), the apparent diffusion coefficient increases with the local contraction levels. A comparison with Figure 7.4(a) indicates that the off-axis values of δ_i are approximately half of those obtained on the intake centreline. In addition, it should be emphasised that the measured vortex core radius evolution is far closer to the vortex filament model, and so a large number of the values of δ_i for the off-axis cases are negative. It is likely that the outlier of δ_i=6 at ($w_c/w_{c,0}$-1)=0.2 is a result of measurement uncertainty, since this behaviour has not been observed in any other cases. In agreement with the results of the centreline cases (Figure 7.4(c)), there is a reduction in scatter when δ_i is normalised by the vortex Reynolds number, Figure 7.5(b).

The analysis of the behaviour of δ_i for centreline and off-axis vortex ingestion scenarios has demonstrated that a curve fit for δ_i/Re_v can be obtained as a function of the local contraction levels ($w_c/w_{c,0}$-1). It has been found that the best curve fit for both centreline

and off-axis cases is that of a second-order polynomial with an intercept of δ_i/Re_v=0 at ($w_c/w_{c,0}$-1)=0, Eqs. 7.10 and 7.11, respectively. A comparison of the curve-fits with the experimental data is shown in Figures 7.6(a) and 7.6(b). Note that only the NACA 0012 wing-tip vortex data has been employed in the calculation of the curve-fit equations. This was to avoid contamination from the impact of the large streamwise velocity deficit associated with the delta wing vortex. Furthermore, the outlier identified in the off-axis data at ($w_c/w_{c,0}$-1)=0.2 (Figure 7.5(b)) has also been removed from the calculation. As shown in Figures 7.6(a) and 7.6(b), the curve-fits provide a good description of the experimental data. This is supported by the R^2 coefficients, which are equal to 0.94 and 0.93 for centreline and off-axis cases, respectively. It is acknowledged, however, that the curve-fit for the off-axis measurements has been generated using a small collection of measurements. Nonetheless, the nature of the off-axis curve is clearly consistent with that obtained from the larger centreline dataset. This establishes confidence in the trend acquired for the off-axis case.

The curve-fits of δ_i/Re_v now provide an approach to calculate the apparent diffusion coefficient for any value of ($w_c/w_{c,0}-1$) and Re_v. Therefore, it is now possible to determine the contribution of diffusion to the vortex intensification process which takes place during vortex ingestion.

$$\frac{\delta_i \times 10^4}{Re_v} = 0.1752\left(\frac{w_c}{w_{c,0}} - 1\right)^2 + 1.0121\left(\frac{w_c}{w_{c,0}} - 1\right) \tag{7.10}$$

$$\frac{\delta_i \times 10^4}{Re_v} = 0.1182\left(\frac{w_c}{w_{c,0}} - 1\right)^2 + 0.0982\left(\frac{w_c}{w_{c,0}} - 1\right) \tag{7.11}$$

A number of important features of the vortex intensification process have been identified from the preceding analysis. As expected, the effects of diffusion increase during the intensification process, which causes a rise in the apparent diffusion coefficient δ_i. For a fixed initial vortex core radius, δ_i provides an indication of the vortex diffusion rates. It has been found that δ_i increases as a function of the local streamtube contraction levels, which is a result of the increase in the diffusion attributed to viscosity and turbulence. It has been demonstrated that the vortex Reynolds number is the most important parameter which captures the diffusion rates for all conditions investigated. The value of δ_i is also strongly dependent on the vortex ingestion trajectory. It has been found that the diffusion rates are less than half of those measured at the same conditions, but along the intake centreline. Based on this analysis, a curve fit of δ_i as a function of $(w_c/w_{c,0} - 1)$ and Re_v

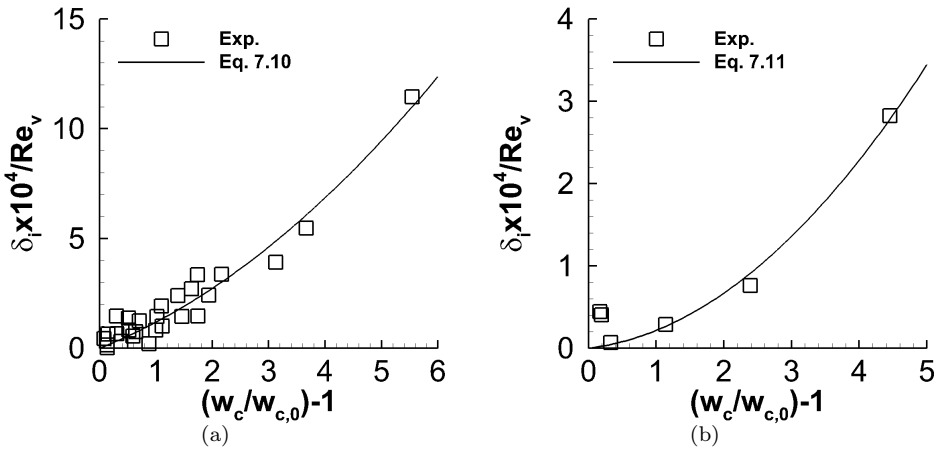

FIGURE 7.6: Curve-fit for apparent diffusion coefficient ($\delta_i \times 10^4/Re_v$), as a function of local streamwise velocity ratio ($w_c/w_{c,0}$-1), (a): Centreline ingestion, (b): Off-axis ingestion

has been developed. This provides the necessary input into the diffusion-corrected vortex filament model which has been proposed in this research.

7.2 Assessment of vortex intensification models

The purpose of this section is to assess the capability of the semi-empirical vortex intensification model which has been developed in the preceding section. The model has been generalised sufficiently, such that the only required inputs are the streamtube contraction levels ($w_c/w_{c,0}$-1), an estimate for the time required for the vortex to convect through the contraction ($t_{1,2}$), and the vortex Reynolds number ($Re_v = \Gamma_c/\nu$) prior to entering the streamtube contraction. It is assumed that, at a particular location in the intake capture streamtube, the streamwise velocity at the vortex centre (w_c) is equal to that of the streamtube in the absence of the vortex. This is a valid assumption provided the vortex streamwise velocity perturbation $w_{c,0}/W_\infty$ is less than 0.15, based on the experimental dataset obtained in this research. To carry out an assessment of the new vortex intensification model, the streamtube velocity field from an inviscid CFD simulation has been acquired using the same sub-scale intake geometry which was used in the experimental measurements. Details of the mesh characteristics are provided in section 6.3.2.1. It should be noted that the velocity field is required to obtain a good estimate of the convection time $t_{1,2}$. Therefore, a similar estimate of the streamtube velocity field may also be obtained from a simple potential model. A first-order estimate of $t_{1,2}$ may also

be acquired by assuming $t_{1,2} = z/(w_c - W_\infty)$, where w_c is the streamwise velocity at the required point in the streamtube contraction. Finally, it is assumed that the vortex and the intake capture streamtube are isolated, and thus any interaction effects with nearby surfaces are neglected.

A number of cases from the experimental dataset have been employed to assess the model validity, as detailed in the following subsections.

7.2.1 Example application 1

In this example, the semi-empirical model has been applied to the case corresponding to an initial vortex Reynolds number of $Re_v = 3.3 \times 10^4$. The intake velocity ratio is VR=10.3, and the vortex is ingested along the intake centreline. The streamwise velocity ratio ($w_c/w_{c,0}$) and the vortex convection time $t_{1,2}$ have been obtained using an inviscid CFD simulation at the correct freestream and intake flow conditions.

The performance of the semi-empirical model can be assessed using the results for the change in vortex core radius (Figure 7.7(a)), peak tangential velocity (Figure 7.7(b)), peak streamwise vorticity (Figure 7.7(c)), average streamwise vorticity (Figure 7.7(d)), and peak flow angularity (Figure 7.7(e)). Note that the experimental measurements show that the local streamtube contraction levels ($w_c/w_{c,0}$) reach a value of 4.1 at $z/D_i = 0.20$. The analysis of the experimental measurements have demonstrated that the effects of diffusion become apparent for $w_c/w_{c,0}$ greater than 2, and thus the vortex intensification measurements for this configuration are in a regime where diffusion is important. The results obtained from the semi-empirical model (VF+D) demonstrate a pronounced improvement over the vortex filament model (VF), Table 7.1. In particular, the vortex intensification levels obtained from the semi-empirical model are very close to the measured levels, and feature an error which is no greater than 4% of the experimental measurements. Such errors are within the measurement uncertainty. Note that the peak streamwise vorticity features a maximum error of 20% at $z/D_i = 0.38$. In contrast, the average core vorticity which results from the semi-empirical model is in very good agreement with the experimental measurements. In chapter 5, it was found that vorticity diffusion is strongest at the vortex centre, and becomes weaker with distance from the vortex centre. Importantly, the apparent diffusion coefficient δ_i is computed using the measured vortex core radius, where the effects of diffusion are known to be smaller. Consequently, δ_i does not reflect the high levels of diffusion which are experienced at the vortex centre, which explains the poor agreement between the model and the measurements. Nevertheless,

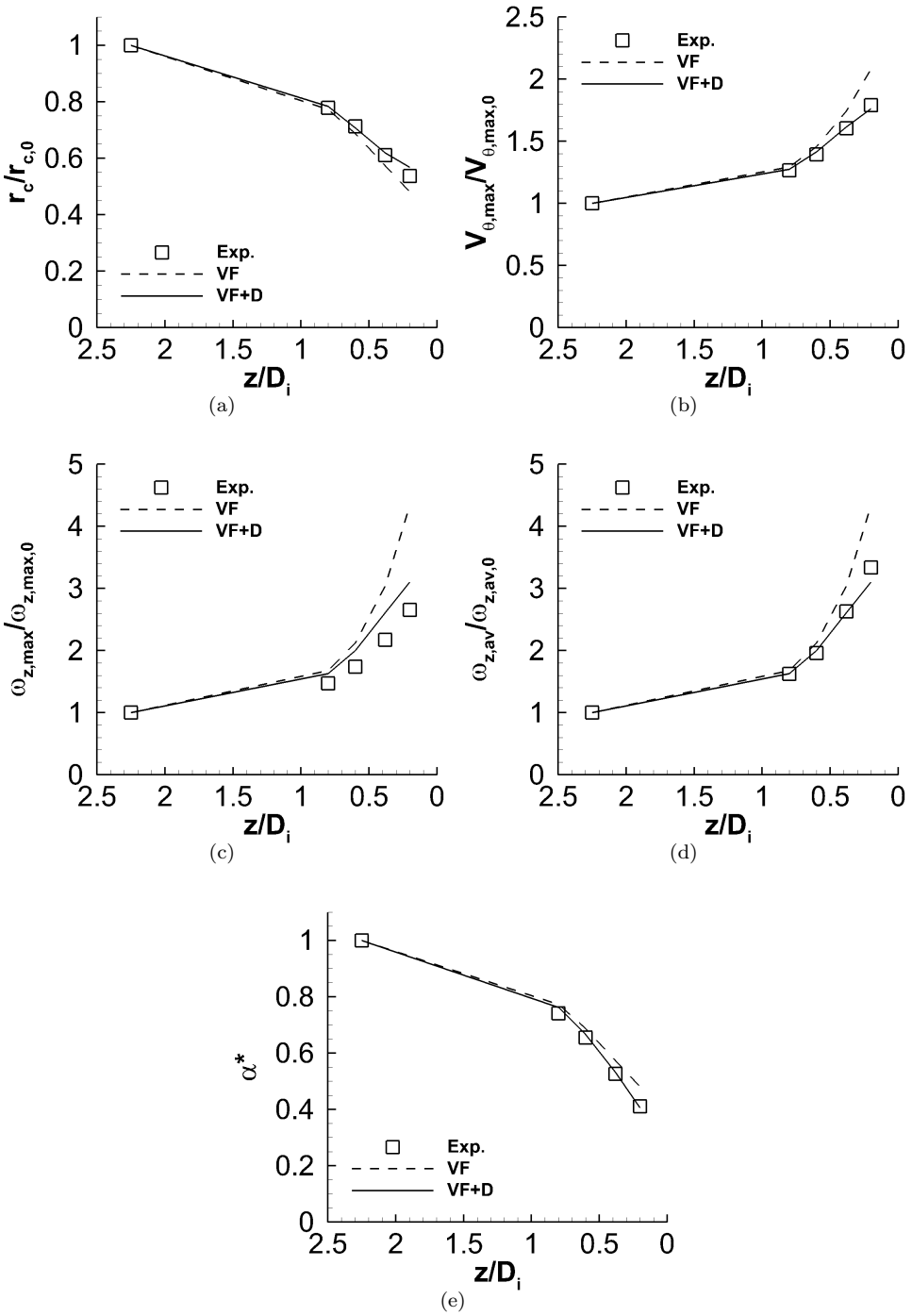

FIGURE 7.7: NACA 0012 vortex generator, $\alpha_{vg} = 12^o$, $Re_v = 3.7 \times 10^4$, $VR = 10.3$, centreline ingestion, normalised by measurement at z/D_i=2.25, (a): Core radius ($r_c/r_{c,0}$), (b): Peak tangential velocity ($V_{\theta,max}/V_{\theta,max,0}$), (c): Peak streamwise vorticity ($\omega_{z,max}/\omega_{z,max,0}$), (d): Average streamwise vorticity ($\omega_{z,av}/\omega_{z,av,0}$), (e): Peak flow angularity (α^*)

with the inclusion of the effects of diffusion, the result from the semi-empirical model is notably closer to the measurements than the vortex filament model result, which features an error of 64%.

TABLE 7.1: Model errors for vortex filament (VF) and semi-empirical (VF + D) vortex models, normalised by experimental measurements of vortex characteristics, NACA 0012 vortex generator, $\alpha_{vg} = 12^o$, $Re_v = 3.7 \times 10^4$, VR=10.3, centreline ingestion

$\frac{z}{D_i}$	Model	$\frac{r_c}{r_{c,exp}}$	$\frac{V_\theta}{V_{\theta,exp}}$	$\frac{\omega_{z,max}}{\omega_{z,max,exp}}$	$\frac{\omega_{z,av}}{\omega_{z,av,exp}}$	$\frac{\alpha^*}{\alpha^*_{exp}}$
0.80	VF	0.993	1.024	1.138	1.031	1.044
	VF+D	1.007	1.010	1.106	1.002	1.030
0.60	VF	0.964	1.045	1.221	1.085	1.049
	VF+D	0.994	1.015	1.149	1.021	1.078
0.38	VF	0.939	1.087	1.400	1.157	1.090
	VF+D	1.014	1.007	1.202	0.994	1.010
0.20	VF	0.894	1.164	1.638	1.302	1.171
	VF+D	1.060	0.984	1.170	0.930	0.990

7.2.2 Example application 2

The second example consists of an initial vortex Reynolds number of $Re_v = 7.4 \times 10^4$. The intake velocity ratio is VR=4.9, and the vortex is ingested along the intake centreline. The streamwise velocity ratio ($w_c/w_{c,0}$) and the vortex convection time $t_{1,2}$ have been obtained using an inviscid CFD simulation at the correct freestream and intake flow conditions.

The comparison of the experimental measurements and the vortex filament model, Figures 7.8(a) to 7.8(e), demonstrate that the semi-empirical model offers a smaller improvement over the vortex filament model than was observed in the previous example. This is a result of the streamtube contraction levels, which are notably smaller in this example. In particular, in this example, the measured value of $w_c/w_{c,0}$ is 2.5, compared with 4.1 in the previous example. The analysis of the experimental measurements has demonstrated that the diffusion only has a small effect on the vortex intensification process when the local contraction levels ($w_c/w_{c,0}$) are less than 2 (section 5.2.1). Therefore, it is unsurprising that the semi-empirical model offers only a modest improvement when compared to the

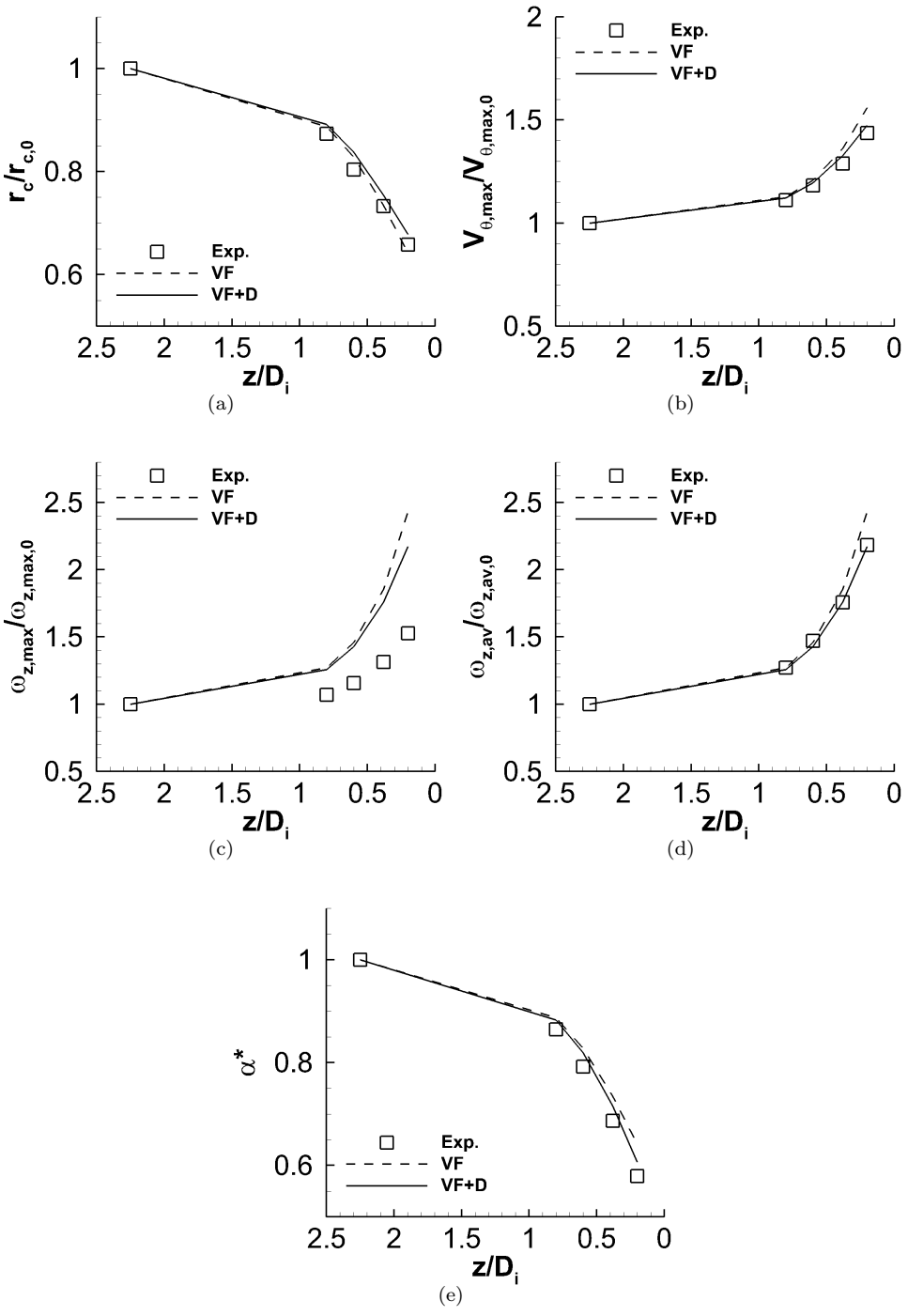

FIGURE 7.8: NACA 0012 vortex generator, $\alpha_{vg} = 12^o$, $Re_v = 7.4 \times 10^4$, $VR = 4.9$, centreline ingestion, normalised by measurement at z/D_i=2.25, (a): Core radius ($r_c/r_{c,0}$), (b): Peak tangential velocity ($V_{\theta,max}/V_{\theta,max,0}$), (c): Peak streamwise vorticity ($\omega_{z,max}/\omega_{z,max,0}$), (d): Average streamwise vorticity ($\omega_{z,av}/\omega_{z,av,0}$), (e): Peak flow angularity (α^*)

vortex filament model results (Table 7.2). It is also important to note that, in a manner similar to the results in section 7.2.1, the semi-empirical model overpredicts the increase in peak streamwise vorticity, but features a small error for the average core vorticity. This behaviour is consistent with the fact that the semi-empirical relationship for δ_i has been developed using the vortex core radius, which is less susceptible to the effects of diffusion than the peak streamwise vorticity. The error associated with $\omega_{z,max}/\omega_{z,max,0}$ for the semi-empirical model is of a similar magnitude to that observed in the preceding example application (section 7.2.1), which features a notably lower contraction level, along with a lower vortex Reynolds number. This result is consistent with the findings in section 5.2.2, where it was demonstrated that the levels of diffusion at the vortex centre increase with the vortex Reynolds number, causing the measured values of $\omega_{z,max}/\omega_{z,max,0}$ to deviate further from inviscid vortex intensification.

TABLE 7.2: Model errors for vortex filament (VF) and semi-empirical (VF + D) vortex models, normalised by experimental measurements of vortex characteristics, NACA 0012 vortex generator, $\alpha_{vg} = 12^o$, $Re_v = 7.4 \times 10^4$, VR=4.9, centreline ingestion

$\frac{z}{D_i}$	Model	$\frac{r_c}{r_{c,exp}}$	$\frac{V_\theta}{V_{\theta,exp}}$	$\frac{\omega_{z,max}}{\omega_{z,max,exp}}$	$\frac{\omega_{z,av}}{\omega_{z,av,exp}}$	$\frac{\alpha^*}{\alpha^*_{exp}}$
0.80	VF	1.016	1.015	1.190	0.999	1.026
	VF+D	1.021	1.010	1.177	0.989	1.021
0.60	VF	1.030	1.022	1.261	0.992	1.045
	VF+D	1.042	1.011	1.234	0.970	1.034
0.38	VF	1.002	1.060	1.413	1.055	1.069
	VF+D	1.028	1.030	1.341	1.001	1.042
0.20	VF	0.974	1.086	1.595	1.116	1.107
	VF+D	1.030	1.027	1.425	0.997	1.046

7.3 Scale effects

The sub-scale measurements have been used to develop a semi-empirical model for vortex intensification. However, it is necessary to assess the suitability of the model for the full-scale applications which are of interest for engine-airframe integration studies. A key difference between sub-scale and full-scale vortex ingestion conditions is the vortex

TABLE 7.3: Full-scale and sub-scale vortex ingestion configurations for the assessment of scale effects, ingestion along intake centreline

Case	Sub-scale exp.	Sub-scale exp.	Sub-scale CFD	Full-scale CFD
VR (W_i/W_∞)	16.3	5.0, 10.3	4.9	4.9
Re_v	2.4×10^4	3.7×10^4	3.1×10^4	1.2×10^6
r_c/D_i	0.087	0.092	0.082	0.055
Re_c	1.3×10^7	3.5×10^5	5.6×10^6	1.5×10^5

Reynolds number. For example, a full-scale canard wing-tip vortex may feature a vortex Reynolds number of the order of 10^6, whereas the sub-scale measurements have been conducted where the vortex Reynolds number are within the order of 10^4. Wing-tip vortex measurements have shown that the levels of turbulence diffusion become greater when the vortex Reynolds number is increased. This behaviour was also observed across the limited range of Re_v which was investigated in the sub-scale vortex intensification studies and the modelling studies. It is therefore crucial that the sub-scale model, which was developed in the preceding section, is assessed at typical full-scale conditions.

At present, there are no measurements of vortex ingestion, or vortex intensification, at vortex Reynolds numbers which correspond to full-scale configurations. Thus, the full-scale and sub-scale CFD results from the CFD scaling studies (section 6.4) have been employed. The CFD simulations have been processed using the same post-processing approach as the experimental measurements (3.6.2). Note that the circular zone resolution was maintained at $0.021r_c$ for both sub-scale and full-scale simulations. In addition, similarly to the analysis conducted in chapter 5, the measurements at $z/D_i = 2.25$ have been selected as the conditions at the start of the contraction process. Inspection of the streamwise velocity (w_c/W_∞) in Figure 5.1(b) confirms that this is an appropriate method for both sub-scale and full-scale simulations, since the influence of the flow contraction at this position is small.

The values of δ_i for the sub-scale and full-scale simulations have been plotted alongside a subset of the experimental measurements in Figure 7.9(a). The conditions which have been employed in the comparisons are given in Table 7.3. The values of δ_i which have been determined from the sub-scale CFD simulations are in excellent agreement with the sub-scale experimental measurements. This provides further support that the CFD method which has been developed in this research permits the correct vortex intensification and diffusion characteristics to be modelled. The full-scale measurements

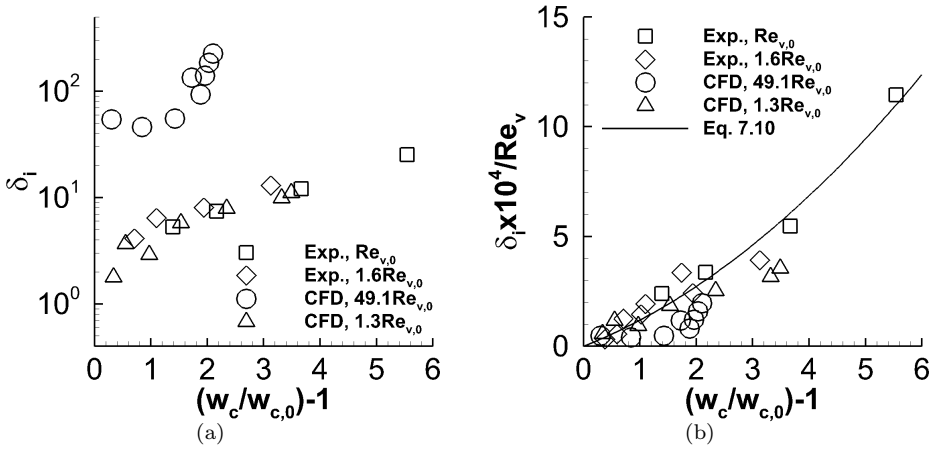

FIGURE 7.9: Apparent diffusion coefficient (δ_i) as a function of local streamwise velocity ratio ($w_c/w_{c,0}$-1), centreline ingestion, (a): Influence of vortex Reynolds number Re_v, where $Re_{v,0} = 2.4 \times 10^4$, (b): δ_i normalised by vortex Reynolds number ($\delta_i \times 10^4/Re_v$)

demonstrate that δ_i is approximately one order of magnitude larger than the sub-scale counterparts. Therefore, the turbulent diffusion levels which occur for full-scale vortex intensification is notably larger than those at sub-scale. The results which were compiled by Bhagwat and Leishman [50], as shown in Figure 2.17, provide clear evidence that the diffusion levels are proportional to Re_v. Furthermore, it is clear from Figure 2.17 that δ is also an order of magnitude larger when Re_v is increased from 1×10^4 to 1×10^6, which is similar to the current measurements in Figure 7.9(a).

In section 7.1.2, it was found that δ_i is proportional to Re_v, and a curve fit for δ_i/Re_v could be obtained. When the values of δ_i in Figure 7.9(a) are normalised in a similar manner, the data which has been acquired at full-scale move closer to the sub-scale measurements and the sub-scale curve fit given in Eq. 7.10, and are now of a similar order. This result shows that the vortex Reynolds number is a key parameter which defines the diffusion levels during the vortex intensification process, and that full-scale vortex intensification is characterised by greater levels of vorticity diffusion. However, it is clear that further CFD simulations on a wider range of sub-scale and full-scale configurations should be conducted to further test the suitability of the trend from the semi-empirical model. In particular, such studies should encapsulate a wider range of vortex Reynolds numbers and intake velocity ratios. The latter will address the suitability of the relationship for δ_i at the large values of $w_c/w_{c,0}$ which have been investigated in the sub-scale measurements.

7.4 Summary

The analysis of vortex ingestion measurements in the preceding chapter highlighted that vortex filament model is only suitable at low contraction levels, where the local streamwise velocity ratio ($w_c/w_{c,0}$) is less than approximately 2. At higher streamtube contractions, diffusion causes large differences between the vortex filament model and the measurements. Analysis with a semi-empirical vortex model has found that the effect of diffusion on vortex evolution can be characterised in terms of the rate at which diffusion takes place, along with the time which elapses during the diffusion process. A semi-empirical model has therefore been developed to capture the flow physics associated with vortex intensification and vortex diffusion. The model includes a semi-empirical parameter δ_i, termed the apparent diffusion coefficient, which captures the rate at which diffusion takes place. It has been found that diffusion rates grow during the vortex intensification process, which is a result of the increase in the vortex core vorticity, along with the presence of turbulent flow inside the vortex core. In addition, the diffusion rates have been found to scale with the vortex Reynolds number. This result is consistent with the findings from studies of wing-tip vortex evolution in uniform freestream flows. It has been hypothesised that the rise in diffusion rates is a consequence of an increase in the turbulence levels inside the vortex core. An important conclusion from the analysis is that the vortex Reynolds number $Re_v = \Gamma_c/\nu$ is the best parameter to characterise diffusion levels. This result is also in agreement with the observations made during the analysis of the experimental measurements (chapter 5). A curve-fit was developed for δ_i/Re_v as a function of the streamtube contraction levels, with which the contribution to diffusion on the vortex intensification process can be calculated. The semi-empirical model developed in this research correctly captures the effects of diffusion which have been observed in the experimental measurements. The results from the semi-empirical model are in good agreement with the measurements for a range of vortex ingestion conditions.

Chapter 8

Conclusions

This research consists of the first extensive study of the behaviour of an isolated streamwise vortex in a contracting intake capture streamtube. The research is focussed on the potential scenario where a streamwise vortex, which has been generated upstream of an aircraft intake, enters the intake capture streamtube and is ingested by the intake. Stereoscopic Particle Image Velocimetry (Stereo PIV) has been employed to obtain quantitative measurements of the vortex evolution upstream of the highlight plane of a $1/30^{th}$ scale intake model. A range of experimental configurations were investigated to elucidate the behaviour of a streamwise vortex during the ingestion process. The intake capture streamtube levels, defined in terms of the intake velocity ratio $VR = W_i/W_\infty$, have been varied through control of the freestream velocity and the intake mass flow. Furthermore, a range of different streamwise vortices were generated in the unperturbed flow upstream of the streamtube contraction. In this way, it was possible to identify the influence that the vortex characteristics, such as the vortex Reynolds number (Re_v), have on the vortex ingestion process. Using this approach, it has been possible to establish new understanding on the vortex intensification process. The experimental measurements have also been employed to establish a validated CFD approach to simulate vortex ingestion flows. The results from the experimental and CFD analyses have important consequences for current engine-airframe integration studies. The following subsections provide a summary of the main findings in this research.

8.1 Flow physics of vortex intensification

Detailed experimental measurements were acquired to address the dearth of knowledge and understanding about the evolution of streamwise vortices inside a contracting intake capture streamtube. A summary of the main findings from this research are provided below.

- The vortex undergoes notable levels of intensification when it passes through the contracting streamtube. The vortex intensification levels are strongly dependent on the local contraction levels ($w_c/w_{c,0}$) inside the intake capture streamtube. This process is characterised by a reduction in the vortex core radius, coupled with an increase in the vortex peak tangential velocity, peak streamwise vorticity, and average core vorticity. In addition, the peak flow angles in the vortex flow reduce during intensification. Therefore, the flow angularity associated with the vortical distortion is damped naturally by the contraction process.

- Fundamental vortex theory was employed to implement an inviscid, incompressible vortex filament model. This provides the first comparison of the vortex characteristics which are estimated from vortex filament theory with experimental measurements of wing-tip vortex intensification.

- The vortex ingestion process is characterised by notable levels of vorticity diffusion inside the vortex core. The diffusion process acts in opposition to vortex intensification. The effects of diffusion arise due to laminar and turbulent momentum transfer, and become increasingly pronounced as the streamtube contraction levels increase. Analysis of the vortex flowfield has revealed that diffusion is strongest at the vortex centre, and has a smaller influence on the vortex characteristics which are evaluated at the vortex core radius. As a result, the vorticity levels inside the vortex core not attain the values which are anticipated from fundamental theory.

- When the local streamtube contraction levels ($w_c/w_{c,0}$) are less than approximately 2.0, the vortex characteristics at the edge of the vortex core, such as the vortex core radius, peak tangential velocity, and peak flow angle, are in good agreement with the results from the vortex filament model. This result demonstrates that the impact of vorticity diffusion is greatest at the vortex centre, and reduces with distance from the vortex axis.

- At streamtube contraction levels $w_c/w_{c,0}$ of greater than 2, the effects of vorticity diffusion become increasingly apparent. A result of this is that the vortex intensification levels become progressively lower than that anticipated from inviscid theory. The differences between the measurements and the inviscid theory are notable. An increase in the vortex Reynolds number ($Re_v = \Gamma_c/\nu$) produces a corresponding rise in the diffusion levels at the vortex centre. This research provides the first evidence to show that vortex intensification features a dependence on Re_v. This result is a consequence of turbulent diffusion inside the vortex core, and is consistent with findings from wing-tip vortex measurements. The impact of Re_v is strongest on the vorticity characteristics at the vortex centre, and parameters which are measured at the edge of the vortex core are only weakly influenced.

- For a particular streamtube contraction, the vortex intensification levels are dependent on the characteristics of the vortex prior to the flow contraction. In particular, the analysis has identified that the vortex Reynolds number (Re_v), the core average vorticity ($\omega_{z,av}$), and the streamwise velocity perturbation ($(V_z - W_\infty)/W_\infty$) have an influence on the vortex intensification process.

- A semi-empirical model was developed to obtain further details of the link between the vortex Reynolds number and the effects of diffusion. The experimental measurements were thus employed to establish a semi-empirical relationship the apparent diffusion coefficient for vortex intensification (δ_i) as a function of the vortex Reynolds number and the local streamtube contraction levels. The model which has been developed in this research provides an approach to determine the vortex characteristics during the intensification process, and has been found to be in good agreement with the experimental measurements.

- Full-scale CFD simulations, which were conducted in this research, confirmed that the diffusion levels were a strong function of the Reynolds number. Furthermore, it demonstrated that the model developed herein is appropriate for use to estimate the evolution of the vortex characteristics at full-scale conditions.

- The vortex intensification characteristics are dependent on the initial location of the vortex relative to the intake centreline. When the vortex follows an off-axis trajectory inside the capture streamtube, the effects of diffusion are reduced when compared to that on the intake centreline axis. Therefore, for a given flow contraction, a vortex which has been ingested at the edge of the intake capture streamtube undergoes greater levels of vortex intensification than that experienced along a centreline trajectory.

8.2 Modelling requirements for CFD simulations of vortex ingestion

Simulations have been performed using Computational Fluid Dynamics (CFD) to identify the correct approach to simulate vortex ingestion. A review of the literature has identified that it can be particularly challenging to simulate wing-tip vortices using CFD. The agreement between simulations and experimental measurements of wing-tip vortices is strongly dependent on the details of the mesh characteristics and the turbulence modelling approach. Few studies have elucidated the requirements for simulating vortex convection and vortex ingestion flows. Studies have been performed in this research to address this lack of knowledge. Wing-tip vortex convection simulations were first conducted to evaluate the impact of the mesh resolution on the ability of the CFD solver to capture the vortex convection process. The evolution of the vortex characteristics was assessed using measurements which are available in the literature.

- The studies have confirmed the findings in the literature that notable levels of numerical diffusion can result when the in-plane and out-of-plane mesh resolution is insufficient. As a consequence, the vortex diffuses rapidly, and the agreement with the measurements is poor. Using the vortex convection results, it has been possible to establish new guidelines on the required mesh resolution to ensure that mesh-related numerical diffusion is minimised.

- Eddy-viscosity turbulence models are inappropriate for simulating vortex convection and vortex ingestion flows. A notable result is that commonly-used eddy-viscosity models, such as the Spalart-Allamras and $k-\omega$ SST models, over-predict the rate at which the wing-tip vortex diffuses. This is a result is in agreement with previously-reported findings in CFD simulations wing-tip vortex flows. Large levels of turbulence inside the vortex core which are generated by the turbulence model. Importantly, eddy-viscosity models rely on the Boussinesq assumption, which states that the turbulence and strain rate tensors are aligned. The experimental measurements which have been obtained in this research, in agreement with those in the literature, show that the Boussinesq assumption is not appropriate for the vortex flows.

- The vortex convection simulations demonstrated that the vortex evolution is in good agreement with the experimental measurements when a Reynolds Stress Model (RSM) is employed. Such models are required to capture the anisotropic turbulent

stresses which occur inside the vortex core. A key requirement for RSM simulations is that appropriate turbulence profiles must be prescribed at the inlet boundary condition. This research has produced a new approach to define turbulence boundary conditions at the inlet plane of the CFD simulation. It has been found that it is necessary to prescribe profiles of the turbulent kinetic energy (k) and the turbulent dissipation rate (ϵ), in conjunction with a turbulence length scale of $l = 1r_c$.

- The sub-scale measurements which have been acquired in the experimental studies have been utilised to create an analytical profile for the turbulent kinetic energy. In this way, it is possible to prescribe suitable turbulence boundary conditions when the vortex turbulence characteristics are not known a priori.

- Simulations were performed using a sub-scale vortex ingestion case which was investigated in the experimental programme. It was found that agreement between the experimental measurements and the results obtained with the $k-\omega$ SST turbulence model were poor. It has been established that that RSM simulations are imperative for vortex intensification and vortex ingestion simulations as long as suitable turbulence profiles are provided in the inlet boundary conditions.

8.3 Consequences for engine-airframe integration studies

- Prior to entering the streamtube contraction, the streamwise vortices which are at risk of ingestion are typically characterised by large flow angles. For example, wingtip vortices which have been generated by canards may feature flow angles of up to 30^o. Such swirl distortions are likely to have a detrimental effect on the turbomachinery performance and stability, and may also result in local flow separations on the intake surfaces.

- During the vortex ingestion process, the peak swirl angle inside the vortex reduces. In particular, the peak swirl angles inside the capture streamtube are inversely proportional to the intake velocity ratio. It can therefore be concluded that the flow contraction has a damping effect on the swirl distortion levels, which may subsequently mitigate the impact of the vortex on the turbomachinery. Conversely, this result shows that vortex ingestion during low intake velocity ratio conditions will result in the greatest swirl distortion levels. Vortex ingestion during end-of-runway operations, such as the rotation and climb-out phases of flight, may result in the largest impact on the turbomachinery performance and stability.

- An inviscid vortex filament model can be used during low intake velocity ratio conditions to estimate the change in the vortex characteristics during ingestion. This knowledge now permits straightforward calculations to be performed to estimate the vortex characteristics and the possible inlet flow distortion characteristics inside the intake.

- A semi-empirical model has been developed to account for the effects of diffusion, and can therefore be employed to provide suitable estimates of the vortex characteristics following ingestion at large intake velocity ratios. This information can also be employed to prescribe CFD inlet boundary conditions to turbomachinery simulations.

- The influence of diffusion is favourable from the perspective of the swirl distortion levels, and the vortex peak swirl angles following ingestion are lower than anticipated from inviscid vortex intensification theory. Consequently, the inviscid vortex filament model can be used to provide a worst-case estimate of the vortex characteristics after ingestion.

- The effects of diffusion on the vortex intensification process are dependent on the ingestion trajectory, and the vortex intensification levels are greatest when the vortex is ingested near the edge of the capture streamtube. Once inside the intake, the vortex ingested on the off-axis trajectory will have greater peak flow angles than those observed for centreline ingestion. Thus, the off-axis ingestion scenario must be considered to be the worst-case for preliminary assessments of vortex ingestion.

- The CFD studies have demonstrated that numerical diffusion can result in an underprediction of the vortex intensification levels during ingestion. Therefore, the inlet flow distortion characteristics may be incorrect if a suitable CFD approach is not employed. Guidelines have been established in this research to minimise the effects of numerical diffusion.

- The vortex ingestion simulation which have been performed in this research is good agreement with the measurements. It can be concluded that it is appropriate to prescribe a known vortex as part of the inlet boundary conditions, as an alternative to simulating the vortex generation process. This has notable benefits. Firstly, the size and complexity of the computational domain can be reduced, and it is possible to, for example, increase the mesh resolution in key areas of the domain, such as the intake boundary layers.

- The CFD approach which has been developed in this research was applied to investigate vortex ingestion along the centreline axis of a full-scale intake. It was demonstrated that the inlet flow distortion which results from the ingestion of a canard vortex is characterised by low levels of total pressure distortion, coupled with a bulk swirl of moderate flow angles. The results are consistent with the limited range of experimental flow distortion measurements which are available in the literature.

- The CFD framework which has been developed in this research can be employed to study a wide range of possible vortex ingestion scenarios. For example, under the instruction of the current PhD research, Heimbucher [115] and Pernod [117] investigated full-scale vortex ingestion using a realistic aircraft intake.

8.4 Recommendations for future work

Based on the findings of this research, it is possible to identify a number of aspects which can be investigated experimentally:

- The experimental studies which have been conducted in this research cover a range of initial vortex characteristics and streamtube contraction conditions. In conjunction with the full-scale CFD simulations, it has been possible to demonstrate that the vortex intensification process is influenced by the vortex Reynolds number. It would therefore be beneficial to obtain measurements of vortex ingestion for a wider range of vortex Reynolds numbers than those which have been considered in this research. This could be achieved using vortex generators with a greater size, or by investigating vortex ingestion for even greater freestream velocities. In addition, measurements should be acquired for a greater number of vortex generator angles of attack. This will permit isolation of the impact of the vortex Reynolds number for a constant chord Reynolds number. These additional conditions will contribute to fundamental understanding of the role of turbulent diffusion on the vortex intensification process, and will provide validation for full-scale CFD simulations.

- The measurements indicate that the streamwise velocity perturbation inside the vortex has a notable effect on the vortex intensification process. A parametric study on the impact of the streamwise velocity perturbation could be performed using swirl generators, such as those employed in [45] or those which are commonly utilised in vortex breakdown experiments [47].

- It was found that the vortex intensification process is dependent on the trajectory which the vortex follows inside the capture streamtube. Additional insight could be obtained by investigating a wider range of off-axis locations across the diameter of the intake capture streamtube.

- The current PIV measurements have been obtained in the flow external to the intake only. Additional insight into the vortex intensification process could be obtained from measurements inside the intake. Although challenging, some success of aerodynamic measurements inside ducts has been reported [118]. Measurements inside the intake would also provide valuable information on the swirl distortion levels inside the intake, and would allow an assessment of the velocity field which is likely to be presented to the fan as a result of vortex ingestion.

This research has established an approach which can be employed to investigate vortex ingestion using CFD. The following could be performed to build upon the findings of this research:

- A wider range of sub-scale vortex ingestion simulations should be conducted to extend the validation of the CFD methods which have been developed in this research.

- The experimental measurements have found that the evolution of the vortex inside the capture streamtube is dependent on the ingestion position. It would thus be beneficial to investigate off-axis ingestion scenarios to provide further insight into the flow physics. This will require careful design of a mesh which will adequately resolve the vortex core along the off-axis ingestion trajectory.

- The full-scale vortex ingestion simulations should be developed to include a fan or the first stage of the aircraft engine, in a manner similar to that conducted by Vunnam and Hoover [14]. This will permit the CFD methods which have been developed in this research to be included in distortion CFD simulations on turbomachinery response.

- Further full-scale vortex ingestion simulations can be conducted to validate the semi-empirical model for use at full-scale vortex Reynolds numbers and for greater streamtube contraction levels.

Appendix A

Test matrix

In this appendix, the test matrix for the sub-scale vortex ingestion measurements is provided. The details include the vortex generator configuration, the freestream and intake flow conditions, the vortex Reynolds number, and the nominal vortex core location relative to the intake centreline at $(x/D_i, y/D_i) = (0,0)$.

TABLE A.1: Test matrix for centreline (CL) and off-axis (OA) vortex ingestion measurements

VG	α_{vg}	W_∞ (ms^{-1})	$Re_c = \frac{W_\infty c}{\nu}$	$Re_v = \frac{\Gamma_c}{\nu}$	$VR = \frac{W_i}{W_\infty}$	x/D_i
CL cases						
0012	12^o	10.9	1.1×10^5	2.4×10^4	5.2	0
0012	12^o	11.0	1.1×10^5	2.4×10^4	16.3	0
0012	12^o	17.2	1.7×10^5	3.7×10^4	2.0	0
0012	12^o	17.2	1.7×10^5	3.7×10^4	5.1	0
0012	12^o	17.3	1.7×10^5	3.7×10^4	10.3	0
0012	12^o	35.4	3.6×10^5	7.4×10^4	2.1	0
0012	12^o	35.4	3.6×10^5	7.4×10^4	4.9	0
0012	6^o	35.4	3.6×10^5	3.4×10^4	2.1	0
0012	6^o	35.4	3.6×10^5	3.4×10^4	4.9	0
Delta	12^o	35.3	4.7×10^5	5.6×10^4	2.1	0
Delta	12^o	35.4	4.7×10^5	5.6×10^4	4.9	0
Delta	6^o	35.3	4.7×10^5	2.3×10^4	4.9	0
OA cases						
0012	12^o	10.9	1.1×10^5	2.4×10^4	5.2	-0.7
0012	12^o	10.9	1.1×10^5	2.4×10^4	16.3	-0.7
0012	12^o	17.2	1.7×10^5	3.7×10^4	5.1	-0.7
0012	12^o	17.2	1.7×10^5	3.7×10^4	10.3	-0.7
0012	12^o	35.4	3.6×10^5	7.4×10^4	4.9	-0.7
0012	6^o	35.3	3.6×10^5	3.4×10^4	4.9	-0.7
Delta	12^o	35.3	4.7×10^5	5.6×10^4	4.9	-0.7

Appendix B

Calculation of vortex characteristics

In this appendix, a description of the PIV post-processing approach is given. In particular, this focuses on the details of the Vorticity Disk Method (VDM) which is used to extract the vortex characteristics from the Stereo PIV measurements. In addition, the effects of wandering are assessed to underline the importance of accounting for the changes in vortex position for each of the instantaneous PIV measurements.

B.1 Vorticity Disk Method

B.1.1 Circular zone size and resolution studies

A central aspect of the Vorticity Disk Method (VDM), as described in section 3.6.2, is that the vortex centre is identified in each instantaneous PIV measurement, and a sub-zone of the PIV measurement is interpolated onto a circular grid. In this way, it is possible to evaluate the circumferentially-averaged flowfield properties and profiles which have been presented throughout the Thesis. Two parameters which must be selected are the radius of the circular zone (r_{max}), and the mesh resolution of the circular zone. This latter characteristic has been defined in terms of the number of mesh points which define the r and θ directions, for a polar coordinate system which is located at the origin of the circular zone, Figure B.1. To evaluate the influence of the size and resolution of the circular zone, a synthetic vortex flowfield has been generated using the Vatistas vortex model, section

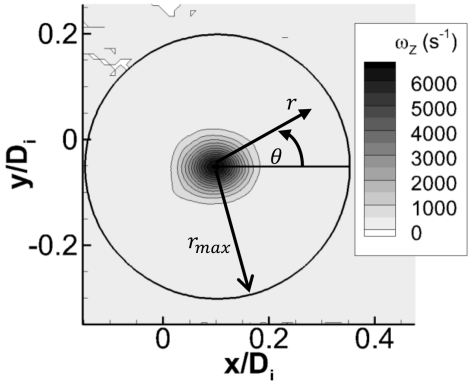

FIGURE B.1: Circular zone with (r,θ) coordinates and circular zone maximum radius (r_{max}) illustrated

TABLE B.1: Circular zone characteristics and corresponding vortex characteristics obtained using the Vorticity Disk Method, influence of circular zone resolution (I_{max}, J_{max}), $r_{max} = 0.025m$

I_{max}	J_{max}	r_{max}	core points	r_c (m)	$V_{\theta,max}$ (ms^{-1})	Γ_c (m^2s^{-1})
30	53	0.025	10	0.00776	20.32	0.991
90	157	0.025	29	0.00787	19.53	0.965
150	261	0.025	48	0.00789	19.39	0.981
210	365	0.025	67	0.00801	19.33	0.973
270	469	0.025	86	0.00809	19.29	0.980
330	577	0.025	106	0.00805	19.27	0.975

6.4.2.3. Only the tangential velocity distribution (Eq. 6.15) has been generated, since the radial velocity is small. A vortex total circulation (Γ_0) and core radius (r_c) of $1.6m^2s^{-1}$ and $0.008m$ have been selected, in addition to a Vatistas parameter of n=1.4. These values are representative of the conditions which have been measured in the unperturbed flow.

Firstly, the influence of the circular zone resolution has been assessed. The mesh resolution inside the circular zone has been defined using I_{max} and J_{max} to refer to the number of mesh points in the r and θ directions, respectively. The ratio J_{max}/I_{max} is constant and equal to 1.74. Using this approach, the mesh spacing in the r and θ directions at $r = r_{max}$ is approximately the same [72]. A range of mesh resolutions, from (30,53) to (330,577), have been investigated with a circular zone resolution of $r_{max} = 0.25m$.

The differences between the prescribed and the calculated vortex characteristics are presented in Figures B.2(a) to B.2(c) as the absolute percentage difference. It is apparent that the errors are less than 5% for all mesh resolutions investigated. There is a notable reduction in the errors to less than 2% when the mesh resolution is increased from (30,53) to (90,157), for which the number of radial mesh points which define the vortex core increases from 10 to 29. The errors reduce slowly for further increases in mesh resolution beyond (90,157), showing that a circular mesh resolution which corresponds to approximately 30 radial points inside the vortex core. It is important to note, however, that the vortex core radius reduces during the ingestion process (section 5.1.2). Therefore, the circular zone must be of sufficient resolution to ensure that reductions in the vortex core radius to not lead to a marked increase in errors. Therefore, a circular zone resolution of (150,261) has been selected. This provides a suitable balance between measurement resolution and memory limitations during post-processing.

A second circular zone parameter which must be evaluated is the maximum radius of the circular zone, r_{max}. This characteristic has a direct influence on the measurement of the vortex total circulation (Γ_0). Circular zone radii of $1.88r_c$, $3.13r_c$, $4.38r_c$, $5.63r_c$, and $6.88r_c$ were investigated (Table B.2). The total circulation which has been calculated increases from $1.429m^2s^{-1}$ for $r_{max} = 1.88r_c$ to $1.595m^2s^{-1}$ for $r_{max} = 6.88r_c$. These values represent errors which reduce from 10.7% to 0.3%, respectively (Figure B.3). This dependence on r_{max} is consistent with existing wing-tip vortex measurements, such as Tung et al. [28] and Martin et al. [33], which have demonstrated that the total circulation of the vortex can only be obtained after a minimum distance of approximately $10r_c$ from the vortex centre. In the current experiments, this would require a circular zone diameter of 0.16m, which is larger than the vertical extent of the useful PIV measurement region. Furthermore, reflections from the intake surfaces were found to cause invalid data at approximately $r/D_i = 0.5$, which corresponds to $r/r_c = 6.25$. It was decided that resolution of the vortex core profiles and the vortex characteristics, with the exception of the total circulation, should be favoured over a reduced circular zone resolution coupled with a large circular zone radius. On this basis, a circular zone radius of $r_{max} = 3.13r_c$ was selected.

B.1.2 Effect of wandering on vortex measurements

A notable feature of wing-tip vortex flows is that the vortex position fluctuates in a random manner [16, 1, 27, 86]. This presents a difficulty for point-based measurements, since the correct position of the vortex centre cannot be determined. The wandering effect causes

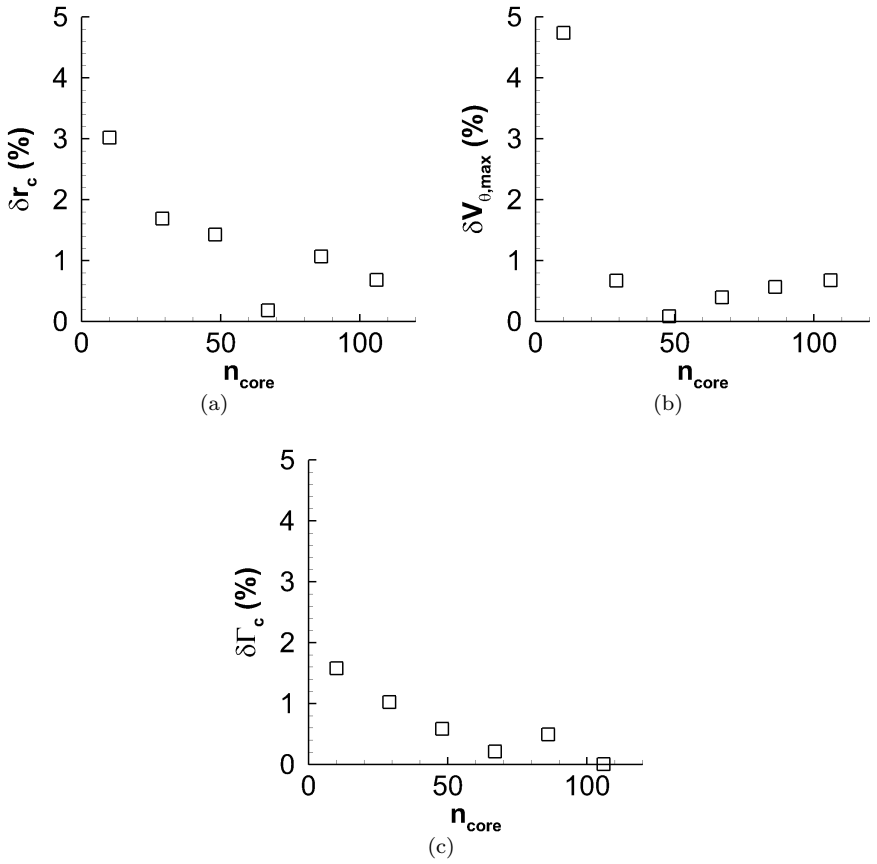

FIGURE B.2: Difference between prescribed and measured vortex characteristics as obtained the Vorticity Disk Method, influence of circular zone resolution. Errors expressed as a percentage difference from prescribed value, (a): Vortex core radius error (δ_{r_c}), (b): Peak tangential velocity error ($\delta_{V_{\theta,max}}$), (c): Core circulation error (δ_{Γ_c})

TABLE B.2: Circular zone characteristics and corresponding vortex characteristics obtained using Vorticity Disk Method, influence of circular zone radius (r_{max}), (I_{max},J_{max}) = (150,261)

r_{max}	r_{max}/r_c	Γ_0 (m^2s^{-1})
0.015	1.88	1.429
0.025	3.13	1.555
0.035	4.38	1.582
0.045	5.63	1.591
0.055	6.88	1.595

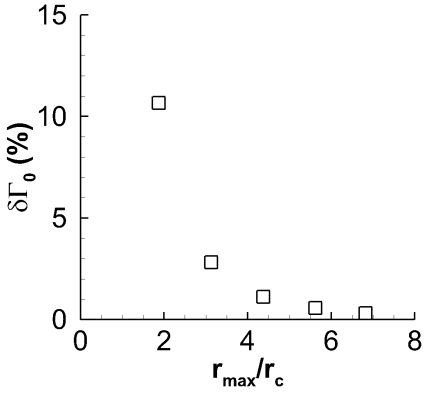

FIGURE B.3: Difference between prescribed and measured vortex characteristics as obtained the Vorticity Disk Method, influence of circular zone maximum radius (r_{max}). Errors expressed as a percentage difference from prescribed value. Vortex total circulation error (δ_{Γ_0})

point-based measurements to over-estimate the vortex core radius, and underestimate the peak tangential velocity and streamwise vorticity levels. Therefore, it is necessary to account for the changes in vortex position. This can be achieved using global measurement methods such as PIV, since the vortex position in each instantaneous measurement can be identified before the vortex characteristics are calculated. This approach has been employed in this research, such that each circular zone which is input into the VDM routine is located at the instantaneous vortex centre position. The average flowfield properties and characteristics are thus calculated. The vortex characteristics and velocity field are thus conditionally-averaged. This is in contrast to a simple flowfield average, where the average velocity field is computed without adjustments for the vortex position, and the vortex characteristics are subsequently computed using the averaged flowfield. To illustrate the differences between the methods, the two processing approaches will be performed using a configuration from the unperturbed wing-tip vortex dataset. The selected case corresponds to the wing-tip vortex produced by the NACA 0012 vortex generator at an angle of attack of $\alpha_{vg} = 12^o$, a chord Reynolds number of 1.7×10^5 and a vortex Reynolds number of 3.7×10^4.

The vorticity contours for the simple-averaged and conditionally-averaged measurements, Figures B.4(a) and B.4(b), demonstrate that the simple-averaging technique results in notably lower streamwise vorticity levels. In particular, the peak streamwise vorticity for the simple average case is 43% lower than that obtained with the conditional-averaging technique. Furthermore, the vortex core radius is 15% larger than the conditional-averaging

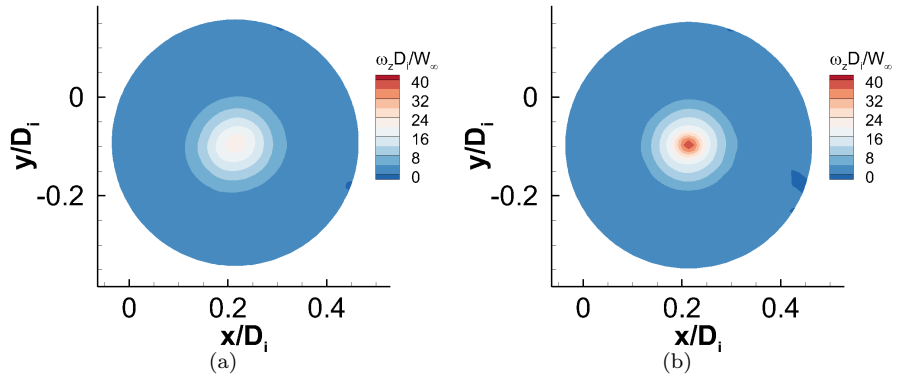

FIGURE B.4: Contours of streamwise vorticity ($\omega_z D_i/W_\infty$), NACA 0012 wing-tip vortex, $\alpha_{vg} = 12^o$, $Re_c = 1.7 \times 10^5$, $Re_v = 3.7 \times 10^4$, influence of PIV post-processing approach, (a): Simple averaging, (b): Conditional averaging

result, and the peak tangential velocity is 11% lower. These results confirm that vortex wandering can result in a diffusion of the true vortex characteristics, and must be accounted for appropriately. This has been achieved in this research by employing the conditional-averaging technique.

B.2 Inviscid intake flow simulations

An assumption which has been employed in the analysis of the vortex ingestion measurements (chapter 5) is that the measurements which were obtained at a distance of $z/D_i = 2.25$ upstream of the intake highlight plane can be considered to be representative of the vortex in the unperturbed, freestream flow. Measurements of the streamwise velocity at the vortex centre for an intake velocity ratio of $VR = W_i/W_\infty = 5.0$, Figure 5.1(b), suggested that this assumption is appropriate. However, to provide further support, simulations of the intake flowfield were performed using CFD. The sub-scale intake geometry was employed in conjunction with the mesh employed for the vortex ingestion studies, section 6.3.2. Simulations were conducted for the vortex ingestion configurations which were conducted at a freestream velocity of $W_\infty = 17.2ms^{-1}$ and intake velocity ratios of VR=10.3, 5.0 and 2.0. The freestream and intake flow conditions were prescribed using the same approach as that described in section 6.3.2.2. Note that the experimental measurements of pressure and temperature were employed directly to prescribe the boundary conditions for the simulations.

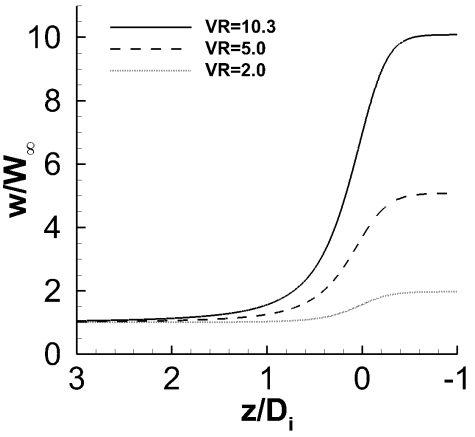

FIGURE B.5: Streamwise velocity normalised by freestream velocity (w/W_∞) along intake centreline axis for intake velocity ratios of VR=10.3, 5.0 and 2.0, $W_\infty = 17.2ms^{-1}$

The simulations demonstrate that the normalised streamwise velocity (w/W_∞) at $z/D_i = 2.25$ is close to a value of 1.0 for all intake velocity ratios. Thus, the perturbation in streamwise velocity due to the presence of the intake is small at this streamwise position. For example, for an intake velocity ratio of 5.0, the streamwise velocity w/W_∞ is equal to 1.043. When the intake velocity ratio is increased to 10.3, the velocity at $z/D_i = 2.25$ associated with the intake w/W_∞ increases to 1.096. However, it should be noted that this value is small in comparison to the range of streamwise velocities which occur between $z/D_i = 2.25$ and $z/D_i = 0.20$. When VR=10.3, for example, the perturbation corresponds to 2.6% of the value of w/W_∞ which occurs at $z/D_i = 0.20$. The effect on the vortex characteristics can be estimated using vortex filament model (section 5.1.2). For a change in velocity of $w_c/w_{c,0} = 1.096$, then the vortex core radius will be 4.7% smaller than the unperturbed value. Therefore, the change in core radius due to the intake perturbation at $z/D_i = 2.25$ is smaller than the measurement uncertainty 3.7. An additional simulation was performed for the conditions corresponding to $W_\infty = 11.0ms^{-1}$ and an intake velocity ratios of VR=16.3. This represents the largest streamtube contraction levels which were investigated in the experimental programme A.1. At this condition, the streamwise velocity perturbation $w/W_\infty - 1$ at $z/D_i = 2.25$ increases to 16.3% of the freestream velocity. Thus, the vortex characteristics at $z/D_i = 2.25$ will feature a change in core radius of 7.8%. Figures B.6(a) to B.6(d) demonstrate the effect of normalising by the vortex characteristics at $z/D_i = 2.25$ (2.25) in comparison to normalising by the unperturbed vortex measurement (U/P). It is evident that, even at the largest intake velocity ratio tested, the impact on the change in vortex characteristics is smaller than the experimental uncertainty.

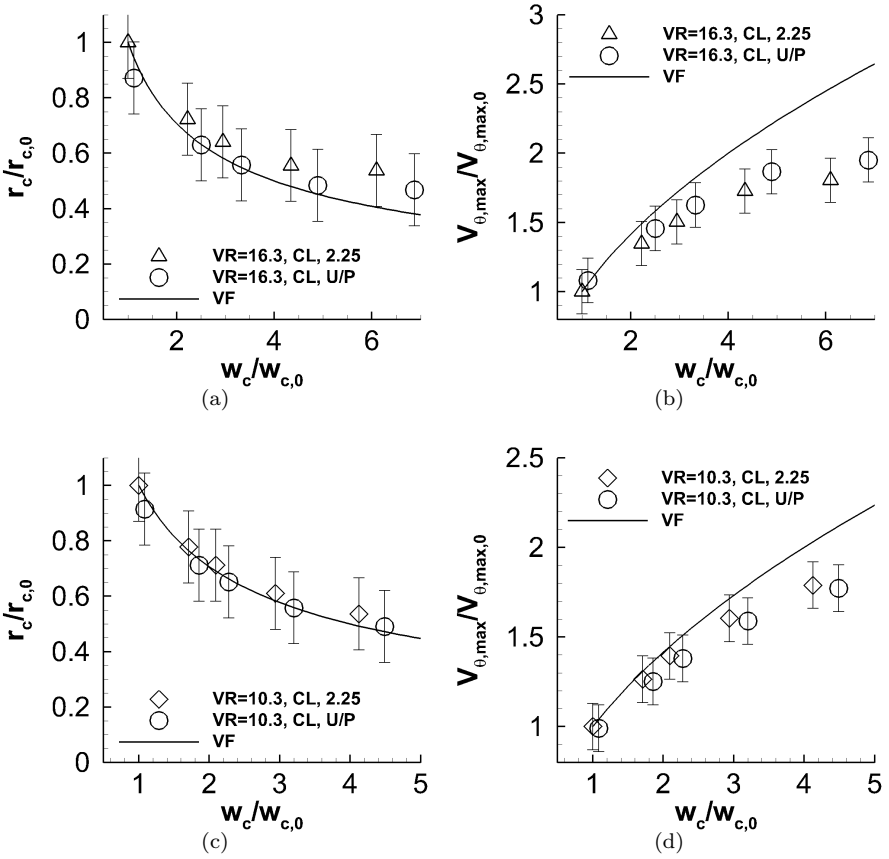

FIGURE B.6: Influence of normalising vortex characteristics by measurement at $z/D_i = 2.25$ (2.25), in comparison to normalising vortex characteristics by measurement in unperturbed flow (U/P), NACA 0012 wing-tip vortex, $\alpha_{vg} = 12^o$, $Re_c = 3.6 \times 10^5$, $Re_v = 7.4 \times 10^4$, (a): Vortex core radius, VR=16.3, (b): Peak tangential velocity, VR=16.3, (c): Vortex core radius, VR=10.3, (d): Peak tangential velocity, VR=10.3

Appendix C

Uncertainty analysis

In this appendix, details of the measurement uncertainties in the experimental work are provided. In particular, the approach which has been used to evaluate the velocity uncertainties on the PIV measurements is given. Additionally, the approach used to determine the intake and freestream flow conditions is described, and the associated uncertainties are provided.

C.1 PIV measurement uncertainties

It is imperative that the measurement uncertainties associated with the velocity measurements which have been obtained using PIV. In this way, it is possible to establish the corresponding uncertainties on the vortex characteristics in the unperturbed and contracting flows.

In general, the total uncertainty attributed to each velocity vector, δ_{tot}, includes contributions from a bias uncertainty (δ_{bias}) and a random uncertainty (δ_{rms}) [87]. The following subsections provide details on the approach which has been used to determine each of these components.

C.1.1 Bias uncertainties

The first contribution to the bias uncertainty is referred to as the registration error [96]. This source of uncertainty is a result of a misalignment between the light sheet and the calibration plane. The source of the uncertainty, and its effect on the PIV measurements,

can be described as follows. Consider a scenario where two PIV cameras are focussed on a region of interest in the x-y plane, Figure C.1(a). The camera calibration was performed using a calibration plate at a location which is displaced by Δz from the position of the light sheet. As a consequence, the measurement on the light sheet is back projected onto the calibration plane. Consequently, the perceived centreline location on the image obtained by Camera 1 is in reality displaced in the positive x direction relative to the centreline, and conversely for Camera 2. This can produce a bias uncertainty in the presence of out-of-plane velocity gradients. Consider the scenario depicted in Figure C.1(b), which features flow in the z-direction only, with a positive velocity gradient $\partial w/\partial x$. The velocity vectors which are measured by Camera 1 and Camera 2 at the centre of their respective images are illustrated in Figure C.1(c). For $\Delta z = 0$, the velocity vectors would be equal in magnitude. However, due to the offset between the light sheet and the calibration plane, the Camera 1 obtains a measurement in a region where the out-of-plane velocity is greater than that at the location which is observed by Camera 2. To obtain a Stereo PIV image, the vectors from Camera 1 and Camera 2 are subsequently combined to produce a final, 3-component PIV vector $\mathbf{V_{PIV}}$. Due to the mismatch between vectors V_1 and V_2, the measured velocity vector contains an in-plane velocity component, u_{bias}. This bias uncertainty is non-physical, and is simply a result of the misalignment Δz.

The magnitude of the registration error can be determined using trigonometry. When the camera axes are at 45^o to the image plane, then the velocity bias u_{bias} is given by Eq. C.1.

$$u_{bias} = \frac{\partial w}{\partial x}\Delta z \tag{C.1}$$

For a laminar pipe flow, Van Doorne et al. [96] demonstrated that a 0.1mm misalignment resulted in an uncertainty which was 1% of the centreline velocity. Therefore, appropriate steps must be taken to ensure that the calibration plane is as close as possible to the position of the light sheet. This was achieved in this research using a calibration plate which has been designed specifically for Stereo PIV calibration. The calibration plate features a thin slot which is aligned with a mirror which is perpendicular to the calibration plane. Using this arrangement, when the light sheet is aligned with the calibration plate, the light sheet will enter the slot, and will be reflected by the mirror, such as the scenario which is illustrated in Figure C.2(a). This method also permits the identification of the orientation of the light sheet plane relative to the calibration plate plane. For example, if the light sheet is tilted relative to the calibration plane, then the reflected light sheet

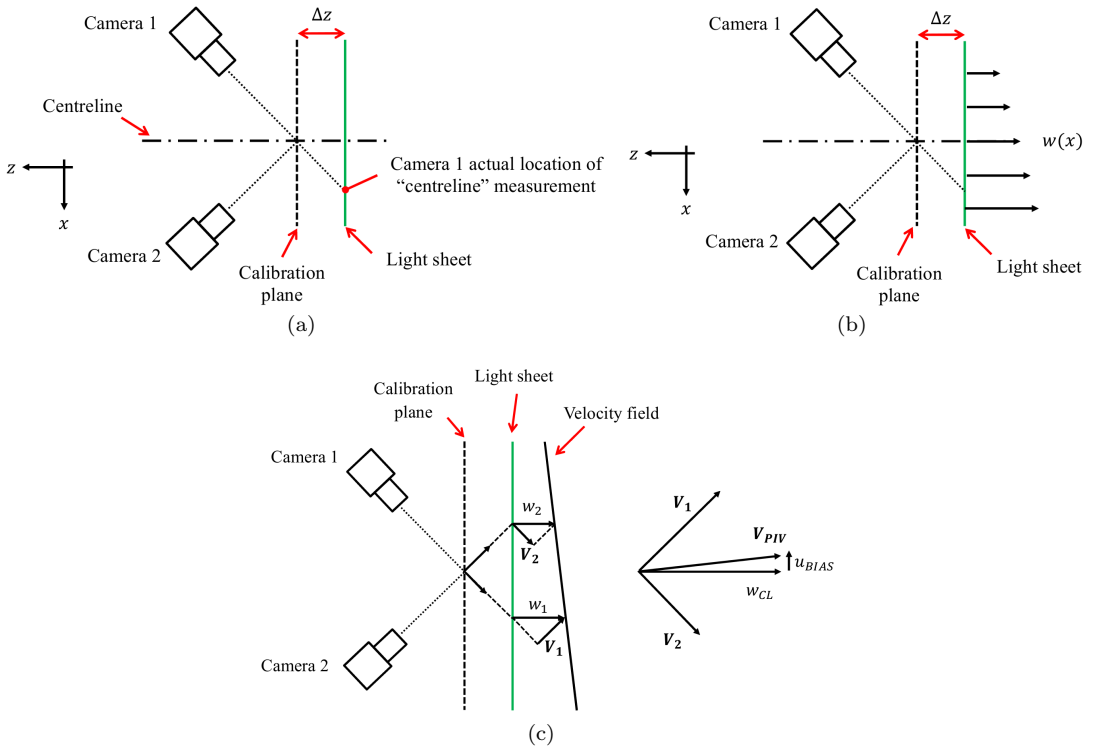

FIGURE C.1: Schematic illustrating the registration error, (a): Nomenclature and general description of offset between PIV calibration plane and laser light sheet, and corresponding optical axis geometry, (b): Example out-of-plane velocity gradient, (c): Qualitative illustration of velocity vectors which are measured by Cameras 1 and 2, and the resulting 3-component PIV vector

will not return along the incident light sheet path. It is then possible to identify the reflected light, Figure C.2(b), and perform adjustments until the light sheet is perpendicular to the calibration plate and in close alignment. This approach minimises uncertainties due to misalignment between the light sheet and the calibration plane, and a possible displacement of no more than 0.25mm is assumed.

As shown in Eq. C.1, the bias uncertainty results when there are in-plane gradients of the out-of-plane velocity. In this research, there are two likely sources of out-of-plane velocity gradients across the region of interest. The first is due to the streamwise velocity perturbation inside the vortex core, which is evident in the sample contours which have been obtained for an unperturbed NACA 0012 wing-tip vortex at $W_\infty = 35ms^{-1}$, Figure C.3(a). Additionally, the intake capture streamtube features notable in-plane gradients of the out-of-plane velocity, as demonstrated in Figure C.3(b). It is thus necessary to consider the possible registration error which results from these in-plane velocity gradients.

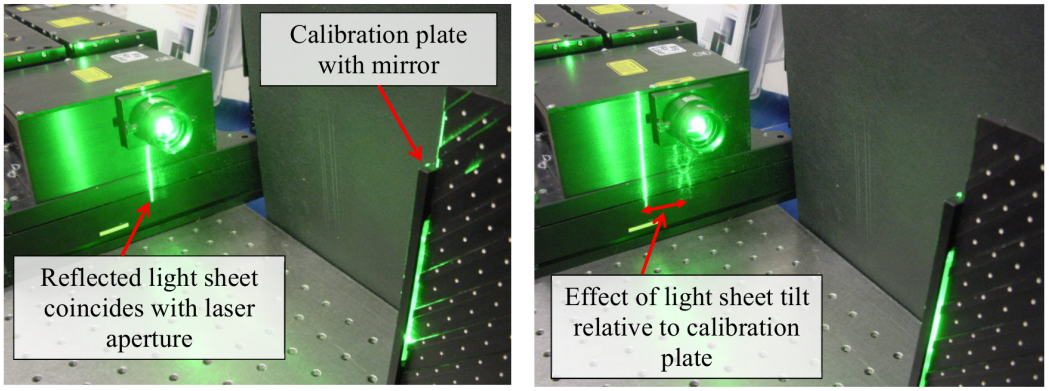

(a) (b)

FIGURE C.2: Illustration of laser light sheet alignment with a PIV calibration plate, (a): Light sheet in good alignment with calibration plate, (b): Light sheet out of alignment with the calibration plate. Images courtesy of TSI Inc.

Assuming a light sheet misalignment of $\Delta z = 0.25mm$, then the registration error contours for the convecting vortex and ingested vortex flows are given in Figures C.3(c) and C.3(d), respectively. Based on these sample images, it is apparent that the maximum values of δ_{reg} correspond to $0.009W_\infty$ at the vortex centre for the wing-tip vortex in the uniform flow, and $0.02W_\infty$ near the edge of the region of interest for the ingestion flows. Note, however, that the streamwise velocity for the ingestion flow corresponds to approximately $97ms^{-1}$ at the centreline, and approximately $58ms^{-1}$ at the location of the maximum values of δ_{reg}. Thus, the peak registration error is $0.012W_\infty$. These uncertainties can also be expressed in terms of the pixel displacement, Eq. C.2, where Δt is the PIV measurement time delay, and M is the magnification.

$$\delta_{reg}(px) = \delta_{reg}(ms^{-1})\Delta t M \tag{C.2}$$

It is clear that the value of the registration error is dependent on the vortex characteristics and the intake capture streamtube characteristics. It has been found that the typical maximum values of the registration error for a wide range of vortex ingestion configurations corresponds to $\delta_{reg} = 0.04px$.

A second source of bias uncertainty is termed peak locking, and can result in the PIV processing stage. When the particle image in the PIV images is less than 2 pixels in diameter, the conventional 3-point interpolation schemes which are employed to locate the correlation peak can become unsuitable [87]. When this happens, the displacement of the particle between two images cannot be determined accurately to sub-pixel resolution,

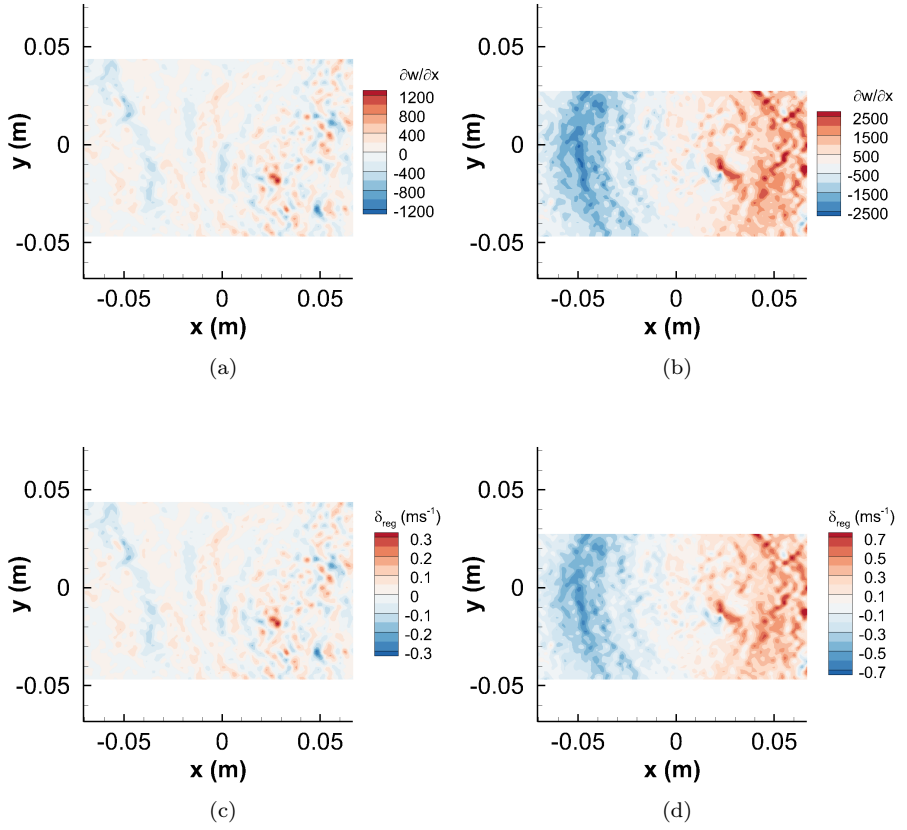

FIGURE C.3: Results pertaining to light sheet misalignment studies, NACA 0012 wingtip vortex, $\alpha_{vg} = 12^o$, $Re_c = 3.6 \times 10^5$, $Re_v = 7.4 \times 10^4$, (a): Contours of $\partial w/\partial x$ for unperturbed vortex, (b) Contours of $\partial w/\partial x$, VR=4.9, $z/D_i = 0.20$, (c): Contours of δ_{reg}, unperturbed vortex, (d): Contours of δ_{reg}, VR=4.9, $z/D_i = 0.20$

and the particle displacement which is obtained from the PIV processing stage tends towards integer pixel displacements. Peak locking can be identified from the particle image displacement histograms for each PIV image. A PIV vector field without peak locking is characterised by a smooth distribution of particle image displacements (left image of Figure C.4). An example of a typical PIV image histogram with peak locking is shown on the right image in Figure C.4. The particle image displacement histograms feature dominant peaks at integer pixel displacements. Peak locking can be avoided using an appropriate optical and seeding configuration to ensure that the particle image diameter is a minimum of 2 pixels. Furthermore, iterative window shifting techniques can be employed to help mitigate the effects of peak locking [87].

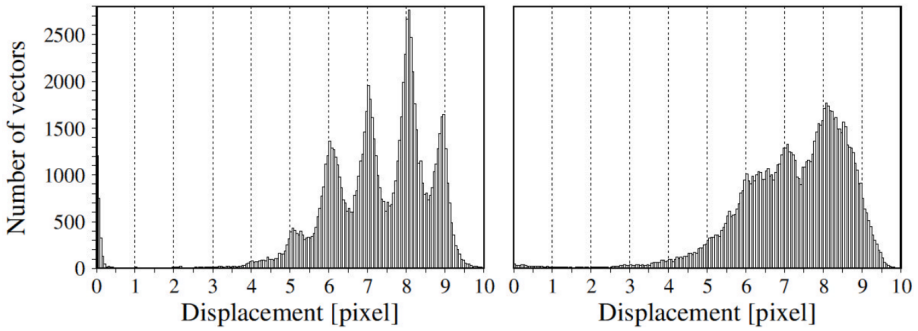

FIGURE C.4: Typical particle image displacement histograms, without (left) and with (right) peak locking [87]

C.1.2 RMS uncertainties

In addition to the bias uncertainties, it is possible to account for a range of RMS uncertainties which arise during the PIV image processing stage. Raffel et al. [87] reported the results of numerical simulations using synthetic PIV images. Using this approach, it is possible to estimate the uncertainty contributions from the particle image size, the image displacement between PIV images, the seeding density, the image quantisation levels, the background noise in the PIV images, and the effect of velocity gradients across the PIV image. As demonstrated in this section, the results of the simulations have been employed to generate uncertainty estimates as a function of the details of the PIV images and the processing approach.

C.1.2.1 Particle image size

In section C.1.1, it was demonstrated that bias uncertainties can result when the resolution of the particle image is insufficient. In addition, an RMS uncertainty can be introduced (Figure C.5). The RMS uncertainty is non-uniform with the number of pixels which define the particle image diameter, and there is an optimum particle image resolution. This optimum is dependent on the size of the interrogation window, such that a particle size of 2.5px is optimum for an interrogation window size of $64 \times 64px$. For an interrogation window of $16 \times 16px$, the optimum particle resolution is approximately 2px. When the particle image size is greater than 2.5px, the correlation peak broadens. This can reduce the signal to noise ratio of the true particle displacement peak relative to the adjacent displacement peaks [119].

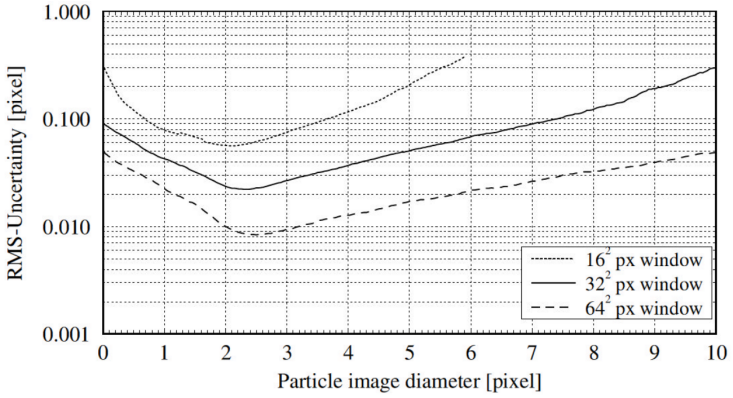

FIGURE C.5: Influence of particle image size on RMS uncertainty [87]

Inspection of the PIV images which have been obtained in this research has revealed that the particle image resolution is approximately 2px. Therefore, since an interrogation window size of $32 \times 32px$ has been employed, the estimated RMS uncertainty due to the particle image size is $\delta_s = 0.03px$

C.1.2.2 Particle image displacement

The particle image displacement refers to the spatial displacement of the particle images inside the interrogation window, as obtained between the two PIV frames. It has been found that the RMS uncertainty increases from zero at zero displacement, in a linear fashion, until the particle image displacement reaches 0.5px (Figure C.6). Thereafter, the uncertainty slowly increases as a function of the particle image displacement. Note that the uncertainty is reduced for smaller particles, in agreement with the results of Figure C.5, and for larger interrogation windows. The low RMS uncertainties which occur for displacements of less than 0.5px can be exploited by using iterative window shifting techniques [87].

An iterative window shifting method with a window size of $32 \times 32px$ has been utilised in this research. Since the typical particle image diameter is 2px, then the maximum RMS uncertainty attributed to the particle image displacement is $\delta_{disp} = 0.01px$.

C.1.2.3 Seeding density

The seeding density of the PIV images can be characterised in terms of the number of seeding particles which are contained in each interrogation window. This can be a notable

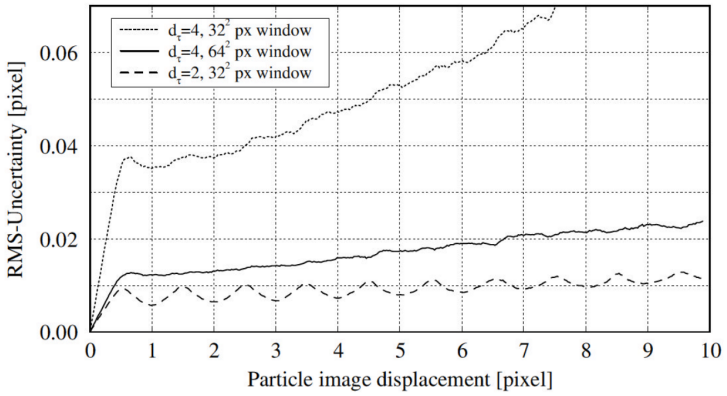

FIGURE C.6: Influence of particle image displacement on RMS uncertainty [87]

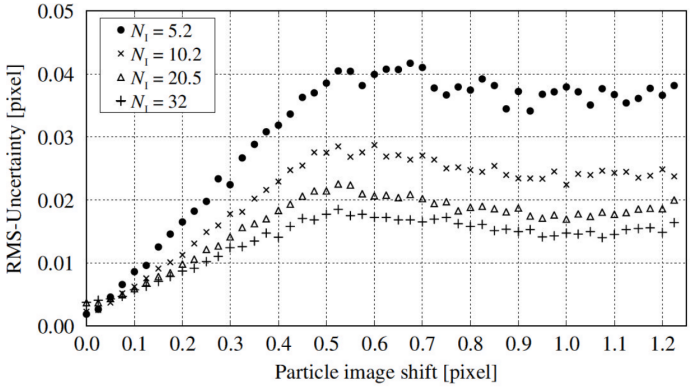

FIGURE C.7: Influence of seeding density on RMS uncertainty [87]

source of RMS uncertainty. When the number of seeding particles is insufficient, the signal to noise ratio of the correlation process reduces, and the likeliness of invalid vectors increases [87]. The results, which have been generated using a $32 \times 32px$ interrogation window, demonstrate that the RMS uncertainty increases for larger particle displacements (Figure C.7).

Inspection of the PIV images has revealed that approximately 10-15 particles are contained in each $32 \times 32px$ interrogation window. Therefore, the RMS uncertainty contribution due to the seeding density is $\delta_{den} = 0.03px$. An exception is found inside the vortex core. Due to the large rotation rates inside the vortex core, the seeding particles experience a centrifugal force which causes the particles to migrate radially outwards from the vortex centre. It has been estimated from inspection of the PIV images that the number of seeding particles is reduced to approximately 5 particles in each interrogation window.

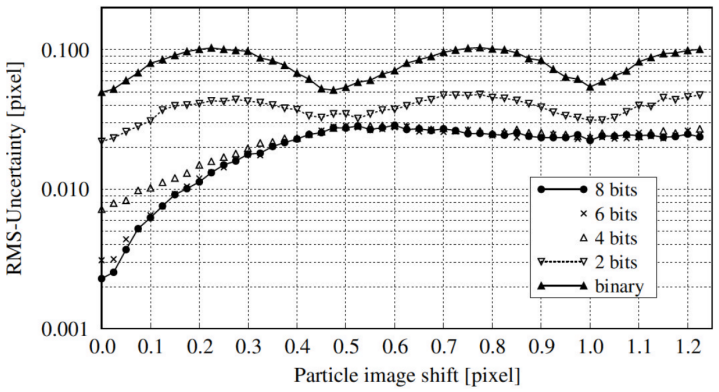

FIGURE C.8: Influence of image quantisation on RMS uncertainty [87]

Therefore, the RMS uncertainty increases to $\delta_{den} = 0.04$ inside the vortex core. This uncertainty has been assumed for all uncertainty calculations.

C.1.2.4 Image quantisation

An RMS uncertainty is also introduced as a result of the number of bits which are utilised by the digital camera to resolve the PIV image intensity levels for each pixel. As these image quantisation levels reduce, there is an increase in the RMS uncertainty of the PIV measurement, Figure C.8.

The cameras used in this research are of 12-bit specification, and so a conservative estimate of the RMS uncertainty associated with the quantisation levels is $\delta_q = 0.03px$.

C.1.2.5 Background noise

In experiments, background noise can arise in the PIV images due to unwanted reflections or due to the ambient light conditions. The RMS uncertainty which was associated with this can be estimated by applying white noise at was applied to each pixel as a fraction of the pixel dynamic range [87]. For a particle image displacement of 0.5px, the RMS uncertainty associated with background noise is small when the background noise is less than or equal to 10% of the pixel dynamic range (Figure C.9). For higher levels of background noise, the uncertainty levels increase in a monotonic fashion.

To provide a conservative estimate of the contribution of background noise to the RMS uncertainty of the PIV measurement, a background noise of 5% has been assumed. This

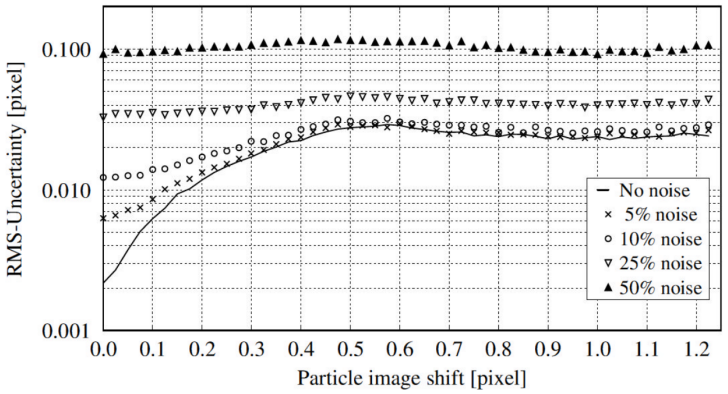

FIGURE C.9: Influence of background noise levels on RMS uncertainty [87]

value was also assumed by Murphy [72] for similar experiments in the same wind-tunnel facility and using the same PIV imaging apparatus. Thus, an RMS contribution of $\delta_{bn} = 0.03$ has been selected, assuming a maximum particle image displacement of 0.5px.

C.1.2.6 Displacement gradients

Certain flows may feature notable in-plane velocity gradients across the PIV measurement region. Examples include vortical flows, such as those of interest in this research, or boundary layer flows. In the presence of a strong in-plane velocity gradient, the displacements of the particles inside an interrogation region may not be the same. The correlation process which is utilised to obtain velocity vector information from the PIV images obtains the average particle velocity inside the interrogation window. Thus, if the particles do not have the same velocity, then the result from the correlation process will contain an uncertainty. In general, the correlation will be biased towards lower velocities, since faster particles are most likely to leave the interrogation window between the two PIV frames. The results demonstrate that the uncertainty is reduced for smaller interrogation windows and increased seeding density levels (Figure C.10).

Assuming that the PIV measurements are acquired on a plane which is perpendicular to the vortex axis, then the possible effects of displacement gradients on the measurement of vortical flow will be greatest inside the vortex core where the vortex tangential velocity gradients are large. An estimate of the displacement gradients which may be encountered in this research can be obtained by assuming a Rankine vortex velocity distribution inside the vortex core, Eq. C.3, as shown qualitatively in Figure C.11.

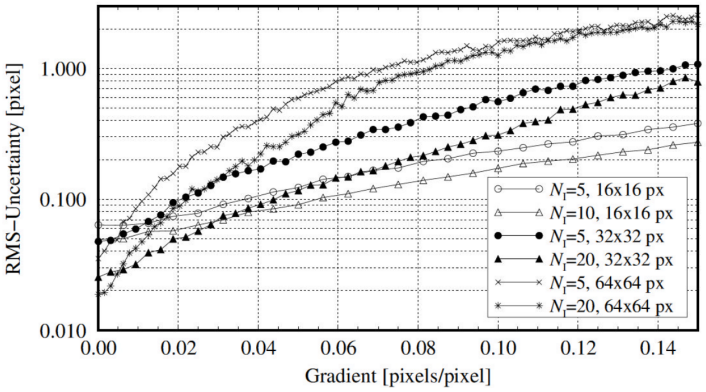

FIGURE C.10: Influence of displacement gradients on RMS uncertainty [87]

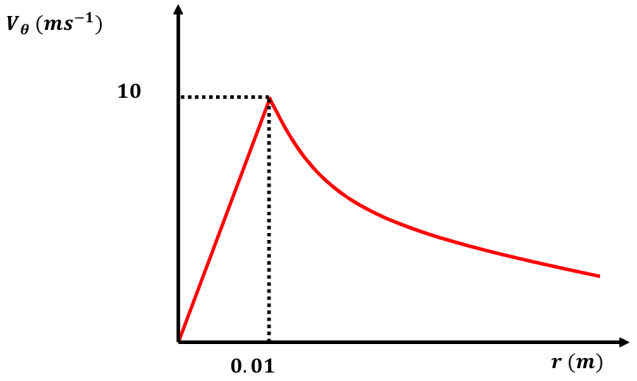

FIGURE C.11: Qualitative illustration of Rankine vortex velocity distribution for displacement gradient uncertainty example

$$V_\theta = \omega r \tag{C.3}$$

The peak tangential velocity ($V_{\theta,max}$) and core radius r_c have been assumed to be equal to $10ms^{-1}$ and $0.01m$ respectively, which are representative of the unperturbed vortex measurements which have been obtained in this research. Therefore, the vorticity ω can be determined (Eq. C.4).

$$\omega = \frac{V_{\theta,max}}{r_c} = \frac{10}{0.1} = 1000s^{-1} \tag{C.4}$$

It is then of interest to estimate the change in velocity which is likely to occur in the radial direction across a single rectangular interrogation window. To do this, a camera configuration corresponding to the current experimental measurements (section 3.4.1) has

been assumed. Thus, the magnification is 0.1, and the imaging hardware consists of a digital camera with a CCD size and resolution of $15 \times 15mm$ and $2048 \times 2048px$. Thus, the physical size of a single pixel is $L_p = 7.3 \times 10^{-5}$, Eq. C.5. The corresponding change in velocity across a single pixel is therefore $0.073ms^{-1}$ (Eq. C.6).

$$L_p = \frac{1}{M}\frac{L_{CCD}}{N_{px}} = \frac{1}{0.1}\frac{0.015}{2048} = 7.3 \times 10^{-5}m \tag{C.5}$$

$$\Delta V_\theta = \omega L_p = 1000 \times 7.3 \times 10^{-5} = 0.073ms^{-1} \tag{C.6}$$

Finally, it is necessary to express the velocity gradient in terms of pixel displacements per pixel. To do this, a time delay of $\Delta t = 20 \times 10^{-6}s$ is assumed, which gives a physical displacement of $\Delta X = 1.46 \times 10^{-6}m$ (Eq. C.7). Finally, using Eq. C.8, the displacement gradient is equal to 0.02px.

$$\Delta X = \Delta V_\theta \Delta t = 0.073 \times 20 \times 10^{-6} = 1.46 \times 10^{-6}m \tag{C.7}$$

$$\delta x = \frac{\Delta X}{L_p} = \frac{1.46 \times 10^{-6}}{7.3 \times 10^{-5}} = 0.02px \tag{C.8}$$

With reference to Figure C.10, for 5 particles inside a $32 \times 32px$ interrogation window, the corresponding RMS uncertainty due to the displacement gradients is 0.1px. A comparison with the RMS uncertainty contributions which have been introduced in the preceding sections highlights that the RMS uncertainty due to displacement gradients can be the dominant source of uncertainty. Fortunately, the effects of displacement gradients on the correlation process can be mitigated using window deformation techniques [87, 91]. Such methods employ an iterative process to deform the particle images. In this manner, the displacement gradients inside the interrogation window can be accounted for, and the RMS uncertainty associated with the displacements can be avoided. Since a window deformation technique has been employed in this research, the contribution of the displacement gradients to the RMS uncertainty (δ_{grad}) has been neglected.

C.1.2.7 Calculation of PIV measurement uncertainty

The total uncertainty which is associated with a single, 3-component, velocity vector from the Stereo PIV measurements can be determined using the bias and RMS uncertainty contributions which have been detailed in the preceding subsections. Note that peak locking does not need to be included in this calculation, since inspection of the current PIV measurements revealed that peak locking did not occur. In addition, the effects of displacement gradients have been neglected, since a window deformation method has been employed as part of the PIV processing approach.

The total RMS uncertainty, δ_{RMS} on a single PIV vector can thus be computed using quadrature as the combination of contributions from the particle image size, particle image displacement, seeding density, image quantisation, and background noise, Eq. C.9.

$$\delta_{RMS} = \sqrt{\delta_s + \delta_{disp} + \delta_{den}\delta_q + \delta_{bn}} = 0.07px \tag{C.9}$$

The RMS uncertainty in Eq. C.9 corresponds to the uncertainty on a single PIV vector from one camera. Thus, Eq. C.10 is employed to compute the total uncertainty for a Stereo PIV measurement. Note that the typical registration uncertainty is included at this stage, since the uncertainty is introduced during the combination of the two velocity vectors to produce a single 3-component velocity vector.

$$\delta_{TOT} = \sqrt{2\delta_{RMS} + \delta_{reg}} = 0.10px \tag{C.10}$$

The pixel displacement uncertainty in Eq. C.10 must now be converted into velocity in physical space. This can be achieved using Eq. C.11, where M is the magnification, Δt is the PIV measurement time delay, L_{CCD} is the edge size of the camera CCD chip, and N_{CCD} is the number of pixels along the dimension L_{CCD}.

$$\delta_u = \frac{\delta_{TOT}}{M\Delta t}\frac{L_{CCD}}{N_{CCD}} \tag{C.11}$$

It is also of interest to determine the uncertainty on the vortex core radius, the vortex core circulation, and the vorticity measurements.

The uncertainty associated with the vortex core radius is limited simply by the spatial resolution of the PIV measurements, which corresponds to approximately $1 \times 10^{-3}m$.

TABLE C.1: PIV measurement uncertainties for a selection of unperturbed vortex and vortex ingestion configurations, NACA 0012 wing-tip vortex at $\alpha_{vg} = 12^o$, $Re_v = 3.7 \times 10^4$, $W_\infty = 17.8ms^{-1}$

Case	Unperturbed	VR=10.3, $z/D_i = 0.20$	VR=5.0, $z/D_i = 0.20$
δ_u (ms^{-1})	0.34	1.60	0.92
δ_u/W_∞ (%)	1.9	8.99	7.88
δ_u/w_c (%)	1.70	1.78	1.71
$\delta_u/V_{\theta,max}$ (%)	3.36	8.99	6.14
$\delta_{\omega_z}/\omega_{z,max}$ (%)	5.08	9.85	7.62
$\delta_{\omega_{z,av}}/\omega_{z,av}$ (%)	10.0	15.2	13.3
δ_{r_c}/r_c (%)	5.75	11.63	9.62
$\delta_{\Gamma_c}/\Gamma_c$ (%)	3.4	9.0	6.1

Thus, a spatial measurement uncertainty of $5 \times 10^{-4}m$ has been assumed. The uncertainty on the vortex core circulation has been determined using the uncertainties on the vortex core radius and the vortex peak tangential velocity measurements.

An estimate of the uncertainty of the out-of-plane vorticity measurements can be obtained by considering a linear calculation of velocity gradients. Therefore, the uncertainty on the in-plane velocity gradients $\partial u/\partial y$ and $\partial v/\partial x$ is given by Eq. C.12, [72].

$$\delta_{\partial u/\partial y} = \delta_{\partial v/\partial x} = \frac{1}{2\Delta x}\sqrt{2\delta_u^2} \tag{C.12}$$

Note that the grid spacing is constant in the x and y directions, such that $\Delta x = 1 \times 10^{-3}m$. Therefore, the total uncertainty on the vorticity measurements is given by Eq. C.13.

$$\delta_{\omega_z} = \sqrt{2\delta_{\partial u/\partial y}^2} \tag{C.13}$$

For all experiments, M=0.1, $L_{CCD} = 0.015m$ and $N_{CCD} = 2048$. The value of Δt varied as a function of the streamwise velocity in each of the vortex convection and ingestion configurations. In this way, it was possible to ensure that the maximum particle displacement was less than 1/4 of the light sheet thickness. This is an important requirement to ensure that the seeding particles remain inside the light sheet for both PIV frames [87]. Therefore, three different cases have been selected to illustrate the range of measurement uncertainties which have been encountered in the experimental programme.

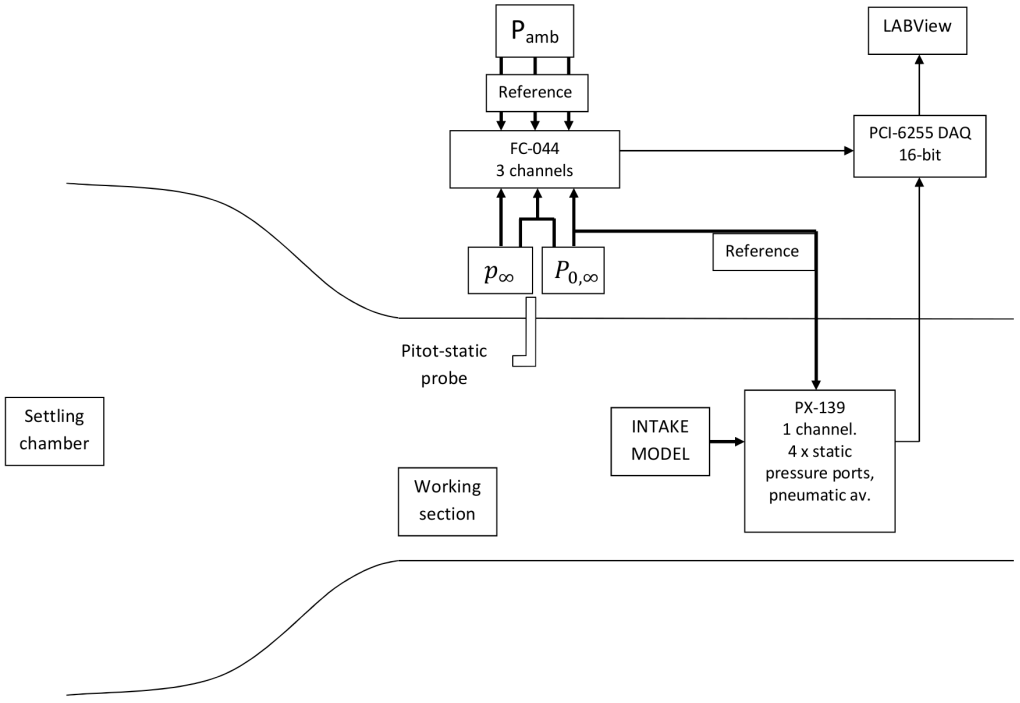

FIGURE C.12: Schematic of the pressure measurement system

C.2 Pressure measurements

C.2.1 Calculation of freestream and intake conditions

To characterise the freestream flow, a Pitot-static probe was mounted in the working section at a location which is outside of the intake capture streamtube, Figure C.12. The reference pressure for the Pitot-static probe measurements was the ambient pressure, P_{amb}, which was measured using a Druck DPI 261 digital manometer. The two measurements from the Pitot-static probe, therefore, correspond to p_{T1} and p_{T2}, Eq. C.14. Two Furness Controls FC-044 differential pressure transducers were employed to measure p_{T1} and p_{T2}.

$$\begin{aligned} p_{T1} &= P_{0,\infty} - P_{amb} \\ p_{T2} &= p_\infty - P_{amb} \end{aligned} \tag{C.14}$$

The dynamic pressure in the working section was determined using Eq. C.15.

$$q_\infty = p_{T1} - p_{T2} \tag{C.15}$$

To calculate the freestream density, ρ_∞, Eq. C.16 was employed, where $R = 287 Jkg^{-1}K^{-1}$. The total temperature T_0 corresponded to the temperature inside the settling chamber of the wind-tunnel.

$$\rho_\infty = \frac{p_\infty}{RT_0} \tag{C.16}$$

Finally, the freestream velocity is then computed with Eq. C.17

$$W_\infty = \sqrt{\frac{2q_\infty}{\rho_\infty}} \tag{C.17}$$

To determine the flow conditions inside the intake, it is assumed that the total pressure inside the intake, $P_{0,i}$, is equal to the freestream static pressure. This is an appropriate assumption, since the total pressure loss associated with the vortex is small. Therefore, it is possible to use isentropic relations to determine the intake flow properties.

The static pressure inside the intake was obtained using the pneumatically-averaged pressure from four static pressure ports which were located at equidistant points around the intake inner circumference. The reference pressure for the static pressure port measurements was the freestream total pressure. Thus, to determine the intake static pressure, Eq. C.18 was employed. The static pressure inside the intake was measured using an Omega PX139-005D4V differential pressure transducer.

$$p_i = p_{T1} + p_{T2} + P_{amb} \tag{C.18}$$

It is then possible to compute the ratio PR, given in Eq. C.19, which can be employed to determine the static temperature (T_i) and the density (ρ_i) inside the intake, Eq. C.20 and C.21, respectively.

$$PR = \frac{P_{0,\infty}}{p_i} \tag{C.19}$$

$$T_i = \frac{T_0}{PR^{\gamma/(\gamma-1)}} \tag{C.20}$$

$$\rho_i = \frac{p_i}{RT_i} \tag{C.21}$$

Finally, the velocity inside the intake can be determined with Eq. C.22, where $c_p = 1005 Jkg^{-1}K^{-1}$. In addition, the mass flow and Mach number are given by Eqs. C.23 and C.24, where $A_i = \pi r_i^2$ is the flow area inside the intake.

$$W_i = \sqrt{2c_p\left(T_0 - T_i\right)} \tag{C.22}$$

$$\dot{m}_i = W_i A_i \rho_i \tag{C.23}$$

$$M_i = \frac{W_i}{\sqrt{\gamma R T_i}} \tag{C.24}$$

C.2.2 Uncertainties

In general, the uncertainty the pressure measurements consist of comprise the transducer uncertainties, and the uncertainties which are attributed to the measurement of the ambient pressure (P_{amb}) and the total temperature (T_0).

The transducer uncertainties consist of the measurement accuracy as given by the manufacturer (δ_{acc}), the resolution uncertainty (δ_{res}), and the calibration uncertainty (δ_{cal}). The measurement accuracy of the FC-044 and PX-139 transducers are, respectively, 0.3% and 0.1% of the full-range, where the full-range pressures are 2500Pa and 34474Pa. The corresponding measurement accuracy values in Pa are provided in Table C.2.The calibration of the transducers was performed using a Druck DPI 603 Pressure Calibrator, and the corresponding calibration curves for $T1$ and $T2$ are given in Figures C.13(a) and C.13(b). The calibration uncertainties were obtained using the LINEST function in Microsoft Excel. The resolution uncertainty is attributed to the number of bits of the DAQ card along with the voltage at which it operates. In this research, a National Instruments PCI-6255 16-bit DAQ card was employed, which featured a 2^{16} bit resolution and an

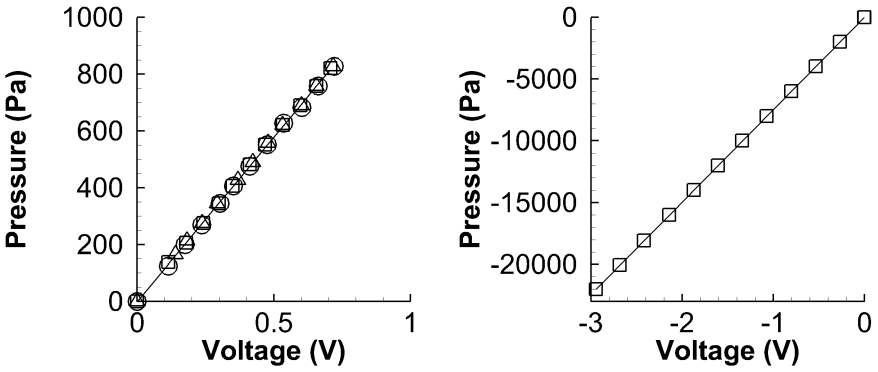

FIGURE C.13: Calibration points and curves, (a): FC-044 ($T1$) calibration, (b): PX-139 ($T2$) calibration

TABLE C.2: Transducer uncertainties

	FC-044 (T1)	PX-139 (T2)
δ_{acc} (Pa)	7.50	34.47
δ_{res} (Pa)	1.37	0.21
δ_{cal} (Pa)	4.42	6.78
δ_{tot} (Pa)	8.81	35.16

operating voltage of 12V. Thus, the resolution uncertainty is given by Eq. C.25. Table C.2 provides the values of the transducer uncertainties.

$$\delta_{res} = \frac{12}{2^{16}} = 1.831 \times 10^{-4} \tag{C.25}$$

The digital manometer which was employed to measure the ambient pressure P_{amb} featured a measurement resolution of 10Pa. Therefore, the uncertainty in the ambient pressure measurements is $\delta_{P_{amb}} = 5Pa$. Finally, the total temperature T_0 was measured to an accuracy of 1K, with a resulting uncertainty of $\delta_{T_0} = 0.5K$. It is now possible to undertake the uncertainty propagation analysis to determine the typical uncertainties on the freestream and intake conditions.

Firstly, the freestream velocity is calculated from Eqs. C.15, C.16. Thus, the uncertainty in the freestream velocity requires use of the uncertainties for P_{amb}, T_0, and the calculation

of the uncertainty levels of p_∞, ρ_∞, and q_∞. Firstly, the uncertainty on p_∞ is given by Eq. C.26.

$$\delta_{p_\infty} = \sqrt{\delta_{P_{amb}}^2 + \delta_{tot_{T1}}^2} = \sqrt{5^2 + 8.81^2} = 10.13Pa \tag{C.26}$$

The freestream static pressure for $W_\infty = 17.8ms^{-1}$ was approximately 102200Pa, which gives a static pressure uncertainty $\delta_{p_\infty}/p_\infty$ of 9.91×10^{-5}, Eq. C.27.

$$\frac{\delta_{p_\infty}}{p_\infty} = \frac{10.13}{102200} = 9.91 \times 10^{-5} \tag{C.27}$$

This can then be used to determine the uncertainty on the freestream density, given by Eq. C.28, where a typical value of $T_0 = 292.15K$ has been employed. In addition, since the dynamic pressure is determined using the difference between the transducer readings T1 and T2, the uncertainty is given by Eq. C.29, given a typical freestream dynamic pressure of $q_\infty = 181Pa$.

$$\frac{\delta_{\rho_\infty}}{\rho_\infty} = \sqrt{\left(\frac{\delta_{p_\infty}}{p_\infty}\right)^2 + \left(\frac{\delta_{T_0}}{T_0}\right)^2} = 1.71 \times 10^{-3} \tag{C.28}$$

$$\frac{\delta_{q_\infty}}{q_\infty} = \frac{\sqrt{\delta_{tot_{T1}}^2 + \delta_{tot_{T2}}^2}}{q_\infty} = 4.87 \times 10^{-2} \tag{C.29}$$

Finally, the uncertainty associated with the freestream velocity, $\delta_{W_\infty}/W_\infty$, can be computed using Eq. C.30.

$$\frac{\delta_{W_\infty}}{W_\infty} = \sqrt{\frac{\delta_{q_\infty}}{q_\infty}^2 + \frac{\delta_{\rho_\infty}}{\rho_\infty}^2} = 2.44 \times 10^{-2} \tag{C.30}$$

The uncertainty on the intake conditions can be determined using the relationships in Eqs. C.18 to C.22. The total uncertainty on the intake static pressure, δ_{p_i}, is given by Eq. C.31. Using a typical static pressure of $p_i = 84000Pa$, it is possible to calculate the typical uncertainty, Eq. C.32.

$$\delta_{p_i} = \sqrt{\delta_{tot_{T1}}^2 + \delta_{tot_{T2}}^2 + \delta_{P_{amb}}^2} = 36.59Pa \tag{C.31}$$

$$\frac{\delta_{p_i}}{p_i} = 4.36 \times 10^{-4} \tag{C.32}$$

The total pressure inside the intake flow is assumed to be equal to that in the freestream. Therefore, the uncertainty $\delta_{P_{0,i}}$ and fractional uncertainty $\delta_{P_{0,i}}/P_{0,i}$ are given in Eqs. C.33 and C.34.

$$\delta_{P_{0,i}} = \sqrt{\delta^2_{P_{amb}} + \delta^2_{tot_{T1}}} = 10.13Pa \tag{C.33}$$

$$\frac{\delta_{P_{0,i}}}{P_{0,i}} = 9.982 \times 10^{-5} \tag{C.34}$$

The uncertainty associated with the pressure ratio is thus calculated using Eq. C.35. It is then necessary to compute the intake static pressure uncertainty, Eq. C.36 and the uncertainty associated with $T_0 - T_i$, Eqs. C.37.

$$\frac{\delta_{PR}}{PR} = \sqrt{\left(\frac{\delta_{P_{0,i}}}{P_{0,i}}\right)^2 + \left(\frac{\delta_{p_i}}{p_i}\right)^2} = 4.47 \times 10^{-4} \tag{C.35}$$

$$\frac{\delta_{T_i}}{T_i} = \sqrt{\left(\frac{\gamma - 1}{\gamma}\frac{\delta_{PR}}{PR}\right)^2 + \frac{\delta {T_0}^2}{T_0}} = 2.32 \times 10^{-3} \tag{C.36}$$

$$\delta_{T_0 - T_i} = \sqrt{\delta^2_{T_0} + \left(\frac{\delta_{T_i}}{T_i} T_i\right)^2} = 0.81K \tag{C.37}$$

Finally, the uncertainty in $(T_0 - T_i)$ can be expressed in terms of Eq. C.38, which permits calculation of the uncertainty on the intake velocity, Eq. C.39.

$$\frac{\delta_{T_0 - T_i}}{T_0 - T_i} = 5.37 \times 10^{-2} \tag{C.38}$$

$$\frac{\delta_{W_i}}{W_i} = 0.5\frac{\delta_{T_0 - T_i}}{T_0 - T_i} = 2.69 \times 10^{-2} \tag{C.39}$$

References

[1] Devenport, W. J., Rife, M. C., Liapis, S. I., and Follin, G. J., "The structure and development of a wing-tip vortex," *Journal of Fluid Mechanics*, Vol. 312, 1996, pp. 67–106.

[2] Seddon, J. and Goldsmith, E., *Intake Aerodynamics*, Collins Professional and Technical Books, London, 1985.

[3] "Kaktus Digital," http://kaktusdigital.4ormat.com/, Accessed: 07/2012.

[4] "UAV Global Datasheet," http://www.uavglobal.com/dassault-neuron/, Accessed: 09/2013.

[5] Gatlin, G. M., Vicroy, D. D., and Carter, M. B., "Experimental Investigation of the Low-Speed Aerodynamic Characteristics of a 5.8-Percent Scale Hybrid Wing Body Configuration," *30th AIAA Applied Aerodynamics Conference, New Orleans, Louisiana, 25-28 June*, No. AIAA 2012-2669, 2012.

[6] Yuhas, A. J., Steenken, W. G., Williams, J. G., and Walsh, K. R., "F/A-18 Inlet Flow Characteristics During Maneuvers with Rapidly Changing Angle of Attack," Tech. Rep. TM 104327, NASA, 1996.

[7] Motycka, D., "Ground Vortex - Limit to Engine/Reverser Operation," *ASME Gas Turbine Conference, Houston, Texas, March 2-6*, No. 75-GT-3, 1975.

[8] Mitchell, G. A., "Effect of Inlet Ingestion of a Wing Tip Vortex on Compressor Face Flow and Turbojet Stall Margin," Tech. Rep. TM X-3246, NASA, 1975.

[9] Meyer, W., Pazur, W., and Fottner, L., "The Influence of Intake Swirl Distortion on the Steady-State Performance of a Low Bypass Twin-Spool Engine," Tech. Rep. CP-498, AGARD, 1991.

[10] Green, J., "Forced Response of a Large Civil Fan Assembly," *Proceedings of ASME Turbo Expo 2008: Power for Land, Sea and Air, Berlin, Germany, June 9-13*, No. GT2008-50319, 2008.

[11] SAE, "A Method for Assessing Inlet Swirl Distortion," Tech. rep., 2007.

[12] SAE, "Predicting Inlet Dynamic Total-Pressure Distortion - Background and Guidance for CFD Developers," Tech. rep., 2012.

[13] Murphy, J. and MacManus, D., "Ground vortex aerodynamics under crosswind conditions," *Experiments in Fluids*, Vol. 50, 2011, pp. 109–124.

[14] Vunnam, K. and Hoover, R., "Modeling of Inlet Distortion using a Combined Turbofan and Nacelle Inlet Model during Crosswind and Low Speed Forward Operation," *Proceedings of ASME Turbo Expo 2011, Vancouver, British Columbia, Canada, June 6-10*, No. GT2011-46466, 2011.

[15] Breitsamter, C., "Wake vortex characteristics of transport aircraft," *Progress in Aerospace Sciences*, Vol. 47, 2011, pp. 89–134.

[16] Green, S. I., *Fluid Vortices*, Dordrecht: Kulwer Academic Publishers, 1995.

[17] Lee, T. and Pereira, J., "Nature of wakelike and jetlike axial tip vortex flows," *Journal of Aircraft*, Vol. 47, 2010, pp. 1946–1954.

[18] Kuethe, A. and Chow, C., *Foundations of Aerodynamics. Bases of Aerodynamic Design*, John Wiley & Sons, Inc., 1998.

[19] Spreiter, J. and Sacks, A., "The Rolling Up of the Trailing Vortex Sheet and Its Effect on the Downwash Behind Wings," *Journal of the Aeronautical Sciences*, Vol. 18, 1951, pp. 21–32.

[20] Leishman, J. G., *Principles of Helicopter Aerodynamics*, Cambridge University Press, 2000.

[21] Dosanjh, D. S., Gasparek, E. P., and Eskinazi, S., "Decay of a Viscous Trailing Vortex," *The Aeronautical Quarterly*, Vol. 13, 1962, pp. 167–188.

[22] Chow, J. S., Zilliac, G. G., and Bradshaw, P., "Mean and Turbulence Measurements in the Near Field of a Wingtip Vortex," *AIAA Journal*, Vol. 35, No. 10, 1997, pp. 1561–1567.

[23] Chow, J., Zilliac, G., and Bradshaw, P., "Turbulence Measurements in the Near Field of a Wingtip Vortex," Tech. Rep. TM 103975, NASA, 1997.

[24] Batchelor, G. K., "Axial flow in trailing line vortices," *Journal of Fluid Mechanics*, Vol. 20, 1964, pp. 645–658.

[25] Anderson, E. A. and Lawton, T. A., "Correlation Between Vortex Strength and Axial Velocity in a Trailing Vortex," *Journal of Aircraft*, Vol. 40, 2003, pp. 699–704.

[26] Bandyopadhyay, P. R., Stead, D. J., and Ash, R. L., "Organized Nature of a Turbulent Trailing Vortex," *AIAA Journal*, Vol. 29, 1991, pp. 1627–1633.

[27] Zhou, Y., Zhang, H. J., and Whitelaw, J. H., "Wing-Tip Vortex Measurement With Particle Image Velocimetry," *34th AIAA Fluid Dynamics Conference and Exhibit, 28 June - 1 July, Portland, Oregon*, 2004.

[28] Tung, C., Pucci, S. L., Caradonna, F. X., and Morse, H. A., "The structure of trailing vortices generated by model rotor blades," *Vertica*, Vol. 7, No. 1, 1983, pp. 33–43.

[29] McAlister, K. W. and Takahashi, R. K., "NACA 0012 Wing Pressure and Trailing Vortex Measurements," Tech. Rep. TP-3151, NASA, 1991.

[30] Ramasamy, M., Johnson, B., and Leishman, J. G., "Turbulent Tip Vortex Measurements Using Dual-Plane Stereoscopic Particle Image Velocimetry," *AIAA Journal*, Vol. 47, No. 8, 2009, pp. 1826–1840.

[31] Baker, G. R., Barker, S. J., Bofah, K. K., and Saffman, P. G., "Laser anemometer measurements of trailing vortices in water," *Journal of Fluid Mechanics*, Vol. 65, 1974, pp. 325–336.

[32] Bailey, S. C. C. and Tavoularis, S., "Measurements of the velocity field of a wing-tip vortex, wandering in grid turbulence," *Journal of Fluid Mechanics*, Vol. 601, 2008, pp. 281–315.

[33] Martin, P. B., Pugliese, G. J., and Leishman, J. G., "High Resolution Trailing Vortex Measurements in the Wake of a Hovering Rotor," *Journal of the American Helicopter Society*, Vol. 48, 2003, pp. 39–52.

[34] Ramasamy, M. and Leishman, J. G., "Interdependence of Diffusion and Straining on Helicopter Blade Tip Vortices," *Journal of Aircraft*, Vol. 41, No. 5, 2004, pp. 1014–1023.

[35] Narasimha, R. and Sreenivasan, K. R., "Relaminarization of Fluid Flows," *Advances in Applied Mechanics*, Vol. 19, 1979, pp. 221–309.

[36] Holzapfel, F., Hofbauer, T., Gerz, T., and Schumann, U., "Aircraft Wake Vortex Evolution and Decay in Idealized and Real Environments: Methodologies, Benefits and Limitations," *Proceedings of the Euromech Colloquium*, 2000.

[37] Bradshaw, P., "The analogy between strestream curvature and buoyancy in turbulent shear flow," *Journal of Fluid Mechanics*, Vol. 36, 1969, pp. 177–191.

[38] Cotel, A. J. and Breidenthal, R. E., "Turbulence inside a vortex," *Physics of Fluids*, Vol. 11, No. 10, 1999, pp. 3026–3029.

[39] Cotel, A. J., "Turbulence inside a vortex: Take Two," *Physics of Fluids*, Vol. 14, No. 8, 2002, pp. 2933–2934.

[40] Ramasamy, M. and Leishman, J. G., "A Generalized Model for TrTransition Blade Tip Vortices," *60th Annual Forum and Technology Display of the American Helicopter Society International, Baltimore, MD, June 7-11*, 2004.

[41] Lamb, H., *Hydrodynamics*, Dover, New York, 6th ed., 1945.

[42] Iversen, J. D., "Correlation of Turbulent Trailing Vortex Decay Data," *Journal of Aircraft*, Vol. 13, No. 5, 1976, pp. 338–342.

[43] Han, Y. O., Leishman, J. G., and Coyne, A. J., "Measurements of the Velocity and Turbulence Structure of a Rotor Tip Vortex," *AIAA Journal*, Vol. 35, No. 3, 1997, pp. 477–485.

[44] Singh, P. I. and Uberoi, M. S., "Experiments on vortex stability," *Physics of Fluids*, Vol. 19, No. 12, 1976, pp. 1858–1863.

[45] Phillips, W. R. C. and Graham, J. A. H., "Reynolds-stress measurements in a turbulent trailing vortex," *Journal of Fluid Mechanics*, Vol. 147, 1984, pp. 353–371.

[46] Ragab, S. and Sreedhar, M., "Numerical simulations of vortices with axial velocity deficits," *Physics of Fluids*, Vol. 7, No. 3, 1995, pp. 549–558.

[47] Leibovich, S., "Vortex Stability and Breakdown: Survey and Extension," *AIAA Journal*, Vol. 22, No. 9, 1983, pp. 1192–1206.

[48] Zeman, O., "The persistence of trailing vortices: A modeling study," *Physics of Fluids*, Vol. 1, 1995, pp. 135–143.

[49] Squire, H. B., "The Growth of a Vortex in Turbulent Flow," *The Aeronautical Quarterly*, Vol. 16, 1965, pp. 302–306.

[50] Bhagwat, M. J. and Leishman, J. G., "Generalized Viscous Vortex Model for Application to Free-Vortex Wake and Aeroacoustic Calculations," *58th Annual Forum and Technology Display of the American Helicopter Society International, Montreal, Canada, June 11-13*, 2002.

[51] Ramasamy, M. and Leishman, J. G., "A Reynolds Number-Based Tip Vortex Model," *61st Annual Forum of the American Helicopter Society International, Grapevine, Texas, June 1-3*, 2005.

[52] Jacob, J., Savas, O., and Liepmann, D., "Trailing Vortex Wake Growth Characteristics of a High Aspect Ratio Rectangular Airfoil," *AIAA Journal*, Vol. 35, No. 2, 1997, pp. 275–280.

[53] Kundu, P. K. and Cohen, I. M., *Fluid Mechanics*, Elsevier Science, Academic Press, London, 2002.

[54] Hall, M., "The structure of concentrated vortex cores," *Progress in Aerospace Sciences*, Vol. 7, 1966, pp. 53–110.

[55] Wu, J.-Z., Ma, H.-Y., and Zhou, M.-D., *Vorticity and Vortex Dynamics*, Springer-Verlag Berlin Heidelberg, 2006.

[56] Shapiro, A. H., "National Committee for Fluid Mechanics Films. Film Notes for Vorticity," Encyclopaedia Britannica Educational Corporation, 1969.

[57] Saffman, P. G., *Vortex Dynamics*, Cambridge University Press, 1993.

[58] Prandtl, L., "Attaining a steady air stream in wind tunnels," Tech. Rep. No. 726, NACA, 1933.

[59] Uberoi, M., "Effect of Wind-Tunnel Contraction on Free-Stream Turbulence," *Aerodynamics Session, 22nd Annual Meeting, IAS, January 25-29, New York*, 1954.

[60] Tsuge, S., "Effects of flow contraction on evolution of turbulence," *Physics of Fluids*, Vol. 8, 1984, pp. 1948–1956.

[61] Uberoi, M. S. and Nishiyama, R. T., "Effect of intake flow on ambient turbulence," *Physics of Fluids*, Vol. 28, 1985, pp. 81–89.

[62] Batchelor, G., *An Introduction to Fluid Dynamics*, Cambridge University Press, Cambridge, 1967.

[63] Buntine, J. D. and Saffman, P. G., "Inviscid swirling flows and vortex breakdown," *Proceedings of the Royal Society of London A*, Vol. 449, 1995, pp. 139–153.

[64] Rusak, Z. and Meder, C., "Near-Critical Swirling Flow in a Slightly Contracting Pipe," *AIAA Journal*, Vol. 42, 2004, pp. 2284–2293.

[65] Leclaire, B., Jacquin, L., and Sipp, D., "Effects of a contraction on a ununiform rotating flow," *4th AIAA Theoretical Fluid Mechanics Meeting, 6-9 June, Toronto, Ontario, Canada*, No. AIAA 2005-4677, 2005.

[66] Rusak, Z., Bourquard, N., and Wang, S., "Vortex Breakdown in Swirling Flows in Diverging or Contracting Pipes," *51st AIAA Aerospace Sciences Meeting including the New Horizons Forum and Aerospace Exposition, 7-11 January, Grapevine, Texas*, No. AIAA 2013-1010, 2013.

[67] Kreyszig, E., *Advanced Engineering Mathematics*, John Wiley & Sons, Inc., 8th ed., 1999.

[68] Rott, N., "On the viscous core of a line vortex," *Zeitschrift fur Angewandte Mathematik (ZAMP)*, Vol. 9b, 1958, pp. 543–553.

[69] Ananthan, S. and Leishman, J. G., "Role of Filament Strain in the Free-Vortex Modeling of Rotor Wakes," *58th Annual Forum of the American Helicopter Society International, Montreal, Canada, June 11-13*, 2002.

[70] Garbeff II, T. J., Huthmacher, R., Tso, J., Martin, P. B., and Tung, C., "An Experimental Survey of a Wing-Tip Vortex in a Contracted Flow," *40th Fluid Dynamics Conference and Exhibit, Chicago, Illinois, 28 June - 1 July*, No. AIAA 2010-4616, 2010.

[71] Talwar, S., "Vortex Effects on Intake Aerodynamics," MSc Thesis, School of Engineering, Cranfield University, 2005.

[72] Murphy, J., "Intake Ground Vortex Aerodynamics," Ph.D. Thesis, School of Engineering, Cranfield University, 2008.

[73] Hodjatzadeh, H., "The Effect of Vortex Ingestion on Intake Aerodynamics," MSc Thesis, School of Engineering, Cranfield University, 2006.

[74] Althoff Gorton, S., Owens, L. R., Jenkins, L. N., Allan, B. G., and Schuster, E. P., "Active Flow Control on a Boundary-Layer-Ingesting Inlet," *42nd AIAA Aerospace Sciences Meeting and Exhibit, 5-8 January, Reno, Nevada*, No. AIAA 2004-1203, 2004.

[75] Rodriguez, D. L., "Multidisciplinary Optimization Method for Designing Boundary-Layer-Ingesting Inlets," *Journal of Aircraft*, Vol. 46, No. 3, 2009, pp. 883–894.

[76] Hercock, H. G. and Williams, D. D., "Distortion-Induced Instability. Aerodynamic Response," Tech. Rep. LS-72, AGARD, 1974.

[77] Anderson, B. H., "The Aerodynamic Characteristics of Vortex Ingestion for the F/A-18 Inlet Duct," Tech. Rep. TM 103703, NASA, 1991.

[78] Wendt, B. J. and Reichert, B. A., "The Effects of Vortex Ingestion on the Flow in a Diffusing S-Duct," Tech. Rep. TM 106652, NASA, 1994.

[79] Mitchell, G. A., "Effect of Inlet Ingestion of a Wing Tip Vortex on Turbojet Stall Margin," Tech. Rep. TM-X-71610, NASA, 1974.

[80] Genssler, H. P., Meyer, W., and Fottner, L., "Development of Intake Swirl Generators for Turbo Jet Engine Testing," Tech. Rep. CP-400, AGARD, 1987.

[81] Egolf, T. A., Wake, B. E., and Berezin, C., "Recent rotor wake simulation and modeling studies at united technologies corporation (invited)," *38th Aerospace Sciences Meeting and Exhibit, 10-13 January, Reno, NV*, No. AIAA 2000-0115, 2000.

[82] Dacles-Mariani, J., Kwak, D., and Zilliac, G., "On Numerical Errors and Turbulence Modeling in Tip Vortex Flow Prediction," *International Journal for Numerical Methods in Fluids*, Vol. 30, 1999, pp. 1561–1568.

[83] Spall, R. E., "Numerical Study of a Wing-Tip Vortex Using the Euler Equations," *AIAA Journal*, Vol. 38, No. 1, 2001.

[84] Wells, J., Salem-Said, A., and Ragab, S. A., "Effects of Turbulence Modeling on RANS Simulations of Tip Vortices," *48th AIAA Aerospace Sciences Meeting Including the New Horizons Forum and Aerospace Exposition, 4-7 January, Orlando, FL*, No. AIAA 2010-1104, 2010.

[85] Smirnov, P. E. and Menter, F. R., "Sensitization of the SST Turbulence Model to Rotation and Curvature by Applying the Spalart-Shur Correction Term," *Journal of Turbomachinery*, Vol. 131, October 2009.

[86] Beresh, S., Henfling, J., and Spillers, R., "Meander of a fin trailing vortex and the origin of its turbulence," *Experiments in Fluids*, Vol. 49, 2010, pp. 599–611.

[87] Raffel, M., Willert, C., Werely, S., and Kompenhans, J., *Particle Image Velocimetry: A Practical Guide*, Springer, Berlin, 2007.

[88] Ramasamy, M., Johnson, B., Huismann, T., and Leishman, J. G., "An Improved Method for Estimating Turbulent Vortex Flow Properties from Stereoscopic DPIV

Measurements," *62nd Annual National Forum of the American Helicopter Society International, May 1-3, Virginia Beach, VA*, 2007.

[89] Ramaprian, B. and Zheng, Y., "Measurements in the Rollup Region of the Tip Vortex from a Rectangular Wing," *AIAA Journal*, Vol. 35, No. 12, 1997.

[90] Polhamus, E., "A Concept of the Vortex Lift of Sharp-Edge DeltaWings Based on a Leading-Edge-Suction Analogy," Tech. Rep. TN D-3767, NASA, 1966.

[91] Scarano, F., "Iterative image deformation methods in PIV," *Measurement Science and Technology*, Vol. 13, 2002, pp. R1–R19.

[92] Ramasamy, M. and Leishman, J. G., "Benchmarking Particle Image Velocimetry with Laser Doppler Velocimetry for Rotor Wake Applications," *AIAA Journal*, Vol. 45, No. 11, 2007, pp. 2622–2633.

[93] Werely, S. T. and Gui, L., "A correlation-based central difference image correction (CDIC) method and application in a four-roll mill flow PIV measurement," *Experiments in Fluids*, Vol. 34, 2003, pp. 42–51.

[94] Westerweel, J. and Scarano, F., "Universal Outlier Detection for PIV Data," *Experiments in Fluids*, Vol. 39, 2005, pp. 1096–1100.

[95] Burley, C. L., Brooks, T. F., Van der Wall, B., Richard, H., Raffel, M., Beaumier, P., Delrieux, Y., Lim, J. W., Yu, Y., Tung, C., and Pengel, K. M. E., "Rotor Wake Vortex Definition - Initial Evaluation of 3-C PIV Results of the HART-II Study," *28th European Rotorcraft Forum, Bristol, UK*, 2002.

[96] Van Doorne, C., Westerweel, J., and Nieuwstadt, F., "Measurement uncertainty of Stereoscopic-PIV for flow with large out-of-plane motion," *Proceedings of the EUROPIV2 final workshop on Particle Image Velocimetry, Zaragoza, Spain*, 2003.

[97] Hall, M., "Vortex Breakdown," *Annual Review of Fluid Mechanics*, Vol. IV, 1972, pp. 195–217.

[98] Wang, F., Milanovic, I., Zaman, K., and Povinelli, L., "A Quantitative Comparison of Delta Wing Vortices in the Near-Wake For Incompressible and Supersonic Free Streams," *Journal of Fluids Engineering*, Vol. 127, 2005, pp. 1071–1084.

[99] Birch, D., Lee, T., Mokhtarian, F., and Kafyeke, F., "Structure and Induced Drag of a Tip Vortex," *Journal of Aircraft*, Vol. 41, No. 5, 2004, pp. 5.

[100] Burley, C. L., Brooks, T. F., Van der Wall, B., Richard, H., Raffel, M., Beaumier, P., Delrieux, Y., Lim, J. W., Yu, Y., Tung, C., and Pengel, K. M. E., "Rotor Wake Vortex Definition Using 3C-PIV Measurements - Corrected for Vortex Orientation," *9th AIAA/CEAS Aeroacoustics Conference, Hilton Head, South Carolina, May 12-14*, 2003.

[101] Zantopp, S., "Jet Engine Ground Vortex Studies," MSc Thesis, School of Engineering, Cranfield University, 2008.

[102] Nichols, R. H., "Algorithm and Turbulence Model Requirements for Simulating Vortical Flows," *46th AIAA Aerospace Sciences Meeting and Exhibit, Reno, Nevada, 7-10 January*, No. AIAA 2008-337, 2008.

[103] Vatistas, G. H. and Kozel, V., "A simpler model for concentrated vortices," *Experiments in Fluids*, Vol. 11, 1991.

[104] Devenport, W. J., Rife, M. C., Liapis, S. I., and Follin, G. J., www.dept.aoe.vt.edu/research/groups/flowdata.

[105] ANSYS Inc., *ANSYS FLUENT 12.0 User's Guide*.

[106] ANSYS Inc., *ANSYS FLUENT 12.0 Theory Guide*.

[107] Stankowski, T., "Computational Method for Vortex Ingestion Aerodynamics," MSc Thesis, School of Engineering, Cranfield University, 2012.

[108] Baldwin, B. S., Chigier, N. A., and Sheaffer, Y. S., "Decay of Far-Flowfield in Trailing Vortices," *AIAA Journal*, Vol. 11, No. 12, 1973, pp. 1601–1602.

[109] "Wolfram MathWorld: Full Width at Half Maximum," www.mathworld.wolfram.com/FullWidthatHalfMaximum.html, Accessed: 09/2013.

[110] Wilcox, D. C., *Turbulence Modeling for CFD*, DCW Industries, Inc., 1994.

[111] Mayer, E. W. and Powell, K. G., "Similarity solutions for viscous vortex cores," *Journal of Fluid Mechanics*, Vol. 238, 1992, pp. 487–507.

[112] Aboelkassem, Y. and Vatistas, G. H., "New Model for Compressible Vortices," *Journal of Fluids Engineering*, Vol. 129, 2007, pp. 1073–1079.

[113] SAE, "A Methodology for Assessing Inlet Swirl Distortion," Tech. Rep. AIR5686, 2007.

[114] Strohmeyer, D. and Seubert, R., "Improvement of a Preliminary Design and Optimization Program for the Evaluation of Future Aircraft Projects," *7th AIAA/USAF/NASA/ISSMO Symposium on Multidisciplinary Analysis and Optimization, St. Louis, September 15-18*, No. 98-4828, 1998.

[115] Heimbucher, P., "Vortex Ingestion Aerodynamics for Aero Engines," MSc Thesis, School of Engineering, Cranfield University, 2012.

[116] Newman, B., "Flow in a Viscous Trailing Vortex," *Aeronautical Quarterly*, Vol. 10, 1959, pp. 149–162.

[117] Pernod, M., "Distortion Ingestion for Aero Engines," MSc Thesis, School of Engineering, Cranfield University, 2013.

[118] Garnier, E., Leplat, M., Monnier, J. C., and Delva, J., "Flow control by pulsed jet in a highly bended S-duct," *6th AIAA Flow Control Conference, 25-28 June, New Orleans, Louisiana*, No. AIAA 2012-3250, 2012.

[119] Adrian, R. J. and Westerweel, J., *Particle Image Velocimetry*, Cambridge University Press, 2011.